

The University of Nottingham

UNITED KINGDOM · CHINA · MALAYSIA

Integrated Geochemical Approaches for Water Remediation in the Golden Triangle, Egypt

Tharwat Hassan

Thesis submitted to the University of Nottingham for the degree of Doctor of Philosophy

[January 2023]

ABSTRACT

Egypt Vision 2030 is centred on a number of national initiatives, including the Golden Triangle Economic zone, the Siemens-Egypt project, the New Suez Canal project, the El-Dabaa power plant, and the New Administrative City. As a consequence, the Egyptian economy will become more competitive on a worldwide scale. The second national mega project, the Golden Triangle Economic zone, is situated in the Eastern Desert stretched between the towns of Qena, Safaga, and Qusir, and it aspires to create a new industrial capital in this attractive region. The Eastern Desert in general and the Golden Triangle in particular are now seeing a renaissance of mining and exploration activity. The initiative intends to create a new economic activity based on the available natural resources and their prime position between the Nile Valley and the Red Sea. Growing the agricultural land in the Nile Valley, establishing new industries and desalination plants, creating new urban settlements, expanding the mining operations, exploiting certain mineral reserves, and creating new resorts and tourist villages are some of the potential development activities. The quality and accessibility of water resources are crucial for achieving these prospective goals.

Heavy metal species and concentrations in the groundwater of the Golden Triangle area of Egypt have been assessed. In particular, the thesis demonstrates the degree of groundwater contamination with heavy metals in the study area, taking into consideration the role of the geogenic and anthropogenic activities. Moreover, a novel geopolymer adsorbent was successfully synthesized from a heterogeneous natural aluminosilicate precursor for the metal ions sequestration. Heavy metal concentrations and species were determined based on the multielement chemical analysis of the groundwater samples. The calculated HPI index revealed that the groundwater in the Golden Triangle area is contaminated with serious heavy metals. The contamination level is in the order of coastal zone>crystalline rocks zone>Nile valley zone. The groundwater samples HW, BH and FKH are not suitable for drinking purposes due to the presence of high levels of toxic metal ions such as As, Mn, Cd, Co, Ni, Se, V, and Tl.

The geopolymerization of a heterogeneous geological precursor, calcareous red mudstone, was investigated. The experimental and analytical techniques confirmed an improved reactivity with increasing the thermal activation up to 800 ºC. Moreover, feeding the geopolymer slurry with a more silicate was necessary during the geopolymerization process to reduce the effect of carbonation and to ensure a well-developed structure. The alkali activation of mudstone

resulted in the formation of various hydration products, including calcium aluminium silicate hydrate, sodium aluminium silicate hydrate and sodium ferrosialate hydrate phases.

The calcareous red mudstone geopolymer adsorbents demonstrated an improved adsorption removal in comparison to the raw material. Cd^{2+}, Co^{2+}, Ni^{2+}, and Mn^{2+} sequestration on the geopolymer surfaces was hypothesised to occur by the ion exchange, surface complexation and the electrostatic interaction mechanisms. The effectiveness of the metal ions removal from groundwater, a highly competitive system, has been examined. The statistical regression analysis showed that the data best fit with the Langmuir adsorption rather than the Freundlich isotherm. Additionally, the interaction between the geopolymer adsorbent and metal ions could be described by a pseudo-second-order kinetic model. Thermodynamics suggested an endothermic, spontaneous, and a chemical adsorption mechanism.

Keywords: Golden Triangle; Geopolymer; Groundwater; Heavy metals; Water treatment; Adsorption; Egypt.

PARTICIPATION IN CONFERENCES AND SYMPOSIUMS

Conferences

1- Annual British Zeolite Association meeting, Birmingham, UK, 2019.
2- Goldschmidt conference, Barcelona, Spain, 2019.
3- 11th Geopolymer Camp, Geopolymer Institute, France, 2019.
4- Annual British Zeolite Association meeting, Durham, UK, 2022.
5- 5th Annual UK porous materials conference, Glasgow, UK, 2022.

Symposiums

1- Postgraduate symposium, School of Chemistry, University of Nottingham, 2019.
2- Postgraduate symposium, School of Chemistry, University of Nottingham, 2021.

ACKNOWLEDGEMENTS

First and foremost, I would like to thank most sincerely my supervisor. Prof. Robert Mokaya for his continuous support and invaluable guidance during my study. In addition, my sincere appreciation also goes to my current and former colleagues in Mokaya's group.

I would like to thank the technician team in the School of Chemistry, University of Nottingham for providing training and support. Special thanks go to Sue for her kind morale and support. I also acknowledge the Researcher Academy, the University of Nottingham, and the Royal Society of Chemistry for the financial support enabling my participation in conferences.

I would like to acknowledge the British Council and the Ministry of Higher Education of Egypt for supporting and funding the PhD research project through a Newton-Mosharafa Scholarship. I would also like to thank the Egyptian Bureau for Cultural and Educational Affairs for their guidance and continuous support.

I would also like to extend special thanks to the staff members at Geology Department, South Valley University for their help during the fieldwork in Egypt.

Finally, from the bottom of my heart, I wish to express my sincere gratitude to my family whose patience, encouragement, and love have given me the power, motivation, and enthusiasm, not only during my study journey but also throughout my life. To them, I humbly dedicate this piece of study.

Tharwat Hassan

LIST OF ABBREVIATIONS

List of abbreviations

ATR- Attenuated Total Reflection

Al_2O_3- Aluminum oxide

BET- Brunauer Emmett Teller

BJH- Barrett-Joyner-Halenda

℃- Celsius

CEC- Cation exchange capacity

CASH- Calcium aluminum silicate hydrate

CaO- Calcium oxide

$CaCO_3$- Calcium carbonate

CSH- Calcium silicate hydrate

CRM- Calcareous Red Mudstone

EDX- Energy Dispersive X-Ray

EPMA- Electron probe-microanalyzer

EBCT- Empty bed contact time

FTIR- Fourier transform infrared

g- Gram

HPI – Heavy metals pollution index

HNO_3- Nitric acid

ICPOES- Inductively Coupled Plasma Optical Emission spectroscopy

IS- Isomer shift

IPD- Intraparticle diffusion model

K_2O- Potassium oxide

K- Kelvin

kV- Kilovolt

K_d- Distribution factor

KOH- Potassium hydroxide

K_2SiO_3- Potassium silicate

Milli-Q- Ultra pure water

mL- Milliliter

LIST OF ABBREVIATIONS

mg/L- Milligram/Liter

MgO- Magnesium oxide

$MgCO_3$- Magnesium carbonate

NaOH- Sodium hydroxide

Na_2SiO_3- Sodium silicate

NaCl- Sodium chloride

Na_2SO_4- Sodium sulphate

Na_2CO_3- Sodium carbonate

NASH- Sodium aluminum silicate hydrate

QS- Quadrupole splitting

PXRD- Powder X-ray Diffraction

PFO- Pseudo-first order

PSO- Pseudo-second order

RMSE- Root mean square error

RSS- Residual sum of squares

R^2- Coefficient of determination

SEM- Scanning electron microscopy

SD- Standard deviation

S_{BET}- Specific surface area

SiO_2- Silicon oxide

S/L- Solid/Liquid

V_t- Total pore volume

ug/L- Microgram/Liter

XRF- X-ray fluorescence

LIST OF EQUATIONS

List of equations

Equation		Number	Page
Chemical precipitation	$M^{2+} + 2(OH^{-}) \leftrightarrow 2M(OH) \downarrow$	(2-1)	12
Geopolymer empirical formula	$Mn^{+}\ [(SiO_2)\ z\text{-}\ AlO_2^{-}]\ n$	(2-2)	21
Heavy metal pollution index (HPI)	$HPI = \frac{\sum_{i=1}^{n} W_i\, Q_i}{\sum_{i=1}^{n} W_i}$	(3-1)	52
	$Q_i = \sum_{i=1}^{n} \frac{\{M_i(-)I_i\}}{(S_i - I_i)}\ x100$	(3-2)	52
Adsorption capacity	$q_t = \frac{(Co - Ct)\mathrm{V}}{m}$	(5-1)	127
Removal efficiency	$(\%) = \frac{(Co-Ct)}{Co}\ X100$	(5-2)	127
Coefficient of determination	$R^2 = \frac{SS_{Regression}}{SS_{Total}}$	(5-3)	128
Mean Square Error	$(MSE) = \sqrt{\sum_{i=1}^{N} (p_i - o_i)^2/N}$	(5-4)	128
Residual Sum of Squares	$RSS = \sum_{i=1}^{N} (\mathrm{y}_i - \tilde{\mathrm{y}}_i)^2$	(5-5)	128
F-Value	$\mathrm{F} = \frac{(\mathrm{RSS}_1 - RSS_2)/(p_2 - p_1)}{RSS_2/(\mathrm{n} - p_2 - 1)}$	(5-6)	128
Pseudo-first order kinetic model	$\ln(q_e - q_t) = \ln q_e - k_1 t$	(5-7)	146
Pseudo-second order kinetic model	$\frac{t}{q_t} = \frac{1}{k_2 q_e^2} + \frac{t}{q_e}$	(5-8)	146
Intraparticle diffusion model	$q_t = K_{id} t^{0.5} + C$	(5-9)	148
Langmuir isotherm model	$\frac{C_e}{q_e} = \frac{1}{q_m b} + \frac{C_e}{q_m}$	(5-10)	150
Freundlich isotherm model	$\log q_e = \log K_F + \frac{1}{n}\ log C_e$	(5-11)	150

LIST OF EQUATIONS

Langmuir separation factor	$R_L = \frac{1}{1 + bC_o}$	(5-12)	152
Vant'hoff	$\ln \mathrm{K_d} = \frac{\Delta \mathrm{S}^0}{\mathrm{R}} - \frac{\Delta \mathrm{H}^0}{\mathrm{RT}}$	(5-13)	153
Empty bed contact time	$EBCT = {bed\ volume}/{flow\ rate}$	(5-14)	155
Adsorption capacity of column	$q = (t \times f \times c)/m$	(5-15)	155

LIST OF FIGURES

Chapter 2 **Page**

Figure 2.1 Chemical precipitation technology……13

Figure 2.2 Coagulation-flocculation technology…….……14

Figure 2.3 Reverse osmosis technology……..……..14

Figure 2.4 Ion exchange technology…….……...15

Figure 2.5 Steps of adsorption process……17

Figure 2.6 Types of adsorption……....18

Figure 2.7 Conceptual model of geopolymerization……23

Figure 2.8 Classification of polysialate structure ……....24

Figure 2.9 Aluminosilicate mineral structure……...27

Chapter 3

Figure 3.1 Anthropogenic sources of contamination……...42

Figure 3.2 Location map of the Golden Triangle area……44

Figure 3.3 Geological map of the study area……45

Figure 3.4 Generalized cross-section for the middle part……46

Figure 3.5 Stream order of the Golden Triangle…….……47

Figure 3.6 Digital elevation model of the study area…….…… 49

Figure 3.7 Groundwater sampling……..……..51

Figure 3.8 Photographs showing various types of wells…….……53

Figure 3.9 Ni, Co, Mn, and Cd concertation……56

Figure 3.10 As, Cu, Zn, and Pb concentration……..……..……57

Figure 3.11 Fe, U, Cs, and V concentration…..……..……59

Figure 3.12 Ba, Se, Cr, Tl, and Rb concentration……61

Figure 3.13 Heavy metals pollution index categories……..……63

Figure 3.14 Heavy metals pollution index for metal ions……64

Figure 3.15 Aerial distribution maps for trace elements…….……65

Figure 3.16 Aerial distribution maps for trace elements……..66

Figure 3.17 Anthropogenic activities and potential sources of contamination……67

Figure 3.18 Sources of contamination in the Nile Valley……69

Figure 3.19 Location of BH and FKH wells, El-Fawakhir…….……70

LIST OF FIGURES

Figure 3.20 Abu-Kharif wolframite mining area……71

Figure 3.21 Scatter diagrams of K^++Na^+ and Ca^{2+}+Mg^{2+} vs total cations……..72

Chapter 4

Figure 4.1 Geopolymerization of the CRM……80

Figure 4.2 Comparison between CRM, fly ash, blast furnace slag, and metakaolin…..……..85

Figure 4.3 Petrography of raw CRM……86

Figure 4.4 XRD analysis of raw material……87

Figure 4.5 Chemical composition of CRM-forming minerals……88

Figure 4.6 FTIR spectrum of raw material……..89

Figure 4.7 SEM micrograph of raw CRM……90

Figure 4.8 Clay minerals in raw CRM……91

Figure 4.9 XRD analysis of calcined CRM at different temperature……...93

Figure 4.10 FTIR spectra of calcined CRM at different temperature……..……95

Figure 4.11 FTIR spectra of calcined CRM……95

Figure 4.12 SEM micrographs of calcined CRM at different temperature……..……96

Figure 4.13 SEM micrographs of calcined CRM at different temperature……..97

Figure 4.14 Si and Al release of thermally activated CRM……98

Figure 4.15 FTIR spectra of calcined CRM after leaching……99

Figure 4.16 Dispersion behaviour of calcined CRM……..……100

Figure 4.17 Reactivity of the calcined CRM……..101

Figure 4.18 Time dependent shift in Si-O-T bond……103

Figure 4.19 XRD analysis for the produced geopolymers……...……..105

Figure 4.20 FTIR spectra of the formulated geopolymers……...……..106

Figure 4.21 SEM micrographs in MR-1 geopolymer……108

Figure 4.22 SEM micrographs I MR-2 geopolymers……..……109

Figure 4.23 EDX spectra and associated SEM images……..……111

Figure 4.24 Ternary diagram of Si, Ca, and Al……..……112

Figure 4.25 Mossbauer spectra for geopolymer samples……..……..114

Chapter 5

Figure 5.1 Geopolymerization of red mudstone for metal ions removal……..….124

LIST OF FIGURES

Figure 5.2 The synthesis procedure of the CRM geopolymer……...126
Figure 5.3 XRD analysis of geopolymer, raw and thermally activated phase…….……..130
Figure 5.4 FTIR spectra of geopolymer adsorbents…….……..131
Figure 5.5 Nitrogen sorption isotherms……..132
Figure 5.6 SEM micrographs of geopolymer adsorbents…….……..134
Figure 5.7 Adsorption removal efficiency of raw CRM at different time…….……135
Figure 5.8 Effect of contact time on the removal of metal ions…….……136
Figure 5.9 Effect of pH on the removal of metal ions……137
Figure 5.10 Residual metal ions concentration of metal ions at pH3……..……...138
Figure 5.11 Effect of adsorbent mass on the removal of metal ions……..……139
Figure 5.12 Effect of initial concentration on the removal of metal ions…….…….140
Figure 5.13 Distribution factor at different initial concentration……..…….……141
Figure 5.14 Effect of grain size of adsorbent on the removal……142
Figure 5.15 Effect of solution temperature……143
Figure 5.16 Saturation of the geopolymer surface with NH_4^+……...144
Figure 5.17 Exchanged cations at different metal ions concentration……..……..…145
Figure 5.18 Kinetic plots for metal ion adsorption……147
Figure 5.19 Intraparticle diffusion plot……..149
Figure 5.20 Adsorption isotherm……...151
Figure 5.21 Langmuir separation factor……153
Figure 5.22 Van't Hoff plot of 1/T versus $link_d$……154
Figure 5.23 Column experiment design and breakthrough curves…….……156
Figure 5.24 Regeneration of CRM geopolymer……...……..157
Figure 5.25 Groundwater samples location……158
Figure 5.26 Metal ions removal from natural groundwater…….……..159
Figure 5.27 Effect of co-existing anions on metal ions removal……160
Figure 5.28 EDX spectrum of CRM adsorbent……...……...161
Figure 5.29 Elemental mapping for CRM geopolymer……...…..……..161
Figure 5.30 Mechanism of metal ions sequestration on CRM geopolymer……...……162
Figure 5.31 Surface saturation of CRM geopolymer…….…..……..163

LIST OF TABLES

Page

Table 2.1 Adsorption kinetic models……...……19

Table 2.2 Adsorption isotherms……...20

Table 2.3 Some results reported in literatures for geopolymer adsorbents…….….30

Table 4.1 Chemical composition of raw CRM and geopolymers……85

Table 4.2 Elemental composition for selected points in MR-1 and MR-2…….110

Table 4.3 Hyperfine parameters obtained from fitting on Mössbauer spectra……...113

Table 5.1 Geopolymer mix designs……126

Table 5.2 Chemical composition of raw CRM and geopolymer adsorbents……..129

Table 5.3 Textural properties of geopolymer adsorbents and raw phases……..……..133

Table 5.4 Elemental composition for selected points in MR-3, MR-4, and MR-5……134

Table 5.5 Cation exchange capacity of geopolymer adsorbents……144

Table 5.6 PFO and PSO kinetic parameters……...146

Table 5.7 Intraparticle diffusion parameters……..149

Table 5.8 Adsorption isotherm parameters……150

Table 5.9 Langmuir separation factor calculations……152

Table 5.10 Calculated thermodynamic parameters……155

Table A-1 Physicochemical characteristics of groundwater samples……173

Table A-2 Groundwater chemistry data……174

Table A-3 Groundwater major cations chemistry and HPI calculations……175

Table B-1 Leaching experiments data of Si and Al release……...176

Table C-1 Batch adsorption data of metal ions using raw material……...177

Table C-2 Batch adsorption data of metal ions at different time intervals, MR-3….……178

Table C-3 Batch adsorption data of meta ions at different time intervals, MR-5…….….179

Table C-4 Batch adsorption data of metal ions at different time intervals, MR-4…….…180

Table C-5 Batch adsorption data of metal ions at different pH……..181

Table C-6 Batch adsorption data of metal ions removal at different initial concentrations...182

Table C-7 Batch adsorption data of meta ions removal at different dose……..183

Table C-8 Batch adsorption data of metal ions removal at different grain size…….…184

Table C-9 Batch adsorption data of metal ions removal at different temperatures……....185

LIST OF TABLES

Table C-10 Dynamic adsorption experimental data……...186

Table C11 Regeneration experiments data…….187

Table C-12 Batch adsorption data for groundwater decontamination……...188

Table C-13 Batch adsorption data of co-existing anions……...189

TABLE OF CONTENTS

Table of Contents

Abstract..... i

Participation in conferences and symposiums.....iii

Acknowledgements..... iv

List of abbreviations.....v

List of equations..... vii

List of figures..... ix

List of tables.....xii

Table of contents..... xiv

Chapter 1.0 General Introduction..... 1

1.1 Background 1

1.2 Statement of the problem 2

1.3 Aim of the research.……..……..……...3

1.4 Research objectives…….……..……3

1.5 Thesis structure…….……...……4

1.5.1 Chapter 2…….....……4
1.5.2 Chapter 3…….....……4
1.5.3 Chapter 4…….....……4
1.5.4 Chapter 5…….……5
1.5.5 Chapter 6…….....……5
1.5.6 Funding…….……..……5
1.5.7 References…….……..……6

Chapter 2.0 Literature Review 8

2.1 Introduction 8

2.2 Heavy metals as a potential contaminant of water bodies…….....…….8

2.2.1 Cadmium……..……..9

2.2.2 Nickel……...…..……..10

2.2.3 Cobalt……...…….....……10

2.2.4 Manganese……..…….10

2.2.5 Copper……..…….....11

2.2.6 Lead……..……...…….11

2.2.7 Zinc…….…….....……...11

2.2.8 Arsenic……..……...11

2.3 Water treatment technologies…….……12

TABLE OF CONTENTS

2.3.1 Chemical precipitation……12

2.3.2 Coagulation-flocculation……13

2.3.3 Reverse osmosis……13

2.3.4 Ion exchange……15

2.3.5 Adsorption……15

2.3.5.1 Mechanism of adsorption……16

2.3.5.1.1 Physisorption……17

2.3.5.1.2 Chemisorption……17

2.3.5.2 Adsorption kinetics and isotherms……18

2.4 Geopolymer as an innovative technology in water purification……21

2.4.1 Concept of geopolymerization……21

2.4.2 Mechanism of geopolymerization……22

2.4.3 Geopolymer structure……22

2.4.4 Factors that control the geopolymerization reaction……24

2.4.4.1 Alkaline activator……24

2.4.4.2 Si/Al ratio……25

2.4.4.3 Dissolved silica……25

2.4.4.4 Liquid/Liquid ratio……26

2.4.4.5 Reactivity of source material……26

2.4.4.6 Curing conditions……28

2.4.5 Adsorption characteristics of geopolymer……28

2.5 References……32

Chapter 3.0 Heavy metals distribution in the Golden Triangle Economic Zone……42

3.1 Introduction……43

3.1.1 General geology……45

3.1.2 Water resources……46

3.1.3 Potential sources of water pollution……48

3.1.3.1 Anthropogenic……48

3.1.3.1.1 Mining activities……49

3.1.3.1.2 Agricultural activities……49

3.1.3.1.3 Industrial activities……50

3.1.3.2 Geogenic……50

3.1.3.2.1 Water-rock interaction……50

3.1.3.2.2 Sea water intrusion……50

TABLE OF CONTENTS

3.2 Material and methods……..51
3.2.1 Groundwater sampling……51
3.2.2 Heavy metal determination……..52
3.2.3 Heavy metal pollution index (HPI)……52
3.3 Results and discussion……..53
3.3.1 Heavy metals specification……53
3.3.1.1 Nickel……..53
3.3.1.2 Cobalt……54
3.3.1.3 Manganese……54
3.3.1.4 Cadmium……..55
3.3.1.5 Arsenic……55
3.3.1.6 Copper……55
3.3.1.7 Zinc……56
3.3.1.8 Lead……57
3.3.1.9 Iron……58
3.3.1.10 Uranium……58
3.3.1.11 Cesium……58
3.3.1.12 Vanadium……58
3.3.1.13 Barium……59
3.3.1.14 Selenium……59
3.3.1.15 Chromium……...60
3.3.1.16 Rubidium……..60
3.3.1.17 Thallium……60
3.3.2 Heavy metals pollution in groundwater……62
3.3.2.1 Heavy metal pollution index……..62
3.3.2.2 Potential causes of heavy metals contamination in groundwater....65
3.3.2.2.1 Groundwater pollution in coastal zone…….....67
3.3.2.2.2 Groundwater pollution in Nile Valley…….....68
3.3.2.2.3 Groundwater pollution in crystalline rocks zone…….....68
3.4 Conclusion……..73
3.5 References……..74

TABLE OF CONTENTS

Chapter 4.0 Synthesis and characterization of rock-based geopolymer: Alkali activation affinity…..80

4.1 Introduction…….....…….……81

4.2 Materials and methods…….....….....……82

4.2.1 Raw material preparation…….....……..……82

4.2.2 Thermal activation…….....……..……82

4.2.3 Geopolymeric affinity of red mudstone…….....……..……82

4.2.3.1 Solubility in alkaline medium…….....……82

4.2.3.2 Reactivity in the early stages of reaction (FT-IR study)…….....…..83

4.2.3.3 Effect of alkaline activator composition (silicate content) ….....83

4.2.4 Analytical methods…….....……83

4.3 Results and discussion…….....…….....….……84

4.3.1Raw material……..…….....……..84

4.3.1.1 Chemical composition…….....……84

4.3.1.2 Mineralogy and mineral chemistry…….....……85

4.3.1.3 FT-IR…….…….....…….89

4.3.1.4 SEM-EDX…….…….....……..90

4.3.2 Thermally activated phase…….……..91

4.3.2.1 Mineralogy…….....……91

4.3.2.2 FT-IR…….....……94

4.3.2.3 SEM-EDX…….....……..96

4.3.3 Geopolymerization of calcined red mudstone…….....……..98

4.3.3.1 Reactivity under alkaline conditions (low temperature system, 25 ºC) 98

4.3.3.1.1 Silicate (Si^{4+}) and aluminate (Al^{3+}) species leaching…....98

4.3.3.1.2 Dispersion and gelation in alkaline medium……..……99

4.3.3.1.3 Evaluation of CRM in alkali activation as a function of time 100

4.3.3.2 Alkali activation of CCRM (low and high silicate systems, 100 ºC) …….....……104

4.3.3.2.1 Chemical composition…….....……104

4.3.3.2.2 Mineralogy……...……104

4.3.3.2.3 FT-IR……105

4.3.3.2.4 SEM-EDX……107

4.3.3.2.5 Mossbauer spectroscopy……113

4.4 Conclusion……116

4.5 References……117

Chapter 5.0 Simultaneous sequestration of Cd^{2+}, Co^{2+}, Mn^{2+} and Ni^{2+} from aqueous solution……123

5.1 Introduction……124

5.2 Materials and methods……125

5.2.1 Raw material preparation……125

5.2.2 Thermal activation……125

5.2.3 Geopolymer adsorbent synthesis……125

5.2.4 Adsorption experiments……127

5.2.5 Analytical methods……127

5.2.6 Quality control and precision……128

5.3 Results and discussion……129

5.3.1 Characterization of geopolymer adsorbents……129

5.3.1.1 Chemical composition……129

5.3.1.2 Mineralogy……129

5.3.1.3 FT-IR……130

5.3.1.4 BET surface area……132

5.3.1.5 SEM analysis……133

5.3.2 Adsorption experiments……134

5.3.2.1 Raw CRM evaluation in metal ion sequestration……134

5.3.2.2 Effect of operating parameters……135

5.3.2.2.1 Effect of contact time……135

5.3.2.2.2 Effect of pH……136

5.3.2.2.3 Effect of geopolymer mass……138

5.3.2.2.4 Effect of initial concentration……139

5.3.2.2.5 Effect of grain size……141

5.3.2.2.6 Effect of temperature……142

5.3.2.3 Cation exchange capacity……143

5.3.2.4 Adsorption kinetics……146

5.3.2.5 Adsorption isotherms……150

5.3.2.6 Thermodynamic study……...……153

5.3.2.7 Dynamic adsorption…….……..155

5.3.2.8 Reusable capacity of CRM geopolymer……....……157

5.3.2.9 A pilot study for groundwater decontamination…….....……...158

5.3.2.10 Effect of co-existing anions…….……159

5.3.2.11 EDX analysis after adsorption……...……..160

5.3.2.12 Mechanism of metal ions sequestration on CRM geopolymer…162

5.3.2.13 Geopolymer active sites saturation…….....…….163

5.3.2.14 Adsorption selectivity interpretation……164

5.4 Conclusion…….....……165

5.5 References…….....……167

Chapter 6.0 Summary and recommendations……..…….171

Appendixes……..…….....……173

CHAPTER 1: GENERAL INTRODUCTION

1.1 Background

Anthropogenic activities along with the role of climate change have impacted the global water resources in terms of availability and quality. Egypt is one of the countries that are facing a high pressure with regard to the available and limited water resources due to increased population and the related upswing in water consumption. Groundwater has been identified as a valuable source of freshwater to meet such growing demand. Several geochemical studies have been conducted in the Golden Triangle area of Egypt aimed at evaluating the groundwater quality. These studies have revealed that the area has a potential reserve of groundwater, especially in the so-called Nubian sandstone aquifers.[1, 2] Sulfate and chloride are the predominant chemical species in the groundwater in the study area. Moreover, the groundwater salinity is high as a result of the water-rock interaction and mixing with brines.[2] Mining activities are one of the potential sources of heavy metals in the environment with the consequence that groundwater quality is seriously endangered owing to the disposal of mining wastes, from which a various and countless pollutants (e.g., heavy metals) can be leached out. As a result, the groundwater quality can deteriorate for several years even after the closure of mines.[3] However, the conditions that modify the groundwater quality through the interaction with wastes, rocks, and minerals are not clear. The lack of information about the groundwater contamination with heavy metals, due to either anthropogenic or geogenic activities, presents challenges to achieving the prospective projects in the Golden Triangle region. Vigorous extraction and exploitation of the economic minerals and metals produce a huge quantity of tailings. Metallic mineral deposits are rich in sulfides such as pyrrhotite and pyrite where the Co and Ni can be released through an oxidation process.[4, 5] In addition, the Cd, Cr, Pb, Zn, Cu, Fe, and Mn metals can enter the environmental system through leaching processes from phosphate rocks, soils, waste, and fertilizers.[3, 6-8] Mineral dissolution and the mobility of metal ions are mainly controlled by the pH of the surrounding environment; the release of heavy metals is high in case of a low pH where the dissolution process is high and the related release of heavy metals is active.[9] Immobilization of hazardous heavy metals can be performed within the structure of porous materials having a good adsorption properties. Zeolites, metal-organic frameworks, and the activated carbon have shown a high performance in this regard.[10-12] Amorphous aluminosilicate materials can be used in the synthesis of inorganic geopolymer adsorbents for the metal ions sequestration. The effectiveness of such materials in the uptake

of heavy metals is attributed to their amorphous 3D aluminosilicate structure which has voids accommodating active sites.

The emergent use of geopolymer in the field of water purification is receiving a great deal of interest. A few studies have discussed the suitability of industrial wastes, apart from the fly ash and blast furnace slag, in the formulation of geopolymer adsorbents. Mining activities produce a huge amount of the waste of a fine-grained nature, containing amorphous constituents. From both the environmental and economic points of view, the transformation of mining wastes into geopolymer adsorbents is an efficient approach not only to reduce the potential contamination of heavy metals but also to make use of such low-cost and sustainable sources for the water purification purposes. However, the reactivity of such materials, either in the form of intact rock or as waste, in the alkali activation is not clear.

1.2 Statement of the problem

The presence of heavy metals in groundwater is a devastating threat to human life and the ecosystem due to their toxicity. Cd^{2+}, Mn^{2+}, Ni^{2+}, and Co^{2+} are the common heavy metals that tend to accumulate in the human body, causing countless diseases.[13-15] Groundwater is the main and important source of water in the arid environments, therefore improving its quality is necessary. The Golden Triangle area of Egypt is the second largest national project, which aims to establish an industrial capital in this economic zone. Groundwater is the main source of freshwater in the study area, which will be used to achieve the prospective goals of the Golden Triangle project. The groundwater quality is well investigated in terms of the general characteristics; however, little is known about the levels and species of heavy metals. Moreover, it is not clear to what extent the anthropogenic activities, in the past, and the natural geogenic processes enriched the groundwater with dangerous heavy metals. The lack of studies regarding the heavy metal contamination of groundwater is probably attributed to the less developed nature of the Golden Triangle where most of the mining activities have been out of operation for decades. After launching the new strategies of the Egyptian government for increasing the mining exploitation, extending cultivated land, establishing new cement factories, and making use of the huge quantities of natural resources, a more research is needed to improve the water quality and mitigate the increased effects of the climate change.

Several materials have been used for water remediation purposes; geopolymer adsorbents were amongst the materials that have received a great deal of interest in this regard. Most of the raw materials that have been used in the geopolymer formulations were industrial by-products,

which showed a superior metal uptake compared to the commercial adsorbents such as zeolites. However, the formulation of geopolymers from the natural aluminosilicate sources of a heterogeneous nature, such as rocks, for water remediation purposes is nearly scant. Moreover, the heterogeneous nature of rocks, that have various mineral phases of different propensity in alkali activation, is not understood. Therefore, initially, understanding the alkali activation affinity of a calcareous aluminosilicate rock is important, and hence other natural rocks, such as igneous and metamorphic, and mining wastes can be used. The world is currently moving toward reducing and/or preventing the CO_2-emitting industrial activities due to the increasing problem of the climate change. Recently, the impacts of climate change have been felt where the water levels in some lakes and rivers in Europe reduced and/or completely evaporated, while in the arid environments, such as the Middle East, the flash flooding invaded the region. Therefore, the use of industrial by-products for the geopolymer adsorbent formulations will be limited and other low-cost precursors are needed. Natural rocks, soil, and mining waste can be used as an alternative to the fly ash, for example. However, these natural materials consist of various minerals that have different degrees of reactivity in the alkali activation, and it is difficult to predict the reaction pathway, degree of polymerization, and the final physicochemical characteristics. Therefore, the synthesis of a geopolymer adsorbent from a heterogeneous natural rock of a simple composition can serve as an initial approach toward understanding the geopolymerization of the natural rocks for the water remediation purposes.

1.3 Aim of the research

The main aim of this research is to identify the degrees of groundwater contamination in terms of heavy metals species and concentrations in the Golden Triangle area of Egypt. Additionally, this research aims to determine whether the heterogeneous natural materials with an aluminosilicate composition (rocks) are suitable for the alkali activation and whether they work well to immobilize metal ions as an unconventional geopolymer adsorbent.

1.4 Research objectives

As aforementioned the main aim of the present research is to identify the most challenging pollutants in the groundwater and to develop a novel geopolymer adsorbent for metal ions sequestration. The objectives of the research in this Thesis are:

(i) To measure trace elements concentration in the groundwater samples collected from the study area.

(ii) To generate spatial distribution maps for the identified trace elements.

(iii) To identify the degree of contamination in the study area using the HPI index.

(iv) To investigate the alkali activation affinity of the raw calcareous mudstone to be used as a geopolymer adsorbent.

(v) To identify the capacity of mudstone geopolymer in the metal ions sequestration under various operating parameters.

(vi) To identify the mechanisms, adsorption kinetics, and the isotherms that control the relationship between the metal ions and geopolymer during the reaction.

(vii) To investigate the applicability of the geopolymer adsorbent on an industrial scale basis.

1.5 Thesis structure

All chapters in this Thesis are based on systematic experimental work. The thesis consists of 6 further chapters as follows:

1.5.1 Chapter 2

This chapter provides a literature review of the heavy metals as hazardous contaminants, water treatment technologies, and the geopolymer adsorbents synthesis. The contents of this chapter focus on the use and characteristics of heavy metals and their impacts on the human health. In addition, the water technologies were discussed in terms of their types and their advantages and disadvantages. The review also focuses on the fundamentals of geopolymers, factors that control the geopolymerization reaction, and chemistry. The literature and the current conclusions about the use of geopolymer adsorbents in the water remediation are also included.

1.5.2 Chapter 3

This chapter discusses the presence of heavy metals in the groundwater of the Golden Triangle area. In addition, the degree of groundwater pollution with heavy metals in the Golden Triangle is determined in the three zones. The distribution of heavy metals in the study area is illustrated by generating spatial distribution maps. The increase in some heavy metals concentration of some locations is discussed in terms of the role of the anthropogenic and geogenic activities.

1.5.3 Chapter 4

This chapter discusses the suitability of natural rocks of a heterogenous composition to undergo a geopolymerization reaction. The raw material was characterized using a various analytical

and characterization techniques to identify the chemical and mineralogical composition. In addition, the reactivity of the raw material was investigated through the thermal activation treatment. The effect of silicate addition on the geopolymerization reaction is discussed and the formed geopolymeric gels and reaction products is characterized.

1.5.4 Chapter 5

This chapter discusses the suitability of the rock-based geopolymer in the heavy metal ions sequestration from an aqueous solution. The investigated geopolymers are synthesized based on the findings of chapter 4. In addition, the produced geopolymer adsorbents are used to remove the most challenging metal ions found in the study area. The effect of operating parameters on the metal ions sequestration was discussed, in addition to identifying the nature of the reaction between the metal ions and geopolymers, metal ions sequestration mechanism, and their applicability in a dynamic mode are also investigated. A pilot study was also conducted for treating real groundwater samples collected from the Golden Triangle area.

1.5.5 Chapter 6

This chapter provides a general summary of this Thesis, recommendations, and future work.

1.6 Funding

This work is funded by the British Council and the Ministry of Higher Education of Egypt through a PhD scholarship (Newton-Mosharafa Fund) awarded to Tharwat Hassan for the study period 2017-2021.

1.7 References

1. M. I. Sherif, M. Sultan and N. C. Sturchio, *Earth and Planetary Science Letters*, 2019, **510**, 37-44.
2. R. Amer, R. Ripperdan, T. Wang and J. Encarnación, *Journal of African Earth Sciences*, 2012, **69**, 13-25.
3. F. A. Abdalla and I. H. Khalifa, *Arabian Journal of Geosciences*, 2013, **6**, 1273-1282.
4. M. C. Moncur, J. L. Jambor, C. J. Ptacek and D. W. Blowes, *Applied Geochemistry*, 2009, **24**, 2362-2373.
5. I. Montes-Avila, E. Espinosa-Serrano, J. Castro-Larragoitia, I. Lázaro and A. Cardona, *Applied Geochemistry*, 2019, **100**, 8-21.
6. S. Kuo, B. Huang and R. Bembenek, *Soil Science*, 2007, **172**.
7. Z. Benredjem, R. Delimi and A. Khelalfa, *Arabian Journal of Chemistry*, 2016, **9**, S446-S450.
8. S. Bandyopadhyay, K. Ghosh and C. Varadachari, *International Journal of Chemical Engineering*, 2014, **2014**, 327153.
9. H. Lin, G. Li, Y. Dong and J. Li, *International Journal of Mineral Processing*, 2017, **165**, 1-7.
10. P. A. Kobielska, A. J. Howarth, O. K. Farha and S. Nayak, *Coordination Chemistry Reviews*, 2018, **358**, 92-107.
11. U. Wingenfelder, C. Hansen, G. Furrer and R. Schulin, *Environmental Science & Technology*, 2005, **39**, 4606-4613.
12. S. Abdulrazak, K. Hussaini and H. M. Sani, *Applied Water Science*, 2017, **7**, 3151-3155.
13. Z. Ahali Abadeh and M. Irannajad, *Chemical Research in Chinese Universities*, 2017, **33**, 318-326.
14. M. Buaisha, S. Balku and S. Özalp-Yaman, *Civil Engineering Journal*, 2020, **6**, 470-477.

15. H. Salman, H. Shaheen, G. Abbas and N. Khalouf, *Journal of Entomology and Zoology Studies*, 2017, **5**, 452-461.

CHAPTER 2: LITERATURE REVIEW

2.1 Introduction

Water is one of the renewable resources needed for general well-being. The consumption and need for water in the industrial activities and household use increase year on year. This increased need is attributed to the rapid growth of the worldwide population and the increased urbanization and industrialization. The widespread problem of water contamination is responsible for the deaths of millions of people each year in numbers greater than any form of violence.[1] Since 1990 about 2.6 billion persons have gained access to a clean drinking water, while about 663 million people still struggle to get access. Moreover, it is expected that by 2030, as estimated by the World Water Council, ca. 3.9 billion individuals will live under water scarcity conditions.[2] Water pollution occurs when the dangerous substances are introduced into the environment contaminating the groundwater aquifers, lakes, rivers, and soil thus jeopardizing human health. Generally, water has the power to dissolve various substances, compared to the other liquids on the earth, which makes it more sensitive to pollution.[1] In the past few years, water pollution has reached alarming levels due to its direct and serious effects on living organisms. The hazardous substances, especially heavy metals, can introduce into the biological system through food, drinking water, and air. Heavy metals are on the top of dangerous pollutants due to their bioaccumulation nature and high toxicity. The industrial activities such as smelting, mining, painting, and the production and use of batteries are responsible for the release of a high percentage of heavy metals into the environment. In addition, the excessive use of pesticides and fertilizers in agricultural activities participates significantly in the dispersion of these harmful contaminants in the environment. As a result, the long-term exposure to heavy metals, beyond safe levels, certainly leads to a serious damage to the vital organs such as kidneys, lungs, liver, and heart. Therefore, the removal of heavy metals from the contaminated water bodies has become a considerable environmental concern. Solving the problem of water pollution is not an easy thing to deal with, however, laws, economics, and education can participate in tackling this challenging problem.[3]

2.2 Heavy metals as a potential contaminant of water bodies

One of the major threats to human health is the environmental pollution and contamination by the so-called ‘‘heavy metals’’. Elements that have an atomic weight between 63.5 and 200.6, and a specific gravity greater than 5, are called heavy metals.[4] Although they are detrimental

to human health, flora, and fauna, these metal ions are necessary for life but within acceptable limits as traces.[5] The highly soluble nature of heavy metals in the aquatic environment facilitates their invasion into the ecosystem. The prolonged exposure to needless heavy metals such as arsenic, lead, cadmium, cobalt, chromium, antimony, zinc, copper, nickel, and manganese, can cause a severe acute and chronic damage to the vital organs, kidney, nervous system, lungs, liver, and bones in the human body and animals.[6] However, the toxicity of heavy metals is controlled by many factors such as the chemical species, route of exposure, dose, gender, genetics, and age.[7] Despite the heavy metals are naturally spreading throughout the Earth's crust, the majority of the environmental contamination and human exposure is due to the anthropogenic activities. Aside from the volcanic eruption and weathering of rocks as natural sources for the heavy metals emission, mining, agriculture, and smelting operations are the main activities responsible for introducing the toxic heavy metals into the ecosystem.[8-10] Nevertheless, the groundwater aquifer lithotype can participate naturally in the groundwater contamination through water-rock interaction processes.[11-13] The significant scientific interest in the heavy metals contamination is due to their tendency to accumulate in the living organisms and due to their non-biodegradable nature, unlike the organic contaminants. Due to the deleterious effects of heavy metals on human health, the World Health Organization (WHO) has announced guidelines values for the heavy metals in drinking water. These guideline values are updated from time to time; for instance, in the 1993 the World Health Organization reduced the standard limit of arsenic in drinking water from 55 ppb to 10 ppb due to the increasing evidence of carcinogenesis resulting from the prolonged exposure.[12] It is thus crucial to evaluate the heavy metal contamination of the environment along with developing effective strategies to eliminate the contamination and protect the human and ecological wellbeing.

2.2.1 Cadmium (Cd)

Cadmium is a heavy metal of an occupational and environmental concern. Cadmium is located in Group 12(IIB) in the periodic table of elements along with mercury and zinc. The average concentration of cadmium in the Earth's crust is about 0.1 mg/kg.[14] Naturally, the highest concentration of cadmium compounds is distributed in the sedimentary rocks where their concentration ranges from 0.1 to 25 ppm. On the contrary, igneous, and metamorphic rocks possess lower concentrations in the range of 0.02 to 0.2 ppm. The cadmium levels in the phosphate fertilizers can reach up to 200 ppm. The occurrence of cadmium is usually associated with sphalerite (zinc ore), where the greenockite mineral (a common cadmium-containing

mineral) can be found.[15] Cadmium has an industrial importance, especially in the production of pigments, batteries, and alloys.[16] The prolonged exposure to cadmium compounds can result in a severe health issues, such as the respiratory, kidney , and neuronal toxicity.[17] According to the world health organization the permissible safe level of cadmium in drinking water is 3 ug/L.[18] The speciation of cadmium in an aqueous environment is significantly dependent on the pH of the adjacent solution and has a significant role in the adsorption through surface chemistry. It has been articulated that Cd^{2+} is prevalent when the pH values of the solution are lower than 7.0; when the pH value is higher than 8 and slightly lower than 9.0, Cd is precipitated out in the form of $Cd(OH)_2$; about 10% $Cd(OH)^+$ and 90% Cd^{2+} are formed when the pH value is 8.0.[19, 20]

2.2.2 Nickel (Ni)

Nickel (Ni) is a heavy metal that is abundant in the industrial and domestic wastewater. Unlike other heavy metals, which are hazardous even at low concentrations, Ni has some functional roles in the lifeforms.[21] However, the high concentration can cause severe diseases such as skin dermatitis, rapid respiration, and lung cancer. The announced permissible level, by the WHO, of Ni in drinking water is 70 ug/L.[18] Nickel is widely used in the manufacture of the electroplating, batteries, nonferrous metal, mineral processing, and stainless steel. Nickel is present in nature in ore deposits including garnierite, nickeliferous limonite and pentlandite.

2.2.3 Cobalt (Co)

Cobalt is a naturally occurring element and is found in three oxidation states (0, +2 and +3). However, an oxidation state of +2 is predominant under environmental conditions.[22] Cobalt is introduced into the ecosystem through the manmade activities such as, the manufacture of batteries, magnetic steels, mineral processing and electroplating.[23, 24] Similar to other metal ions, cobalt is necessary to human nutrients but at low levels; however, the prolonged exposure to cobalt at levels above the WHO permissible values can cause a damage to the human health including vision difficulties, thyroid damage, vomiting, and heart problems. It has been predicted that about 81 Co minerals occur in the Earth's crust.[25]

2.2.4 Manganese (Mn)

Manganese is the twelfth most abundant element in the Earth's crust with an estimated concentration of about 0.095%.[26] Manganese is a constituent of over 100 minerals, where the manganese carbonate, manganese dioxide, and manganese silicate are the most common mineral forms. Although manganese occurs in various oxidation states (+2, +3, +4, +6 and

+7), the divalent species is the most dominant manganese form in water of a pH ranges between 4 and 7.[27] Manganese is widely used in the steel manufacturing, pharmaceutical, chemical, food and electrochemical applications.[26] Although manganese is vital for the human life, its presence in drinking water at levels exceeding the values announced by the WHO can cause a severe damage to the nervous system.[28]

2.2.5 Copper (Cu)

Copper is commonly used in various industrial applications, such as the electroplating, etching, plastics, and metal finishing. Accordingly, the concentration of copper in wastewater is usually high. Copper is highly toxic even at low concentration, and according to the WHO the copper concentration in drinking water should not exceed 2 mg/L.[29] The prolonged exposure to copper can cause a serious toxicological concerns due to its deposition in kidney, liver and brain.[30]

2.2.6 Lead (Pb)

Lead has various, industrial, and domestic applications and is found in low concentrations in the Earth's crust in form of sulphide minerals such as galena (PbS) and plumbojarosite ($PbFe_6(SO_4)_4(OH)_{12}$).[31, 32] However, the wide dissemination of lead in the environmental system is significantly related to the human activities such as, production of lead-acid batteries, recycling of the lead, mining, pigments, smelting and fertilizers.[33, 34] Lead is highly toxic and even can be absorbed through the skin, in addition to the digestive and respiratory systems; as a result can cause severe damages to the kidneys, heart, brain, skeleton, liver and the nervous system.[35]. According to the WHO, the permissible level of lead in drinking water is 10 ug/L.[18] In an aqueous environment, the speciation of lead is mainly controlled by the pH. The predominant species at the pH of about 6.0 are Pb^{2+}, $PbOH^{+}$ (soluble species), and $Pb(OH)_2$ (precipitate). At the pH values between 7.0 and 12.0 soluble forms $Pb(OH)^{3-}$ and $Pb(OH)_4^{2-}$, in addition to solid hydroxide are prevalent.

2.2.7 Zinc (Zn)

Zinc is common in the wastewater discharged from the industrial activities such as pigments, mining, battery manufacturing, and electroplating. The presence of zinc in drinking water above the permissible level (0.5 mg/L, WHO) can cause a devastating health problems.[36] Zinc is contained naturally in various minerals, such as ZnS, ZnO, Zn_2SiO_4 and $ZnCO_3$. The high intake of zinc can cause a serious damage to the brain, respiratory tract, and prostate.[37]

2.2.8 Arsenic (As)

Arsenic originates from both the anthropogenic activities and natural sources. Arsenic occurs naturally in four chemical oxidation states (0, -3, +3 and +5).[38] The most common natural arsenic compounds are arsenite (As (III) – H_3AsO_3) and arsenate (As (V) – $HAsO_4^{2-}$). Arsenic speciation in the aqueous environment is a pH dependent where As (III) is neutral (H_3AsO_3) at pH lower than 9.2, while the predominant species of As (V) are $HAsO_4^{2-}$ and H_2AsO^{4-}. Moreover, the oxidation – reduction conditions control the presence of arsenic species; As (V) is the dominant arsenic species under oxidizing conditions and presents as oxyanions of arsenic acid ($H_2AsO_4^{2-}$, H_3AsO_4, AsO_4^{3-} and $HAsO_4^{2-}$), whereas As (III) presents as arsenious acid ($HAsO_3^{2-}$, H_3AsO_3 and $H_2AsO_3^{-}$).[39] As (III) is more mobile compared as the As (V), its toxicity is about 60 times more than As (V).[40, 41] Due to the high toxicity of Arsenic the WHO stated a permissible limit of 10 ug/L in drinking water.

2.3 Water treatment technologies

Affordable and sustainable supply of a safe, adequate, and clean water is one of the thorniest issues our world is facing. The water problem has required that both scientific and industrial communities find new strategies for upgrading the water treatment techniques. Over the last few decades, various water treatment techniques have been developed and used for the sequestration of various pollutants from water. These techniques include ion exchange, chemical precipitation, adsorption, reverse osmosis, photochemical, ultrafiltration and coagulation methods. Although the aforementioned techniques showed a satisfactory potential in the contaminants removal, most of them are still of a limited use. Choosing a suitable treatment method is controlled by some factors such as economic feasibility, high removal efficiency and reducing the concentration of targeted contaminants to match the established regulatory standards.

2.3.1 Chemical precipitation

Chemical precipitation is one of the well-known techniques used in the removal of heavy metals from water.[42-44] The idea of this technique is mainly based on the transformation of the metal ions from their soluble species in the water to insoluble form through a chemical reaction to sequestrate the metal ions in the form of a precipitate (hydrated metal oxides or hydroxides), Figure (2-1). The heavy metal removal by chemical precipitation is indicated by this equation.[44]

$$M^{2+} + 2(OH^-) \leftrightarrow 2M(OH) \downarrow \qquad (2-1)$$

Where M^{2+} represents the dissolved metal ions, OH^- is the precipitant and $M(OH)_2$ is the insoluble metal hydroxide. Moreover, the sequestration of heavy metals through the chemical precipitation technique can be improved by adjusting the pH of a solution to basic conditions (pH 9-11).[45] Although the chemical precipitation is acceptable in terms of the economic considerations, its use in the case of diluted solutions is less efficient.[46, 47] In addition, this process results in the formation of a massive amount of sludge which represents another environmental challenge.[45]

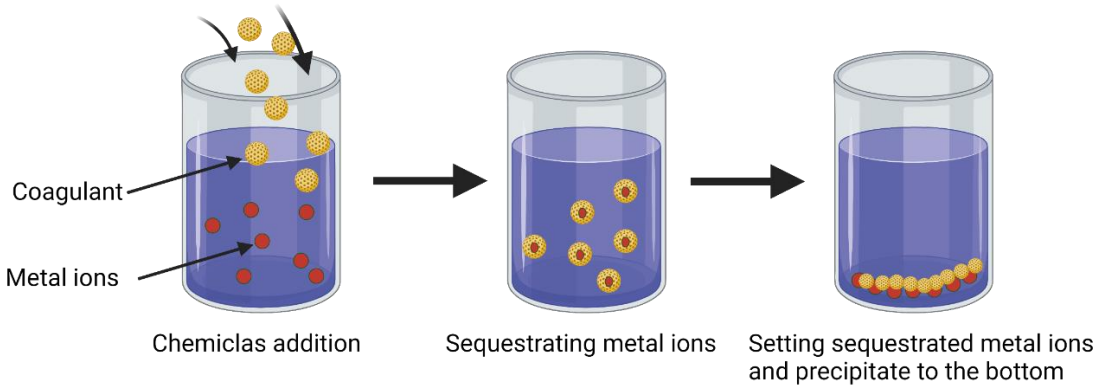


Figure 2-1: Chemical precipitation technology.

2.3.2 Coagulation – flocculation

The coagulation-flocculation processes widely used in the field of industrial wastewater treatment aiming at the removal of suspended particles and a colloidal turbidity reduction.[48-50] The coagulation – flocculation technology is mainly based on neutralizing the negatively charged suspended solids using a coagulant chemical that has an opposite charge to the suspended solids.[51] The neutralization results in the sticking of the suspended particles together forming the so-called flocs, Figure (2-2). The process by which the flocs grow and form through the slow mixing is called flocculation. Although this technology is acceptable in the field of water treatment, it is still costly and generates a massive amount of sludge that introduces another economic pressure, and requires a careful disposal, wherein the disposal cost represents more than half the total cost of operation.[52, 53]

2.3.3 Reverse osmosis

Reverse osmosis is a treatment process to get a low salinity fresh water from brackish and sea water, in addition to the separation of larger particles and the undesirable molecules from

drinking water, Figure (2-3).[54] Reverse osmosis is a natural process similar to the way by which the plant roots soak up minerals and water from the soil, and the absorption of water from blood by kidneys. However, the reverse osmosis, unlike the natural osmosis process, requires energy to push water (diffusion process) through the membrane and involves applying high pressures. This technique is very effective in the desalinisation, and the removal of bacteria and organics from the water bodies. This technology has no impact on the chemistry and pH of the product, and no heat degradation results as a significant heating is not applied.[55] Notwithstanding, this technology is still costly in operation and requires a high maintenance. Furthermore, the fouling process due to the rapid membrane clogging represents an additional challenge.[56] Generally, the reverse osmosis results in a reduction in some of the beneficial minerals, such as magnesium and calcium, which shows negative impacts on the health especially muscles and heart.

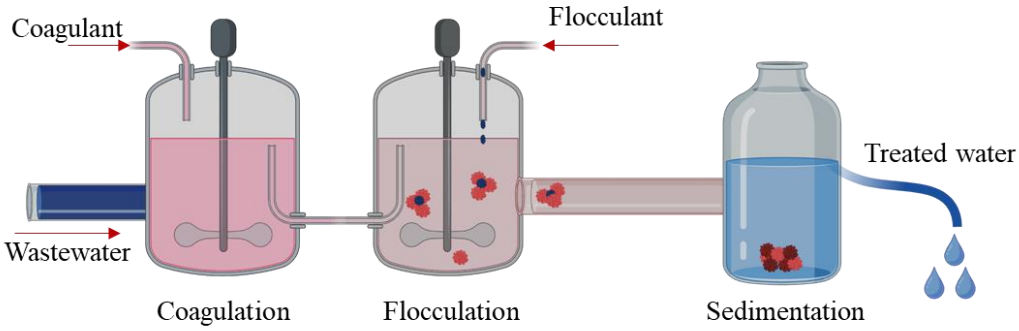


Figure 2-2: Coagulation-flocculation technology.

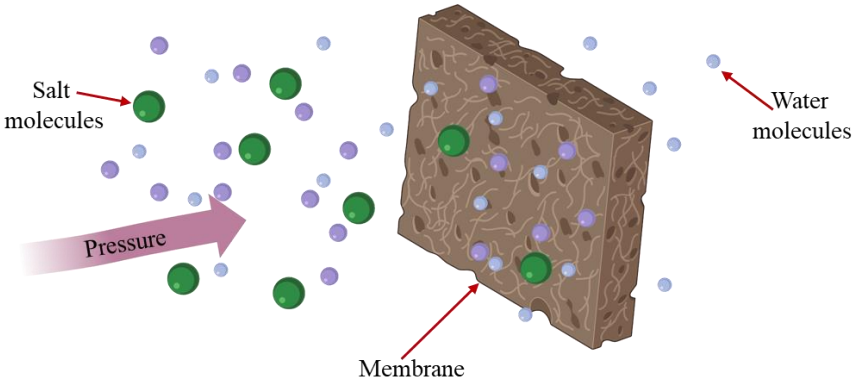


Figure 2-3: Reverse osmosis technology.[57]

2.3.4 Ion exchange

Ion exchange is the most widely used method in the water treatment industry due to its high effectiveness in heavy metals removal especially from water of a low heavy metal concentrations, Figure (2-4). Moreover, the solid materials that are used as an ion exchanger are low-cost materials which meet the economic needs. This method involves either a cation or anion exchange process between the solid material and the surrounding solution, where the undesirable harmful metal ions can be replaced by harmless ones.[47] The positively charged ions such as Na and K (exchangeable sites) in the solid material are exchanged with the positively charged metal ions, such as Cd, Co, Mn, in the aqueous solution. In the same way, the negatively charged ions in the solid material are exchanged with the negative ions in the solution. Ion exchange is based on a reverse chemical reaction and has a distinguished selective removal aspect.[47] Zeolites are amongst the materials that have been used widely in the removal of metal ions with a distinguished exchange capability; metal organic frameworks are another good candidate material that was suggested recently as an ion exchanger.[58, 59]

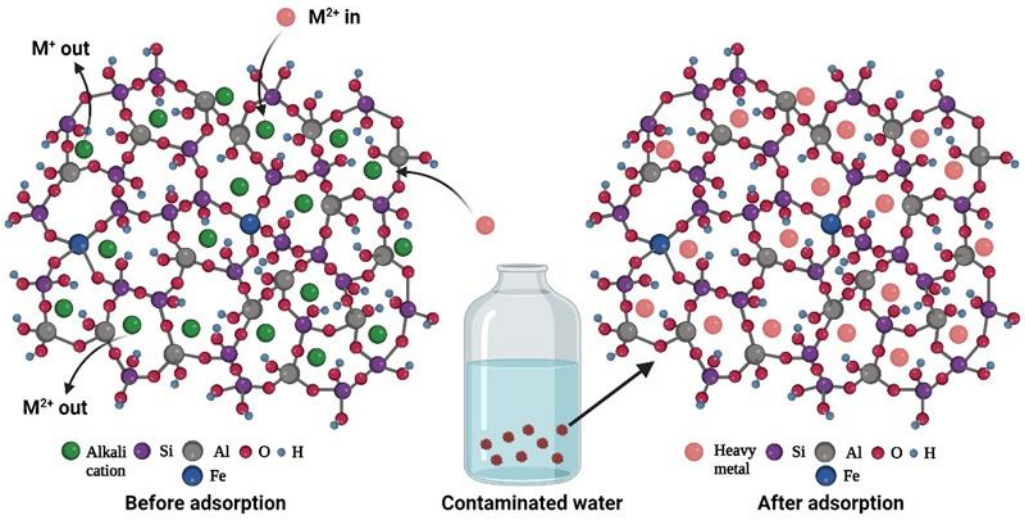


Figure 2-4: Ion exchange technology.

2.3.5 Adsorption (solid - liquid related system)

Although the above-mentioned methods showed a good potential in the water purification, they still have some drawbacks such as the sensitive operating conditions, costly disposal procedures, poor efficiency, and high energy consumption.[60] Adsorption is among these water treatment methods. However, adsorption has superior properties over other methods; this is attributed to its simplicity in operation and low-cost of operation. Adsorption is the process by

which the mass transfer of ions and molecules from the liquid or gas phase proceeds to be adsorbed onto solid surfaces.[61, 62] Due to the active energy-rich sites on the solid surfaces, these surfaces are able to interact with the ions or molecules in the adjacent aqueous solution due to their electronic and spatial characteristics. The energy of the active sites is variable, resulting in the heterogeneity of the surface energies. The solid material that adsorbs the ions is referred to as the *adsorbent*; the species that are adsorbed onto the surface of the solid material is referred to as the *adsorbates*. Hence, the adsorption is a surface process, and thus, the surface area is an important factor determining the quality of the adsorbent. The adsorption process involves four steps: (1) bulk diffusion, (2) film diffusion, (3) pore diffusion, and (4) adsorption reaction (chemical or physical), Figure (2-5).[63] The reverse process of adsorption is called the *desorption*. The nature of the interaction between the adsorbent and adsorbate are referred to as the chemisorption and physisorption.[60] Any material to be used as an effective adsorbent should have some properties as follows.[64]

- High chemical and mechanical stability where it can be used under severe conditions.
- Reusable and easily separated.
- Effective and tuneable porous structure which enables a high surface area and faciliates the diffusion process.
- Rich in chemistry reflecting the presence of various and large number of active groups which play a significant role in determining the adsorption capacity and selectiviety.

2.3.5.1 Mechanism of adsorption

Identifying the mechanism of adsorption (Figure 2-5) is controlled by the nature of both the adsorbate and adsorbent which can be simple (single identified interaction) or involves various interactions that take place concurrently.[65] In the case of surfaces with different charges, the mechanism of adsorption is controlled by the electrostatic interaction, the hydrogen bonding is configured between the surface functional groups, the interaction between benzene rings (organic molecules) and adsorbent is controlled by the formation of π-π interactions, when the pollutant is hydrophobic in nature and the adsorbent is non-polar, hydrophobic interactions are prevail.[63]

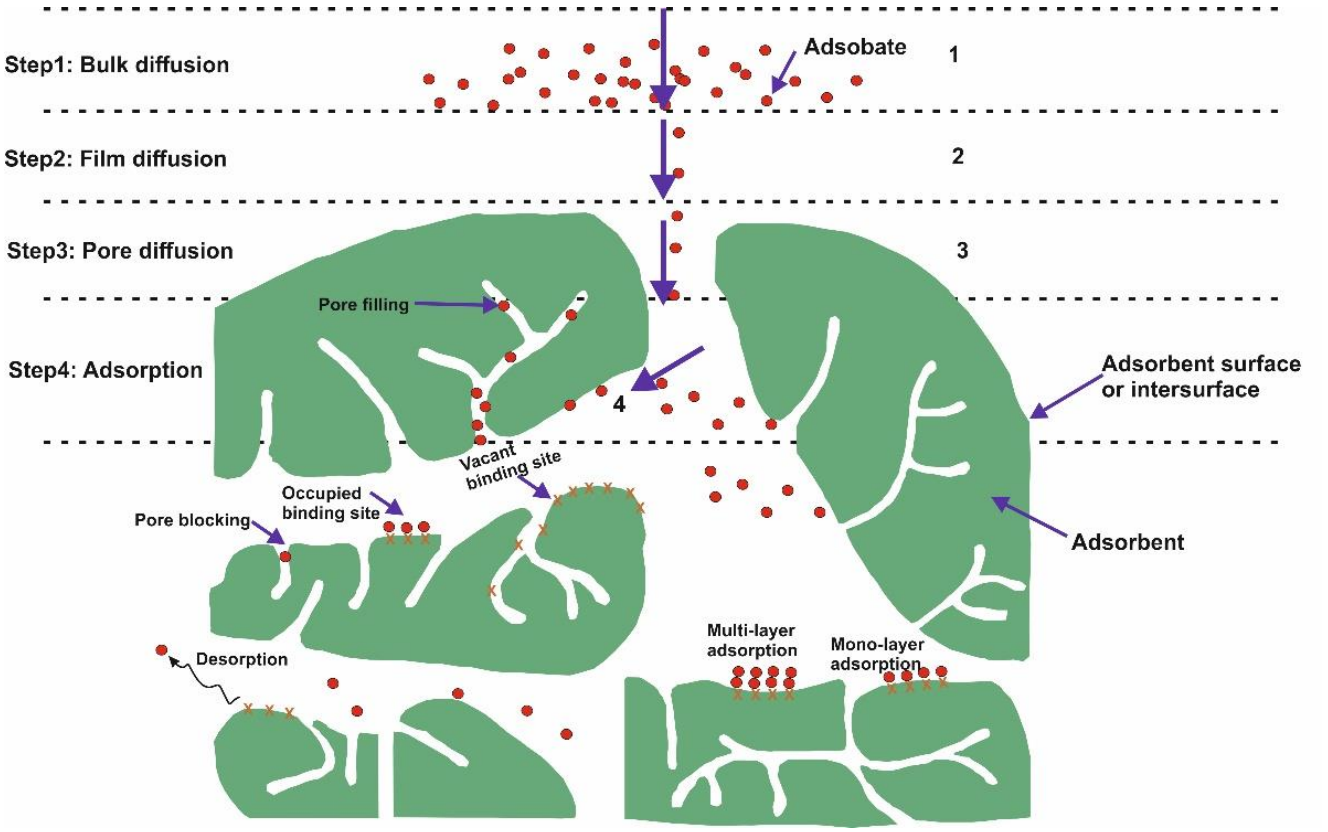


Figure 2-5: Steps of adsorption process.[63]

2.3.5.1.1 Physisorption (physical adsorption)

In physisorption, the molecules are attracted to the surface of the adsorbate by the weak van der Waal's forces. This type of adsorption takes place at low temperature (heat of adsorption of 20-40 kJ/mol) meaning that the extent of physisorption decreases with increasing temperature. Physisorption results in a multimolecular layers and is reversible. Moreover, this kind of adsorption does not need any activation energy. It is worth noting that the physisorption is a broader term that describes various interactions between the substrate and adsorbed molecules such as the size-selective adsorption (pore filling), electrostatic interaction, π-π interactions, hydrogen bonding, and hydrophobic interaction.[66, 67]

2.3.5.1.2 Chemisorption (chemical adsorption)

When the adsorbate is chemically bonded with the adsorbate, the process is called chemisorption or chemical adsorption. This type of adsorption results in a monolayer of adsorbate on the adsorbent and takes place at a range of temperatures (heat of adsorption of 40-400 kJ/mol). In this kind of adsorption, the forces of bonding between the adsorbent and adsorbate are very strong. Chemisorption increases with increasing the temperature to a limit

and after that it starts to decrease. Moreover, it increases with a greater surface area and occurs only where the chemical bonding, covalently bound, between the adsorbate and adsorbent can occur. Therefore, the chemisorption is highly specific. Moreover, the desorption is not usually possible due to the strong bonding between the adsorbent and adsorbate.

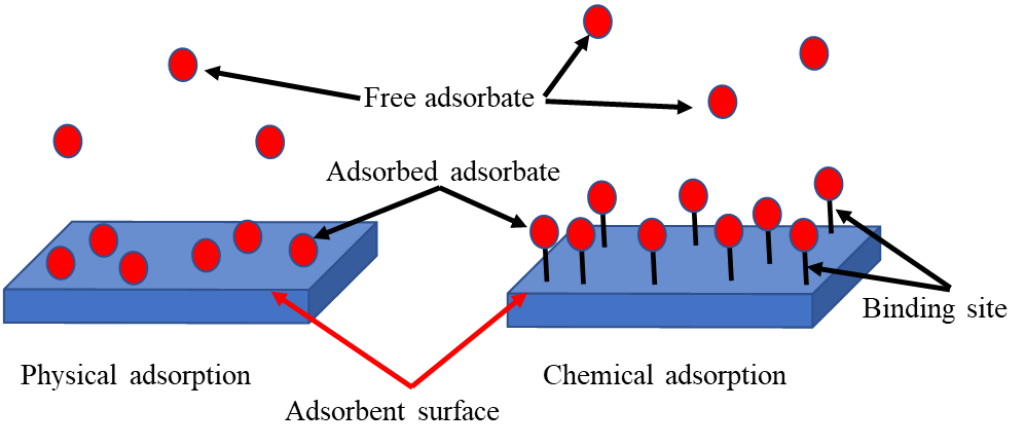


Figure 2-6: Types of the adsorption processes: chemosorption and physisorption.

2.3.5.2 Adsorption kinetics and isotherms

Evaluating the adsorption process and mechanism is usually conducted using mathematical models which are known as the adsorption kinetics and isotherms. The rate of solute adsorption and diffusion behaviour is described as the adsorption kinetics, while the equilibrium concentration between the solute concentration on the surface of adsorbent and that in the liquid at constant temperature is called the adsorption isotherm.[68]

Although several kinetic models are presented to describe such reactions, the suitable reaction model is selected consistent with the mechanism of the adsorption process, where the mass transport and chemical reactions processes can be explained (rate-controlling steps), in addition to taking into consideration the applicability of other models.[63, 69] The most common kinetic models are summarised in Table (2-1). Several adsorption isotherms are used to describe the adsorption process. Understanding of these isotherm models is necessary for the design of the adsorption processes and to optimize the use of adsorbent. The adsorption isotherms reflect the relationship between the liquid phase concentration and adsorption capacity at constant temperature.

Table 2-1: Equations of the most used adsorption kinetics.

Models		Equations
Adsorption diffusion model	Intraparticle diffusion	$q_t = k_{id}t^{0.5} + C$
	Liquid film diffusion	$In\left(1 - \frac{q_t}{q_e}\right) = k_{fd}t$
Adsorption reaction models	Pseudo-first order	$\frac{dq_t}{dt} = k_{p1}(q_e - q_t)$
	Pseudo -second order	$\frac{dq_t}{dt} = k_{p2}(q_e - q_t)^2$
	Elovich	$\frac{dq}{dt} = ae^{-aq}$

Langmuir and Freundlich isotherm models are the common mathematical models that have been widely used to describe such processes. Fitting the experimental data with the Langmuir isotherm model indicates a homogeneous and monolayer adsorption process, whereas fitting the experimental results with the Freundlich isotherm model reflects a heterogenous and multilayer adsorption process. The Langmuir adsorption isotherm assumes that there is no interaction between the molecules that are adsorbed next to one another. Moreover, the adsorption is a reversible process, and each adsorbent has different energy sites while the adsorption energy is uniformed for all sites.[70] additionally, both the desorption and adsorption are involved in the Langmuir adsorption isotherm.

Although, the Freundlich isotherm is based on the relationship between the adsorption capacity (q_e) and liquid phase concentration (C_e), this isotherm model is not valid for the low ion concentration.[71, 72] Some of the common isotherm models are presented in Table (2-2).

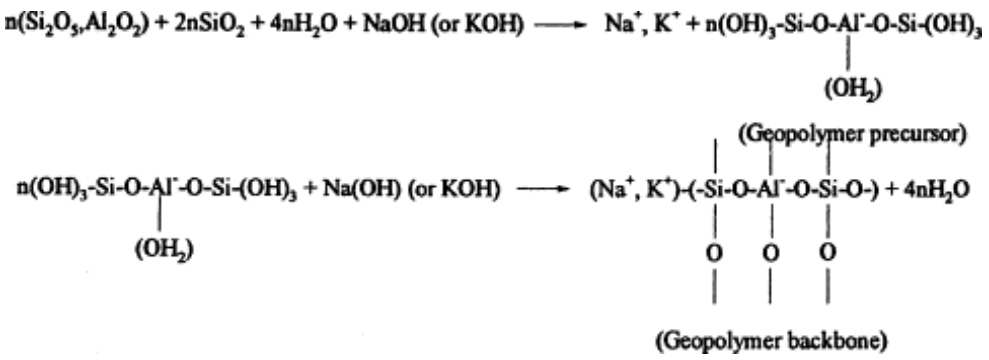
Table 2-2: The most common adsorption isotherms.

Isotherm models	Equation form	Parameters
Langmuir	$q_e = \frac{K_L q_m C_e}{1 + K_L C_e}$ **Plot**: C_e vs C_e/q_e	**C_e**: represents the equilibrium concentration of adsorbate, **q_e**: is the amount of sorbed material per gram of adsorbent, **q_m**: maximum monolayer coverage capacity of sorbent, **K_L**: is the Langmuir isotherm constant
Freundlich	$q_e = K_F C_e^{1/n}$ **Plot**: log q_e vs log C_e	**n**: is the adsorption intensity (heterogeneity parameter), **K_f**: represents the Freundlich isotherm constant (reflects the approximate indicator of adsorption capacity)
Redlich -Peterson	$q_e = \frac{K_R C_e}{1 + a_R C_e^g}$	**K_R** and **a_R**: Redlich – Peterson isotherm constants, **g**: Redlich – Peterson exponent
Temkin	$q_e = \frac{RT}{b_T} In(A_T C_e)$ **Plot**: q_e vs 1n C_e	**b**: is the Temkin constant, **T:** is the absolute temperature, **A:** is the Temkin isotherm constant, **R**: is the gas constant
Toth	$q_e = \frac{K_T C_e}{(a_T + C_e)^{1/T}}$	**K_T**: Toth isotherm constant
Dubinin–Radushkevich	$q_e = q_m \exp(-\beta\varepsilon^2)$ **Plot**: 1n q_e vs ε^2	**B**: is the constant of adsorption energy, **ε**: is the adsorption potential, **q_m**: maximum adsorption capacity

2.4 Geopolymer as an innovative technology in water purification

2.4.1 Concept of geopolymerization

Geopolymerization is an innovative technology that coverts the waste materials of an aluminium silicate composition into a concrete and other new materials for a variety of purposes.[73] The term "geopolymer" has been coined for the first time in the 1970s by Prof. Joseph Devidovids to describe a family of mineral binders, similar in structure to the man–made zeolite, composed of a Si–O–Al polymer system. Unlike zeolite, the geopolymeric material is almost amorphous to semi-crystalline.[74, 75] Moreover, the geopolymer is synthesized at a lower temperature than zeolite. Although geopolymers are the same as polymers, the geopolymer term has been used due to the resemblance of the synthetic materials to the minerals that are formed in the Earth's crust. Therefore, the geopolymers are categorized as a member of the inorganic polymer family.[74] The pathway of geopolymerization reaction is summarized as follow:[76]



The geopolymer composition can be expressed by the following general empirical formula:

$$Mn^{+}\,[(SiO_2)_z\text{-}\,AlO_2^{-}]_n \qquad (2\text{-}2)$$

Where M^+ represents an alkali cation (Na^+, K^+ or Ca^{2+}). This cation is necessary for balancing the negative charge on the Al^{3+}; Z is the number of silicate units (Si/Al ratio), and n is the degree of polymerization.[77]

Many scientific terms have been introduced to describe the geopolymer composites such as geocement, inorganic polymer concrete, alkali-activated cement, and low-temperature aluminum silicate glass.[78-81] Over the last decades, these multi-application materials have received a great deal of interest worldwide owing to their green synthesis approach.[82-85] Geopolymers emit about 80-90% less CO_2 than Portland cement and have excellent mechanical strength.[86]

2.4.2 Mechanism of geopolymerization

Geopolymers are formed through a chemical reaction between a solid aluminum-silicate material and a highly concentrated alkali hydroxide (NaOH, KOH) or silicate solution.[74] Despite the extensive studies conducted on geopolymer and its related applications, the exact chemical mechanism that controls the gel formation is not well understood.[87, 88] This challenge is attributed to the heterogeneity of the used precursors where different raw materials of various chemical compositions are used.[89] In the 1950s, nearly 26 years before the invention of the geopolymer science by Davidovits, Glukhovsky explained the process that controls the alkali activation of a material of aluminium silicate structure according to a model which has three stages: (i) destruction-coagulation, (ii) coagulation - condensation, and (iii) condensation – crystallization.

Duxson et al.[90] presented their view about the geopolymerization by proposing a conceptual model for simplifying the reaction mechanism of geopolymerization (Figure 2-7). Accordingly, the dissolution of a solid aluminium silicate material in an alkaline medium result in the liberation of silicate and aluminate monomers. The silicate and aluminate species incorporate into the liquid phase forming a complex mixture of aluminate, silicate, and aluminium silicate species. Due to the rapid dissolution of the aluminium silicate at a high pH, a supersaturated aluminium silicate solution is formed. Oligomers are condensed forming large networks leading to the gel formation. After gelation, the system continues to reorganize forming a three-dimensional aluminosilicate network structure. Although this model represents a sequential pattern for the reaction, the processes that are included in the reaction occur concurrently. The setting of the geopolymerization reaction can occur instantaneously or take days depending on the processing conditions (curing temperature and time) and mix design.[83]

Van Deventer et al.[91] proposed the term ‘transformation’ to describe the occurrence of a post-polycondensation reaction (third stage). The post-reaction stage can lead to a further crystallization, modifying the final chemo-physical properties of the geopolymer. Moreover, the chemistry and final characteristics of the geopolymer are controlled by the Si and alkali cation (e.g., Na^+) concentrations.

2.4.3 Geopolymer structure

The structure of the yielded geopolymers is classified into four categories depending on the Si/Al ratio (Figure 2-8): (i) poly(sialate) (-Si-O-Al-O-), (ii) poly(sialate-siloxo) (Si-O-Al-O-Si-

O), (iii) poly(sialate-disiloxo) (Si-O-Al-O-Si-O-Si-O), and (iv) sialate link.[83, 92] The dissolution and condensation reactions are influenced by the Si/Al ratio. In the low Si/Al ratio geopolymer system, a condensation reaction occurs between the silicates and aluminate species and as a result, a poly (sialate) geopolymer structure forms, whereas in the high Si/Al geopolymeric system, the condensation reaction preferentially occurs between the silicate species leading to the oligomeric silicate formation. These oligomeric silicates condense with the $Al(OH_4)^{4-}$ forming a poly (sialate- siloxo) and poly (sialate-disiloxo) geopolymer structures.[93]

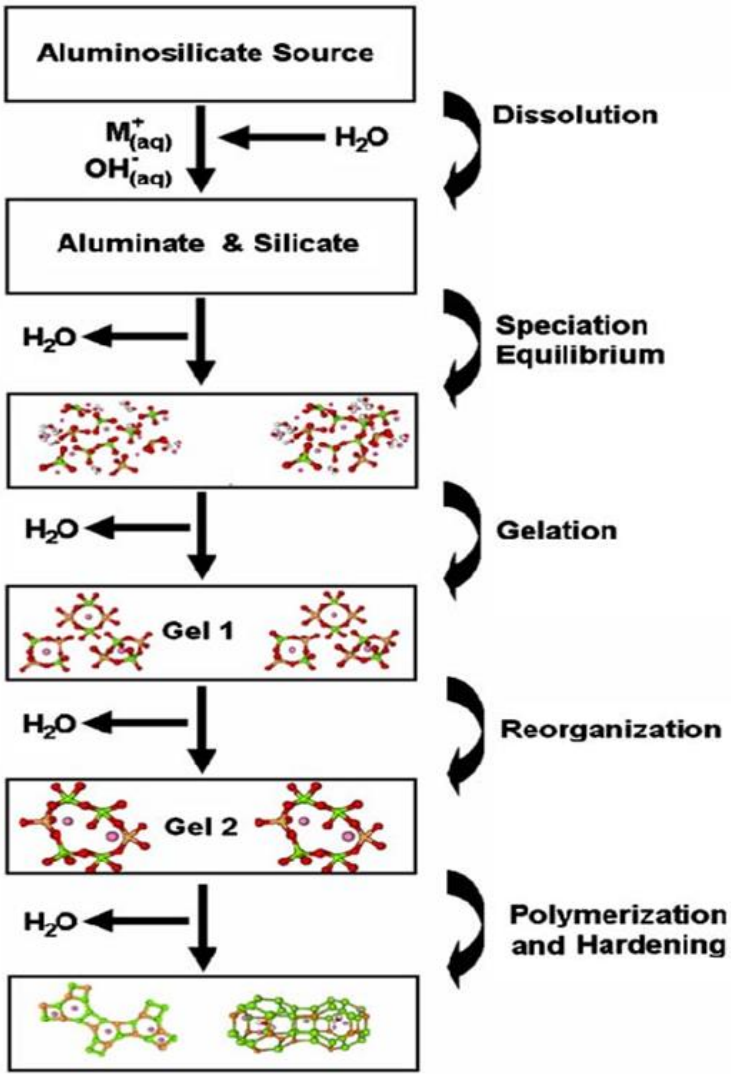


Figure 1-7: Conceptual model of geopolymerization.

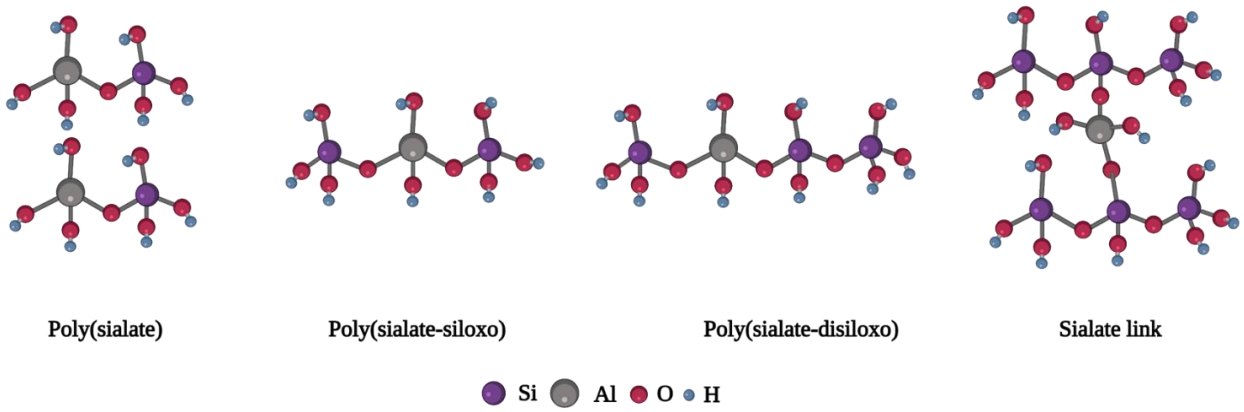


Figure 2-8: Classification of polysialate structures

2.4.4 Factors that control the geopolymerization reaction

The geopolymerization process is controlled by several factors affecting its mechanical and chemical characteristics. These factors are summarized as follows:

2.4.4.1 Alkaline activator

The alkaline activator plays a key role in the geopolymerization process; the most common alkaline activators are the NaOH, KOH, Na_2SiO_3 and K_2SiO_3. The role of alkaline activator in the geopolymerization is to dissolve the silicate and aluminate species from the source material through breaking the Si-O-Si and Al-O-Al covalent bonds. The breaking of such bonds is accelerated in the presence of a highly alkaline medium where the (OH^-) ions in the alkaline medium plays a significant role.[83] Therefore, the more alkaline solution in contact with the reactive aluminium silicate material the more silicate and aluminate monomers are released.[94, 95] However, the impact of the alkaline activator on the geopolymerization of a given material is controlled by an optimum concentration limit of the activator; a reverse reaction prevails in case of crossing this limit which has a negative impact either on the mechanical or adsorption characteristics. Since the geopolymers have a negatively charged tetrahedral aluminium sites in the three-dimensional network, the charge balance is achieved by the alkali metal cations such as potassium and sodium.[96] The formation of a geopolymer network structure with an enhanced aluminium incorporation is mainly based on the instant availability of the soluble silica ions in an alkaline-activated media; in the early stage of reaction the availability of silica is important for assisting the nucleation of silicon and aluminium from the unreacted particles

in the source material.[97] The rate of the geopolymerization reaction is high in the case of using an alkaline activator composed of NaOH and Na_2SiO_3 compared to the use of NaOH, individually. The combination of Na_2SiO_3 is necessary with NaOH to increase the compressive strength of geopolymer where the Na_2SiO_3 increases the Si/Al ratio leading to the formation of more -Si-O-Si- bonds that are stronger than the Al-O-Al and Si-O-Al bonds improving the overall mechanical characteristics.[94, 98, 99]

Xu et al.[100] have studied the effect of the alkali metals on the extent of geopolymerization for a mixture composed of stilbite and kaolinite minerals. The obtained results indicated that alkali activators affected not only the dissolution of Al and Si but also the mechanical characteristics. The Na^+ ions enhanced the dissolution of aluminium and silicate species compared to the K^+ ions. In contrast, the K^+ ions improved the mechanical characteristics of geopolymer compared to the Na^+ ions. This behaviour has been attributed to the small size of the Na^+ ion compared to the K^+ ion.[85]

2.4.4.2 Si/Al ratio

The structure of geopolymer is significantly affected by the Si/Al ratio; during the reaction of the aluminium silicate with alkaline solution the -Si-O-Si- or -Si-O-Al- bonds in the source material break, as a result, active Si^{4+} and Al^{3+} are released. The reaction of the active Si^{4+} and Al^{3+} species will form aluminium silicate oligomers composed of a AlO_4 and SiO_4 tetrahedra.[99, 101] The condensation process in a system that has a high Si concentration tends to oligomeric silicates formation, leading to a [poly(sialate–siloxo) and poly(sialate–disiloxo)] 3D polymeric structures, while a system with low Si concentration will produce a poly(sialate) polymer structure.[96, 102] Alteration of the Si/Al ratio has a significant impact on the porosity of geopolymer, where the porosity decreases with the increase in the concentration of NaOH as more Si and Al are leached, improving the degree of polycondensation. Moreover, a study conducted by Duxson et al.[103] showed that the geopolymer with a $Si/Al \leq 1.4$ has a microstructure that is characterized by large, interconnected pores while in the geopolymer with $Si/Al \geq 1.65$, some smaller isolated pores have been observed.[99, 103] However, as the geopolymer can be synthesized using various alumino-silicate precursors, these results cannot be generalized.

2.4.4.3 Dissolved Silica (Si^{4+})

Geopolymers are generally amorphous; however, under certain conditions a crystalline phase is formed (zeolite). The key factor that determines the amorphous nature of the synthetized

geopolymer is the amount of silica present in the activation solution. Geopolymer samples that were synthetized in the absence of dissolved silica had abundant crystal phases and showed a decrease in the mechanical strength compared to samples that are activated in the presence of dissolved silica. On the contrary, the increase in the silicate content of the alkaline solution resulted in a decrease in the formation of crystalline phases. This relationship has been noticed in geopolymer that was synthesized from the fly ash and metakaolin.[90, 104]

2.4.4.4 Liquid/Liquid ratio (Na_2SiO_3/NaOH)

Sukmak et al.[105] investigated the effect of liquid/liquid ratio (Na_2SiO_3/NaOH) on the compressive strength characteristics of the clay-fly ash geopolymer; in their study different liquid/liquid ratios, 0.4, 0.7,1, 1.5 and 2.3 were considered. After applying the compressive strength tests on samples that have been treated at different days of curing, the results indicated that the optimum liquid/liquid ratio was 0.7. However, Ridtirud et al.[106] found that the liquid/liquid ratio of 1.5 is the optimum ratio for the preparation of flay ash based geopolymer. Villa et al.[107] studied the effect of the Na_2SiO_3/NaOH ratio during the preparation of zeolite based geopolymers. In this study a wide range of liquid/liquid ratios of 0.4, 1.5, 5, 10, 15 was used. The obtained results indicated that with increase in the liquid/liquid ratio from 0.4 to 1.5, an increase in the compressive strength was noticed, while after this ratio the compressive strength decreased. Lee and Van Deventer[108] attributed such a phenomenon to the retarding of the geopolymerization reaction by the precipitation of Al-Si phase due to the presence of excessive sodium silicate, hindering the contact between the source material and the alkaline activator solution. Chindaprasirt et al.[109] suggested the Na_2SiO_3/NaOH ratio in a range between 0.67 and 1 as an optimum ratio for producing geopolymers with a high strength. Moreover, the geopolymer synthesized by Cheng et al.[110] from metakaolin using a liquid/liquid ratio equal to 1 showed an excellent adsorption capacity.

2.4.4.5 Reactivity of source material (alumino-silicate precursor)

Dissolution of the alumino-silicate precursor during the alkali activation is the most important factor influencing the pathway and extent of geopolymerization. It has been proved that the reactivity of the raw material can be improved through a milling process (mechanical activation), this process results in a reduction in the particle size, and hence an increase in the surface area.[111] Theoretically, the natural aluminosilicate materials (rocks and their forming minerals) can be used in the synthesis of geopolymer due to their chemical richness which comprises Al and Si, the main building units of geopolymer. However, one of the challenges

that prevents the use of natural aluminosilicate in the geopolymerization is their low reactivity during the alkali activation meaning that the release of aluminate and silicate species is low. Therefore, combining two or more pre-activation treatments (mechanical – thermal - chemical) is necessary to enhance the dissolution of natural alumino-silicate in the alkaline solution.[112] The dissolution of alumino-silicate minerals is controlled by the nature of the crystalline structure; therefore, the presence of Al and Si in the structure does not guarantee a successful geopolymerization. Kaolinite mineral, which is categorized as a clay mineral of 1:1 layer lattice, is more reactive after the thermal activation between 500 and 800 °C. Thermal activation cause a disruption (dehydroxylation) and results in the formation of four, five and sixfold coordinated Al. Unlike the crystalline 1:1 layer lattice structure mineral, the reactivity of the crystalline 2:1 layer lattice structure mineral is low, and the formation of the aluminosilicate inorganic polymer was unsuccessful, even after a thermal activation step at 800 °C. The unsuccessful formation of the geopolymer from such kinds of minerals is attributed to the absence of an amorphous phase (metastable), by contrast with the mineral kaolinite (1:1 layer lattice structure). The formation of an amorphous Al-O-Si is necessary to facilitate the release and leaching of the Al from the surface of particles and to initiate the formation of Gel I (Al-dominated phase, stage1). The retention of the crystalline 2:1 layer structure in the dehydroxylated phase of 2:1 mineral, where lower and upper Si-O sheets enclose and cover the Al-O sheet, prevents the alkaline attack and hence the release of the aluminate species.[112]

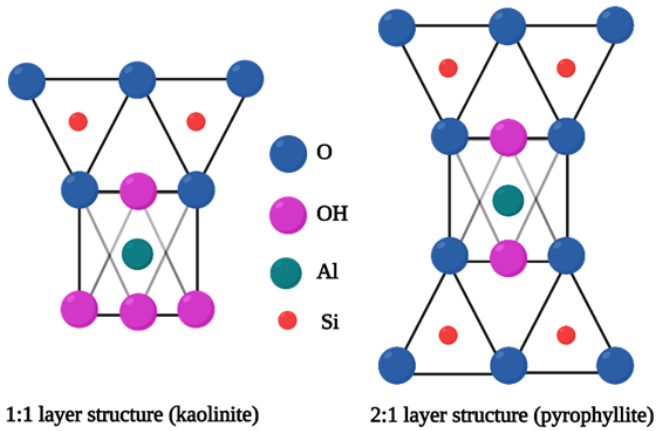


Figure 2-9: Aluminosilicate mineral structure.

Geopolymers synthesized from the mechanically activated fly ash showed an increase (80%) in the compressive strength compared to the geopolymers formed from fly ash without any mechanical treatment.[113] This finding has been attributed to the higher dissolution rate of the

fly ash as a function of the particle size reduction. Mechanical activation improves the surface reactivity of the solid material without changing the overall chemistry. However, the interatomic bonds can be broken and rebuilt during grinding. Grinding results in the formation of an amorphous Al-O-Si phase, which consequently facilitates the leaching of aluminum.[114-116]

2.4.4.6 Curing conditions

Geopolymers can be synthesized at both room and elevated temperatures. However, the setting time is faster in the case of curing at elevated temperature than at room temperature. The successful conversion of the source material to a geopolymer gel occurs when samples are cured in sealed moulds for a period of time and under a slightly elevated temperature.[83, 117]However, the geopolymerization gel will crystallize into zeolite if kept warm and sealed, especially at a lower Si/Al.[118] Although the geopolymerization reaction and aging time are accelerated at elevated temperature, an initial period of curing (pre-curing) should be carried out to allow the development of geopolymer microstructure. Samples that are cured at an elevated temperature should be maintained as a closed system to prevent exposure to the carbon dioxide, leaching of pore fluids and moisture loses, since these factors lead to a significant change in the overall system. Curing of metakaolin geopolymer at 23 °C and ageing for 28 days produced a featureless microstructure in the SEM, whereas the metakaolin cured at 95 °C for 28 days showed a dramatic restructuring, forming very large interconnected pores.[83] Curing the geopolymer at an elevated temperature enhanced the mechanical strength. However, higher curing temperatures do not always guarantee a higher compressive strength .[119, 120] Curing temperatures used during the first 4 to 48 hours are critical for the geopolymer manufacturing.[113]

2.4.5 Adsorption characteristics of geopolymers

The use of geopolymer in water and wastewater treatment has gained a great deal of interest in the last decade. The increased interest in the use of geopolymers is attributed to their simplicity of synthesis, mechanical and chemical stability, low carbon footprint, availability of source materials, and scalable production. Moreover, the geopolymer technology support the circular economy through the use of industrial and domestic waste in their synthesis/fabrication; this not only reduces the potential environmental hazards from such wastes but also ensures zero waste technologies. Geopolymers showed excellent capabilities in the removal of various pollutants from the aqueous solutions as shown in Table (2-3). The negatively charged

alumino-silicate framework provides suitable active sites, where the metal ions (e.g., heavy metals) can be sequestrated in the voids. These voids, which are formed due to sharing of all oxygen atoms of the linked aluminium and silicate tetrahedral units, are considered the main locations of the exchangeable cations. The appearance of such a negative charge in the framework is attributed to the replacement of Si by Al. Therefore, the alkali activator plays a significant role in providing the alkali cations where the negatively charged Al (for fold coordination) are balanced.

Cheng et al.[110] tested the adsorption characteristics of geopolymer synthesized from metakaolin, and their potential for the removal of Pb^{2+}, Cu^{2+}, Cr^{3+} and Cd^{2+} from aqueous solution. This study indicated that the adsorption process is an ionic reaction whereby Pb^{2+}, Cu^{2+}, Cr^{3+} and Cd^{2+} metal ions are exchanged with Na^{+} in the geopolymer, confirming the dominance of the ion exchange mechanism. Furthermore, the adsorption of heavy metals on the geopolymer surface increased with increasing the pH values due to the preference of adsorbent to adsorb H^{+} from the solution when the concentration of H^{+} is higher. Moreover, they found that the heavy metal ions are dissociated in a highly acidic environment; this behaviour has been attributed to the destruction of the original structure of geopolymer since part of the aluminium is removed as a function of the soaking time.

Wang et al.[121] indicated that the geopolymer synthetized by a solid–state fusion reaction between a fly ash and NaOH has a porous structure (larger pore structure) which enhanced the adsorption capacity for Cu^{2+} (90 mg/g) compared to the fly ash (0.1 mg/g) and natural zeolite (3.4 mg/g). The high efficiency of geopolymer in the removal of Cu^{2+} compared to zeolite and fly ash is due to the transformation of the crystalline structure into an amorphous porous one which provides more sorption sites accommodating Cu^{2+} ions.

López et al.[122] tested the adsorption characteristics of the geopolymer synthesized from meta-kaolin and rice husk ash for the removal of Cu^{2+}, Cd^{2+}, Zn^{2+}, Pb^{2+}, Cs^{+} and Ni^{2+} metal ions from a multicomponent aqueous system. This study showed that the geopolymer has a selective adsorption behaviour for the metal ions following the order of $Cs^{+} > Pb^{2+} > Cu^{2+} > Cd^{2+} > Ni^{2+} > Zn^{2+}$. Moreover, the adsorption behaviour is a function of the Si/Al ratio in the matrix of geopolymer where the Si/Al = 2 was the optimum ratio for the selective adsorption of Cs^{+} and Pb^{2+}.

Al-Harahsheh et al.[85] tested the efficiency of the raw coal fly ash and coal fly ash geopolymer for the removal of Cu^{2+} from an aqueous solution; the results indicated that the removal efficiency of the geopolymer was 87.7% (43.9 mg/g), while the efficiency of the raw ash was

25.5 % (12.6 mg/g). They attributed the high efficiency of the geopolymer in the removal of Cu^{2+} to the existence of available sorption sites as a result of the alkali activation.

The alkaline activator type and modulus ratio played a significant role on the adsorption characteristics of the geopolymer adsorbents in the heavy metals removal.[123, 124] Anguile et al.[125] indicated that the liquid/liquid ratio of the alkaline activator (Na_2SiO_3/NaOH) affected the adsorption of Mn^{2+} on the geopolymer adsorbent synthetized from the volcanic ash. Moreover, they attributed the efficiency of the geopolymer in Mn^{2+} adsorption to the presence of nucleophiles group – OH and Si-O-Al on the geopolymer surface, which are effective in manganese ion fixation.

Table 2-3: Some results reported in literatures for the geopolymer adsorbents.

Geopolymer	Adsorbate	C_i (mg/L)	Optimum pH	Adsorption capacity (mg/g)	References
Metakaolin	NH^{4+}	10-1000	4-8	21.07	[126]
Metakaolin, Fly ash	Cs^{+}	266	7	565	[127]
Metakaolin	Pb^{2+}	50-300	4-5	147	[110]
Fly ash (A type)	Cu^{2+}	350-748	n.d	77.3	[128]
Blast furnace slag	Ni^{2+}	2	6	3.7	[13]
Metakaolin, fly ash	Sr^{2+}	175	7-11	85	[129]
Ba-blast furnace	SO_4^{2-}	856	7-8	119	[130]
Fe oxide geopolymer	As (III), As (V)	n.d	n.d	0.614, 1.689	[131]
Zn-LDSGP	F^{-}	50	5	60	[132]
Fly ash	Cu^{2+}	100	6	152.3	[85]
Metakaolin	Mn^{2+}	100	6.09	72.3	[133]
Metakaolin	Co^{2+}	100	6.08	69.2	[133]
Zeolite-based geopolymer	Cu^{2+}	94.7	n.d	52.63	[134]
Fly ash	Pb^{2+}	100	5	63.42	[135]

Luukkonen et al.[13] indicated that the blast furnace slag geopolymer is more efficient in the simultaneous removal of As(III), Sb(III) and Ni(II) from a mine effluent compared to the raw blast furnace slag, raw metakaolinite and metakaolinite geopolymer. In addition, the nature of the water matrix has a significant impact on the adsorption capacitiy where a high competition between As(III), Sb(III) and Ni(II) and other ions in the water matrix were high.

Incorporation of other components, such as sodium alginate, Fe_2O_3 and zeolitic tuffs, during or after the geopolymer synthesis improved the adsorption performance of the geopolymers as compared to the non-modified geopolymers.[136, 137] Geopolymer also showed a good performance, after the incorporation of copper, as an antibacterial material. Moreover, the use of geopolymers as a pH modifier agent has been confirmed where they acted as a pH buffering material preventing the pH drop during the wastewater sludge biogasification. This potential in acting as a buffering agent is attributed to the leachability of the free alkalis in the geopolymer pore solution.[138] Modification of the surface of the blast furnace slag geopolymer by incorporating Ba^{2+} in the framework structure instead of Na^{+} was very efficient in the removal of SO_4^{2-} where the maximum adsorption capacity reached up to 119 mg/g at pH 7-8.[130] Incorporation of the mining wastes, such as iron ore tailings, during the synthesis of the fly ash geopolymer showed a good potentiality in the removal of heavy metals such as copper. The replacement of fly ash by iron ore tailings encouraged the formation of a well-developed porous structure with a total porosity of 74.6%. As a result, the removal efficiency of the produced geopolymer reached up to 97.9% after 70 min and at pH 5, which is higher compared to the non-porous reference geopolymer.[139]

References

1. M. Denchak, Water Pollution: Everything You Need to Know, https://www.nrdc.org/stories/water-pollution-everything-you-need-know).
2. J. Xu, Z. Cao, Y. Zhang, Z. Yuan, Z. Lou, X. Xu and X. Wang, *Chemosphere*, 2018, **195**, 351-364.
3. C. Woodford, Water pollution: an introduction, https://www.explainthatstuff.com/waterpollution.html).
4. L. Järup, *British medical bulletin*, 2003, **68**, 167-182.
5. N. K. Srivastava and C. B. Majumder, *Journal of Hazardous Materials*, 2008, **151**, 1-8.
6. N. Bolan, M. Kumar, E. Singh, A. Kumar, L. Singh, S. Kumar, S. Keerthanan, S. A. Hoang, A. El-Naggar, M. Vithanage, B. Sarkar, H. Wijesekara, S. Diyabalanage, P. Sooriyakumar, A. Vinu, H. Wang, M. B. Kirkham, S. M. Shaheen, J. Rinklebe and K. H. M. Siddique, *Environment International*, 2022, **158**, 106908.
7. G. K. Kinuthia, V. Ngure, D. Beti, R. Lugalia, A. Wangila and L. Kamau, *Scientific Reports*, 2020, **10**, 8434.
8. S. Tomiyama and T. Igarashi, *Current Opinion in Environmental Science & Health*, 2022, **27**, 100347.
9. A. Alengebawy, S. T. Abdelkhalek, S. R. Qureshi and M.-Q. Wang, *Toxics*, 2021, **9**, 42.
10. V. Srivastava, A. Sarkar, S. Singh, P. Singh, A. S. F. de Araujo and R. P. Singh, *Frontiers in Environmental Science*, 2017, **5**.
11. a. P. A. R. J. L. Barringer, *London, United Kingdom: IntechOpen*, 2013.
12. P. L. Smedley and D. G. Kinniburgh, *Applied Geochemistry*, 2002, **17**, 517-568.
13. T. Luukkonen, H. Runtti, M. Niskanen, E.-T. Tolonen, M. Sarkkinen, K. Kemppainen, J. Rämö and U. Lassi, *Journal of Environmental Management*, 2016, **166**, 579-588.
14. P. B. Tchounwou, C. G. Yedjou, A. K. Patlolla and D. J. Sutton, *Exp Suppl*, 2012, **101**, 133-164.

15. H. Morrow, in *Kirk-Othmer Encyclopedia of Chemical Technology*, DOI: https://doi.org/10.1002/0471238961.0301041303011818.a01.pub3, pp. 1-36.
16. A. Turner, *Science of The Total Environment*, 2019, **657**, 1409-1418.
17. K. Rehman, F. Fatima, I. Waheed and M. S. H. Akash, *Journal of Cellular Biochemistry*, 2018, **119**, 157-184.
18. G. WHO, *World Health Organization*, 2011, **216**, 303-304.
19. R. Leyva-Ramos, P. E. Diaz-Flores, A. Aragon-Piña, J. Mendoza-Barron and R. M. Guerrero-Coronado, *Separation Science and Technology*, 2005, **40**, 2079-2094.
20. T. Liu, Y. Lawluvy, Y. Shi, J. O. Ighalo, Y. He, Y. Zhang and P.-S. Yap, *Journal of Environmental Chemical Engineering*, 2022, **10**, 106502.
21. E. Noman, A. Al-Gheethi, R. M. Saphira Radin Mohamed, M. Al-Sahari, M. S. Hossain, D.-V. N. Vo and M. Naushad, *Chemosphere*, 2022, **291**, 132862.
22. J. H. Kim, H. J. Gibb and P. Howe, *Cobalt and inorganic cobalt compounds*, World health organization, 2006.
23. M. K. Uddin, *Chemical Engineering Journal*, 2017, **308**, 438-462.
24. M. A. Islam, D. W. Morton, B. B. Johnson, B. K. Pramanik, B. Mainali and M. J. Angove, *Environmental Nanotechnology, Monitoring & Management*, 2018, **10**, 435-456.
25. R. M. Hazen, G. Hystad, J. J. Golden, D. R. Hummer, C. Liu, R. T. Downs, S. M. Morrison, J. Ralph and E. S. Grew, *American Mineralogist*, 2017, **102**, 108-116.
26. D. S. Patil, S. M. Chavan and J. U. K. Oubagaranadin, *Journal of Environmental Chemical Engineering*, 2016, **4**, 468-487.
27. A. Eaton, *ACS ES&T Water*, 2021, **1**, 2450-2458.
28. M. Sidoryk-Wegrzynowicz and M. Aschner, *Journal of Internal Medicine*, 2013, **273**, 466-477.
29. H. Aydın, Y. Bulut and Ç. Yerlikaya, *Journal of Environmental Management*, 2008, **87**, 37-45.
30. S. S. Al Moharbi, M. G. Devi, B. M. Sangeetha and S. Jahan, *Applied Water Science*, 2019, **10**, 23.

31. H.-C. Kim, T.-W. Jang, H.-J. Chae, W.-J. Choi, M.-N. Ha, B.-J. Ye, B.-G. Kim, M.-J. Jeon, S.-Y. Kim and Y.-S. Hong, *Ann Occup Environ Med*, 2015, **27**, 30-30.

32. M. Hoshino, M. Zhang, M. Suzuki, K. Tsukimura and M. Ohta, *Water, Air, & Soil Pollution*, 2020, **231**, 176.

33. A. Z. Aris, W. Y. Lim and L. J. Looi, in *Environmental Management of River Basin Ecosystems*, eds. M. Ramkumar, K. Kumaraswamy and R. Mohanraj, Springer International Publishing, Cham, 2015, DOI: 10.1007/978-3-319-13425-3_21, pp. 455-476.

34. L. M. Pfadenhauer, J. Burns, A. Rohwer and E. A. Rehfuess, *Systematic Reviews*, 2014, **3**, 36.

35. M. Balali-Mood, K. Naseri, Z. Tahergorabi, M. R. Khazdair and M. Sadeghi, *Frontiers in Pharmacology*, 2021, **12**.

36. A. Hawari, Z. Rawajfih and N. Nsour, *Journal of Hazardous Materials*, 2009, **168**, 1284-1289.

37. L. M. Plum, L. Rink and H. Haase, *Int J Environ Res Public Health*, 2010, **7**, 1342-1365.

38. S. I. Siddiqui and S. A. Chaudhry, *Process Safety and Environmental Protection*, 2017, **111**, 592-626.

39. I. S. Siddiqui and A. S. Chaudhry, *Current Environmental Engineering*, 2017, **4**, 81-102.

40. W. Wong, H. Y. Wong, A. B. M. Badruzzaman, H. H. Goh and M. Zaman, *Nanotechnology*, 2016, **28**, 042001.

41. B. Pan, B. Pan, W. Zhang, L. Lv, Q. Zhang and S. Zheng, *Chemical Engineering Journal*, 2009, **151**, 19-29.

42. S. Y. Bratskaya, A. V. Pestov, Y. G. Yatluk and V. A. Avramenko, *Colloids and Surfaces A: Physicochemical and Engineering Aspects*, 2009, **339**, 140-144.

43. J. Esalah and M. M. Husein, *Separation Science and Technology*, 2008, **43**, 3461-3475.

44. L. K. Wang, D. A. Vaccari, Y. Li and N. K. Shammas, in *Physicochemical Treatment Processes*, eds. L. K. Wang, Y.-T. Hung and N. K. Shammas, Humana Press, Totowa, NJ, 2005, DOI: 10.1385/1-59259-820-x:141, pp. 141-197.

45. M. A. Barakat, *Arabian Journal of Chemistry*, 2011, **4**, 361-377.

46. S. Kocaoba, *Desalination*, 2009, **244**, 24-30.

47. A. Dąbrowski, Z. Hubicki, P. Podkościelny and E. Robens, *Chemosphere*, 2004, **56**, 91-106.

48. S. Gautam and G. Saini, *Global Journal of Environmental Science and Management*, 2020, **6**, 553-578.

49. T. Freitas, V. M. Oliveira, M. T. F. d. Souza, H. C. L. Geraldino, V. C. Almeida, S. L. Fávaro and J. C. Garcia, *Industrial Crops and Products*, 2015, **76**, 538-544.

50. D. S. Dhanjal, S. Singh, D. Bhatia, J. Singh, N. R. Sharma and R. S. Kanwar, *Pollut Res*, 2018, **37**, S32-S38.

51. A. H. Amran, N. S. Zaidi, K. Muda and L. W. Loan, *International Journal of Engineering & Technology*, 2018, **7**, 34-37.

52. H. Wei, B. Gao, J. Ren, A. Li and H. Yang, *Water Research*, 2018, **143**, 608-631.

53. D. Mowla, H. N. Tran and D. G. Allen, *Biomass and Bioenergy*, 2013, **58**, 365-378.

54. M. H. Abd El-Salam, in *Encyclopedia of Food Sciences and Nutrition (Second Edition)*, ed. B. Caballero, Academic Press, Oxford, 2003, DOI: https://doi.org/10.1016/B0-12-227055-X/00762-8, pp. 3833-3837.

55. H. N. Lazarides and E. Katsanidis, in *Encyclopedia of Food Sciences and Nutrition (Second Edition)*, ed. B. Caballero, Academic Press, Oxford, 2003, DOI: https://doi.org/10.1016/B0-12-227055-X/00761-6, pp. 3827-3833.

56. G. Crini and E. Lichtfouse, *Environmental Chemistry Letters*, 2019, **17**, 145-155.

57. S. H. Joo and B. Tansel, *Journal of Environmental Management*, 2015, **150**, 322-335.

58. Y. F. Tao, S. Y. Qiu Y Fau - Fang, Z. Y. Fang Sy Fau - Liu, Y. Liu Zy Fau - Wang, J. H. Wang Y Fau - Zhu and J. H. Zhu.

59. Q.-R. Fang, D.-Q. Yuan, J. Sculley, J.-R. Li, Z.-B. Han and H.-C. Zhou, *Inorganic Chemistry*, 2010, **49**, 11637-11642.

60. W. S. Chai, J. Y. Cheun, P. S. Kumar, M. Mubashir, Z. Majeed, F. Banat, S.-H. Ho and P. L. Show, *Journal of Cleaner Production*, 2021, **296**, 126589.

61. M. T. Yagub, T. K. Sen, S. Afroze and H. M. Ang, *Advances in Colloid and Interface Science*, 2014, **209**, 172-184.

62. I. Ali and V. K. Gupta, *Nature Protocols*, 2006, **1**, 2661-2667.

63. L. Wang, C. Shi, L. Wang, L. Pan, X. Zhang and J.-J. Zou, *Nanoscale*, 2020, **12**, 4790-4815.

64. D. Chen, L. Wang, Y. Ma and W. Yang, *NPG Asia Materials*, 2016, **8**, e301-e301.

65. C.-Y. Cao, J. Qu, F. Wei, H. Liu and W.-G. Song, *ACS Applied Materials & Interfaces*, 2012, **4**, 4283-4287.

66. R. A. Sims, S. L. Harmer and J. S. Quinton, *Polymers*, 2019, **11**.

67. M. Králik, *Chemical Papers*, 2014, **68**, 1625-1638.

68. K. Y. Foo and B. H. Hameed, *Chemical Engineering Journal*, 2010, **156**, 2-10.

69. I. Anastopoulos, M. Karamesouti, A. C. Mitropoulos and G. Z. Kyzas, *Journal of Molecular Liquids*, 2017, **229**, 555-565.

70. B. Raut, Langmuir Adsorption Isotherm – Assumptions, Derivation, and Limitations, https://chemistnotes.com/physical/langmuir-adsorption-isotherm-assumptions-derivation-and-limitations/).

71. M. D. Alves, F. M. Aracri, É. C. Cren and A. A. Mendes, *Chemical Engineering Journal*, 2017, **311**, 1-12.

72. S. A. Sadeek, N. A. Negm, H. H. H. Hefni and M. M. A. Wahab, *International Journal of Biological Macromolecules*, 2015, **81**, 400-409.

73. M. S. Morsy, S. H. Alsayed, Y. Al-Salloum and T. Almusallam, *Arabian Journal for Science and Engineering*, 2014, **39**, 4333-4339.

74. J. Davidovits, *Journal of thermal analysis*, 1991, **37**, 1633-1656.

75. P. Baran, M. Nazarko, E. Włosińska, A. Kanciruk and K. Zarębska, *Journal of Cleaner Production*, 2021, **293**, 126112.

76. H. Xu and J. S. J. Van Deventer, *International Journal of Mineral Processing*, 2000, **59**, 247-266.

77. J. Davidovits and S. Cordi, *Spe Pactec*, 1979, **79**, 151-154.

78. M. Sofi, J. S. J. van Deventer, P. A. Mendis and G. C. Lukey, *Cement and Concrete Research*, 2007, **37**, 251-257.

79. A. Palomo and J. I. López dela Fuente, *Cement and Concrete Research*, 2003, **33**, 281-288.

80. H. Rahier, B. Van Mele, M. Biesemans, J. Wastiels and X. Wu, *Journal of Materials Science*, 1996, **31**, 71-79.

81. P. V. Krivenko, *Proceedings of the First International Conference on Alkaline Cements and Concretes*, 1994, 11-129.

82. J. Forsgren, C. Pedersen, M. Strømme and H. Engqvist, *PLoS One*, 2011, **6**, e17759-e17759.

83. J. L. Provis and J. S. J. Van Deventer, in *Geopolymers*, eds. J. L. Provis and J. S. J. van Deventer, Woodhead Publishing, 2009, DOI: https://doi.org/10.1533/9781845696382.1, pp. 1-11.

84. J.-X. Quan, H.-Y. Zhang, L.-Y. Zhou, Y. Zhou and J.-W. Su, *Procedia Engineering*, 2017, **210**, 45-52.

85. M. S. Al-Harahsheh, K. Al Zboon, L. Al-Makhadmeh, M. Hararah and M. Mahasneh, *Journal of Environmental Chemical Engineering*, 2015, **3**, 1669-1677.

86. S. Özen and B. Alam, *Periodica Polytechnica Civil Engineering*, 2018, **62**, 64-71.

87. D. Dimas, I. Giannopoulou and D. Panias, *Journal of Materials Science*, 2009, **44**, 3719-3730.

88. J. G. S. van Jaarsveld, J. S. J. van Deventer and G. C. Lukey, *Chemical Engineering Journal*, 2002, **89**, 63-73.

89. Sindhunata, J. S. J. van Deventer, G. C. Lukey and H. Xu, *Industrial & Engineering Chemistry Research*, 2006, **45**, 3559-3568.

90. P. Duxson, A. Fernández-Jiménez, J. L. Provis, G. C. Lukey, A. Palomo and J. S. J. van Deventer, *Journal of Materials Science*, 2007, **42**, 2917-2933.

91. J. S. J. van Deventer, J. L. Provis, P. Duxson and G. C. Lukey, *Journal of Hazardous Materials*, 2007, **139**, 506-513.

92. J. Davidovits, *J. Davidovits.–Saint-Quentin, France (Issue January 2008)*, 2020.

93. W. K. Part, M. Ramli and C. B. Cheah, *Construction and Building Materials*, 2015, **77**, 370-395.

94. A. Palomo, M. W. Grutzeck and M. T. Blanco, *Cement and Concrete Research*, 1999, **29**, 1323-1329.

95. D. Khale and R. Chaudhary, *Journal of Materials Science*, 2007, **42**, 729-746.

96. P. De Silva, K. Sagoe-Crenstil and V. Sirivivatnanon, *Cement and Concrete Research*, 2007, **37**, 512-518.

97. A. Hajimohammadi, J. L. Provis and J. S. J. van Deventer, *Journal of Colloid and Interface Science*, 2011, **357**, 384-392.

98. M. Criado, A. Palomo and A. Fernández-Jiménez, *Fuel*, 2005, **84**, 2048-2054.

99. X. Y. Zhuang, L. Chen, S. Komarneni, C. H. Zhou, D. S. Tong, H. M. Yang, W. H. Yu and H. Wang, *Journal of Cleaner Production*, 2016, **125**, 253-267.

100. H. Xu, J. Van Deventer and G. Lukey, *Industrial & Engineering Chemistry Research*, 2001, **40**, 3749-3756.

101. J. He, J. Zhang, Y. Yu and G. Zhang, *Construction and Building Materials*, 2012, **30**, 80-91.

102. L. Weng, K. Sagoe-Crentsil and S. S. Zhang, *Journal of the Chinese Ceramic Society*, 2005, **33**, 276-280.

103. P. Duxson, J. L. Provis, G. C. Lukey, S. W. Mallicoat, W. M. Kriven and J. S. J. van Deventer, *Colloids and Surfaces A: Physicochemical and Engineering Aspects*, 2005, **269**, 47-58.

104. A. P. Ana M. Fernandez-Jimenez and L.-H. Cecilio, *ACI Materials Journal*, **103**.

105. P. Sukmak, S. Horpibulsuk and S.-L. Shen, *Construction and building Materials*, 2013, **40**, 566-574.

106. C. Ridtirud, P. Chindaprasirt and K. Pimraksa, *International Journal of Minerals, Metallurgy, and Materials*, 2011, **18**, 100-104.

107. C. Villa, E. T. Pecina, R. Torres and L. Gómez, *Construction and Building Materials*, 2010, **24**, 2084-2090.

108. W. K. W. Lee and J. S. J. van Deventer, *Colloids and Surfaces A: Physicochemical and Engineering Aspects*, 2002, **211**, 49-66.

109. P. Chindaprasirt, T. Chareerat and V. Sirivivatnanon, *Cement and Concrete Composites*, 2007, **29**, 224-229.

110. T. W. Cheng, M. L. Lee, M. S. Ko, T. H. Ueng and S. F. Yang, *Applied Clay Science*, 2012, **56**, 90-96.

111. S. Usha, D. G. Nair and S. Vishnudas, *INTERNATIONAL JOURNAL OF CIVIL ENGINEERING ANDTECHNOLOGY*, 2014, **5**.

112. K. J. D. MacKenzie, S. Komphanchai and R. Vagana, *Journal of the European Ceramic Society*, 2008, **28**, 177-181.

113. J. Temuujin, R. P. Williams and A. van Riessen, *Journal of Materials Processing Technology*, 2009, **209**, 5276-5280.

114. J. Temuujin, K. Okada, T. S. Jadambaa, K. J. D. MacKenzie and J. Amarsanaa, *Journal of the European Ceramic Society*, 2003, **23**, 1277-1282.

115. L. Chen, G. Ye, D. Xu, L. Zhu, Z. Lu, L. Dong and Y. Liu, *Materials Letters*, 2012, **85**, 91-94.

116. S. Kumar and R. Kumar, *Ceramics International*, 2011, **37**, 533-541.

117. T. W. Cheng and J. P. Chiu, *Minerals Engineering*, 2003, **16**, 205-210.

118. J. L. Provis, G. C. Lukey and J. S. J. van Deventer, *Chemistry of Materials*, 2005, **17**, 3075-3085.

119. D. L. Y. Kong, J. G. Sanjayan and K. Sagoe-Crentsil, *Cement and Concrete Research*, 2007, **37**, 1583-1589.

120. D. Hardjito, C. C. Cheak and C. H. L. Ing, *Modern applied science*, 2008, **2**, 3-11.

121. S. Wang, L. Li and Z. H. Zhu, *Journal of Hazardous Materials*, 2007, **139**, 254-259.

122. F. J. L¨®pez, S. Sugita, M. Tagaya and T. Kobayashi, *Journal of Materials Science and Chemical Engineering*, 2014, **Vol.02No.07**, 12.

123. T. Lan, P. Li, X. Li, J. Guo, Q. Huang, J. Geng, Q. Zhao, W. Yang and S. Guo, *Environmental Technology*, 2021, DOI: 10.1080/09593330.2021.1946597, 1-10.

124. T. Luukkonen, E.-T. Tolonen, H. Runtti, K. Kemppainen, P. Perämäki, J. Rämö and U. Lassi, *Journal of Materials Science*, 2017, **52**, 9363-9376.

125. J. J. Anguille, G. G. O. Mbega, T. Makani and K. J. Mbadcam, *International Journal of Basic Applied Chemistry Sciences*, 2013, **3**, 7-18.

126. T. Luukkonen, M. Sarkkinen, K. Kemppainen, J. Rämö and U. Lassi, *Applied Clay Science*, 2016, **119**, 266-276.

127. X. Chen, Y. Guo, S. Ding, H. Zhang, F. Xia, J. Wang and M. Zhou, *Journal of Cleaner Production*, 2019, **207**, 789-800.

128. M. N. Mužek, S. Svilović and J. Zelić, *Desalination and Water Treatment*, 2014, **52**, 2519-2526.

129. Y. L. Chen, Y. Y. Tong, R. W. Pan and J. Tang.

130. H. Runtti, T. Luukkonen, M. Niskanen, S. Tuomikoski, T. Kangas, P. Tynjälä, E.-T. Tolonen, M. Sarkkinen, K. Kemppainen, J. Rämö and U. Lassi, *Journal of Hazardous Materials*, 2016, **317**, 373-384.

131. N. Thakur and D. W. Armstrong, *Journal of Cleaner Production*, 2021, **291**, 125931.

132. C. Sarkar, J. K. Basu and A. N. Samanta, *Chemical Engineering Research and Design*, 2019, **142**, 165-175.

133. I. Kara, D. Tunc, F. Sayin and S. T. Akar, *Applied Clay Science*, 2018, **161**, 184-193.

134. H. Baykara, M. d. L. Mendoza Solorzano, J. J. Delgado Echeverria, M. H. Cornejo and C. V. Tapia-Bastidas, *R Soc Open Sci*, 2022, **9**, 211644-211644.

135. K. Al-Zboon, M. S. Al-Harahsheh and F. B. Hani, *Journal of Hazardous Materials*, 2011, **188**, 414-421.

136. M. Naghsh and K. Shams, *Applied Clay Science*, 2017, **146**, 238-245.

137. Y. Ge, X. Cui, C. Liao and Z. Li, *Chemical Engineering Journal*, 2017, **311**, 126-134.

138. R. M. Novais, M. P. Seabra and J. A. Labrincha, *Journal of Cleaner Production*, 2017, **143**, 1114-1122.

139. P. Duan, C. Yan, W. Zhou and D. Ren, *Ceramics International*, 2016, **42**, 13507-13518.

CHAPTER3: HEAVY METALS DISTRIBUTION IN THE GOLDEN TRIANGLE ECONOMIC ZONE

Abstract

This chapter discusses the distribution of heavy metals in the Golden Triangle area of Egypt. Fieldwork involved groundwater sampling from the available water points from the coastal, crystalline rocks and Nile valley zones. The study area has a complex geology and has been subjected to extensive mining activities in the past, which contributed, to some extent, to the groundwater contamination with the serious presence of heavy metals. The chemical analysis of water samples revealed the presence of various metal ions with concentrations above or close to the upper permissible limit. The heavy metal pollution index calculations showed a high pollution in the study area in the order coastal zone>crystalline rocks zone>Nile valley zone. Dangerous metals, such as As (55 ug/L), Ni (171 ug/L), Cd (11 ug/L), Co (5 ug/L), Mn (1227 ug/L), Tl (5 ug/L), V (23 ug/L), U (30 ug/L), and Se (37 ug/L) were found in a high concentration. The heavy metals pollution index for each individual water point was calculated, indicating that some samples in the coastal (HW= 662) and crystalline rock zones (BH=159, FKH=100) are above and/or close to the critical limit (HPI=100). The contamination in the crystalline rocks and coastal zones is a result of the mining and geogenic processes (water-rock interactions), while in the Nile valley the contamination was attributed to the agricultural activities and infiltration of the untreated sewage water (44% of samples), and the geochemical characteristics of groundwater aquifer (55% of samples).



Figure 3-1: Anthropogenic sources of contamination.

3.1 Introduction

Egypt is now confronting several problems including rapid population expansion and climate change. As a result, new solutions are required to fulfil the country's rising water and energy needs. In order to boost the economy and provide a new employment, the Egypt Vision 2030 is centred on a number of national initiatives, including the Golden Triangle Economic zone, the Siemens-Egypt project, the New Suez Canal project, the New Administrative City, and El-Dabaa power plant.[1] As a consequence, the Egyptian economy will become more competitive on a worldwide scale. The second national mega project, the Golden Triangle Economic zone, is situated in the Eastern Desert between the towns of Qena, Safaga, and Qusir (Figure 3-2), and it aspires to create a new industrial capital in this attractive region.[2] The region is renowned for being abundant in the key minerals and resources. Although there have been a several mining operations in the Golden Triangle over the last century to extract a variety of minerals and materials, including gold, wolframite, quartz, talc, phosphate, and ornamental rocks, the majority of these activities are no longer in operation.[3-7] However, the Eastern Desert in general and the Golden Triangle, in particular, are now seeing a renaissance of mining and exploration activity. Three sections make up the Golden Triangle region: the Nile Valley zone, the crystalline rocks zone, and the coastal zone. The initiative intends to create a new economic activity in the three zones based on the available natural resources and their prime position between the Nile Valley and the Red Sea. The Golden Triangle covers ca. 9,000 km^2 in total.[8] Growing the agricultural land in the Nile Valley, establishing new industries and desalination plants, creating new urban settlements, expanding mining operations, exploiting certain mineral reserves, and creating new resorts and tourist towns are some of the potential development activities. The region's two major roadways, which connect the Nile Valley with the Red Sea cities, are extensively used for the transportation, exportation, and importation of products via the Safaga and Qusir ports. In recent years, a new road network has been established.[9] This initiative is intended to improve the economy, provide job opportunities, and considerably advance the development in Upper Egypt. The quality and accessibility of water resources are crucial for achieving the prospective goals.

Since groundwater is the primary source of freshwater, enhancing its quality is crucial to support the water management plans. Several studies have investigated the general characteristics of groundwater and its quality in terms of the major ions.[10-12] Although a few studies have revealed the presence of hazardous metal ions in groundwater of some locations, little is still known, however, about the impacts of the mining, agricultural and other industrial

activities in raising the metal ions concentration in groundwater systems.[13, 14] The lack of studies, in terms of the heavy metals, in the study area could be attributed to several reasons: (i) the area was less developed and, as a consequence, this type of research was considered less important (or to have less impact), (ii) the access to some locations was challenging, and/or (iii) the lack of research funding. With the development of the Golden Triangle project, for establishing a new economic communities, investigating the impacts of the anthropogenic and geogenic processes on the groundwater quality along with proposing a new, inexpensive, and sustainable methods for water treatment becomes an urgent matter. The current research project endeavour is primarily concerned with identifying and mapping the most challenging heavy metals in the groundwater. The obtained results will support the water resources management strategies and improve the water quality by proposing new treatment methods.

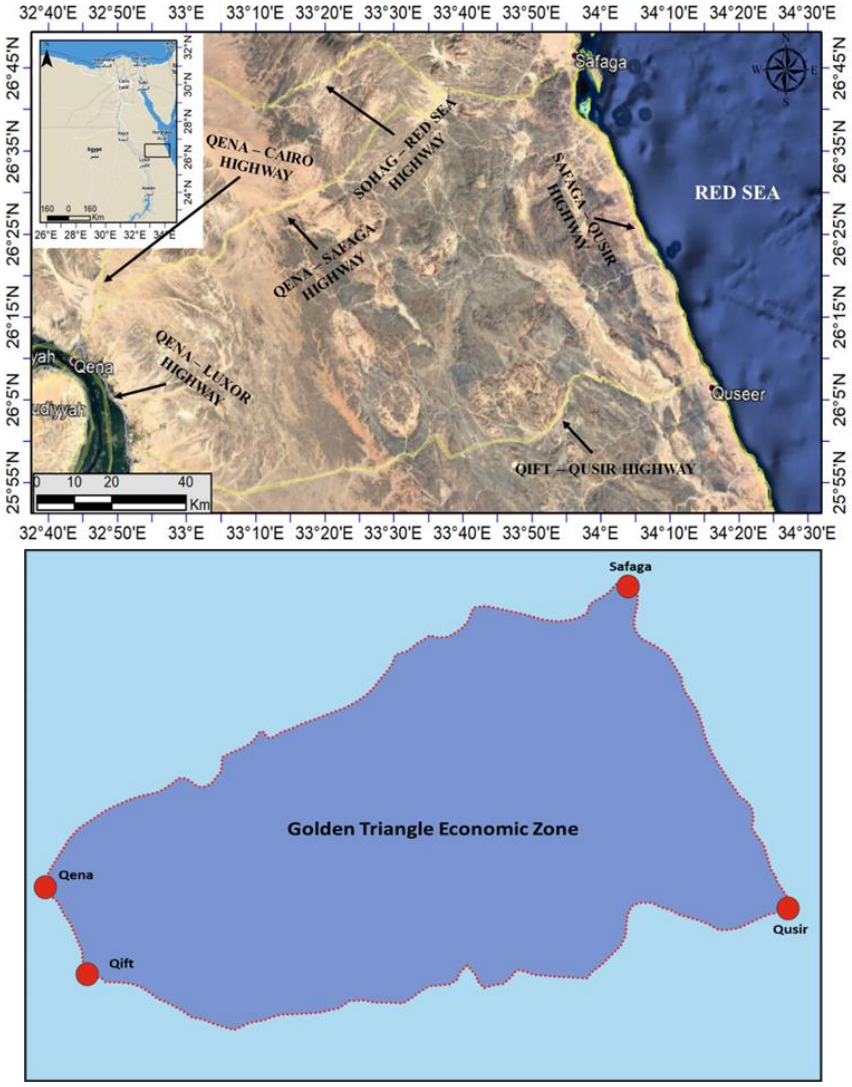


Figure 3-2: Location map of the Golden Triangle area.

3.1.1 General geology

The Golden Triangle Economic Zone is located in the central part of the Eastern Desert. The Eastern Desert is the graben shoulder of the Cenozoic Red Sea Rift system and exposes the Pan-African basement complex.[3] The area is mainly occupied by the Precambrian basement complex and Phanerozoic sedimentary successions (Figure.3-3&4).[15]The Precambrian basement complex, outcrop in the Red Sea hills, are represented by different igneous (basic and acidic) and metamorphic rocks. Igneous rocks are varied and comprise of granitoids and volcanics. The granitoids are further subdivided into older and younger varieties with many different phases based on their mineralogy, petrogenesis, tectonic setting and geochemistry. Most of the rock units are cut by several dike swarms of different compositions, widths, and lengths. The geological map of the study area is depicted in Figure (3-3).

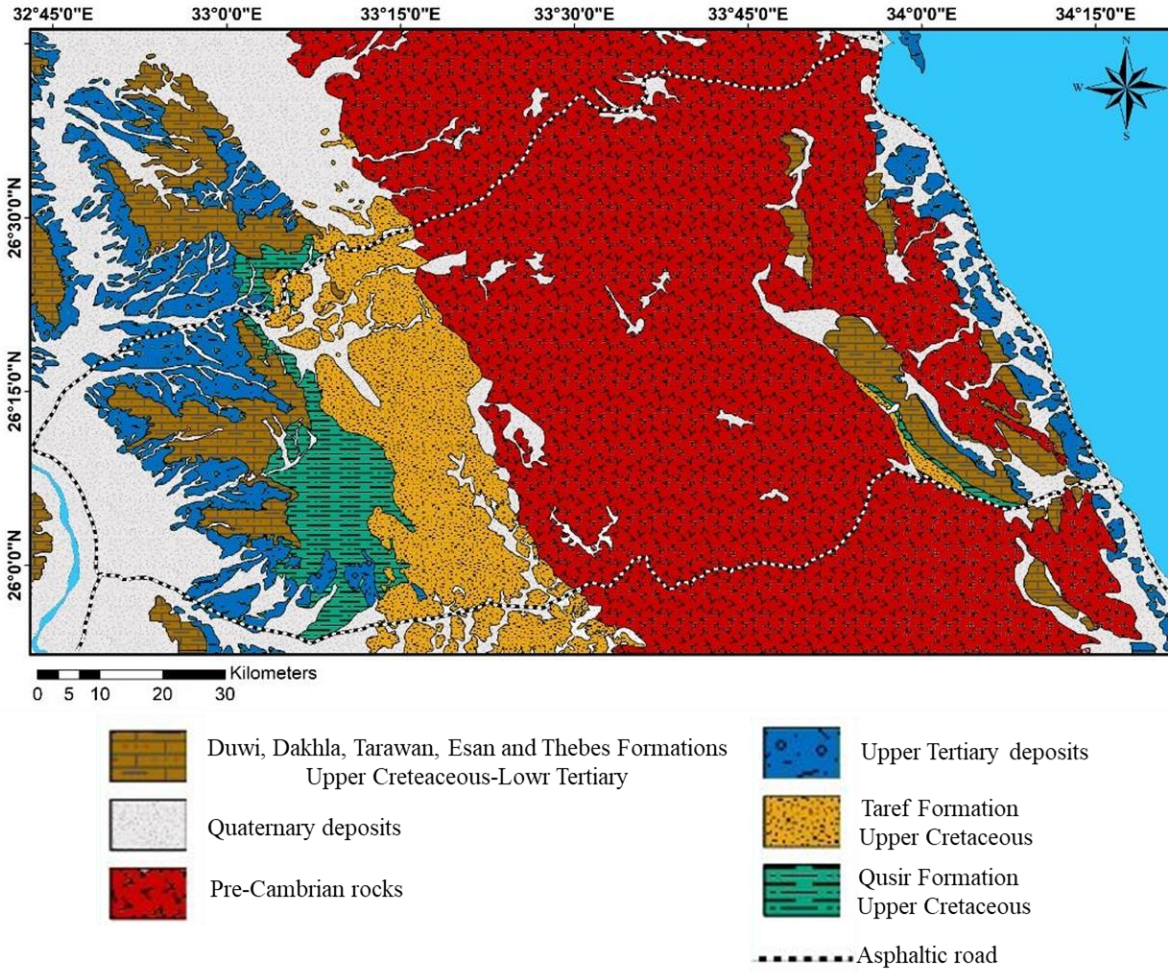


Figure 3-3: Geological map of the study area, modified after Ismaiel et al.[16]

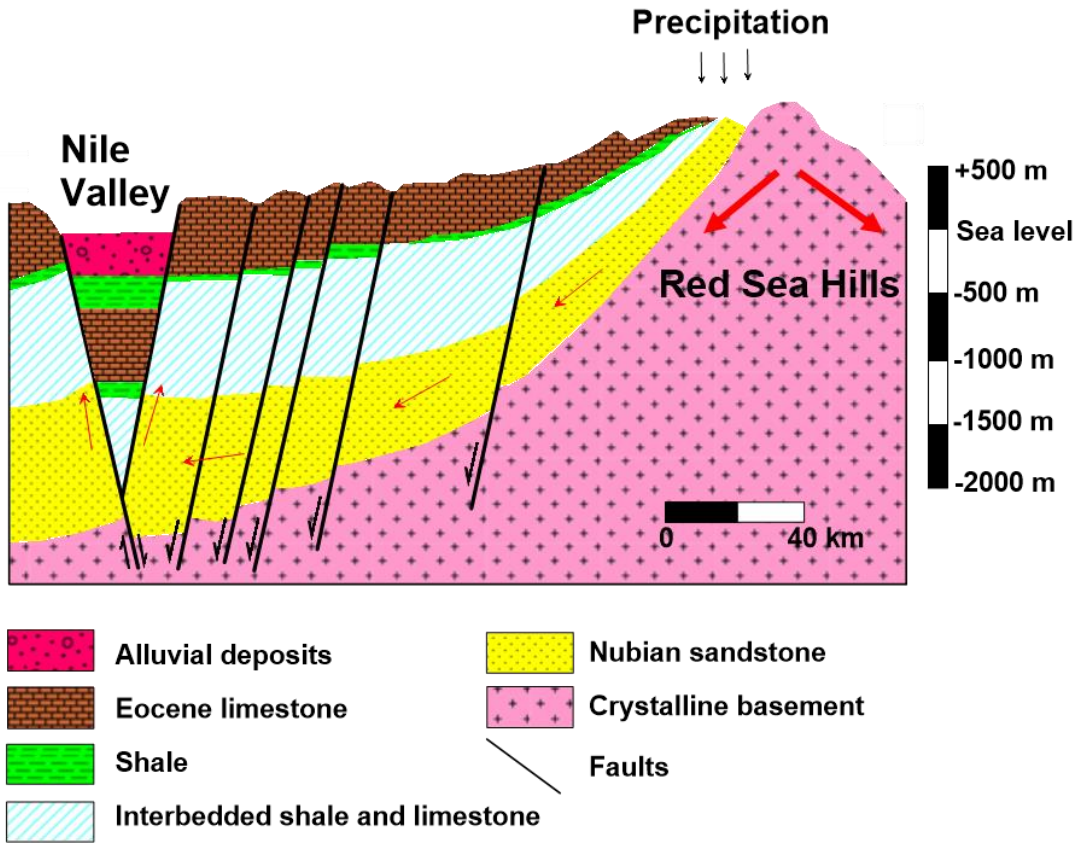


Figure 3-4: Generalized cross section for the middle part, modified after Embaby and Redwan.[17]

3.1.2 Water resources

The Golden Triangle area is distinguished by a dry and hot weather due to its location in the arid zone. The average yearly temperature ranges from the lowest of 23 ^{0}C in the winter season to a maximum temperature of 42 ^{0}C in the summertime.[18] Moreover, the study area is characterized by the prevalence of a low precipitation and excessive water evaporation.

Generally, groundwater represents the main source of water in arid and semi-arid regions in the world. The Golden Triangle is characterized by extremely limited surface water resources where the annual precipitation on the Eastern Desert is less than 35 mm.[15] The study area has a small recharge which is significantly comes from the infiltration of flash flooding water due to the seasonal heavy rains.[19] The high percentages of such flash flood seeps to the fractured basement aquifers and shallow alluvial aquifers.

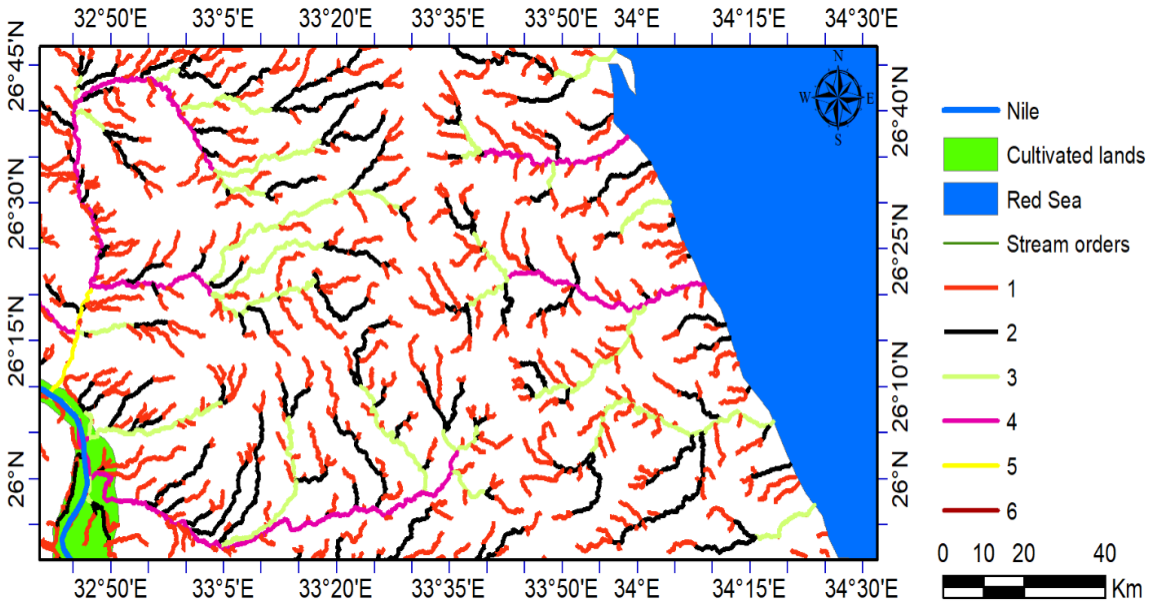


Figure 3-5: Stream order of the Golden Triangle.

The water resources in the Golden Triangle area could be classified into three categories:[11]

(i) Surface potable water from the Nile River

Water from the Nile River is the main source of water for the area located near the river and is used for the domestic purposes, agriculture, and other industrial activities. Additionally, the Red Sea cities also receive a transported potable water from the Nile through a pipeline system cutting-through the Golden Triangle.

(ii) Desalinated water

Desalination plants in the Red Sea are used to provide a treated water to the cities of Safaga and Qusir in addition to some touristic villages.

(iii) Groundwater

Groundwater in the Golden Triangle is the essential source of water for the area far from the Nile, supporting the mining, industrial and agricultural activities. Moreover, the groundwater, without any treatment, represents the predominant source of drinking water.[10]

The main groundwater aquifers in the Golden Triangle involve the Nubian sandstone aquifer, fractured basement aquifers, and shallow alluvial aquifers.[10, 18-20]

(i) Fractured basement aquifers

The fractured basement aquifers occur as a permeable and porous fracture zones within the metamorphic and igneous rocks. These rocks are characterized by a dense and massive faults

and fractures intersecting with each other allowing the recharge process. Consequently, the groundwater accumulates and migrates through the connected fracture system. Usually, the quantity of water is pretty limited and controlled by the width, depth and the extension of fractures.[21] These kind of aquifers are mainly located in the mountainous part of the study area. The groundwater quality of the fractured basement aquifers are impacted by the local climate and host rock chemistry.[22]

(ii) Alluvium aquifers

This kind of aquifers, form most of wadi tributaries, is shallow in depth and is consisted of gravel, sand, and boulders. These aquifers are characterized by a high storage capacity. However, they are small and their yields differ geographically and seasonally.[10] These aquifers are of high importance as a shallow groundwater supply in the study area.

(iii) Nubian sandstone aquifer

The Nubian sandstone aquifer is the deepest, located at a depth between 300-500 m, and occurs under confined to semi-confined conditions.[18, 22] This aquifer is occasionally recharged through the infiltration of rains. The Nubian sandstone aquifer is composed of a fine to coarse-grained sandstone alternated with clay and shale beds. The Nubian sandstone aquifer of the Central Eastern Desert is characterized by a very high exploitation potential. Moreover, the quality of water varies from one place to another.[22]

(iv) Fractured limestone aquifer

Groundwater also occurs under confined conditions in the fractured limestone. This formation is consisted of a combination of oyster limestone and marl and is intercalated with phosphatic layers. This aquifer is recharged through the rainfall on the catchment Precambrian rocks as well as from the deeper Nubian sandstone aquifer through the upward leakage along the fracture planes.[11, 12]

3.1.3 Potential sources of water pollution

3.1.3.1 Anthropogenic

The anthropogenic activity in the Golden Triangle involves mining, agriculture, industry, and urbanization, Figure (3-6). The groundwater quality in the Golden Triangle will be a matter of a serious concern due to the prospective expansion of the agricultural, industrial, and recreational activities.

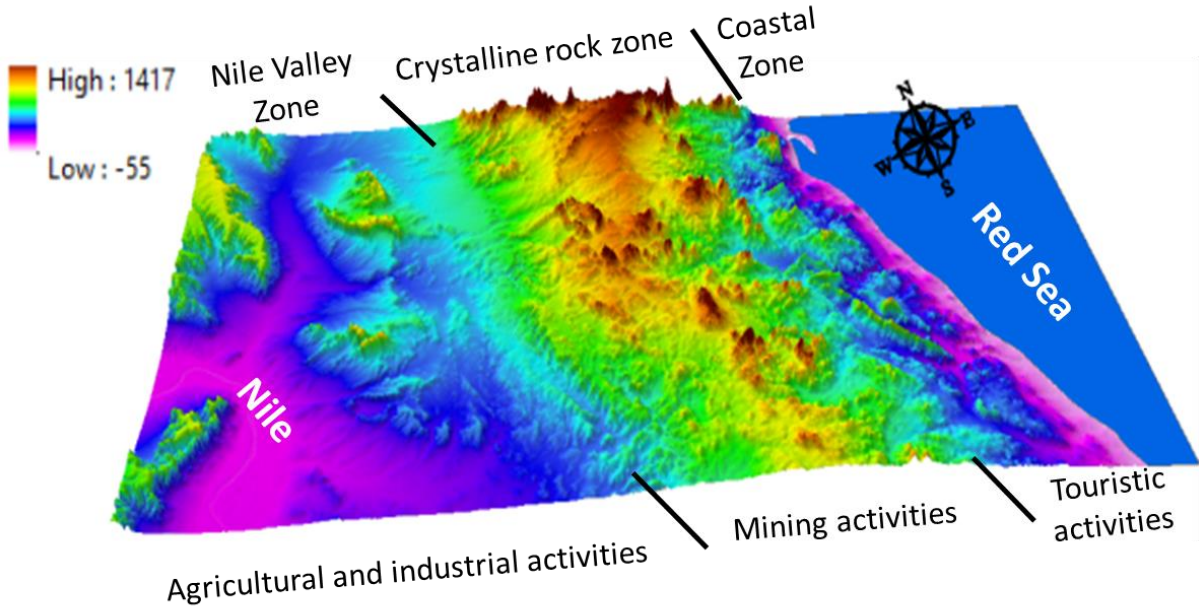


Figure 3-6: Digital elevation model of the study area, showing the three economic zones and related activities.

3.1.3.1.1 Mining Activities

The Eastern Desert of Egypt poses several types of ore mineralization, including gold, wolframite, phosphate, sulphides, copper, tin, emerald, etc.[23-26]As a consequence, since the pharaonic epoch, ca. 5000 years ago, the study area has witnessed a substantial mining activity. The study area was mined for the wolframite [(Fe, Mn)WO_4] in Abu-Kharif and for gold (Au) in the El-Fawakhir, Fatira, and Abu-Marawat mines.

Phosphate mining is distributed in various locations, including El-Dawi, Rabah, Um El-Hwaitate, Hamadat and El-Bieda. In addition, other minerals such as talc, quartz and feldspars were mined in various locations. The groundwater pollution was attributed to certain mining operations such as in the Wadi Quieh (the north-eastern portion of the study area), where a rise in the concentration of manganese, copper, chromium, and iron in groundwater has been noted. This pollution was as a result of heavy metals, from phosphate waste heaps, leaking into the subsurface water.[14]Although, most of the mining activities are not in operation, their contribution in increasing the heavy metal levels in groundwater is expected to be high.

3.1.3.1.2 Agricultural activities

The agricultural activities are mainly distributed around the Nile, in addition to wadi Qena, Wadi El-Matully, and few occurrences in wadi Quieh. The cultivated land in the Nile valley is

mainly irrigated from the Nile, while the farms that are far from the Nile are irrigated from several scattered pumping wells in Wadi Qena, El-Matully and Quieh. Pesticides and fertilizers are heavily used in Egypt in general. As a result, the farming area around the Nile has contributed in releasing various amounts of the persistent organic pollutants and metal ions into the main water supply (Nile River).[27]

3.1.3.1.3 Industrial activities

Various industrial activities in the study area are in operation and more prospective activities are planned. These activities represent a potential source of groundwater contamination. The sugarcane factories are distributed along the Nile between the Qena and Qift cities. The Aluminium company of Egypt is located in the Qena governorate. The cement factories are located in the Nile valley zone, while the phosphate deposits are exported through El-Qusir, El-Hamrawien and Safaga ports. The heavily use of Qena-Safaga, Qift-Qusir and Qusir-Safaga roads contributes to the emission contaminants (air pollution with fine particles). Moreover, the dust particles are emitted from El-Hamrawien port during phosphate exporting.

3.1.3.2 Geogenic (natural)

3.1.3.2.1 Water-rock interaction

The groundwater quality in the Golden Triangle is impacted by water-rock interaction processes, meaning that mineral/rock composition plays a significant role in the occurrence of heavy metals in groundwater. The dissolution of sulfate mineral and the weathering of carbonate and silicate phases were the main water-rock interaction process.[11] The groundwater chemistry reflects the water source, chemical characteristics, the aquifer lithology, pressure, temperature, and the extent of chemical reactions during weathering processes.[28] The release and solubility of the metal ions is significantly controlled by the pH of water.[29]

3.1.3.2.2 Sea water intrusion

The groundwater of the coastal zone is influenced by the seawater intrusion as a result of the over-exploitation and the sea level change (climate change). However, this processes are mostly impacts the unconfined coastal aquifers.[30] The mixing of seawater with the coastal aquifers can increase the mobility of some heavy metals.[31, 32]

3.2 Materials and Methods

3.2.1 Groundwater sampling

A total of 23 samples were collected, during field expedition, from the representative groundwater wells tapping the fractured basement aquifers, the Nubian aquifer, and the shallow alluvial aquifers, Figure (3-7). The groundwater samples were collected after 10 minutes of pumping out. The pH, temperature, electrical conductivity, and TDS were determined in situ using a portable multimeter (430 pH/ Cond. Meter, JENWAY), which was calibrated prior to use. Collected samples were filtered using 0.45 um filter and injected into polyethylene bottles (100 mL). Each bottle was rinsed with groundwater sample before being fully filled. All samples (for elemental analysis) were acidified by nitric acid (conc. 67%), sealed, and labelled systematically. Additionally, the groundwater samples were collected in 500 mL bottles without any kind of treatment. All bottles were kept in an ice box filled with ice bags during the continued field work, and then were preserved in a refrigerator before being sent to the UK for further analysis. For each sample, the depth of water was determined using Solnist level measurement device (Model 101 Water Level Meter). The coordinates and elevation of each point were recorded using a handheld Global Positioning System device (Garmin GPS 72H).



Figure 3-7: Groundwater sampling and recording. Water samples were filtered and injected into polyethylene bottles and labelled. (Refer to Appendix A for samples code).

3.2.2 Heavy metals determination

Multi-element analysis was undertaken using the Inductively coupled plasma mass spectrometry (ICP-MS), Thermo-Fisher iCAP-Q. All the groundwater samples were acidified with concentrated HNO_3 (69%) before being measured. A dilution step was not applied prior to the analysis as the concentration of ions was in the range of the calibration curve. The liquid blanks were measured before and after analysis.

3.2.3 Heavy metal pollution index (HPI)

The HPI reflects the suitability of water and its quality for drinking purposes regarding the metal ions. The HPI is calculated by equation (3-1).[33, 34]

$$HPI = \frac{\sum_{i=1}^{n} W_i\, Q_i}{\sum_{i=1}^{n} W_i} \qquad (3-1)$$

Where W_i is the weight unit of *i*th parameter and n is the number of estimated metals. Qi is the individual quality and sub-index of *i*th and is calculated by equation (3-2).

$$Q_i = \sum_{i=1}^{n} \frac{\{M_i(-)I_i\}t}{(S_i - I_i)}\, x100 \qquad (3-2)$$

Where M_i is the monitored value of metal ions of *i*th parameter, S_i is the standard value of *i*th parameter, I_i is the ideal value of *i*th parameter. According to the HPI, the critical contamination index value for drinking water is 100.



Figure 3-8: Photographs showing various types of wells in the study area. A&B) underground pond, C) drilled well in the coastal zone, D) spring water between coastal and crystalline rocks zones, E) drilled well in the Nile valley, F) Hand dug well in the crystalline rock zone. (Refer to Appendix A for groundwater wells location).

3.3Results and discussion

3.3.1 Heavy metals specification

There is no published work related to heavy metals concentration and distribution in the study area. However, the measured heavy metals concentration were compared with the permissible limits proposed by the WHO and/or US EPA, and the Chinese's Ministry of Health.

3.3.1.1 Nickel (Ni)

The maximum concentration of nickel in drinking water is 0.02 mg/L(WHO).[35] Usually, Ni occurs in mafic silicates and sulphide-bearing minerals.[36] Several minerals, such as millerite NiS, pentlandite $(Ni, Fe)_9S_8$, nickeline (NiAs) and garnierite $(Ni, Mg)_3Si_2O_5(OH)_4$, contain Ni in their structure.[37-40] The Ni concentration in the study area varies between 0.25 and 171.2 ug/L (mean 8.84 ug/L). Generally, Ni concentration of the three zones is low compared to the guideline values (20 ug/L, WHO).[35] However, a high concentration in the costal aquifer (HW) was remarkable and above the guideline values. The increase in the Ni concentration is mostly

attributed to the dissolution of phosphate rock and piles, which has a high Ni concentration.[41] The Ni concentration in the crystalline rock zone ranges between 0.59 to 6.4 ug/L (mean 1.62 ug/L) with a relatively high concentration at El -Fawakhir area (FKH). The appearance of Ni in the Nile valley zone is only restricted to the wells that are located in the cultivated land (NQ3, NQ4, NQ5 and NQ6), assuming the role of fertilizers in releasing the Ni into the groundwater. The Ni concentration in the Nile valley zone range between 0.25–4.88 ug/L (mean 4.78 ug/L).

3.3.1.2 Cobalt (Co)

Co is combined with other metals forming skutterudite (CoAs3), sulfidic cobaltite (CoAsS), cattierite (CoS_2), glaucodot [(Fe, Co)AsS], and safflorite ($CoAs_2$) minerals.[42-45] Moreover, the sedimentary, and igneous rocks have Co in the structure of Fe and Mg-rich minerals, partially substituting Fe.[17] The Co concentration varies from one zone to another, reflecting the contribution of geology and anthropogenic activities. Generally, the Co values in the study area were in the range of 0.007-5.02 ug/L (mean 0.52 ug/L). The Co values in the crystalline rock zone in the range of 0.01-5.02 ug/L (mean 1.12 ug/L). Two samples located in the crystalline rock zone, BH and FKH, exceeded the WHO standards (1-2 ug/L).[35] The Co concentration in the Nile valley zone was between 0.007 and 0.87 ug/L (mean 0.29 ug/L). The higher concentration was found in the NQ3, NQ4, NQ5, and NQ6, which are located in the cultivated land. The Co concentration in the coastal zone is much lower compared to that in crystalline and Nile valley zones, where the Co values ranged between 0.01 and 0.27 ug/L (mean 0.09 ug/L).

3.3.1.3 Manganese (Mn)

Mn is contained in the Mn-bearing minerals disseminated in the composition of igneous, metamorphic, and sedimentary rocks. Mn occurs in several minerals such as pyrolusite (MnO_2), rhodochrosite ($MnCO_3$), and manganite [MnO (OH)].[46-48] The Mn concentration in the study area ranged between 1.39 and 1227 ug/L (165.3 ug/L) which is above the permissible limit (300 ug/L, WHO).[35] The highest values, in the crystalline rock zone, ranged between 2.16 and 1227 ug/L (mean 203.9 ug/L). The Mn values in the coastal zone were between 1.39 and 688 ug/L (mean 181.6 ug/L), where the highest values appeared in the QH1 and NK1 samples. The distribution of Mn in the Nile valley varies from one well to another ranging between 23.8 and 245.4 ug/L (mean 120 ug/L), where the highest values appeared in cultivated land. It is worth nothing that the mobility of Mn is controlled by the water flow conditions, mineral and rock geochemistry, and the redox conditions.[49]

3.3.1.4 Cadmium (Cd)

Cd occurs naturally as a greenockite mineral (CdS), associated with sulphide ores, and in the skarn deposits.[50, 51] Moreover, the Cd appears in the greenockite, alteration product, as a result of Cd-rich sphalerite decomposition.[51] The redox potential and pH of solution are the main two factors controlling the Cd mobility.[52] Generally, the Cd concentration is low in the study area except for a few locations in the coastal zone. The Cd values ranged from 0.012 to 11.3 ug/L (mean 0.54 ug/L), with the maximum values recorded in the HW sample which is above the permissible level (3 ug/L, WHO).[35] The Cd values in the coastal zone were in the range of 0.02 -11.3 ug/L (mean 2 ug/L). These values became much lower in the crystalline rock and the Nile valley zones, where the Cd concentration ranged between 0.01-0.08 (mean 0.04 ug/L), and 0.012–0.03 ug/L (0.019 ug/L), respectively.

3.3.1.5 Arsenic (As)

As occurs naturally as traces in the composition of some minerals such as sulphides, arsenopyrite (FeAsS), tennantite ($Cu_{12}As_4S_{13}$) and nickeline (NiAs), and serpentinite minerals such as antigorite.[53, 54] Generally, Arsenic concentration in the groundwater is lower than the permissible values. An increase in the As values, however, was remarkable and above the permissible limits in the crystalline rock zone at the FKH well (10 ug/L, WHO).[35] The As values ranged between 0.04 and 55.6 ug/L (mean 3.8 ug/L). The concentration of As in the crystalline rock zone was in the range of 0.46-55.6 ug/L (mean 8.6 ug/L), while in the coastal zone the As values were between 0.24 and 5.7 ug/L (mean 1.3 ug/L). The As concentration in the Nile valley zone varies from one location to another in a range between 0.04 and 5.3 ug/L (mean 1.36 ug/L) and appeared in the cultivated land.

3.3.1.6 Copper (Cu)

Cu occurs naturally in sulphide, such as chalcocite (Cu_2S), cuprite (Cu_2O), chalcopyrite ($CuFeS_2$), and carbonate minerals, such as azurite [$Cu_3(CO_3)_2(OH)_2$], and malachite [$Cu_2(CO_3)(OH)_2$].[55, 56] The Cu concentration in the study area showed a significant variation in the three zones. The Cu concentration ranged from 1.2 to 18.6 ug/L (mean 6.3 ug/L) which is lower than the WHO standards (2000 ug/L).[35] The crystalline rock zone has the highest values compared to the Nile valley and coastal zones, where its values ranged from 3.8 to 18.6 ug/L (mean 9.2 ug/L). The Cu concentration in the Nile valley zone was in the range of 1.2-14 ug/L (mean 4.7 ug/L), where the maximum value recorded in NQ3 well. The Cu values in the coastal zone

were in the range of 1.7-8.8 ug/L (mean 4.7 ug/L), where the maximum value appeared in the HW well.

3.3.1.7 Zinc (Zn)

Zn occurs naturally in several minerals such as sphalerite (ZnS), wurtzite [(Zn, Fe)S], and smithsonite ($ZnCO_3$), in addition to its presence as traces in biotite-bearing granites.[57-59] The Zn values in the study area are below the standard values (3000 ug/L, WHO), where their concentrations ranged between 4.3 and 1170 ug/L (mean 68.3 ug/L).[35] In the coastal zone, the Zn values were in the range of 7.3-1170 ug/L (mean 213 ug/L), with the maximum value observed in HW. The Zn concertation in the Nile valley was between 4.3 and 37.1 ug/L (mean 15.6 ug/L). In the crystalline rock zone Zn concentrations varied between 10.2 and 26.4 ug/L (mean 18.7 ug/L).

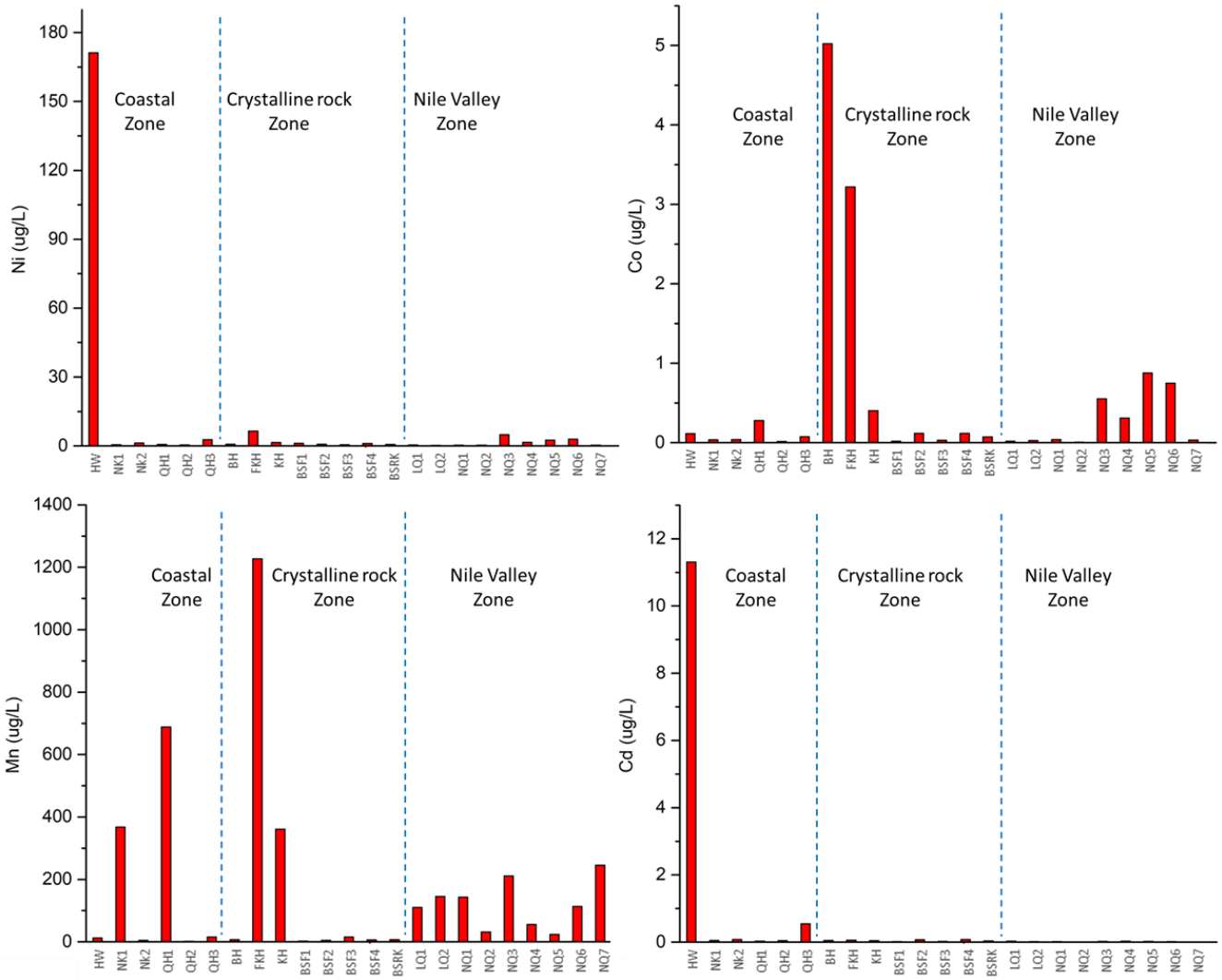


Figure 3-9: Ni, Co, Mn, and Cd concentration in the three zones. Refer to Appendix A-1 and A-2 for samples location and their elemental composition.

3.3.1.8 Lead (Pb)

Pb occurs naturally in the sulphide and carbonate minerals such as anglesite ($PbSO_4$), galena (PbS), and cerussite ($PbCO_3$), which are considered the potential sources of Pb in groundwater.[17] The Pb concentrations in the study area showed a wide variation in the three zones. Generally, the Pb values were below the permissible limits (10 ug/L, WHO) ranging between 0.02 and 0.45 ug/L (mean 0.16 ug/L).[35] The values of Pb in the crystalline rock zone and coastal zone are greater than those in the Nile valley where the concentrations ranged from 0.07 to 0.45 ug/L (mean 0.2 ug/L), and from 0.02 to 0.23 ug/L (mean 0.09 ug/L), respectively. In the coastal zone, the Pb values were between 0.04 and 0.3 ug/L (mean 0.2 ug/L).

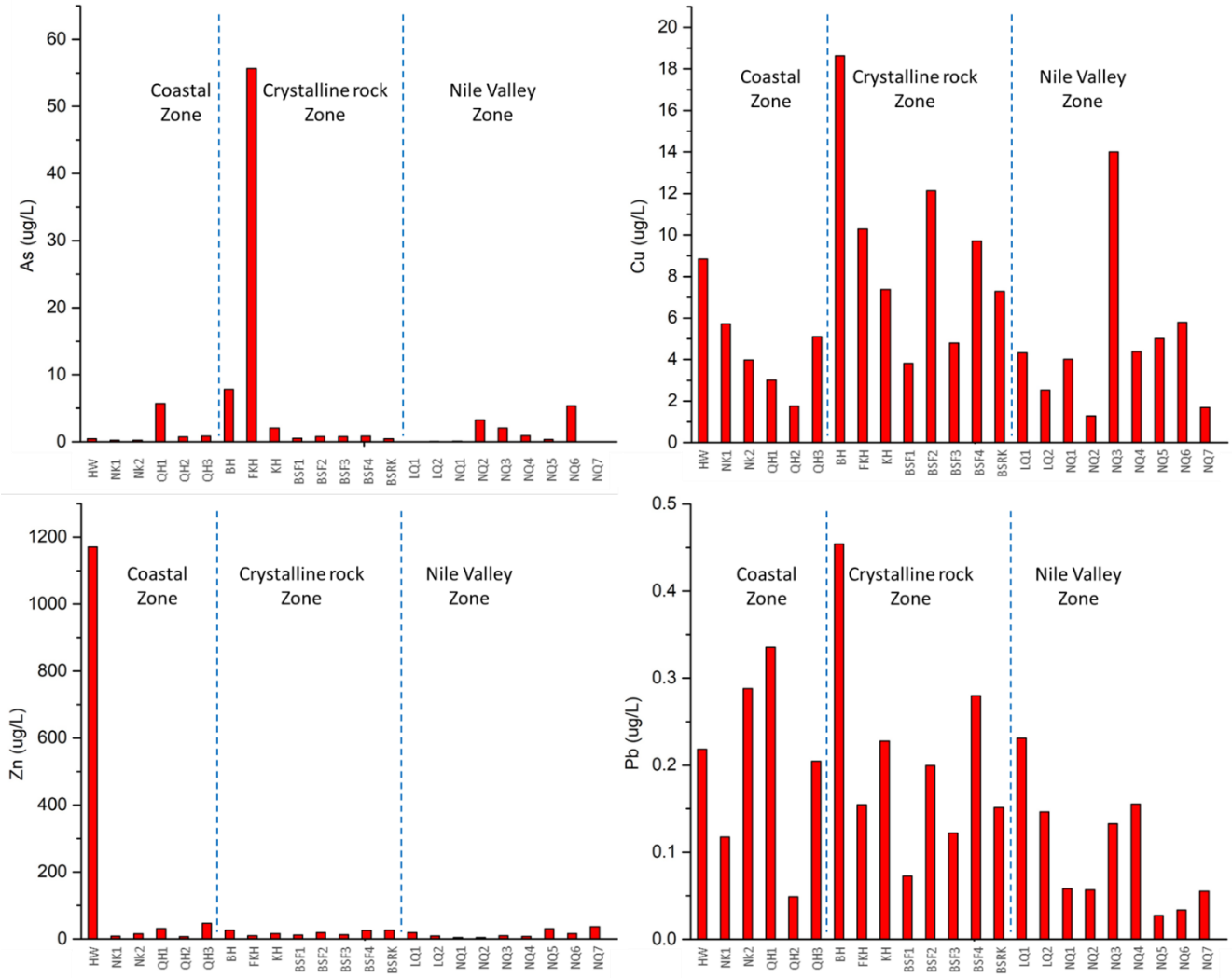


Figure 3-10: As, Cu, Zn, and Pb concentration in the three zones. Refer to Appendix A-1 and A-2 for samples location and their elemental composition.

3.3.1.9 Iron (Fe)

Fe occurs naturally in some minerals such as magnetite (Fe_3O_4), hematite (Fe_2O_3), siderite ($FeCO_3$), limonite ($FeO.nH_2O$), pyrite (FeS_2), in addition to its presence as a structural iron substituting the other elements in the octahedral sites of silicate and aluminosilicate minerals. The Fe values in the study area were between 2.3 and 374 ug/L (mean 57.3 ug/L), where the highest values were located in the Nile valley. The Fe concentration in the Nile Valley were between 2.3 and 374 ug/L (mean 85 ug/L), and in the coastal zone these values were between 4.9 and 84 ug/L (mean36.6), where these values were between 8 and 156 ug/L (mean 41.6 ug/L) in the crystalline rocks zone. The permissible limit of Fe in drinking water is 400 ug/L (WHO).[35]

3.3.1.10 Uranium (U)

U occurs in the structure of some minerals such as uranophane ($CaUO_2$), uraninite (UO_2), autunite [$Ca(UO_2)_2(PO_4)$].[60-62] In addition, U can be found in phosphate, granite, and sandstone rocks. The U values varied in the three zones where its concentration was between 0.02 and 30.8 ug/L (mean 3.3 ug/L). The values in the Nile valley ranged from 0.026 and 6.4 ug/L (mean 1.4 ug/L), while in the crystalline rocks zone the values were between 1.1 and 5.8 ug/L (mean 3.5 ug/L), and in the coastal zone were in the range of 0.08-30.8 ug/L (mean 6.1 ug/L). The U concentration is above the permissible limit stated by the WHO (15 ug/L) in the HW.[35]

3.3.1.11 Caesium (Cs)

Cs occurs naturally as pollucite [$(Cs, Na)_2Al_2Si_4O_{12}.2H_2O$], pezzottaite [$Cs(Be_2Li)Al_2Si_6O_{18}$], and avogadrite $(K,Cs)BF_4$ minerals, in addition to its presence in the beryl and pegmatite mineralization.[63-66] The Cs values in the study area were between 0.002 and 1.3 ug/L (mean 0.23 ug/L). In the Nile valley its values ranged from 0.006 to 1.3 ug/L (mean 0.28 ug/L), while the Cs concentration in the crystalline rocks zone were between 0.002 and 0.0.019 ug/L (mean 0.01 ug/L), and in the coastal zone were between 0.02 and 0.98 ug/L (mean 0.4 ug/L).

3.3.1.12 Vanadium (V)

V occurs in the structure of some minerals such as tourmaline, mica, magnetite, and ilmenite.[67-69] The V concentrations in the study area were between 0.05 and 23.6 ug/L (mean 7.3 ug/L). The V values in the crystalline rocks zone varied in the range of 3.3-22 ug/L (mean 12.6 ug/L), while these values in the Nile valley zone were between 0.05 and 23.6 ug/L (mean 4.9 ug/L), and they were in the range of 0.09-11.2 ug/L (3.6 ug/L) in the coastal zone. Generally, the V concentration is lower than the standard values stated by the WHO (100 ug/L).[35]

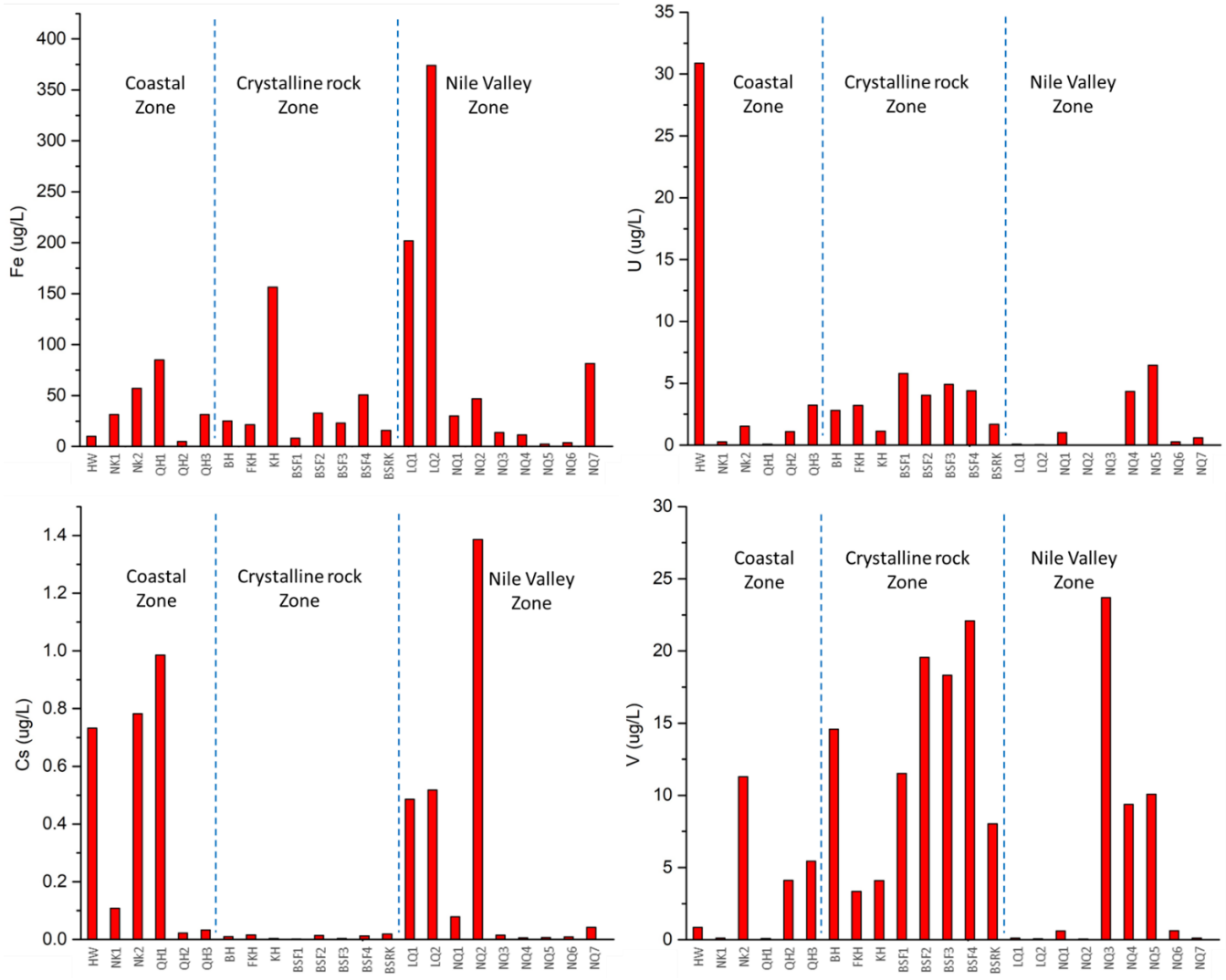


Figure 3-11: Fe, U, Cs, and V concentration in the three zones. Refer to Appendix A-1 and A-2 for samples location and their elemental composition.

3.3.1.13 Barium (Ba)

Ba occurs in nature in form of barite ($BaSO_4$) and witherite ($BaCO_3$) minerals.[70, 71] Moreover, Ba occurs in the structure of feldspar minerals.[57] The Ba values in the study area were in the range of 18-245 ug/L (mean 61.8 ug/L) which is lower than the permissible limit (500 ug/L, WHO).[35] The Ba values in the crystalline rocks zone were in the range of 33-124 ug/L (mean 55.3 ug/L), in the Nile valley zone Ba were between 18 and 204 ug/L (mean 67 ug/L) and were in the range of 18.9-245 ug/L (mean 61.4 ug/L) in the coastal zone.

3.3.1.14 Selenium (Se)

Se occurs in nature associated with the sulphide ores, and as a pure mineral such as selenate and selenide.[72, 73] Moreover, the Se occurs in a high concentration in the composition of

phosphate rock.[74] The selenium concentration in the study area varied in the three zones and were in the range of 0.01-39.3 ug/L (mean 7 ug/L). The Se values in the coastal zone were between 0.03 and 37.3 ug/L (mean 11.1 ug/L), in the crystalline rock zone in the range of 0.7-24 ug/L (mean 5.5 ug/L), while the values in the Nile valley zone were between 0.01 and 39.3 ug/L (mean 5.5 ug/L). Generally, the concentration of selenium in the study area is lower than 50 ug/L (MCLG and MCL).[75]

3.3.1.15 Chromium (Cr)

Cr occurs in the structure of rock-forming minerals, and as a chromite mineral ($FeCr_2O_4$), and is associated with ilmenite and magnetite.[57, 76] Generally, the Cr concentrations in the study area are lower than the permissible limits (50 ug/L, WHO).[35] The Cr values were between 0.03 and 17.8 ug/L (mean 2 ug/L). The values in the coastal zone were in the range of 0.14-3.2 ug/L (mean 1.46 ug/L) and were between 0.3 and 17.8 ug/L (mean 3.6 ug/L) in the crystalline rock zone. In the Nile valley zone Cr values were in the range of 0.03-6.3 ug/L (mean 1.09 ug/L).

3.3.1.16 Rubidium (Rb)

Rb occurs in nature in the structure of mica and feldspar minerals in addition to its presence in pegmatite, granite rocks, and clay minerals.[57, 77, 78] Generally, the Rb concentration in the study area is lower than the permissible level (100 ug/L, WHO).[35] The Rb values varied in the three zones and ranged between 0.26 and 53 ug/L (mean 8.8 ug/L). In the Nile valley Rb concentrations were in the range of 1.4-18.9 ug/L (mean 7.5 ug/L), and in the range of 2.5-53 ug/L (mean 20 ug/L) in the coastal zone. In the crystalline rock zone Rb values were between 0.26 and 5.9 ug/L (mean 1.7 ug/L).

3.3.1.17 Thallium (Tl)

The geochemistry of Tl is similar to Rb and occurs in the minerals of hydrothermal origin.[79] Tl is a highly toxic metal and occurs in seawater and marine sediments.[80, 81] Tl concentration in the study area is low, except for the coastal zone, ranging between 0.01 and 5.7 ug/L (mean 0.2 ug/L). In the Nile valley zone, the Tl concentrations were in the range of 0.001-0.008 ug/L (mean 0.003 ug/L), and in the range of 0.002-0.018 ug/L (mean 0.005 ug/L) in the crystalline rocks zone. The Tl values in the coastal zone were between 0.002 and 5.7 ug/L (mean 1 ug/L). The highest TI values were recorded in HW, which is above the US EPA limits (13 ug/L) and Chinese Ministry of Health (0.1 ug/L).[82, 83]

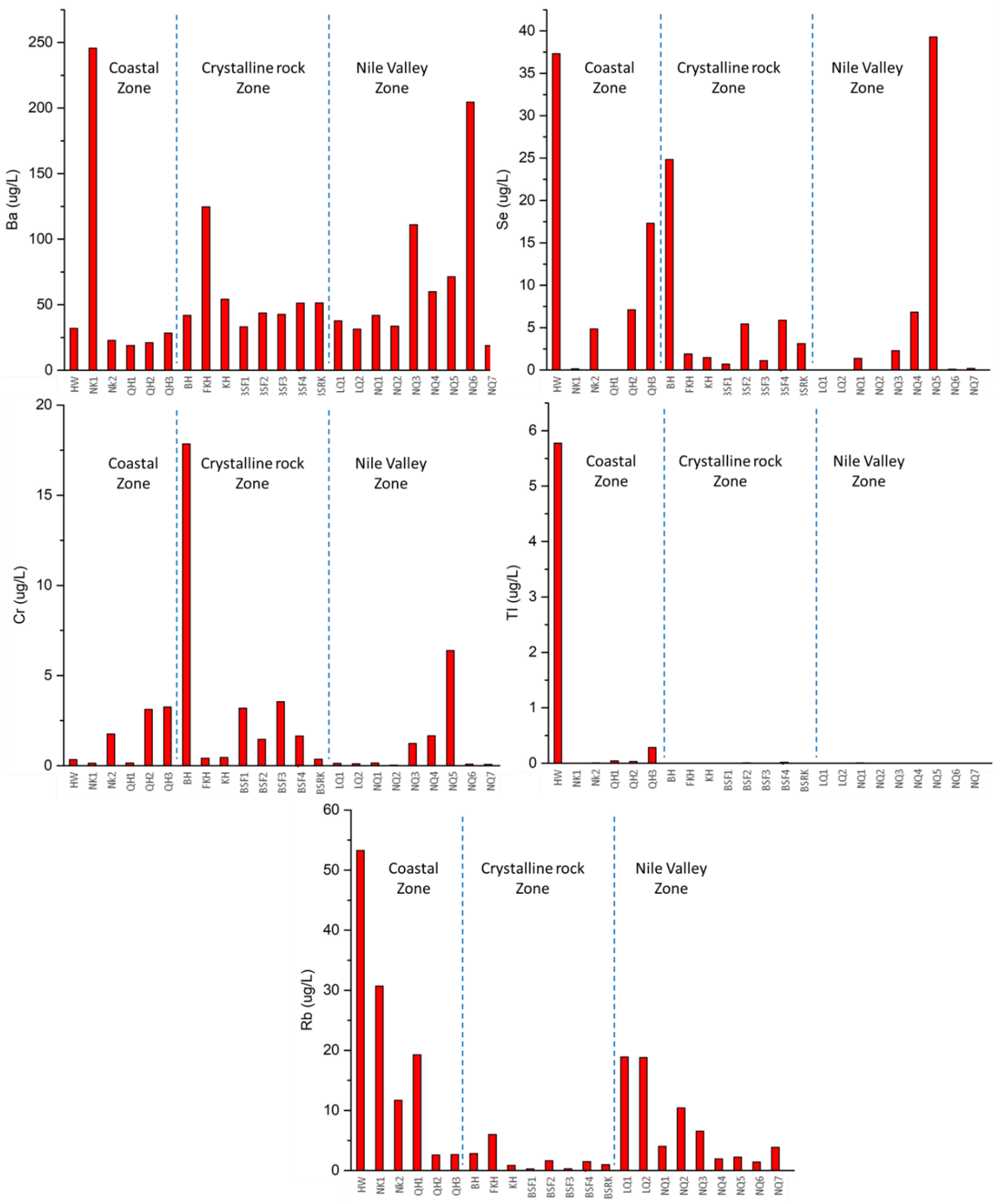


Figure 3-12: Ba, Se, Cr, Tl, and Rb concentration in the three zones. Refer to Appendix A-1 and A-2 for samples location and their elemental composition.

3.3.2 Heavy metals pollution in groundwater

3.3.2.1 Heavy metal pollution index (HPI)

The heavy metal pollution index is an effective approach to evaluate the groundwater contamination, where the composite impact of heavy metals on the overall water quality are represented.[84] The calculated HPI values for the three zones are depicted in Figure (3-13). The HPI values in the study area varies between the three zones. The HPI in the coastal zone is above the critical pollution index (HPI=100), reflecting the presence of more contaminants in the groundwater and hence its unsuitability for drinking purposes. In the crystalline rock zone, the HPI is about 50, which is categorized as a highly polluted water, while in the Nile valley zone the HPI is categorized as a moderate polluted water.

The HPI was calculated as well for the individual groundwater samples, and the results are depicted in Figure (3-13). The groundwater wells in the coastal zones were in the order of, in terms of the HPI, HW>QH3>QH1>NK2>QH2>NK1. Accordingly, the HW is not suitable for drinking and would have serious effects on the human health. In the crystalline rock zone, the groundwater quality was in the order of BH>FKH>BSF4>BSF2>BSF3>KH>BSF1>BSRK. The groundwater wells FKH and BH have a high concentration of heavy metals and the potential of causing a serious damage either to humans or livestock is certain. The HPI in the Nile valley was in the order of NQ3>NQ5>NQ6>NQ4>LQ1>NQ1>LQ2>NQ7>NQ2. The NQ3 and NQ5 showed the highest HPI values compared to other wells in the Nile Valley.

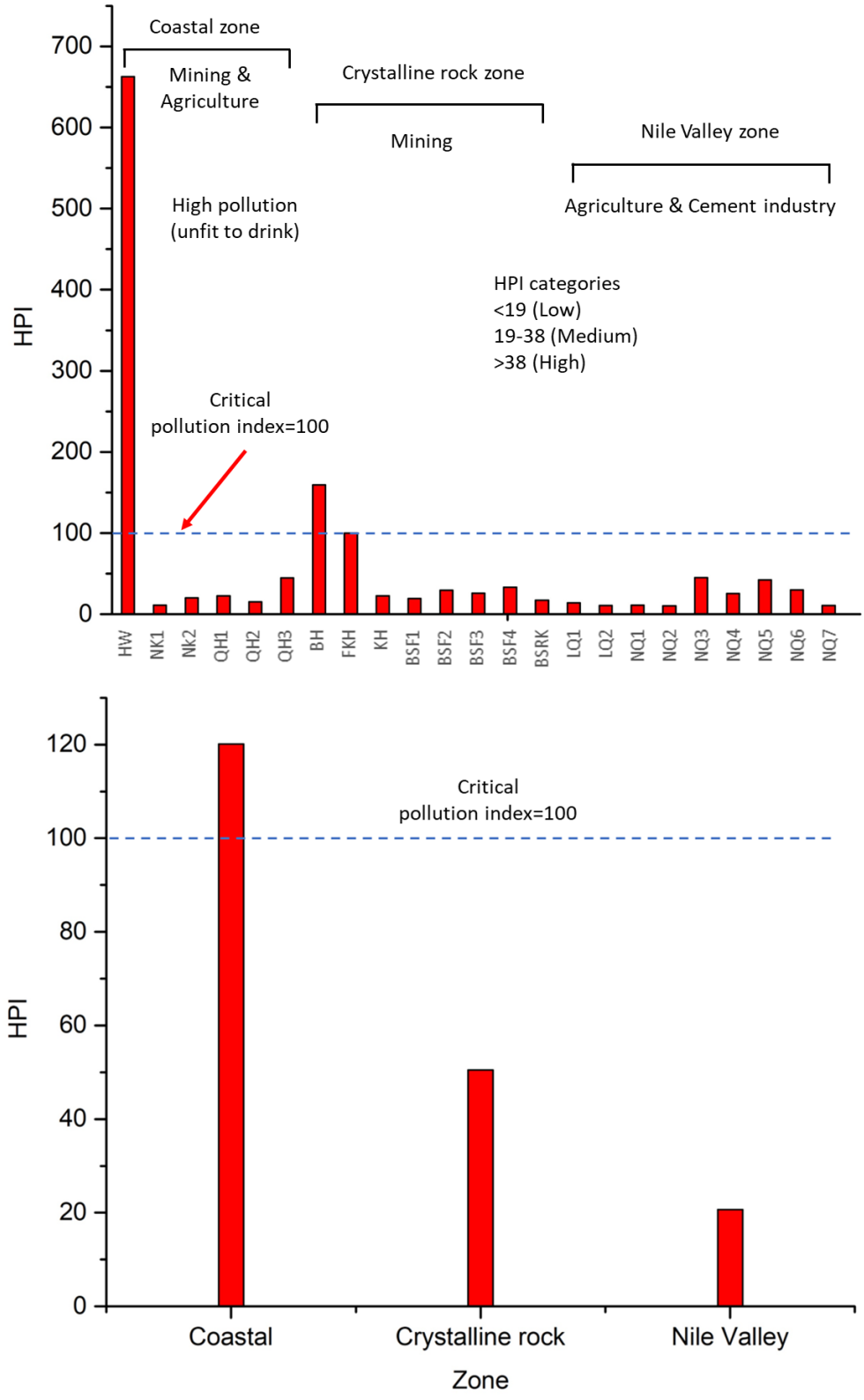


Figure 3-13: Heavy metals pollution index categories for groundwater samples in the three zones. Refer to Appendix A-3 for the HPI calculations.

Figure (3-14) shows the HPI values for each heavy metal in the study area. The HPI diagram shows that Co, Cd, Ni, As, Se, V, and Tl are higher than the HPI values of the co-existing metal ions. Therefore, the Co, Ni, Cd, and Mn ions will be considered in the water remediation experiments in the next chapters; the oxyanions such as, As, Se and V will not be included in the remediation study.

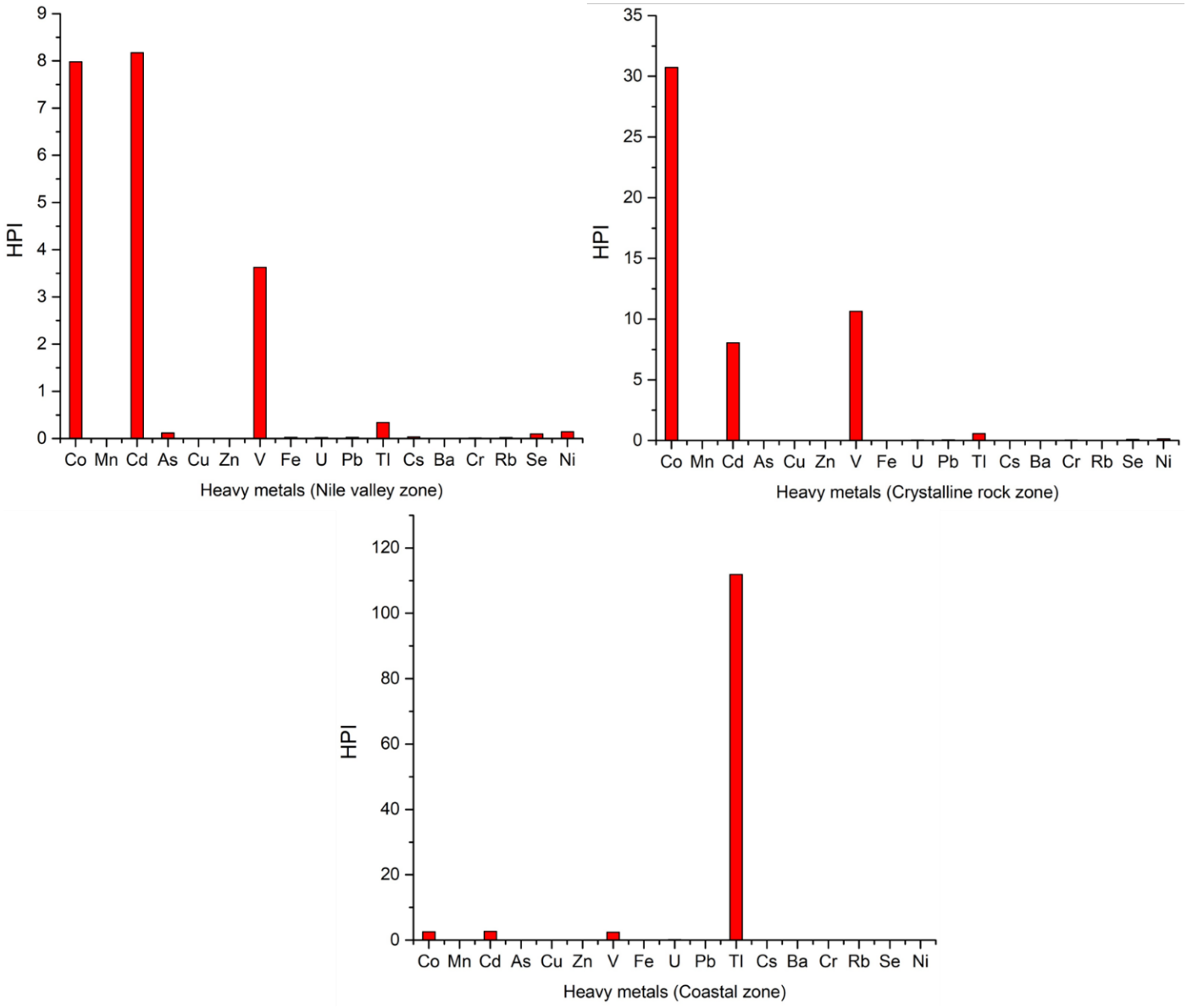


Figure 3-14: Heavy metals pollution index for each metal ion. The HPI values of heavy metals in the Nile Valley zone indicated that Co, Cd, V, TI, Se, and Ni are high. The HPI of heavy metals in the crystalline rock zone showed that Co, Cd, V and TI possess a serious impact, while the HPI in the coastal zone revealed that TI, Co, Cd, and V are the dangerous species. Refer to Appendix A-3 for the HPI calculations.

3.3.2.2 Potential causes of heavy metals contamination in groundwater

Based on the obtained results, the presence of metal ions in groundwater can be attributed to both the geogenic and anthropogenic activities. The spatial distribution maps of the measured metal ions are depicted in Figure (3-15&16).

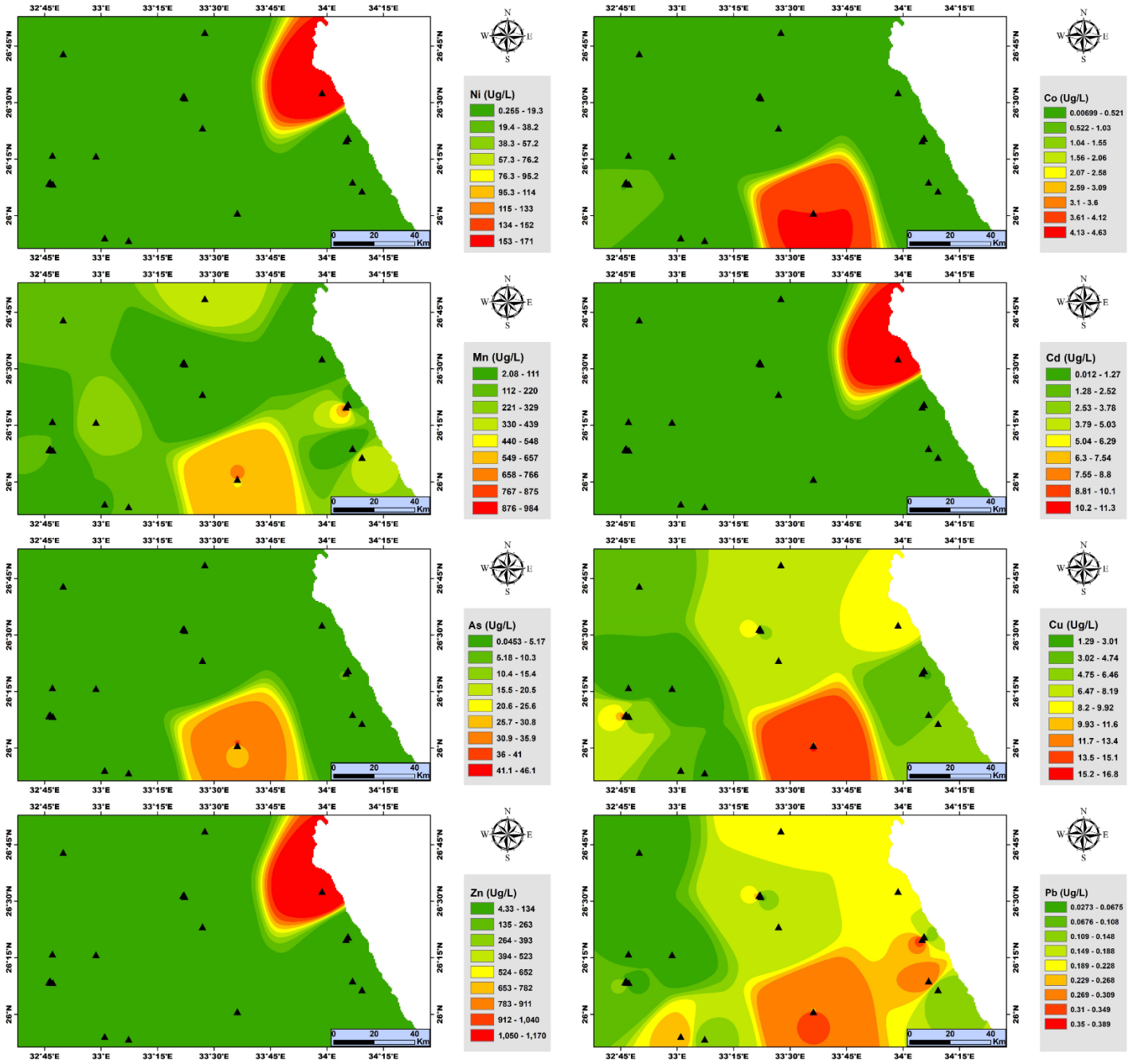


Figure 3-15: Aerial distribution maps of trace elements in the study area.

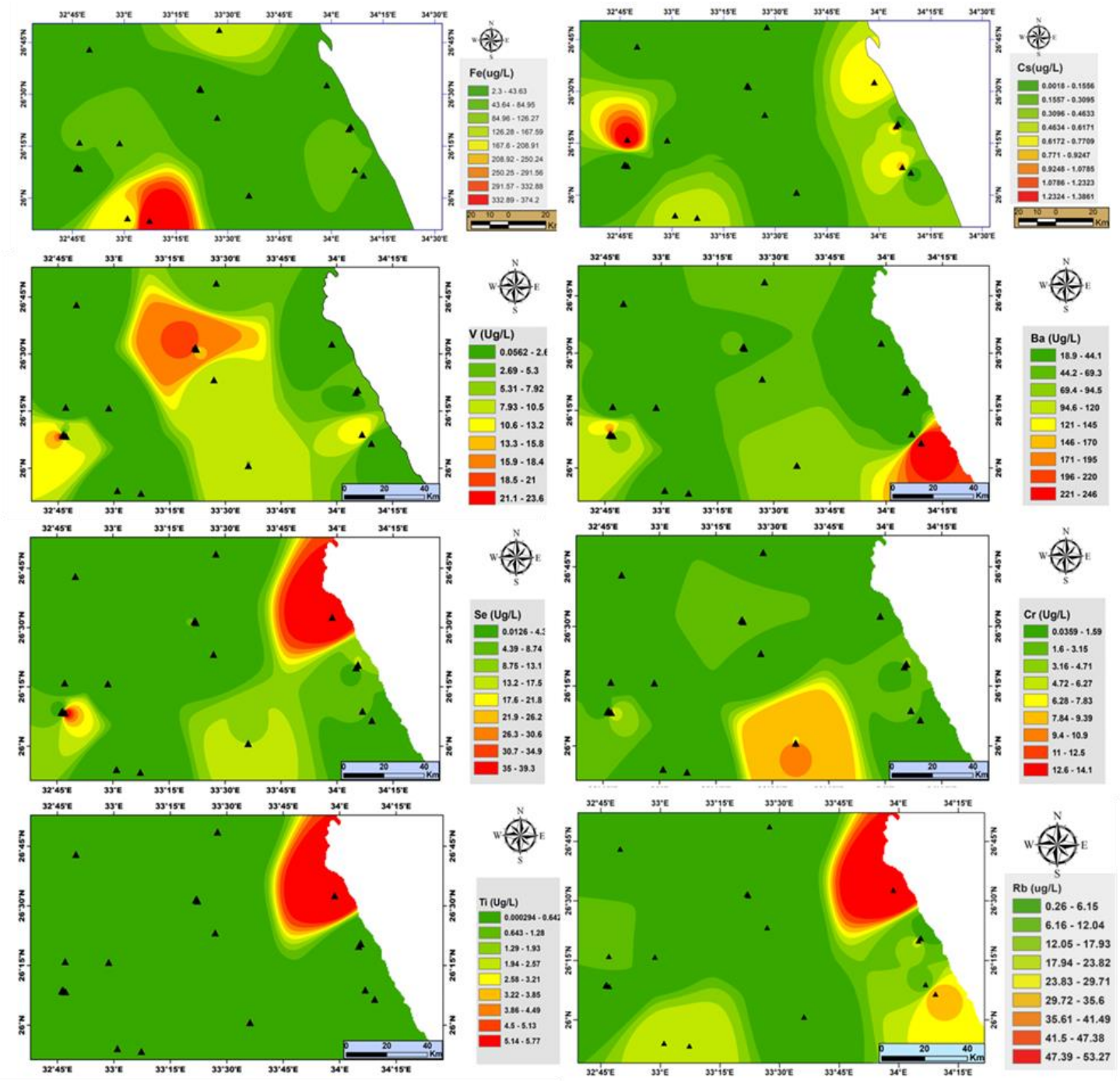


Figure 3-16: Aerial distribution maps of trace elements in the study area.

3.3.2.2.1 Groundwater pollution in coastal zone

Figure (3-17) shows the potential sources of heavy metals contamination. The appearance of a high concentration of heavy metals in the HW is mainly attributed to the water-rock interaction processes. This well is located in a phosphate-rich aquifer and is significantly impacted by the seawater intrusion, the occurrence of Ni, Co, Cu, Cd, U, Rb, Zn and Pb is very common in the Red Sea phosphate rock.[41]

Groundwater collected from the Nubian sandstone aquifer is characterized by the presence of various concentrations of Fe, Mn, As, Co, Cu, Pb, Rb and Zn. This aquifer is located at a depth of >300 m, suggesting that the occurrence of such metal ions is mainly related to the water-rock interaction processes. Moreover, the phosphate piles contributed to the release of metal ions into groundwater.[14]



Figure 3-17: Anthropogenic activities and potential sources of contamination, coastal zone.

3.3.2.2.2 Groundwater pollution in Nile valley

In the Nile valley zone, cultivated area (samples NQ3, NQ4, NQ5, and NQ6), the anthropogenic activities mainly controlled the distribution of metal ions in the groundwater aquifers. Groundwater in these locations occurs under unconfined conditions. As the water table in these aquifers is shallow, their susceptibility to contamination is very high.[13]

U, P, Tl, Ba, Cd, Cr, and Rb are below the permissible limits in the 4 wells. However, the concentration of these metal ions is expected to increase in the future due to the increased agricultural activities, sewage discharge and the lack of sanitation network infrastructure.[13] The concentration of Se and Cs is high in the NQ5 and NQ3, respectively. The As values are closer to the permissible limit in the NQ6 and showed a slight increase in the NQ3. The Co values in the NQ6 and NQ5 are very close to the lower permissible limit, while these values were medium in the NQ3 and NQ4 locations. This anomaly in the metal ion concentration may be attributed to the excessive use of pesticides and fertilizers, in addition to the subsurface infiltration of sewage water from El-Salhyia sewage plant. The superphosphate fertilizers are widely used in Egypt; superphosphate fertilizers have a high concentration of trace elements as impurities.[85] Moreover, the impact of fertilizers in increasing the metal ions concentration in groundwater was reported in the agricultural area around the Nile.[13]

The NQ1, NQ2, NQ7, LQ1, and LQ2 are collected from the Nubian sandstone aquifer. The Cs concentration is above the permissible limit in the NQ2, LQ1, and LQ2. The Mn and Fe concentrations are high in the NQ7, LQ1, and LQ2. The high concentration of Mn, Cs and Fe in groundwater is related to the aquifer lithotype, where various chemical processes take place, as this aquifer is deep and the possibility of anthropogenic contamination is hard to confirm.[86] Figure (3-18) depicts the effect of El-Salhyia sewage plant, pesticides use, and Fe impacts.

3.3.2.2.3 Groundwater pollution in crystalline rocks zone

In the crystalline rock zone, Co, As, V, Mn and Fe are very high and above the permissible limits, except for the Fe ions. An abnormal concentration of As (5 times higher than the standard values) was recorded in the FKH sample along with Co and Mn ions. El-Fawakhir area was subjected to extensive gold mining activities in the past and the possibility of anthropogenic contamination is almost certain.[87] However, the variation in the values of these metals in FKH and BH, which are located in the same area, suggests that the bed rock chemistry played a major role in increasing the levels of metal ions (Figure 3-19). The gold mineralization is associated with As-bearing minerals such as pyrite (FeS_2) and arsenopyrite (FeAsS).[3]

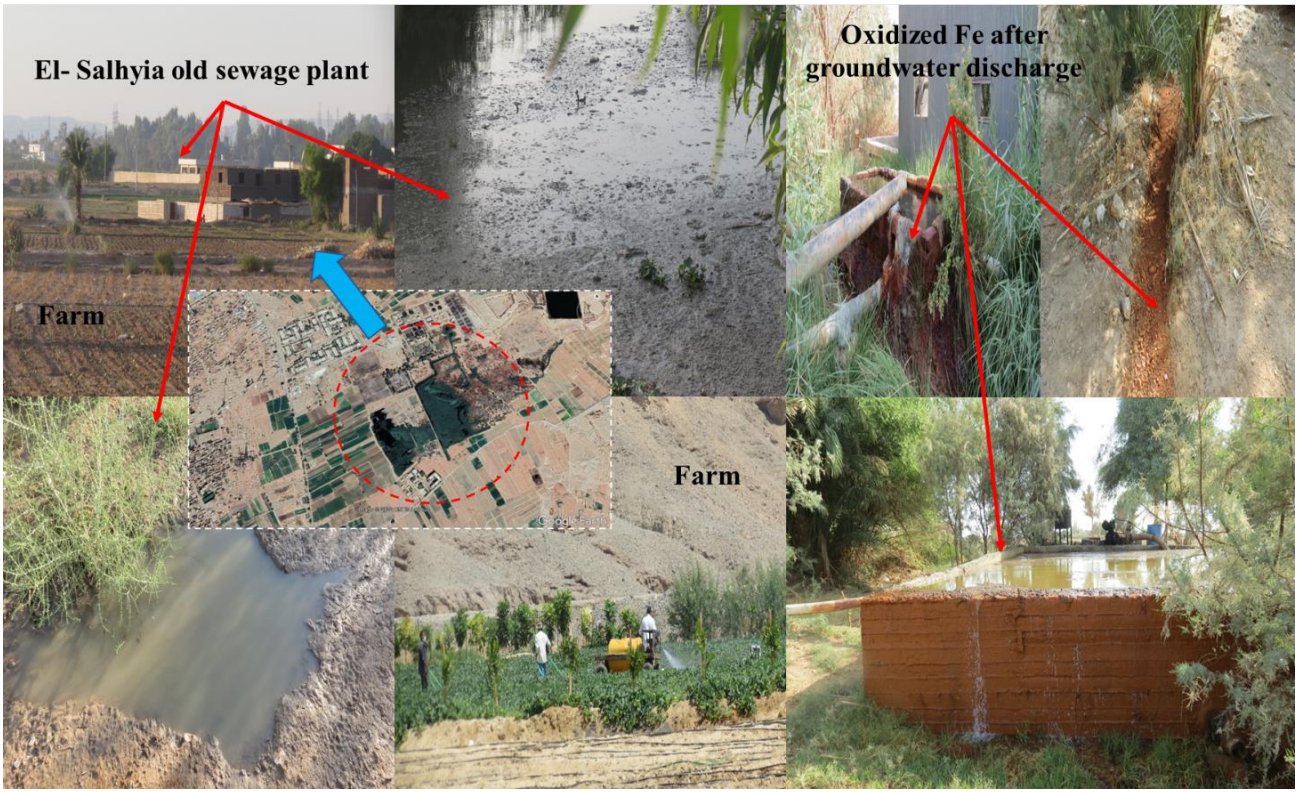


Figure 3-18: Sources of contamination in the Nile valley zone.

Serpentinite rocks, which contain the water body, include sulphide and iron oxides as minor constituents.[88] The high arsenic concentration in the FKH reflected the leaching of sulphide-bearing phases. Antigorite is one of the serpentinite minerals [$(Mg, Fe)_3Si_2O_5OH_4$] where the presence of As in its composition is common.[54] In addition, the high concentration of Mn and Fe in groundwater is probably inherited from the antigorite mineral dissolution. Moreover, the high salinity nature of the FKH has a contribution in facilating the As leaching as a result of the long period of interaction.[17]

Although the BH and FKH are located in the same area and the distance between them is about 75 m, their heavy metals concentration are varied, where the V, Cr, Co, Zn, Pb, Cu and Se concentrations are higher in the BH compared to FKH. However, the Ba, Mn, Ni and As are higher in the FKH compared to BH. This variation suggests that the release of metal ions is mostly related to the water-rock interactions, which is controlled by the geochemical characteristics of rocks; the BH is located in the fractured granite while the FKH is located in the serpentinite rock, Figure (3-19). Moreover, a contribution from the mining waste, which is located nearby the BH, is possible as a result of leaching and weathering processes; mining waste was a significant source in increasing the Se, Cu, Pb concentration in groundwater.[89]

A high concentration of Fe and Mn was observed in the KH. This well is located in Abo Kharif area, which was subjected to an extensive wolframite (tungsten) mining, in addition to the presence of wolframite [(Fe, Mn) WO_4] mineralization. Tungsten mineralization occurred in the quartz veins and disseminated in the alteration zones as well.[5] The presence of a high concentration of both Mn and Fe in the same well suggests that they are inherited from a wolframite-rich deposits or wastes through weathering and dissolution processes. Moreover, this well is located in the fractured granites at a shallow depth, therefore its susceptibility to contamination is very high. As indicated in Figure (3-20), this aquifer is recharged from the rainfall where the Abo Kharif is considered a catchment zone.

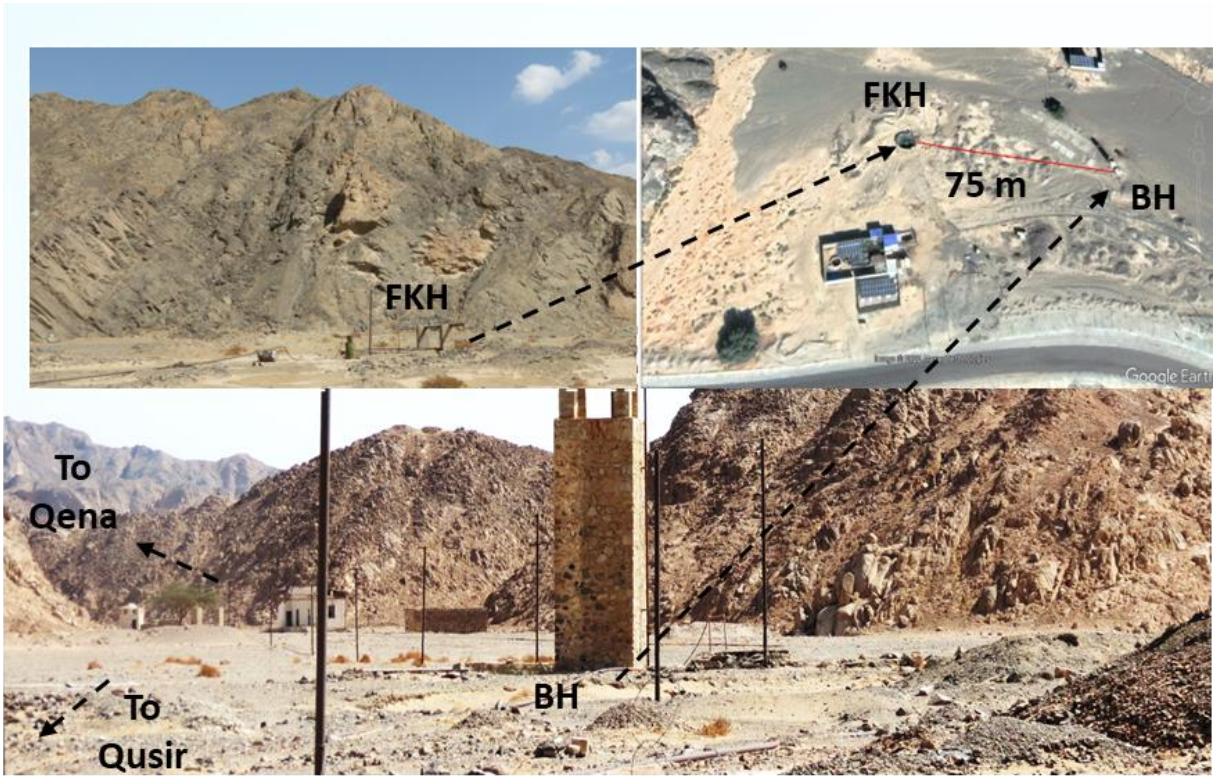


Figure 3-19: Location of the BH and FKH wells, El-Fawakhir mining area, crystalline rocks zone.

The BSF1, BSF2, BSF3, BSF4 and BSRK were collected from an area occupied by granitic rocks and are very close to the Qena-Safaga motorway. Vanadium was found in granitic rocks in the Eastern Desert of Egypt.[57, 90] The V concentrations in the groundwater are above the permissible limit. The ability of V in forming various molecular arrangements reflects its ability in participating in a wide range of chemical interactions, having a complex geochemistry. The increase in V values is due to the weathering and dissolution of rock-forming minerals, in addition to the chemical transformation (modification in the oxidation state) which plays a role in controlling the concentration of V in groundwater.[91]

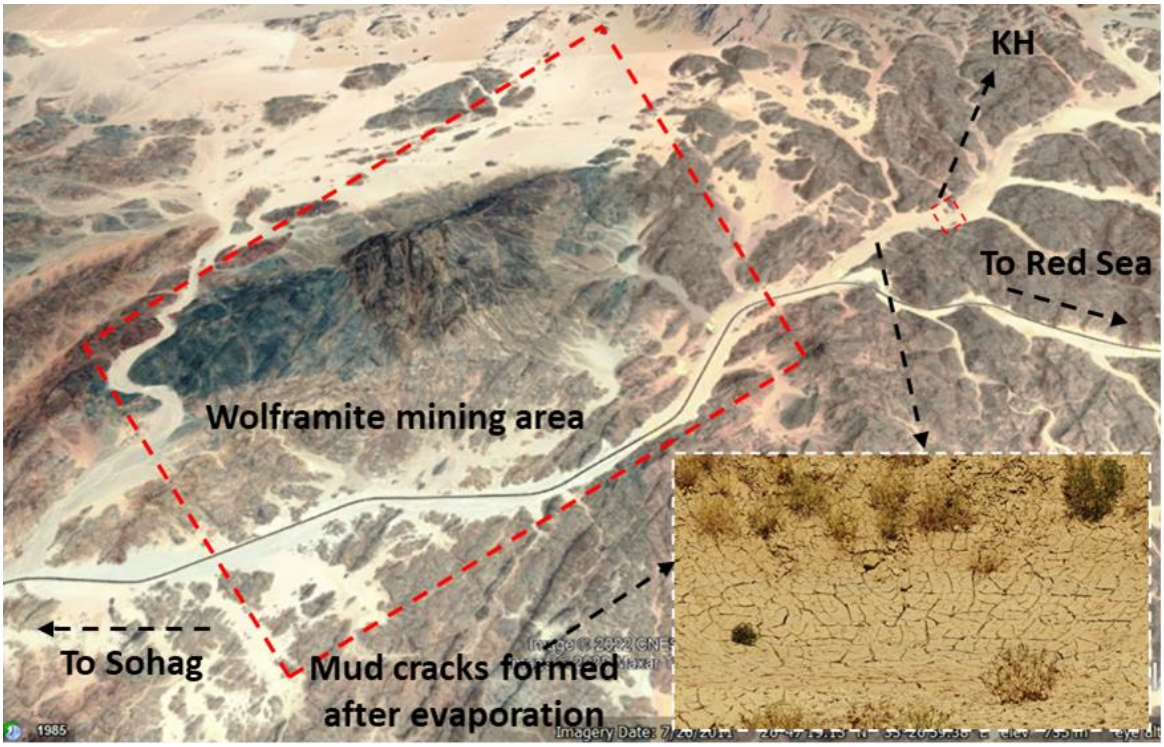


Figure 3-20: Abu-Kharif wolframite mining area, crystalline rocks zone.

Figure (3-21) shows the scatter diagrams of major cations. These diagrams can be used to reconstruct the sources of the dissolved major cations in groundwater as a result of a water-rock interaction process.[11] The interaction between rock/ mineral and water not only releases major ions but also can participate in the trace metals release.[92] The amount of released cations is dependent on the chemistry of the parent rock.[93]

Estimating the relationship between the total cations and (K^++Na^+) can be used to understand the silicate weathering. The largest number of groundwater samples of the three zones were plotted on or close to the (K^++Na^+) = 0.5 total cations. This behaviour indicated that the (K^++Na^+) contributed (moderately) to groundwater as a result of silicate weathering. Moreover, the values of K^++Na^+ versus total cations ratio was in the range of 0.39-0.80 (mean 0.5) in the coastal zone, 0.40-0.84 (mean 0.69) in crystalline rocks zone, and 0.42-0.93(mean 0.61) in Nile valley zone, confirming the role of silicate weathering.[11]

The Ca^{2+}+Mg^{2+} versus total cations plot indicated that most of the samples in the Nile valley fall on or close to the 0.5 line, while the samples of crystalline rocks and coastal zones fall between the 0.5 and 1 lines, indicating that the source of cations is not only from silicate weathering but also shows a contribution from the carbonate degradation.[11, 93] The values of Ca^{2+}+Mg^{2+} versus total cations were in the range of 0.1-0.60 (mean 0.49) in the coastal zone, in the range of 0.15-0.59 (mean 0.30) in the crystalline rocks zone, while these values were

between 0.06 and 0.57 (mean 0.38). However, an experimental investigation is still needed to confirm and understand the conditions that control the metal ions release and mobility.

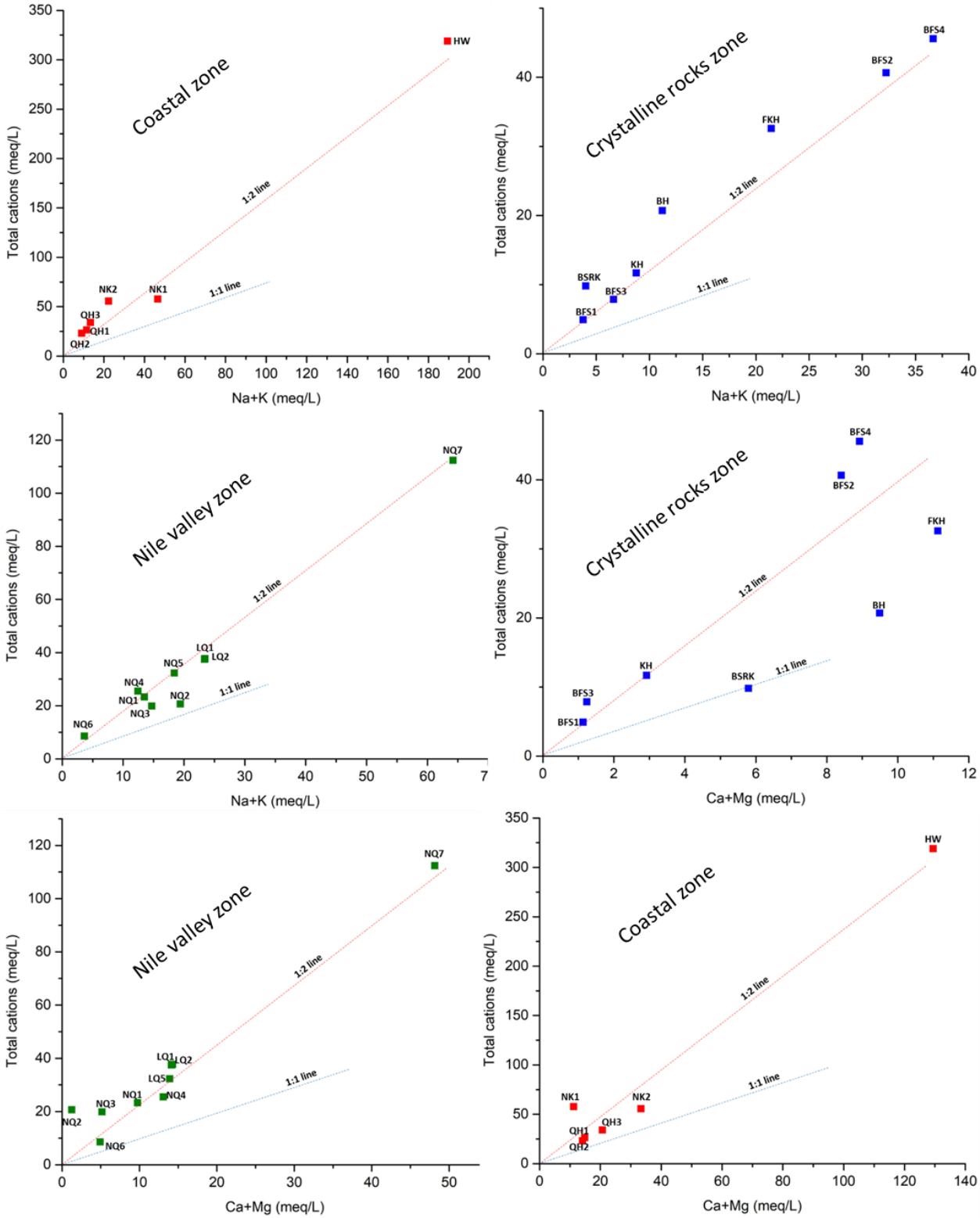


Figure 3-21: Scatter diagrams of K^{+}+Na^{+} vs total cations, and Ca^{2+}+Mg^{2+} for groundwater samples of the three zones. Refer to Appendix A-3 for used data.

Conclusion

Filed observations revealed that the study area is occupied by various lithologies, including igneous, metamorphic, and sedimentary rocks. The elemental analysis of groundwater samples indicated the presence of a high pollution related to specific heavy metals, such as As, Ni, Co, Mn, Cd, Se, and TI. The concentrations of such heavy metals is either above or approaching the standard limits proposed by the World Health Organization. The quality of water was determined using the heavy metals pollution index. Accordingly, the study area can be classified into moderately polluted (Nile Valley zone), highly polluted (crystalline rocks zone), and very high polluted (coastal zone).

The high values of As (55 ug/L) were recorded in the crystalline rock zone (FKH sample) in El-Fawakhir area which is known for its richness in the sulphide-bearing deposits such as gold. This area has been subjected to an extensive mining activity in the past which significantly contributed to the heavy metals release into groundwater. However, the contribution of the bed rock composition in releasing As is not well-understood and requires an extensive research.

The high concentration of Ni (171 ug/L), Cd (11.30 ug/L), Zn (1170 ug/L), TI (5.7 ug/L) and U (30 ug/L) are mainly distributed in the coastal zone (HW sample) which is not suitable for drinking or any other activities. Anomaly, in the concentration of Se and As was found in the BH and FKW which might be attributed to the difference in geology.

The presence of heavy metals in the groundwater can be attributed to both the geogenic and anthropogenic activities, where the mining activities and the use of fertilizers significantly contributed to such a contamination. Moreover, the natural geological processes such as water-rock interactions were the main drive of heavy metals release in the groundwater systems of both deep confined aquifers, in addition to, the fractured aquifers. The alkali scatter diagrams confirmed the contribution of silicate and carbonate dissolution in increasing the cations concentration, which consequently associated with the metal ions release. An experimental study for the water-rock interactions is still needed to reveal the conditions that controlled the metal ions release and mobility into groundwater.

3.5 References

1. *Golden Triangle, Growing Business Through Regulation*, N Gage Consulting, March 2016.
2. N. B. o. Egypt, *Economic Bulletin*, 2017, **76**, 5-73.
3. B. A. Zoheir, R. A. Creaser and B. Lehmann, *International Geology Review*, 2015, **57**, 1418-1432.
4. M. Abd El Monsef, M. Slobodník and I. A. Salem, *Arabian Journal of Geosciences*, 2020, **13**, 1034.
5. N. G. Abdel Wanees, M. M. El-Sayed, K. I. Khalil and H. A. Khamis, *Geological Magazine*, 2022, **159**, 441-467.
6. I. Gaafar, A. El-Shershaby, I. Zeidan and L. S. El-Ahll, *NRIAG Journal of Astronomy and Geophysics*, 2016, **5**, 160-172.
7. E. S. Schandl, M. P. Gorton and N. A. Sharara, *Journal of African Earth Sciences*, 2002, **34**, 259-273.
8. D. A. Ruban, E. S. Sallam, T. M. Khater and V. A. Ermolaev, *Geoheritage*, 2021, **13**, 54.
9. S. F. Elbeih, A. A. B. Belal and E.-S. A. Zaghloul, *The Egyptian Journal of Remote Sensing and Space Science*, 2011, **14**, 15-28.
10. R. Amer, R. Ripperdan, T. Wang and J. Encarnación, *Journal of African Earth Sciences*, 2012, **69**, 13-25.
11. R. G. M. Ibrahim, *Arabian Journal of Geosciences*, 2019, **12**, 1-16.
12. M. A. Awad, M. S. Hamza, S. M. Atwa and M. K. Sallouma, *Environmental Geochemistry and Health*, 1996, **18**, 47-54.
13. F. Abdalla and R. Khalil, *Journal of African Earth Sciences*, 2018, **141**, 164-178.
14. F. A. Abdalla and I. H. Khalifa, *Arabian Journal of Geosciences*, 2013, **6**, 1273-1282.
15. M. I. Sherif, M. Sultan and N. C. Sturchio, *Earth and Planetary Science Letters*, 2019, **510**, 37-44.

16. H. Ismaiel, Askalany, M. and Ali, A., *Journal of Geoscience and Environment Protection*, 2021, **9**, 46-60.

17. A. Embaby and M. Redwan, *Environmental Monitoring and Assessment*, 2019, **191**, 686.

18. G. M. Kamal El-Din, D. Abdelaty, K. Moubark and M. Abdelkareem, *Arabian Journal of Geosciences*, 2021, **14**, 839.

19. M. Sultan, N. C. Sturchio, H. Gheith, Y. A. Hady and M. El Anbeawy, *Groundwater*, 2000, **38**, 743-751.

20. M. Sultan, S. Metwally, A. Milewski, D. Becker, M. Ahmed, W. Sauck, F. Soliman, N. Sturchio, E. Yan, M. Rashed, A. Wagdy, R. Becker and B. Welton, *Journal of Hydrology*, 2011, **403**, 14-24.

21. M. Yousif and A. H. M. El-Aassar, *Bulletin of the National Research Centre*, 2018, **42**, 4.

22. A. A. Abdel Moneim, *Hydrogeology Journal*, 2005, **13**, 416-425.

23. M. Yousif and O. Sracek, *Arabian Journal of Geosciences*, 2016, **9**, 670.

24. M. A.-M. Mohamed, *Arabian Journal of Geosciences*, 2013, **6**, 775-782.

25. I. M. Shalaby, E. Stumpfl, H. M. Helmy, M. M. El Mahallawi and O. A. Kamel, *Mineralium Deposita*, 2004, **39**, 608-621.

26. M. W. Ali-Bik, S. M. Hassan and M. F. Sadek, *Geological Journal*, 2020, **55**, 5330-5354.

27. H. Dahshan, A. M. Megahed, A. M. Abd-Elall, M. A. Abd-El-Kader, E. Nabawy and M. H. Elbana, *J Environ Health Sci Eng*, 2016, **14**, 15.

28. K. Tanji and L. Valoppi, *Agriculture, Ecosystems & Environment*, 1989, **26**, 229-274.

29. A. Król, K. Mizerna and M. Bożym, *Journal of Hazardous Materials*, 2020, **384**, 121502.

30. T. E. Idowu and K. H. Lasisi, *Scientific African*, 2020, **8**, e00402.

31. G. Du Laing, R. De Vos, B. Vandecasteele, E. Lesage, F. M. G. Tack and M. G. Verloo, *Estuarine, Coastal and Shelf Science*, 2008, **77**, 589-602.

32. J. A. Acosta, B. Jansen, K. Kalbitz, A. Faz and S. Martínez-Martínez, *Chemosphere*, 2011, **85**, 1318-1324.

33. B. Prasad and J. Bose, *Environmental Geology*, 2001, **41**, 183-188.

34. S. V. Mohan, P. Nithila and S. J. Reddy, *Journal of Environmental Science and Health . Part A: Environmental Science and Engineering and Toxicology*, 1996, **31**, 283-289.

35. World Health Organization (WHO), Fourth edn., 2011.

36. R. A. M. Ali, I. K. Pitcairn, A. E. Maurice, M. K. Azer, B. R. Bakhit and M. G. Shahien, *Precambrian Research*, 2020, **337**, 105565.

37. Y. Choi, I. Lee and I. Moon, *Frontiers in Earth Science*, 2021, **9**.

38. Y. Han, Y. Liu and W. Li, *Frontiers in Earth Science*, 2020, **8**.

39. V. Kalugin, V. Gusev, N. Tolstykh, A. Lavrenchuk and E. Nigmatulina, *Journal*, 2021, **11**.

40. T. E. Gore, MSc Thesis Laurentian University, 2020.

41. F. Hellal, S. El-Sayed, R. Zewainy and A. Amer, *Bulletin of the National Research Centre*, 2019, **43**, 11.

42. L. Xi, J. Yang, C. Lu, Z. Mei, W. Zhang and L. Chen, *Chemistry of Materials*, 2010, **22**, 2384-2394.

43. Y. Li, N. Kitadai and R. Nakamura, *Journal*, 2018, **8**.

44. V. Y. Prokof'ev, L. D. Zorina, V. A. Kovalenker, N. N. Akinfiev, I. A. Baksheev, A. N. Krasnov, G. A. Yurgenson and N. V. Trubkin, *Geology of Ore Deposits*, 2007, **49**, 31-68.

45. J. A. Speer, J. R. Craig and R. J. Hill, *Rocks & Minerals*, 1978, **53**, 130-134.

46. S. K. Ghosh, *ACS Omega*, 2020, **5**, 25493-25504.

47. S. Namgung and G. Lee, *Environmental Science & Technology*, 2021, **55**, 14436-14444.

48. T. Miao, L. Deng, W. Yang, J. Ni, C. Zheng, J. Etheridge, S. Wang, H. Liu, H. Lin, Y. Yu, Q. Shi, P. Cai, Y. Zhu, T. Yang, X. Zhang, X. Gao, C. Xi, M. Tian, X. Wu, H.

Xiang, E. Dagotto, L. Yin and J. Shen, *Proceedings of the National Academy of Sciences*, 2020, **117**, 7090-7094.

49. F. Liao, G. Wang, Z. Shi, X. Huang, F. Xu, Q. Xu and L. Guo, *Exposure and Health*, 2018, **10**, 211-227.
50. J. Liu and S. Zhang, *Minerals*, 2017, **7**.
51. B. Mishra and P. Hazarika, *Ore Geology Reviews*, 2016, **72**, 1327-1334.
52. A. Kubier and T. Pichler, *Sci Total Environ*, 2019, **689**, 831-842.
53. C. Reimann and P. de Caritat, *Chemical Elements in the Environment: Factsheets for the Geochemist and Environmental Scientist*, Springer Berlin Heidelberg, 1998.
54. L. Niu, MSc, University of Ottawa, 2011.
55. N. Toro, C. Moraga, D. Torres, M. Saldaña, K. Pérez and E. Gálvez, *Journal*, 2021, **11**.
56. N. Frenzel, M. Mehne, S. Bette, S. Kureti and G. Frisch, *RSC Advances*, 2021, **11**, 3153-3161.
57. A. M. Asran, T. M. Amron and T. M. Hassan, *Arabian Journal of Geosciences*, 2021, **14**, 2856.
58. K. Yazawa, J. S. Mangum, P. Gorai, G. L. Brennecka and A. Zakutayev, *Journal of Materials Chemistry C*, 2022, **10**, 17557-17566.
59. A. Füger, M. Méheut, V. Mavromatis, A. Leis and M. Dietzel, *Chemical Geology*, 2018, **495**, 76-89.
60. M. Stark and M. Noller, *Physics and Chemistry of Minerals*, 2022, **50**, 2.
61. M. René, Z. Dolníček, J. Sejkora, P. Škácha and V. Šrein, *Journal*, 2019, **9**.
62. D. M. Wellman, K. M. Gunderson, J. P. Icenhower and S. W. Forrester, *Geochemistry, Geophysics, Geosystems*, 2007, **8**.
63. M. A. Mikhailov, I. V. Rozhdestvenskaya and I. I. Bannova, *Crystallography Reports*, 2012, **57**, 759-767.
64. R. C. Wang, H. Hu, A. C. Zhang, F. Fontan, P. de Parseval and S. Y. Jiang, *Contributions to Mineralogy and Petrology*, 2007, **153**, 355-367.

65. L. V. Shvanskaya, O. V. Yakubovich, A. V. Koshelev and A. N. Vasiliev, *Physics and Chemistry of Minerals*, 2018, **45**, 633-640.

66. E. Lambruschi, G. D. Gatta, I. Adamo, D. Bersani, E. Salvioli-Mariani and P. P. Lottici, *Journal of Raman Spectroscopy*, 2014, **45**, 993-999.

67. T. Grammatikopoulos, A. Mcken, C. Hamilton and O. Christiansen, *Cim Bulletin*, 2002, **95**, 87-95.

68. M. Jafarzadeh, K. Bónová, T. Mikuš, J. Bóna, M. Rezaei-Kahkhaei and A. Taheri, *Geological Journal*, 2021, **56**, 4645-4666.

69. C. H. Lee and H. K. Lee, *Journal of Asian Earth Sciences*, 2003, **21**, 343-351.

70. A. Baldasari and J. A. Speer, *American Mineralogist*, 1979, **64**, 742-747.

71. S. M. Bulatovic, in *Handbook of Flotation Reagents: Chemistry, Theory and Practice*, ed. S. M. Bulatovic, Elsevier, Amsterdam, 2015, DOI: https://doi.org/10.1016/B978-0-444-53083-7.00034-8, pp. 129-141.

72. J. Hatten Howard, *Geochimica et Cosmochimica Acta*, 1977, **41**, 1665-1678.

73. A. L. Ryser, D. G. Strawn, M. A. Marcus, J. L. Johnson-Maynard, M. E. Gunter and G. Möller, *Geochemical Transactions*, 2005, **6**, 1.

74. J. Bech, M. Suarez, F. Reverter, P. Tume, P. Sánchez, J. Bech and A. Lansac, *Journal of Geochemical Exploration*, 2010, **107**, 136-145.

75. *Basic Information about Selenium in Drinking Water* US EPA, 2015.

76. M. Pownceby and P. Bourne, *Mineralogical Magazine*, 2006, **70**, 51-64.

77. I. V. Pekov and N. N. Kononkova, *Geochemistry International*, 2010, **48**, 695-713.

78. E. C. Simmons, in *Geochemistry*, Springer Netherlands, Dordrecht, 1998, DOI: 10.1007/1-4020-4496-8_278, pp. 555-556.

79. M. Ikramuddin, Y. Asmeron, P. M. Nordstrom, K. P. Kinart, W. M. Martin, S. J. M. Digby, D. D. Elder, W. F. Nijak and A. A. Afemari, *Journal of Geochemical Exploration*, 1983, **19**, 465-490.

80. F. Zhao and S. Gu, *Minerals*, 2021, **11**.

81. A. D. Matthews and J. P. Riley, *Chemical Geology*, 1970, **6**, 149-152.

82. *US EPA. National recommended water quality criteria*, EPA–822-R-02–047. Office of Water, Office of Science and Technology, 2002b.

83. *Chinese Ministry of Health (CMH). Standards for Drinking water quality*, National Standard of the Peoples Republic of China, GB 5749 2006.

84. M. Ghaderpoori, B. Kamarehie, A. Jafari, A. Ghaderpoury and M. Karami, *Data Brief*, 2018, **16**, 685-692.

85. M. Molina, F. Aburto, R. Calderón, M. Cazanga and M. Escudey, *Soil and Sediment Contamination: An International Journal*, 2009, **18**, 497-511.

86. H. Khozyem, A. Hamdan, A. A. Tantawy, A. Emam and E. Elbadry, *Arabian Journal of Geosciences*, 2019, **12**, 523.

87. K. M. AbdelMaksoud, *International Journal of Earth Sciences*, 2020, **109**, 197-199.

88. A.-A. M. Abdel-Karim and S. A. El-Shafei, *Geological Journal*, 2018, **53**, 580-599.

89. L. A. Bullock, J. Parnell, M. Perez, J. Feldmann and J. G. Armstrong, *Minerals*, 2017, **7**.

90. B. Zoheir, R. Goldfarb, A. Holzheid, H. Helmy and A. El Sheikh, *Geoscience Frontiers*, 2020, **11**, 325-345.

91. M. T. Wright and K. Belitz, *Ground Water*, 2010, **48**, 515-525.

92. C. R. Bern, J. E. Birdwell and A. M. Jubb, *Environmental Science: Processes & Impacts*, 2021, **23**, 1198-1219.

93. B. K. Das and P. Kaur, *Environmental Geology*, 2001, **40**, 908-917.

CHAPTER 4: SYNTHESIS AND CHARACTERIZATION OF ROCK-BASED GEOPOLYMER: ALKALI ACTIVATION AFFINITY

Abstract

In this study, the geopolymerization of a heterogeneous geological precursor was investigated. The analyses confirmed the heterogeneity of the used precursor, where carbonaceous and aluminosilicate made up the main components of the CRM rock. A thermal activation step was crucial to attaining an acceptable level of reactivity. The experimental and analytical techniques confirmed an improved reactivity with increasing thermal activation up to 800 ºC. Moreover, feeding the geopolymer slurry with a more silicate was necessary during the geopolymerization process to reduce the effect of carbonation and to ensure a well-developed structure. The alkali activation of the calcined CRM resulted in the formation of various hydration products, including calcium aluminum silicate hydrate, sodium aluminum silicate hydrate, and sodium ferrosialate hydrate phases. Various ions, in addition to Na^+ from the alkali activator, which was inherited from the precursor, participated, to some extent, in balancing the negative charge in the geopolymer aluminosilicate framework. The findings of this research are fundamental for a further work on the geopolymerization of the ferro-aluminosilicate materials of a geological origin.

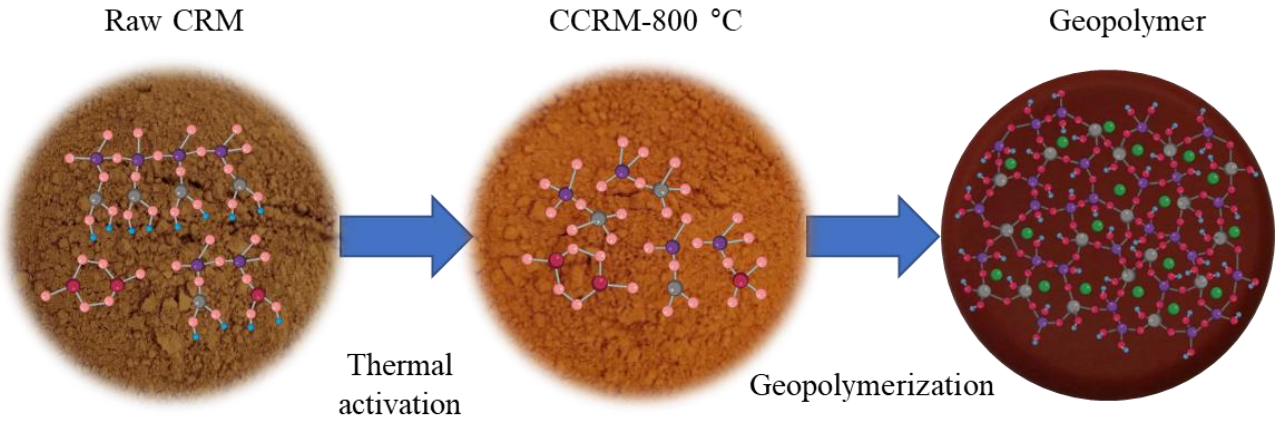


Figure 4-1: Geopolymerization of the CRM.

4.1Introduction

Geopolymerization of industrial wastes, such as the fly ash, blast furnace slag, and mining wastes is an effective approach to reducing their negative environmental impacts. The generated geopolymers may be applied in various applications such as the concrete production and improvement, water purification, thermal insulation, and the fire resistant materials.[1-6] The use of metakaolinite in the geopolymer synthesis has received a great deal of attention in various applications due to its high reactivity in the alkali activation.[7-9] However, the available industrial wastes will be limited in the future due to the new measures introduced to reduce the CO_2-emitting industrial activities. Therefore, the use of other available low-cost precursors with a suitable level of reactivity in the geopolymer production is necessary. Geological materials, such as rocks and minerals, are at the top of the alternatives that can be used to replace the current precursors to ensure a more sustainable future. However, due to the heterogeneity and high crystalline nature of rocks, their affinity in the alkali activation and their geopolymerization cannot be predicted. The main drawback in the geopolymerization of natural minerals is their crystal lattice which controls the release of Al.[10] The presence of soluble silicate is not effective alone to formulate a chemically consolidated material, therefore, Al is a necessary chemical trigger for the chemical hardening.[11] It has been concluded that a pre-treatment step is necessary to enhance the reactivity of such available and low-cost precursors.[12, 13] These pre-treatment steps include chemical, thermal and mechanochemical treatments.[14] Thermal activation is widely used to activate the crystalized hydrated and carbonate-bearing phases. As a result, a highly crystalized constituents are transformed into a glassier and highly reactive states. Thermal activation involves dehydroxylation and decarbonation processes depending on the composition and degree of crystallinity of the rock-forming minerals. The dehydroxylation of rock-forming minerals, such as hydrated minerals, results in the loss of the structural water from the octahedral sheets, forming a metastable phase.[15, 16] Most of the rock-forming minerals consist of an aluminosilicate compositions, and the released amorphous phases mainly contain Al-O and Si-O species which form the main backbone of the geopolymer skeleton. Decarbonation of the carbonate-bearing minerals resulted in the loss of the carbonate group, forming a highly reactive amorphous phases.[17, 18]

Calcareous red mudstone is a heterogeneous system of an aluminosilicate and carbonaceous minerals. The propensity of the raw material in the alkali activation is low due to the high crystallinity of its constituents. Thermal activation of the CRM can result in the release of a highly reactive Al, Si, Mg, Ca, and Fe phases. The presence of a such reactive phases indicates

the richness of the precursor in chemistry, which can lead to the formation of various hydration products upon the alkali activation. As a result, a new geopolymer with a distinguished chemical and physical properties is produced. However, understanding the chemical processes that control the geopolymerization is still unclear and is critical to their large-scale deployment. This study will serve as an initial approach to understanding the behavior of the sedimentary, igneous, and metamorphic rocks with respect to undergoing a geopolymerization reaction.

4.2Materials and methods

4.2.1 Raw material preparation

The CRM, 10 kilograms of different sizes, was crushed to <5mm in size using a Jaw Crusher machine, followed by a milling process for 5 minutes using a Tema mill machine. The produced powder was further manually ground to get a more finer grain size. In order to get a representative and a homogeneous sample, the ground CRM was split manually using the quadrant method[19], followed by sieving process to get a uniform grain size of 63 microns. The prepared powder was kept under vacuum and/or in an oven at 50 ºC until use.

4.2.2 Thermal activation

The raw CRM, 10 grams placed in a heat resistant porcelain crucible, was thermally activated at different temperatures (500, 600,700, 800, 900 ºC) with a heating rate of 5 ºC/min in a programmable Carbolite box furnace for 1 hour in static air. All samples were kept in air-free and tightly closed desiccators and/or containers until use.

4.2.3 Geopolymeric affinity

4.2.3.1 Solubility in alkaline medium (leaching test)

The reactivity of Al and Si in the calcined marlstone in an alkaline medium was evaluated by an alkaline leaching test. In brief, an amount of the calcined CRM was mixed with NaOH (6 M) and leached for 24 hours at room temperature with an occasional shaking (after 3 and 12 hours). After leaching, an amount from the leachate (1 mL) was separated from the residual solid particles and diluted with HNO_3 (2%) and kept in a fridge prior to the analysis. The Si and Al concentration was determined by using the inductively coupled plasma-optical emission spectrometer (ICP-OES), Perkin Elmer spectrometer Optima 2000 DV. Standard calibrations for the Al were prepared using a standard solution (100 mg/L multi-element solution, Fisher Chemicals), while the Si standard solutions were prepared using a standard Si solution (100

mg/L, Fisher Chemicals). The residual solids (1 gram) were oven dried at 100 ^{0}C for 24 hours and crushed into a fine powder then analyzed with the Panalytical Epsilon 3XL energy dispersive X-ray spectrometer to determine the change in composition. All the used glassware, containers and tools were rinsed using MilliQ water and HNO_3 (6%).

4.2.3.2 Reactivity in the early stages of reaction (FT-IR study)

An amount of the calcined CRM, 10 grams, was mixed with an alkaline activator at a solid-to-liquid ratio of 5:3.5. The slurry was mixed manually in a polypropylene beaker for 5 minutes and poured in a 35 mm square molds. Afterwards, the slurry was vibrated for 10 min using a vibrating table. The alkaline activator consisted of a mixture of Na_2SiO_3 (Na_2O = 7.5-8.5%, SiO_2 = 25.5-28.5 %, Sigma Aldrich) and NaOH at SiO_2/Na_2O = 2.25. The resulting slurry was cured at room temperature and the FTIR spectra of the slurry were recorded at a predetermined time intervals.

4.2.3.3 Effect of alkaline activator composition (Silicate content)

Two geopolymer samples were synthesized by mixing the calcined CRM with the alkaline activator at a solid/liquid ratio of 5:3. The first sample of low silica content denoted as MR-1 and had a SiO_2/Na_2O ratio of 3:5; and the second sample of high silica content, denoted as MR-2, had SiO_2/Na_2O ratio of 6:5. The activation solution was prepared from a mixture of NaOH (Reagent grade, 98%) and extra pure Na_2SiO_3 solution (Na_2O = 7.5-8.5%, SiO_2 = 25.5-28.5 %, Sigma Aldrich). The calcined CRM was mechanically mixed with the alkaline activator in a polypropylene beaker for 5 minutes until getting a homogenous geopolymer slurry and poured in a 35 mm square molds. Afterward, the slurry was vibrated for 10 minutes using a vibrating table, and then hydrothermally cured in an oven at 100 ºC for 24 hours.

4.2.4 Analytical methods

Mineralogy was investigated using the polarized light microscopy and powder X-ray diffraction (PXRD). Small slabs were cut from the intact CRM samples in order to make polished thin sections for the mineralogical phase identification and mineral chemistry investigation. The petrographical investigation was conducted before the XRD analysis to identify the major components and textural characteristics of the CRM using a ZEISS transmitted light polarization microscope equipped with a video camera. The PXRD analyses was conducted on a PANalytical X'Pert Pro X-ray diffractometer, which uses CuKα radiation at a tube voltage of 40 kV and current of 40 mA. The raw CRM, thermally activated phase, and

formed geopolymers were scanned over a sampling range of 3-70 º2θ with a step size of 0.0066° and a scan speed of 0.023 °2θ per second. All samples were measured with sample holders of 20 mm diameter. The obtained data were analysed using the X'Pert HighScore Plus software for phase identification. The results were compared with petrographic investigation to confirm the essential mineral composition.

The CRM and/or geopolymers were also analysed using a Panalytical Epsilon 3XL energy dispersive X-ray spectrometer. The chemical signature of the CRM-forming minerals was identified using an Electron Probe Micro Analysis (EPMA), JEOL JXA-8200 superprobe. The measurements were conducted under operating conditions of a voltage of 15 kV, a current of 20 nA, and a defocused 10 μm beam. The Brunauer-Emmett-Teller (BET) surface area was determined using a Micromeritics Tristar instrument with nitrogen gas at 77 K. All samples were degassed at 100 °C before being measured. The analysis of the morphology was conducted using a JEOL7100F scanning electron microscope equipped with an EDX detector. The raw material, thermally activated phase, and geopolymer fragments and/or powders were coated with carbon to obtain the required conductivity using Edward coating system (E306A).

Vibrational functional groups were identified using an Attenuated Total Reflection Fourier Transform Infrared (ATR-FTIR) spectrometry using a Bruker Alpha FTIR spectrometer to record the transmittance in the range of 400 – 4000 cm^{-1}, and the data were analysed using OPUS software. The identification of iron oxidation states and the local environments along with ^{57}Fe Mössbauer spectra of the raw CRM, calcined CRM and the produced geopolymers were determined using Mössbauer spectroscopy on a Wissel constant acceleration spectrometer, using a ^{57}Co source in a rhodium matrix at room temperature.

4.3 Results and discussion

4.3.1 Raw material

4.3.1.1 Chemical composition

The elemental composition of raw material and geopolymer is given in Table (4-1). The chemical composition of the raw CRM reflects the presence of a suitable amount of Al, Fe and Si components which are needed to formulate the backbone of geopolymer. A comparison between the CRM and other precursors used in the synthesis of geopolymer are depicted in Fig (4-2).[20-28] Though the CRM has a suitable chemical composition to undergo an alkali activation

reaction, its reactivity in the alkali activation is dependent on the propensity of its forming minerals to dissolve in an alkaline medium.

Table 4-1: Chemical composition of raw CRM and geopolymers.

Samples	**SiO_2**	**Al_2O_3**	**Na_2O**	**K_2O**	**CaO**	**Fe_2O_3**	**MgO**
Raw material	44.41	14.45	0.90	3.15	10.07	6.3	10.15
MR-1	41.88	9.36	18.70	2.33	7.12	4.19	8.14
MR-2	42.24	8.19	17.49	2.15	6.48	3.97	6.48

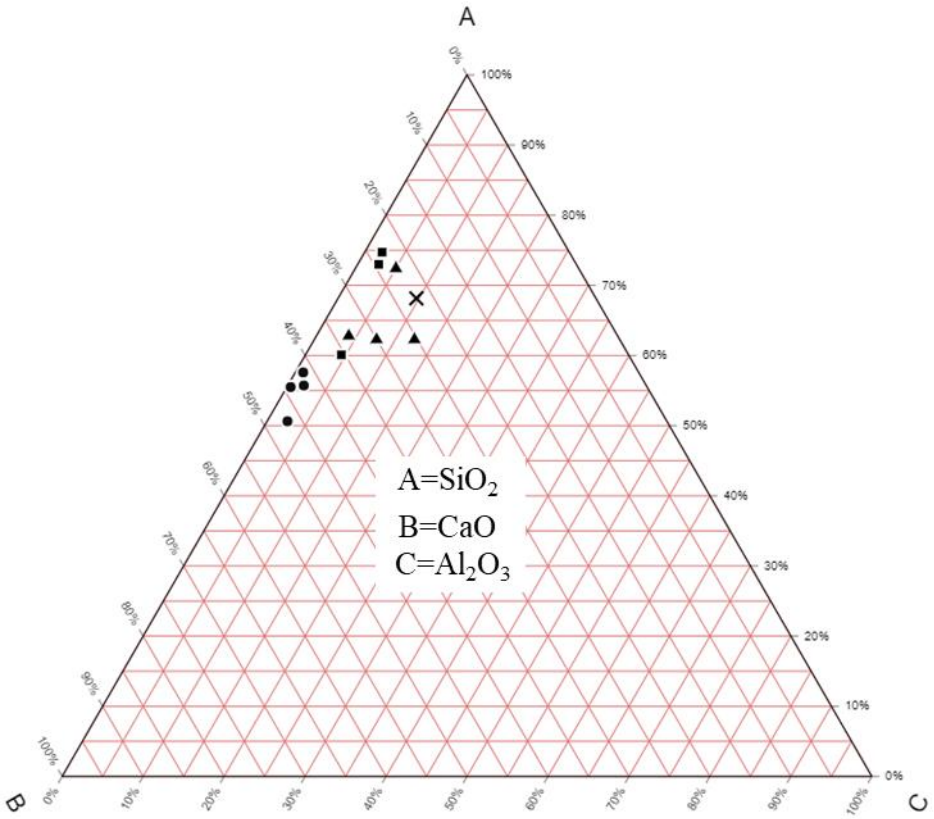


Figure 4-2: Comparison between CRM (**X**), fly ash (▲), blast furnace slag (■), and metakaolin (◉).

4.3.1.2 Mineralogy and mineral chemistry

The mineralogical composition of the raw CRM was characterized by polarized light microscopy to determine the essential minerals as shown in Figure (4-3). Two phases of minerals, alumino-silicate, and carbonate were identified. The aluminosilicate phase includes clays, feldspar, mica, and quartz. Clay minerals are the prevalent phase and are distributed in the matrix forming a network-like structure cementing other minerals; while feldspar, quartz and mica occur as accessory minerals. The carbonate phase comprises calcite and dolomite, whereas dolomite is more prevalent than calcite. The XRD analysis of the raw material is shown in Figure (4-4). Generally, The XRD analysis is consistent with the petrographical

investigation. The analyses revealed the presence of various clay minerals included illite, kaolinite, chlorite, and palygorskite. Although the petrographical investigation revealed that the clay minerals are the main constituent, their peak intensities on the XRD diffractogram is low. The reduction in peak intensity of clay minerals may be attributed to the presence of Fe^{3+} or Fe^{2+} which can replace Al^{3+} in mineral structure affecting on its crystallinity by causing structural imperfections.[29] This can be further supported by the variation in the interference colour of clay phase from brown to darkish brown, Usually such change in colour reflects the change in chemical environments. Mineral chemistry analysis confirmed the carbonaceous – alumino silicate nature of marlstone as depicted in Figure (4-5), where Al and Si are mainly concentrated in the structure of clay minerals, mica, quartz, and feldspar, while Fe occurs mainly in the clay phases (possibly substituting Al and Mg in the octahedral sites), in addition to the occurrence in the crystalized iron-bearing phase, hematite. The Ca and Mg occur together in dolomite crystal lattice, reflecting the presence of a layered chemical structure, while Ca occurs mainly in the structure of calcite.

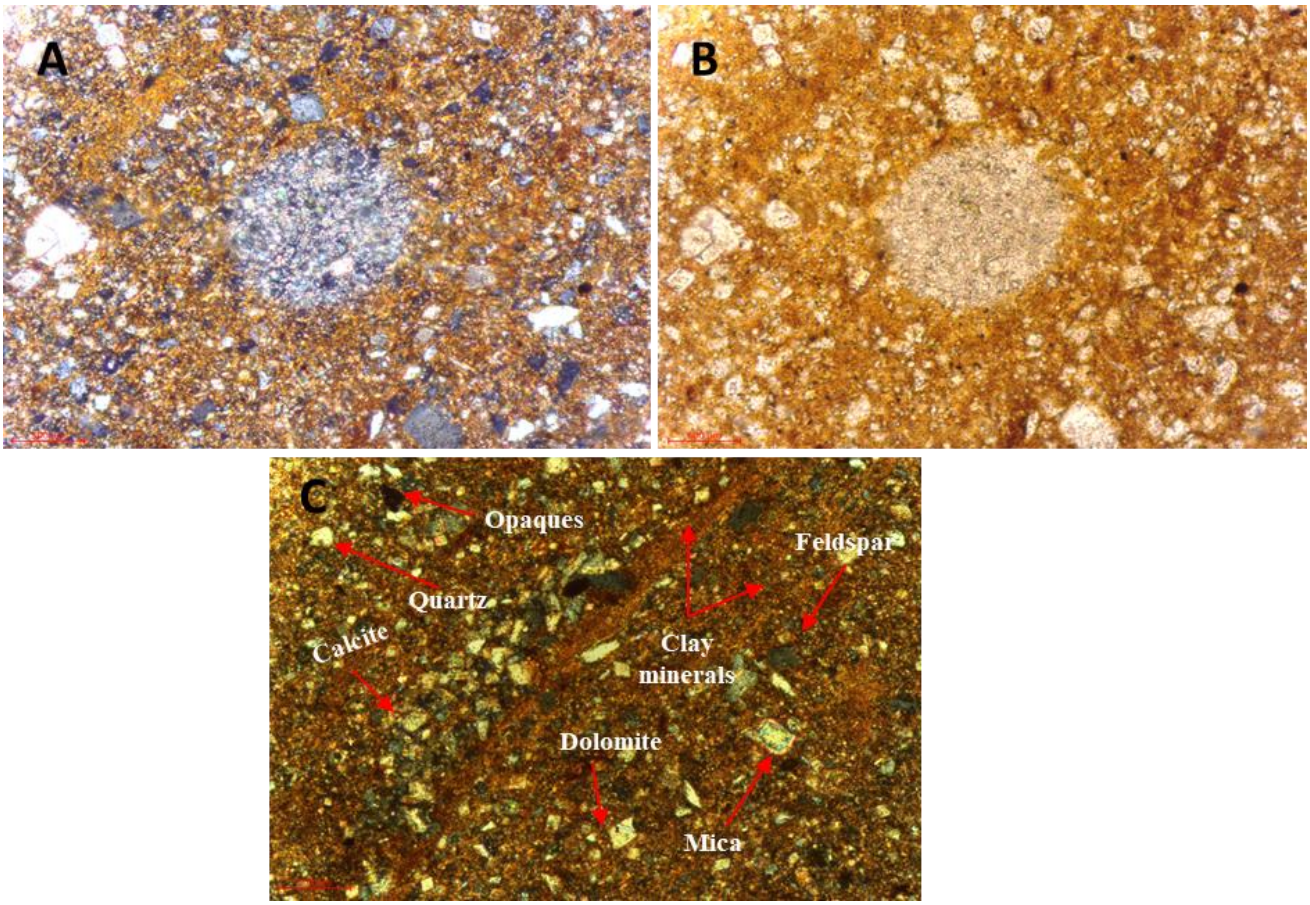


Figure 4-3: Petrography of raw CRM. A and C under Cross-Nicole; B under polarized light. Clay minerals are the dominant phases followed by dolomite. The clay minerals show a fibrous

and network pattern. Feldspar showed a simple twining, quartz showed a wavy extinction while calcite characterized with a twinkling and more than one set of cleavages.

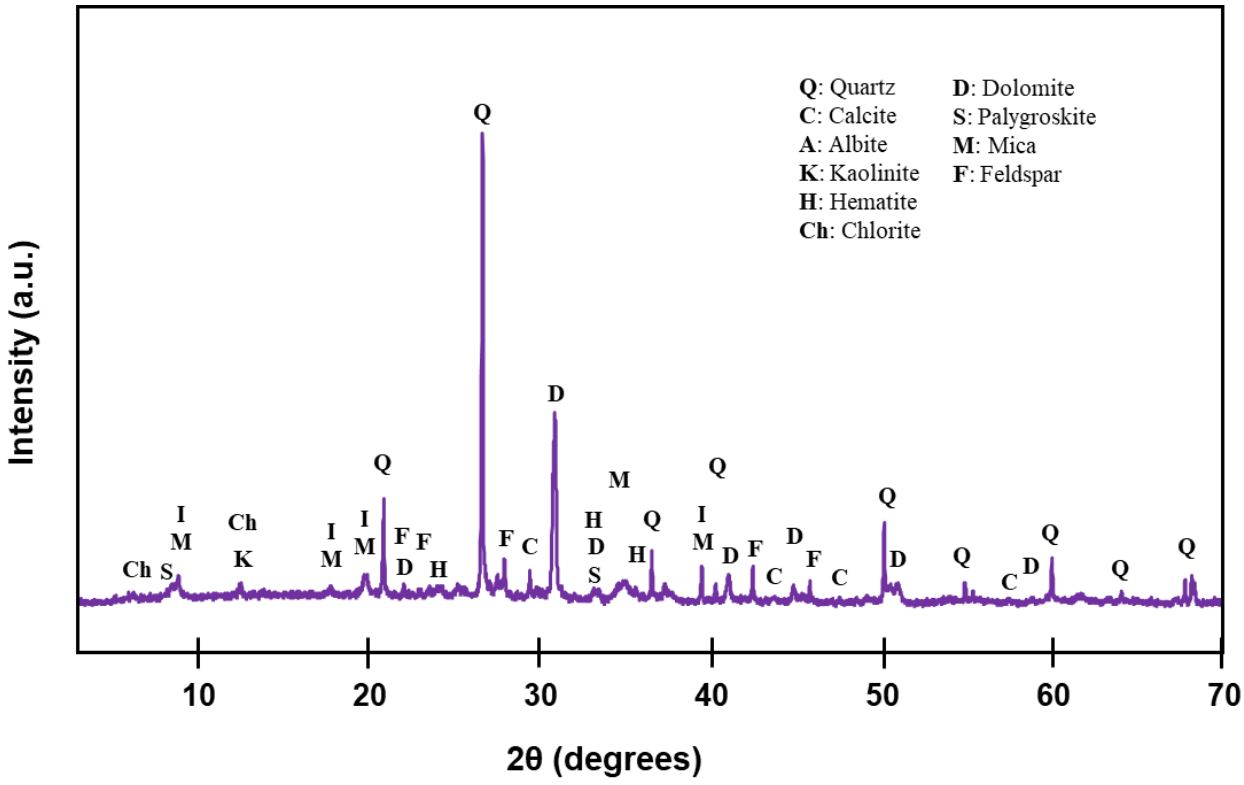


Figure 4-4: XRD analysis of the bulk raw material (non-oriented). Mineral phases were determined using the X'Pert HighScore plus software.

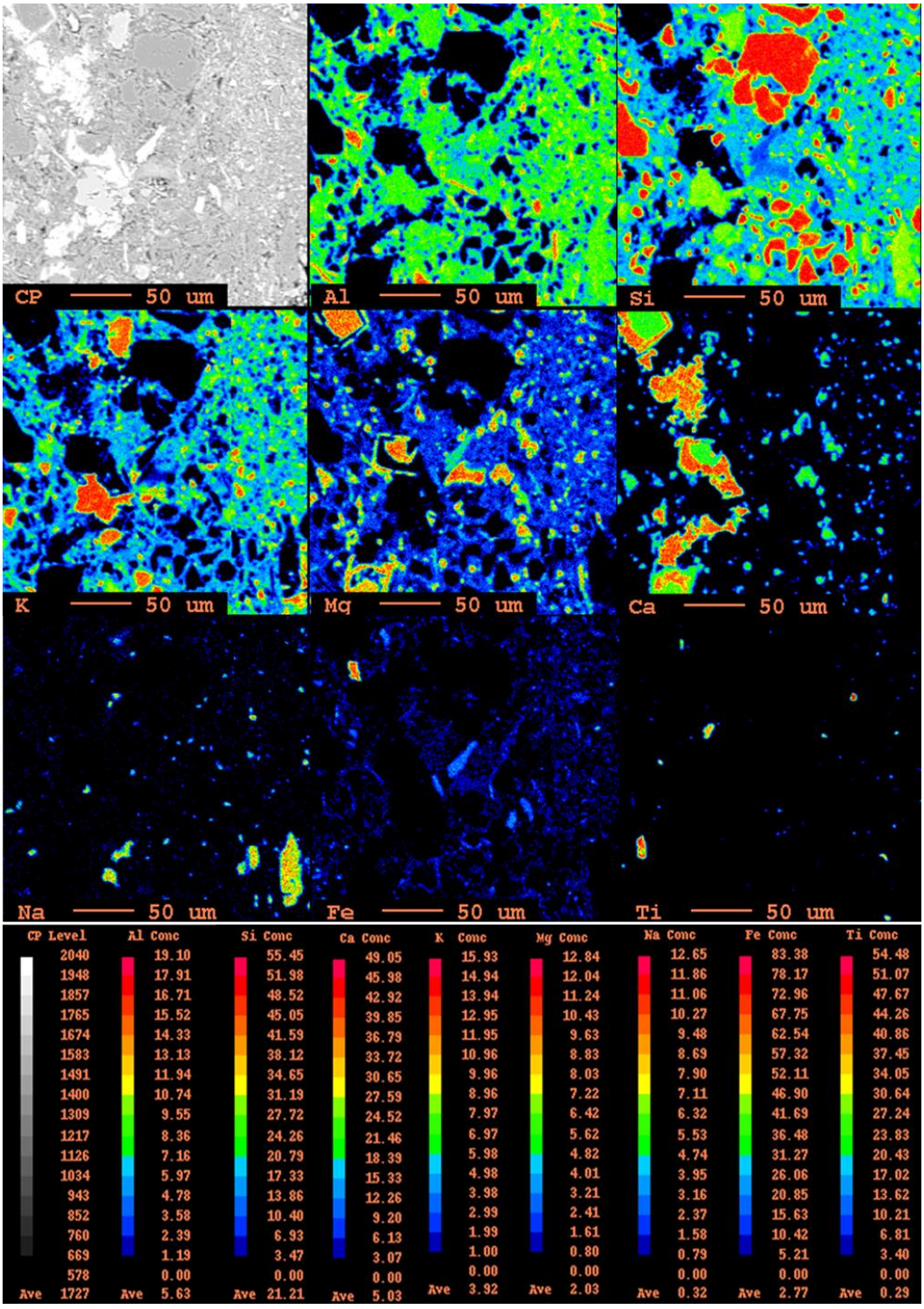


Figure 1-5: Chemical composition of the CRM-forming minerals. The Al and Si are mainly distributed in clay, feldspar, and mica. Ca and Mg are mainly distributed in dolomite and calcite. Fe is contained mainly in a crystalized phase (hematite) and widely distributed in other minerals such as clays and mica.

4.3.1.3 FT-IR

Fig (4-6) shows the infrared absorption spectrum of the raw CRM. The main aluminosilicate characteristic absorption band is located at ca. 991 cm^{-1}. This band is assigned to the Si-O-T (T= Si or Al) asymmetric stretching mode.[30] Sharpness of this band indicates the presence of an ordered and well-crystalline structure. The distinctive doublet bands at 797 cm^{-1} and 778 cm^{-1} are ascribed to the Si-O-Si stretching vibrations.[29] The absorption band at 424 cm^{-1} is attributed to the Fe-O vibration in hematite. The absorption bands at 693 cm^{-1} and 513 cm^{-1} are assigned to the Si-O-Si and O-Si-O mixed modes,[30, 31] while those at 464 cm^{-1} and 643 cm^{-1} are attributed to the Si-O and Al-O bending vibrations.[29, 32, 33] The absorption band at 727 cm^{-1} [ν_4 (CO_3^{-2})] and at 880 cm^{-1} [ν_2 (CO_3^{-2})] are assigned to the vibration bending modes of dolomite and calcite, respectively.[34] The peak at 1456 cm^{-1} is attributed to C-O stretching vibration mode of ν_3 (CO_3^{-2}). The band at 1653 cm^{-1} is due to the H-O-H bending mode of the unbound zeolitic water within the clay minerals channels.[29] The small shoulder at 838 cm^{-1} may be attributed to the H-O-Al or H-O-Fe^{3+} vibration bending modes. These vibrations usually appear when the trivalent ions occupy the octahedral sites, and are observed in the range of 800–920 cm^{-1}.[29]

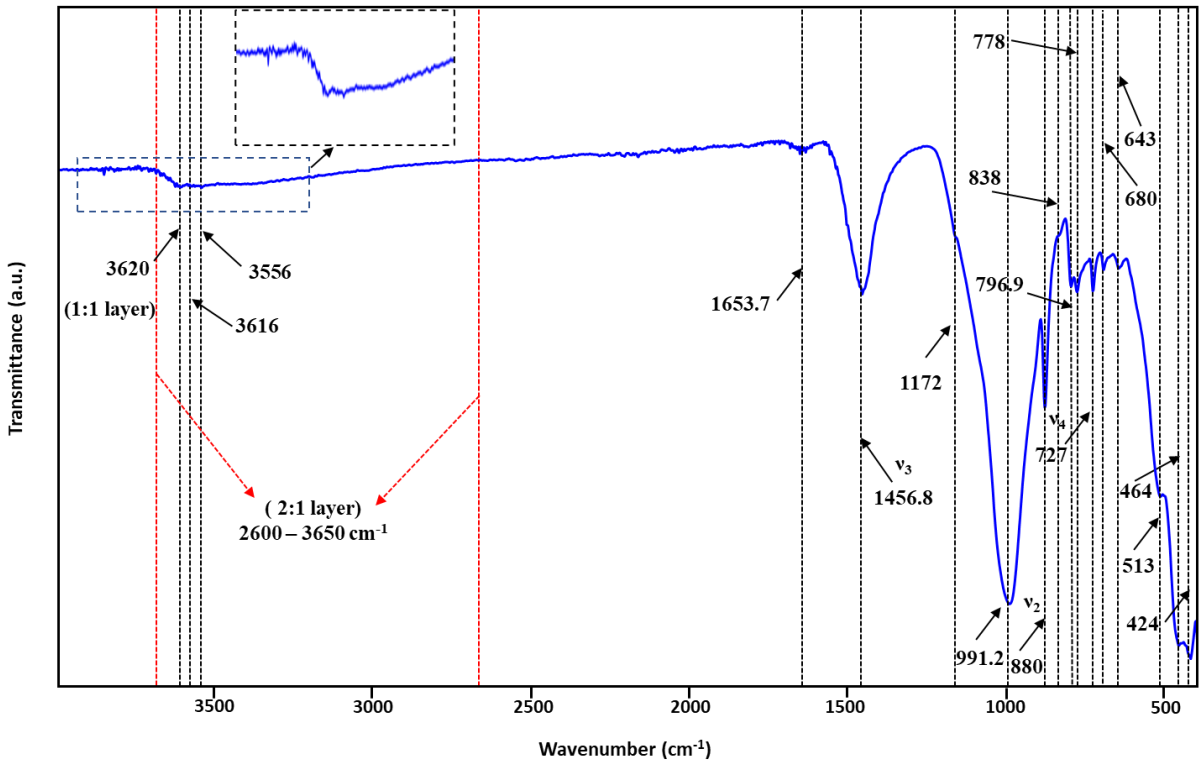


Figure 4-6: FT-IR spectrum of the raw CRM confirmed the carbonaceous and aluminosilicate nature of the precursor.

In summary, the absorption bands at 991 cm^{-1}, 3542 cm^{-1} and 464 cm^{-1} were assigned to magnesium-rich chlorite.[35] The absorption bands at 778 cm^{-1}, 418 cm^{-1}, 424 cm^{-1}, 464 cm^{-1}, and 643 cm^{-1} were assigned to feldspar minerals.[29, 35] The absorption bands near 3600 cm^{-1} are attributed to the 1:1 layer clay (e.g. kaolinite), while the wide absorption in the region of 2600~3650 cm^{-1} is assigned to the 2:1 layer clay (e.g. illite, palygorskite, chlorite). The absorption bands at 797 cm^{-1}, 778 cm^{-1}, 680 cm^{-1}, 464 cm^{-1}, 513 cm^{-1} and 1172 cm^{-1} are assigned to quartz mineral. The absorption bands at 880 cm^{-1} , 727 cm^{-1} and 1456 cm^{-1} are ascribed to the carbonate – containing phases.[35]

4.3.1.4 SEM-EDX

Figure (4-7&8) depicts the distinguishing morphological features of the CRM-forming minerals. Kaolinite shows a booklet and a layered morphology (35 nm), while illite appears as a hairy and fibrous aggregates (24 nm). Chlorite is characterized by a fan shaped (rosette-shapes) morphology. The palygorskite mineral shows a fibrous morphology. The corresponding semi-quantitative analysis (EDS) confirmed the heterogeneous nature of the raw material, reflecting the ferro-aluminosilicate and carbonaceous composition.

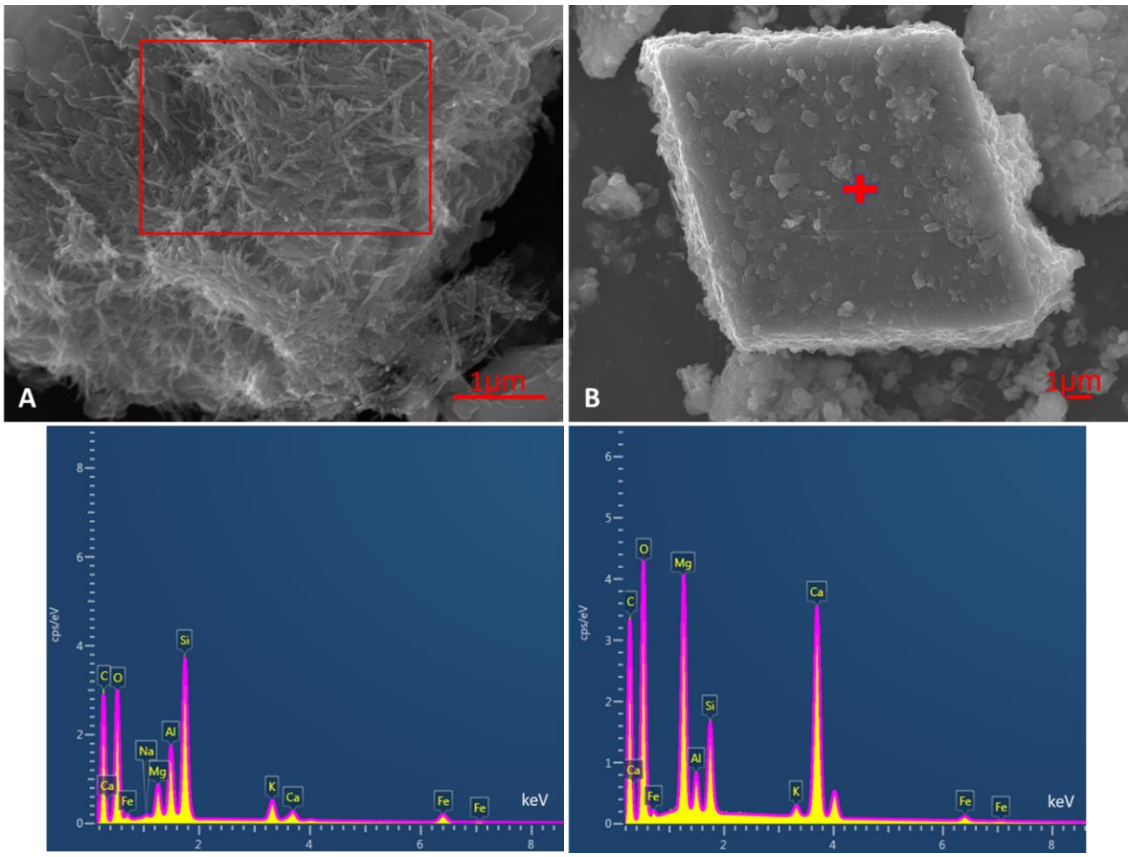


Figure 4-7: SEM micrographs of the raw CRM. A) clay mineral phases; B) dolomite crystal.

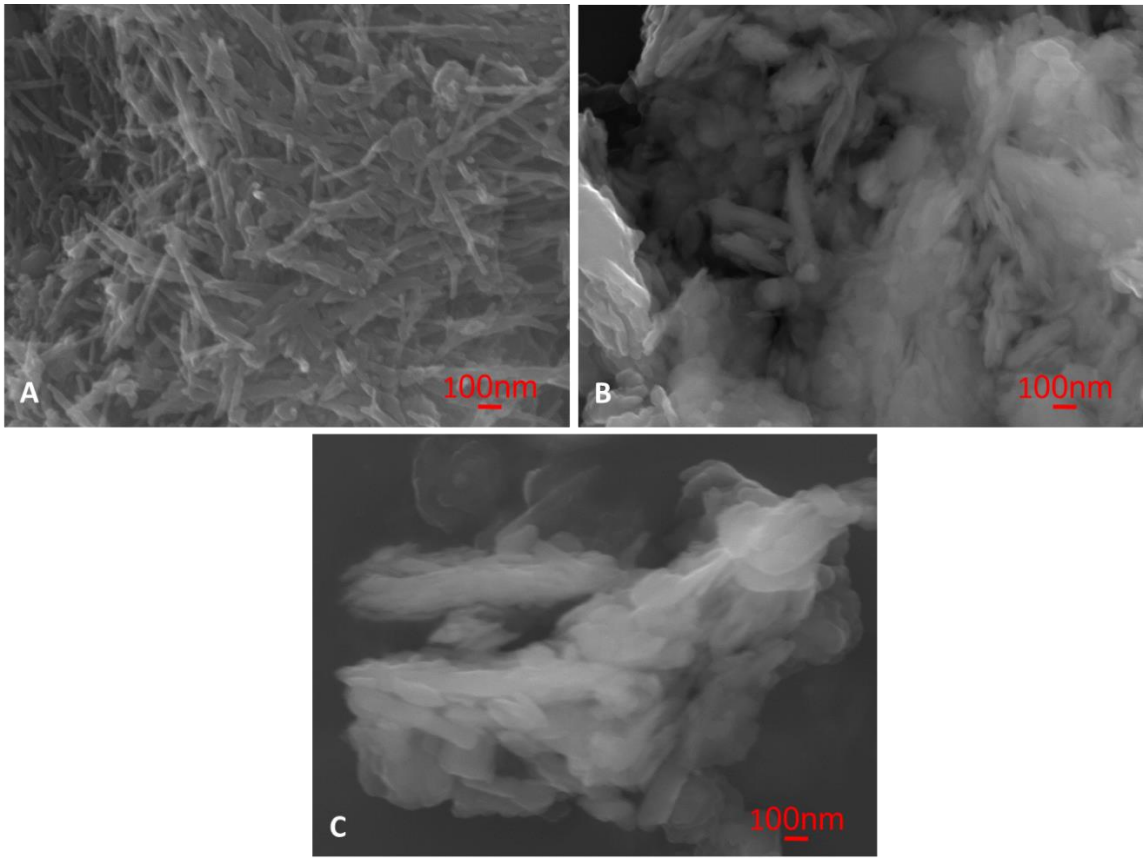


Figure 4-8: Clay minerals of the raw CRM. A) fibrous illite, B) fibrous and hairy palygorskite, and C) layered kaolinite and fan-shaped chlorite.

4.3.2 Thermally activated phase

4.3.2.1 Mineralogy

Heat treatment was accompanied by a significant structural modification in the rock – forming minerals as indicated by the XRD patterns in Figure (4-9). This step was crucial to ensure a suitable geopolymerization reaction, which is mainly dependent on the availability of amorphous phases. As indicated, kaolinite dehydroxylated between 600 ^{0}C and 700 ^{0}C, confirming the transformation into X-ray amorphous metakaoline.[36, 37] There is a change in the illite peaks up to 800 ^{0}C, implying a crystal deformation (i.e., formation of dehydroxylated illite). Illite peaks remarkably diminished between 800 ^{0}C and 900 ^{0}C; the complete collapse of illite structure usually occurs at 950 ^{0}C.[38, 39] A modification in the chlorite peaks appeared between 500 ^{0}C and 600 ^{0}C, where the peak at $2\theta = 12.4^{0}$ disappeared and was accompanied by an increase in the peak at $2\theta = 6.4^{0}$. As the calcination temperature increased, this peak became broader and completely disappeared at 800 ^{0}C. Palygroskite retained some of its

crystallinity up to 700 ^{0}C. Feldspars (microcline and albite) showed a structural modification with increasing temperature. A new calcic-rich feldspar (anorthite mineral) formed at 600 ^{0}C, at the expense of the reactive phases. Anorthite peaks increased with increasing temperature, which suggests a solid-state reaction between the reactive components. The intensity of hematite peaks increased with temperature. The increase in the intensity of hematite peaks may be attributed to the oxidation of released structural Fe during the clay mineral decomposition. The change in marlstone colour to orange at higher temperature confirmed the formation of a new Fe_2O_3 phase, which is responsible for the colorant in the calcined materials.[36] Calcite peaks decreased between 700 ^{0}C and 800 ^{0}C and completely disappeared above 800 ^{0}C, while the dolomite peaks decreased with increasing temperature and completely disappeared above 800 ^{0}C. Lime (CaO) and periclase (MgO) appeared as reactive oxides formed due to the decarbonation of dolomite and calcite.[18] The appearance of a sharp periclase peak at 900 ^{0}C indicted a complete decarbonation process for dolomite. Enstatite ($MgSiO_3$) and diopside ($MgCaSi_2O_6$) minerals formed at higher temperature (800 ^{0}C-900 ^{0}C) through a solid-state reaction (recrystallization) between the reactive Mg, Si and Ca phases.

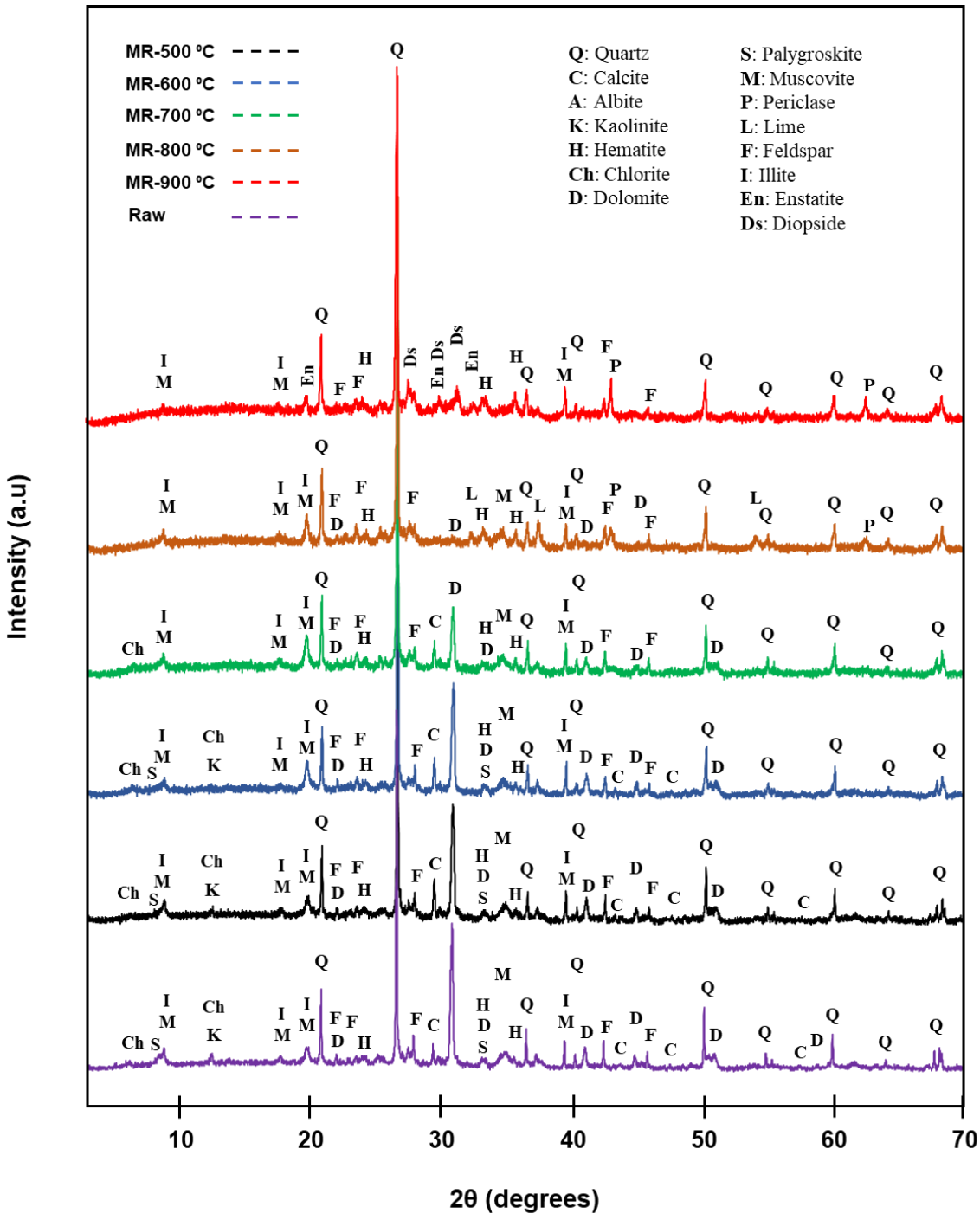


Figure 4-9: XRD analysis of the calcined CRM at different temperatures. The CRM samples were calcined ex situ in a box furnace prior to analysis.

4.3.2.2 FT-IR

FT-IR spectra of the calcined CRM are shown in Figure (4-10&11). Phase changes in the calcined CRM-forming minerals were confirmed and are consistent with the XRD data. The absorption bands of carbonate-containing phases (calcite and dolomite) decreased with increasing temperature. The absorption band related to calcite disappeared at 800 ^{0}C, confirming the occurrence of decarbonation between 700 ^{0}C and 800 ^{0}C, while the absorption band of dolomite significantly reduced at 800 ^{0}C and completely disappeared at 900 ^{0}C. The appearance of a small broad absorption band at 1400 cm^{-1} at 800 ^{0}C suggests the presence of dolomite remnants, which is in accordance with the XRD data. The absorption bands related to OH decreased with increasing temperature from 500 ^{0}C to 700 ^{0}C, and completely disappeared at 800 ^{0}C, indicating a complete transformation of clay minerals into a metastable amorphous phase. Broadening of the main absorption Si-O-T band was noticeable with increasing temperature, and reached the maximum at 900 ^{0}C. The change in the position and sharpness and/or shortening of the Si-O-T band potentially imply a remarkable modification in the local environment of Si and Al atoms in the tetrahedral and octahedral sheet of clay minerals. This modification resulted in the formation of a 3 dimensional amorphous silica network (disordered structure).[40] The disappearance of the absorption band at 516 cm^{-1} after activation at 600 ^{0}C may be attributed to the distortion in the kaolinite layers. This behaviour is consistent with the reduction in the peak intensities of kaolinite at 600 ^{0}C. The two absorption bands at 557 cm^{-1} and 553 cm^{-1} that appeared after thermal activation at 700 ^{0}C and 800 ^{0}C, respectively, are due to the Si-O-Al bending vibration.[41] The appearance of such absorption bands is consistent with the formation of calcic-feldspar (anorthite mineral). The band at 424 cm^{-1} shifted to 442 cm^{-1} after heating at 800 ^{0}C; this band is attributed to the stretching Fe-O bond in hematite.[42, 43]

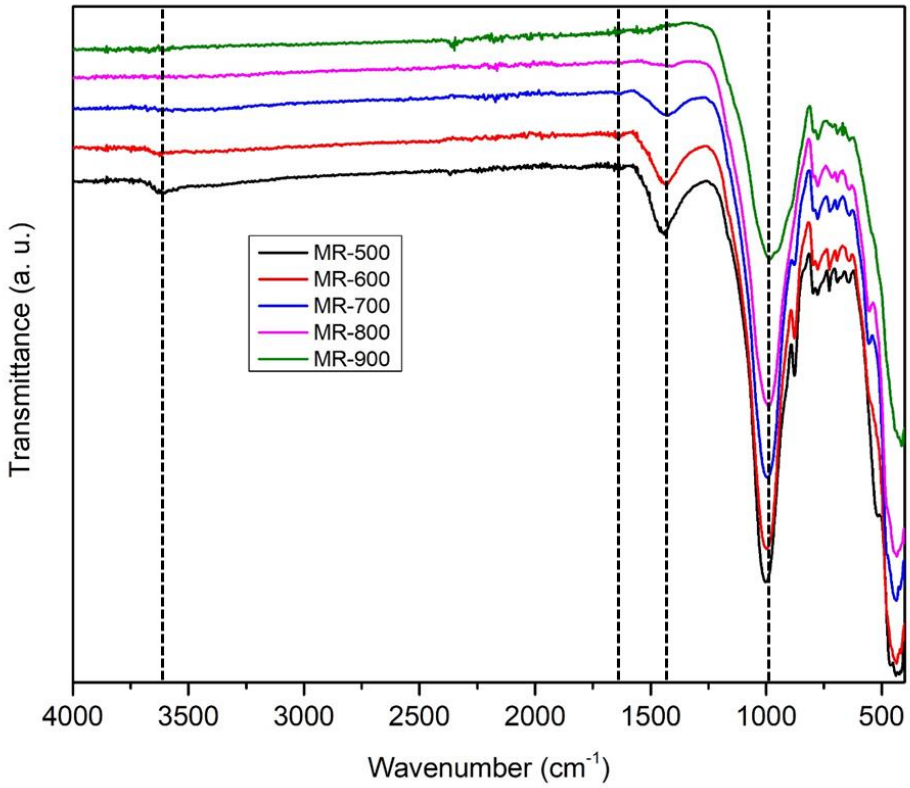


Figure 4-10: FTIR spectra of the calcined CRM at different temperatures between 500 ºC and 900 ºC. The CRM samples were calcined ex situ in a box furnace prior to analysis.

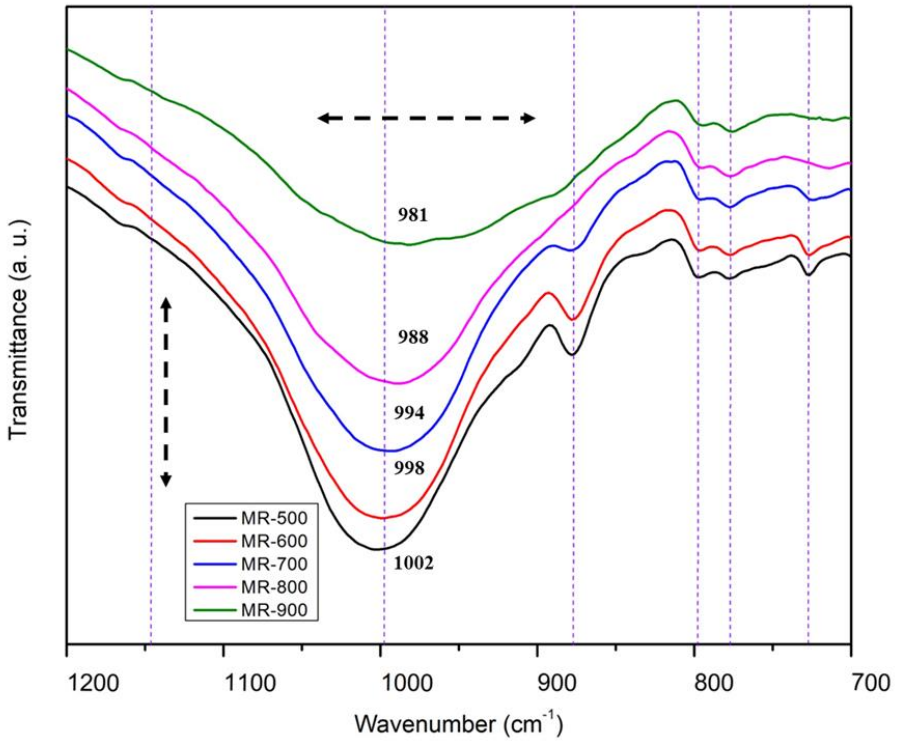


Figure 4-11: FTIR spectra of calcined CRM showing the modification in Si-O-T and CO_3^{2-} bands. The CRM samples were calcined ex situ in a box furnace prior to analysis.

4.3.2.3 SEM-EDX

Thermal activation at 500 ^{0}C to 900 ^{0}C was accompanied by morphological changes in both carbonate and clay phases as indicated in Figures (4-12&13). Temperature rise from 500 ^{0}C to 800 ^{0}C changed the fibrous nature of clay minerals, with a glassy matrix formed at 800 ^{0}C. Small aggregated crystallized particles appeared at 900 ^{0}C, suggesting the occurrence of recrystallization. These new small, crystallized morphologies may be attributed to the enstatite and/or diopside minerals. There is no change in the morphology of dolomite crystals at 500 ^{0}C and 600 ^{0}C, while cracking propagation was noticed at 700 ^{0}C, illustrating crystal deformation and the partial dissociation of $MgCO_3$ and $CaCO_3$ layers in dolomite crystals. Dolomite crystals became more deformed and collapsed at 800 ^{0}C. As a result, clustering of small, rounded grains appeared which may be attributed to periclase (MgO) and lime (CaO) phases.[44] The dolomite crystals completely destructed and a new crystalized phases were formed at 900 ^{0}C.

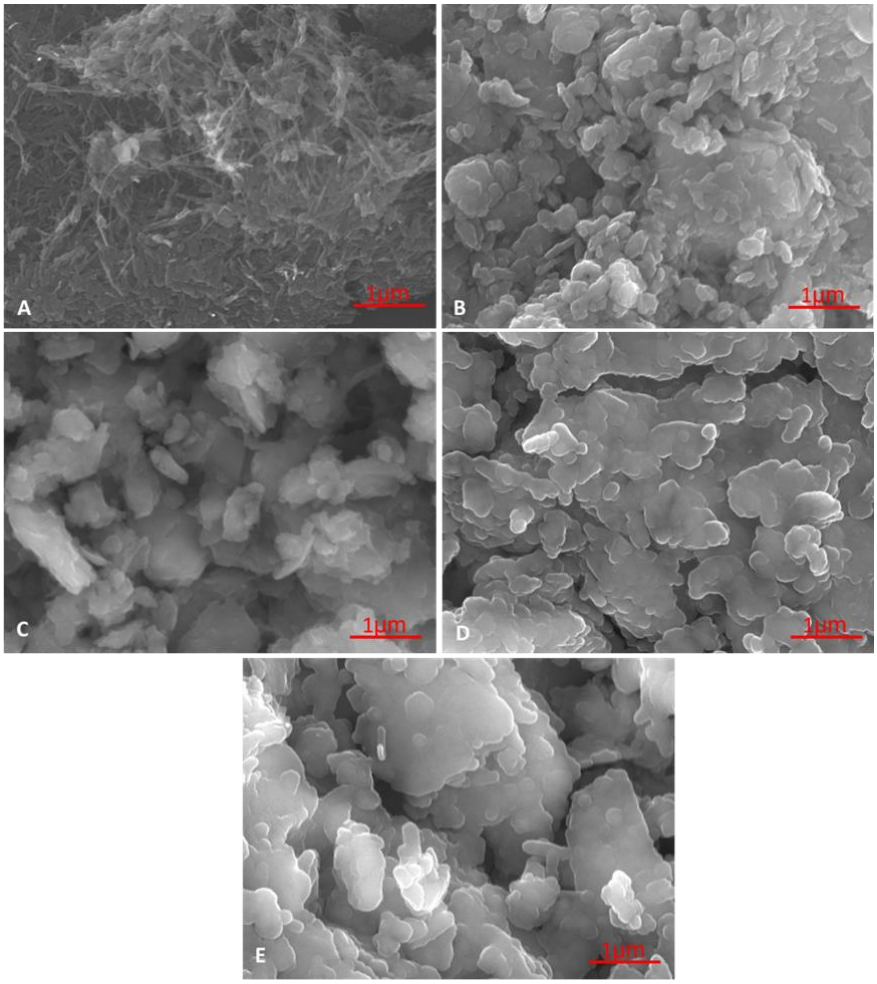


Figure 4-12: SEM micrographs of calcined CRM at different temperatures showing the modification in clay minerals morphologies. A = 500 ºC, B= 600 ºC, C= 700 ºC, D= 800 ºC, and E= 900 ºC. The morphology changed from being fibrous into a glassy matrix at 800 ºC.

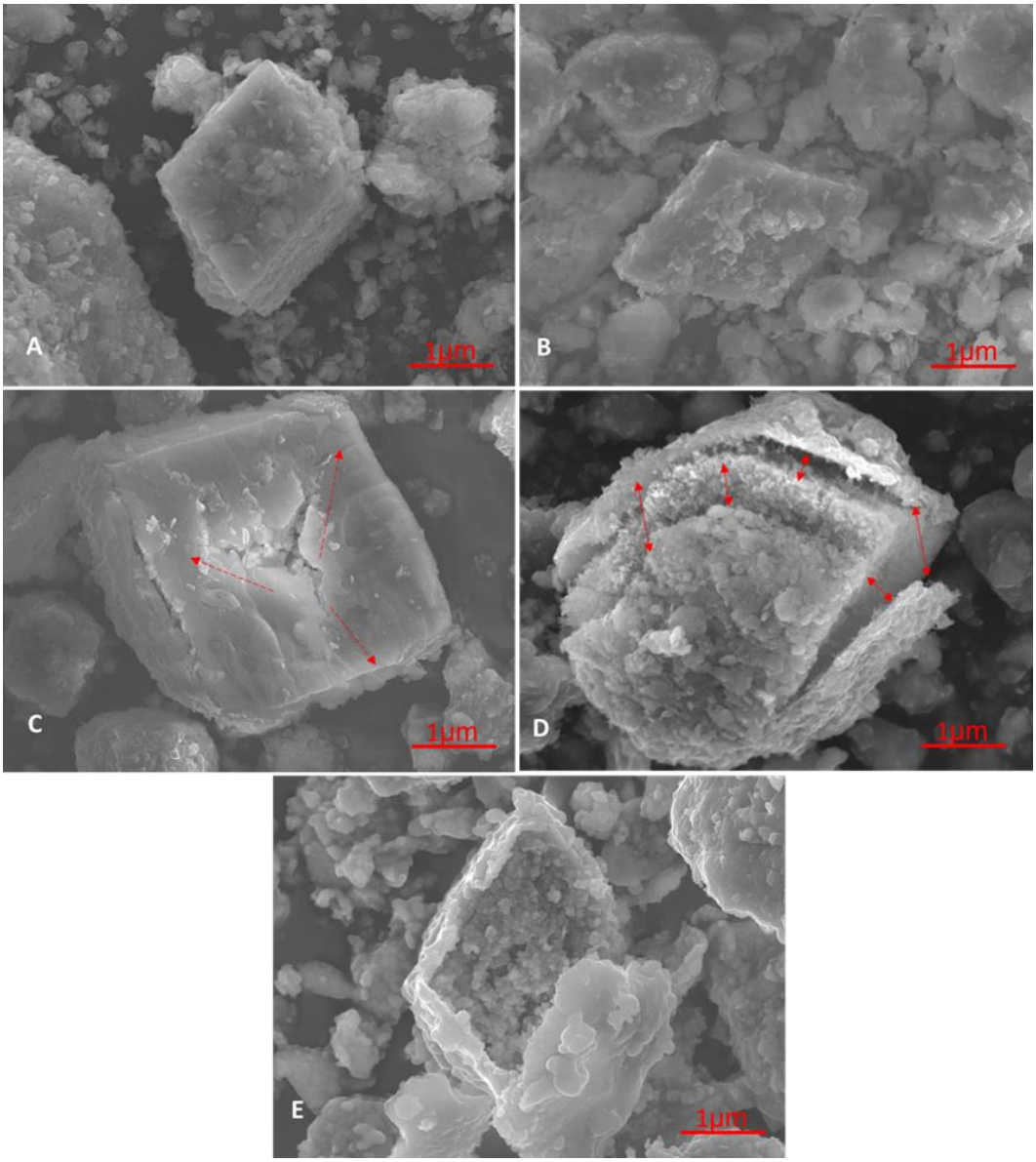


Figure 4-13: SEM micrographs of calcined CRM at different temperatures showing the modification in carbonate-bearing phase. A = 500 ºC, B = 600 ºC, C = 700 ºC, D = 800 ºC, and E = 900 ºC. Notice the change in the morphology of dolomite crystal, there was no substantial change in the morphology at 500 ºC and 600 ºC. The propagation of cracking was clearly noticed at 700 ºC confirming the start of crystal deformation due to heating. The dolomite crystal collapsed at 800 ºC and its crystal layers became more deformed. Although the dolomite crystal retained a weak crystal habit, the formed oxides (MgO and CaO), after decomposition, crystalized at 900 ºC through a solid-state reaction forming diopside ($MgCaSi_2O_6$) and enstatite ($MgSiO_3$) minerals.

4.3.3 Geopolymerization of calcined calcareous-red mudstone

4.3.3.1 Reactivity under alkaline conditions (low temperature system, 25 ^{0}C)

4.3.3.1.1 Silicate (Si^{4+}) and aluminate (Al^{3+}) species leaching

The dissolution of rock-forming minerals in the alkaline solution is depicted in Figure (4-14). Interestingly, the amount of released Si and Al increased simultaneously with the increase in calcination temperature from 500 ^{0}C to 800 ^{0}C and decline after 800 ^{0}C. This behaviour is consistent with the structural modification in the rock-forming minerals and clay minerals upon thermal activation, indicating the formation of a metastable phase. The decrease in the dissolution efficiencies of Al_2O_3 and SiO_2 after 900 ^{0}C is attributed to the sintering-melting reactions. FT-IR of the calcined CRM after leaching is depicted in Figure (4-15). The absorption bands related to carbonate at 1429-1433 cm^{-1}, and 878-879 cm^{-1} increased with increasing temperature from 500 ^{0}C to 800 ^{0}C, and decreased significantly at 900 ^{0}C. The increase in the carbonate absorption bands is attributed to the presence of a highly reactive components, mostly CaO, which carbonized by the reaction with the atmospheric CO_2. The decrease in carbonation effect at 900 ^{0}C is potentially due to the formation of a more crystalline and inactive phases.[45] There is a significant change in the position of the Si-O-T band from 500 ^{0}C to 600 ^{0}C but with no further change at 700 ^{0}C. Shifting the main band to a low wavenumber implies some degree of polymerization with the Al is penetrating the Si tetrahedral.

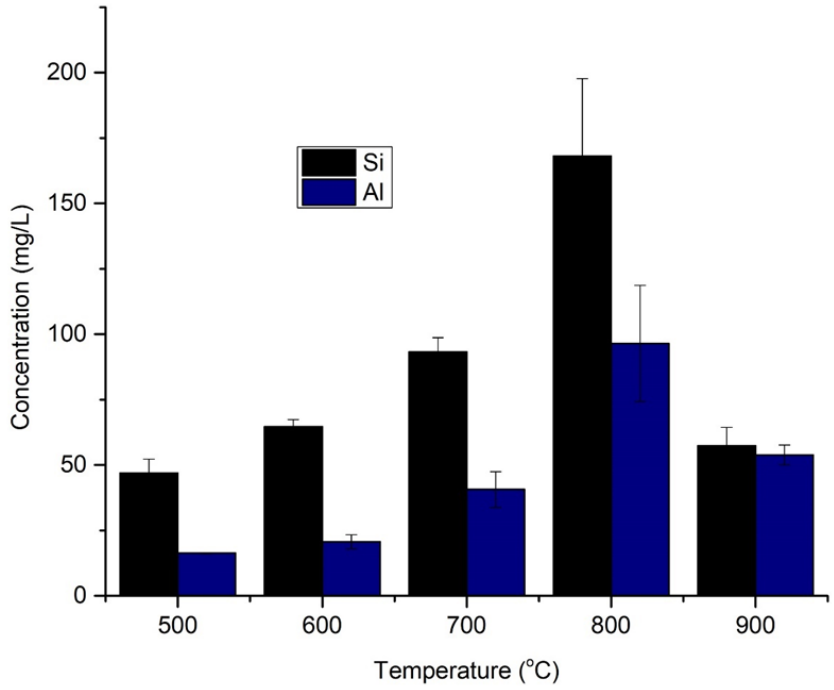


Figure 4-14: Si and Al release of thermally activated CRM at different temperatures.

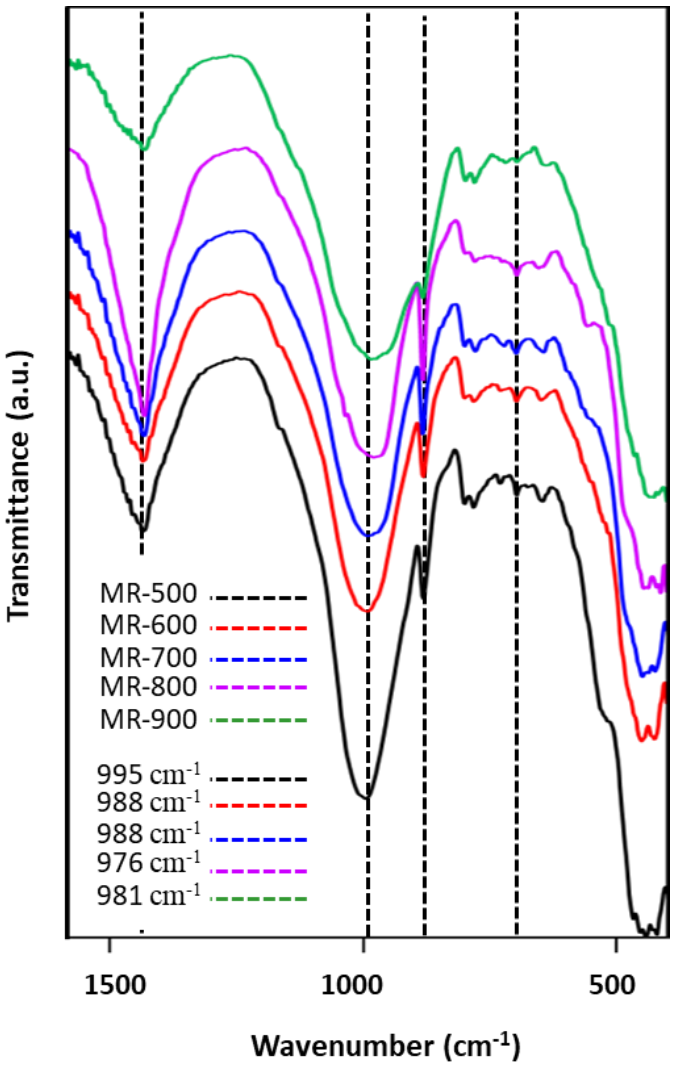


Figure 4-15: FTIR spectra of the calcined CRM after leaching showing a shift in the Si-O-T to a lower wavenumber. Notice the change in the intensity of calcite absorption bands due to carbonation.

4.3.3.1.2 Dispersion behavior of the calcined CRM after leaching

Dispersion of the calcined CRM, at different temperatures, is presented in Figure (4-16). There is a decrease in the dispersion (turbidity) of the calcined CRM particles with increasing calcination temperature from 500 ^{0}C to 800 ^{0}C. After calcination at 800 ^{0}C, the dispersion became completely clear after 5 min of shaking. The decrease in the dispersion was remarkable at 800 ^{0}C. The decline in the dispersion can be taken as evidence on the change in the physicochemical properties of the calcined CRM after leaching, confirming the nucleation of geopolymeric particles. However, the consolidation (gelation) and the quick deposition of the calcined CRM at 800 ^{0}C suggested that, in addition to the incorporation of Al into the system,

the released reactive Ca and Mg played a major role in this process, while this effect was absent at 900 ^{0}C and less effective at 500 ^{0}C, 600 ^{0}C and 700 ^{0}C. It is known that the presence of a free reactive CaO and MgO significantly contributes to the rapid hardening of the geopolymer slurry.[46, 47] The reactivity of the calcined CRM was determined based on the bulk geochemical analysis (XRF) after leaching and the result is depicted in Figure (4-17). Generally, there is an increase in the reactivity starting from 500 ^{0}C to 800 ^{0}C and a remarkable decrease occurs between 800 ^{0}C and 900 ^{0}C. This behaviour is consistent with other results, thus confirming the occurrence of dehydroxylation, decarbonation and recrystallization processes, which controlled the overall reactivity of the calcined CRM. Surprisingly, three trends were identified, from 500 ^{0}C to 700 ^{0}C the sequence of reactivity was K> Al> Si> Mg> Ca> Fe, this sequence changed at 800 ^{0}C and 900 ^{0}C to be Al>Si>K>Mg>Ca>Fe, and K> Fe> Al> Si> Ca> Mg, respectively.

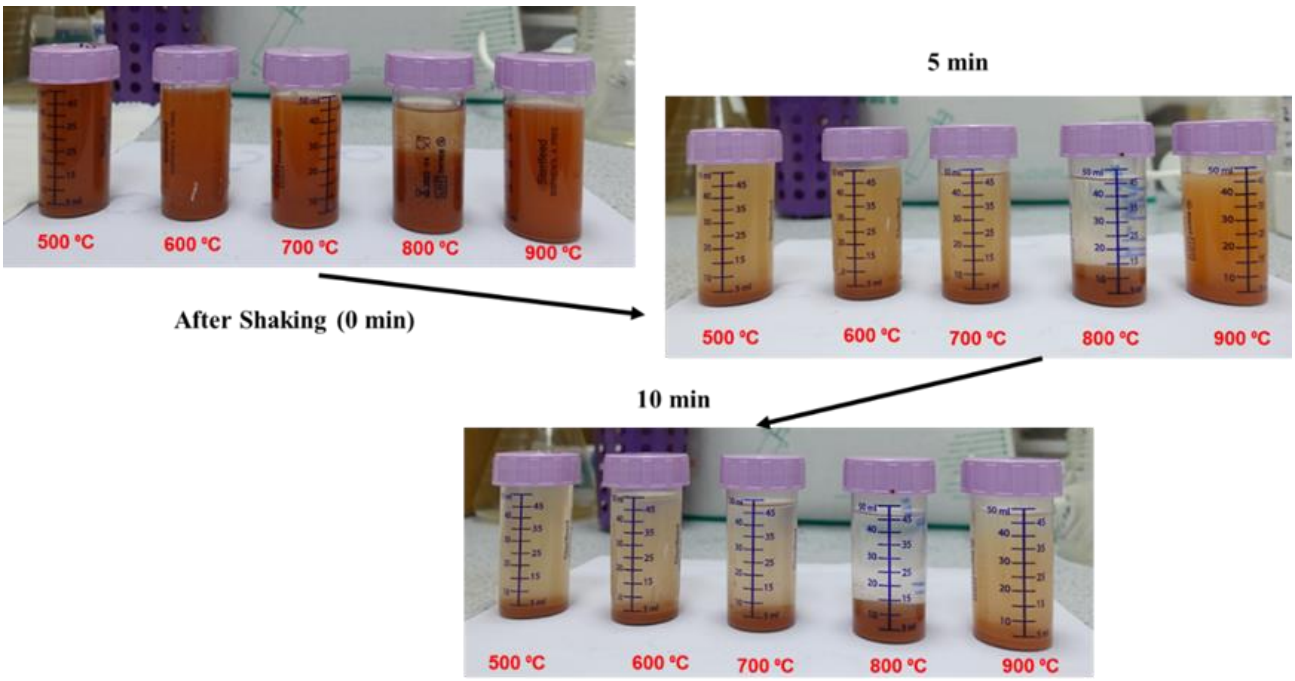


Figure 4-16: Shows the dispersion behaviour of the calcined CRM at different temperatures (500 ^{0}C, 600 ^{0}C, 700 ^{0}C, 800 ^{0}C, and 900 ^{0}C). The solution was very turbid at 500 ^{0}C and decreased gradually from 500 ^{0}C to 800 ^{0}C then increased at 900 ^{0}C. The solution became clear at 800 ^{0}C after 5 minutes of shaking and became more clearer after 10 minutes. The calcined CRM at 900 ^{0}C retained a higher degree of turbidity after 10 minutes compared to at 500 ^{0}C and 600 ^{0}C.

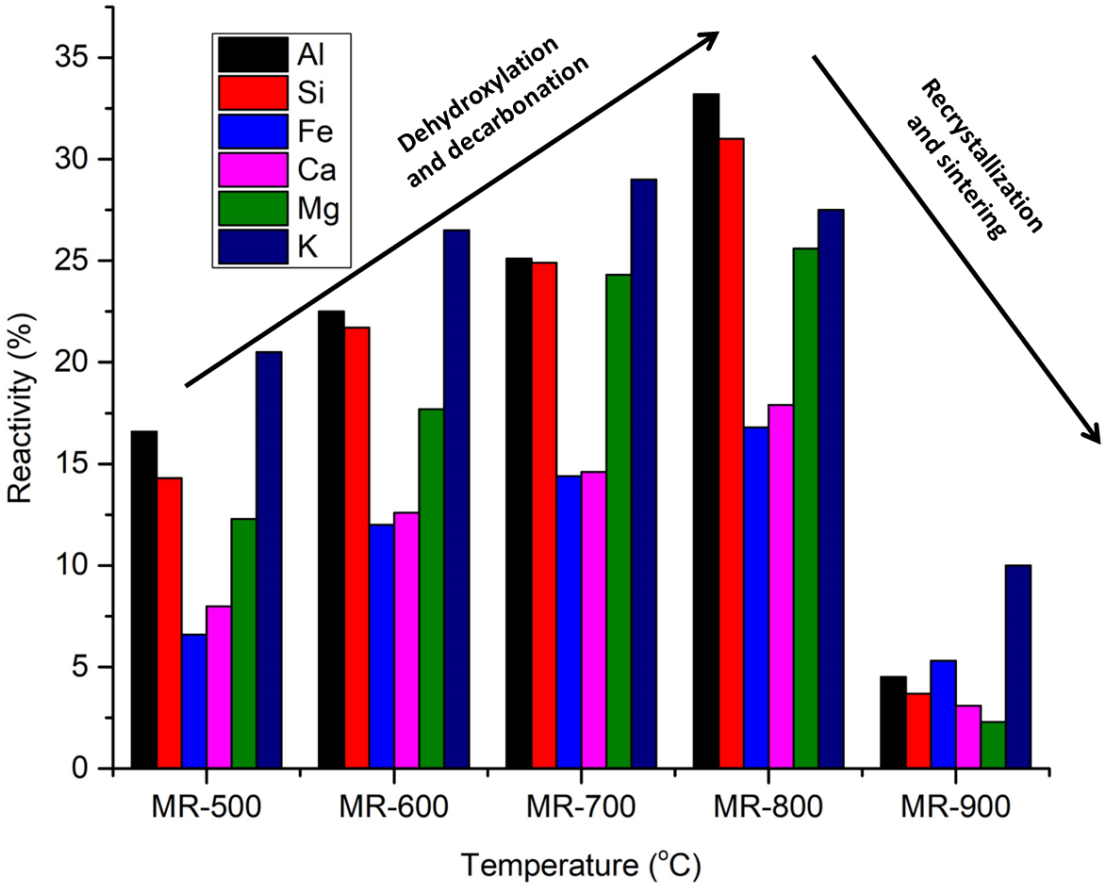


Figure 4-17: Shows the dissolution reactivity of the calcined CRM at different temperatures. The dehydroxylation and decarbonation was the prevalent process from 500 ^{0}C to 800 ^{0}C while the recrystallization process was prevalent at 900 ^{0}C. The dissolution of K, Al, Si, Mg, Ca, and Fe was dominant from 500 ^{0}C to 700 ^{0}C consistent with the dehydroxylation of kaolinite, chlorite and palygorskite (K, Al, Si, Mg, and Fe) in addition to the decarbonation of calcite (Ca). the dissolution of Al and Si was higher at 800 ^{0}C indicating the increase in the formation of amorphous phases due to the decomposition of clay minerals. The overall reactivity of the calcined CRM was significantly low at 900 ^{0}C confirming the recrystallization process of reactive products at high temperature increasing the resistance of dissolution in the alkaline medium. The reactivity trend at 900 ^{0}C was K, Fe, Al, Si, Ca, and Mg. the dissolution of K was higher compared to the corresponding elements which may be attributed to illite and mica. The reactivity of Ca and Mg was the lower due to the formation of diopside and enstatite minerals.

4.3.3.1.3 Evaluation of the CRM in alkali activation as a function of time

The FTIR analyses, in situ, on the geopolymer slurries were valuable and versatile techniques to demonstrate the structural evolution of the geopolymerization processes (dissolution, reorganization and polycondensation), and the related gels [(N, K)-A(F)-S-H) and C-(A)-S-H]. The affinity of the calcined CRM in the alkali activation is depicted in Figure (4-18). This study was conducted under the geopolymerization conditions where samples cured at room and elevated temperature. The shift in the position of the main band (Si-O-T) at different periods of the reaction time was monitored as an indicator of the degree of geopolymerization. The change in the position and intensity of the Si-O-T band reflected the formation of a geopolymer gel. The first observation is that of a noticeable change in the position of the band with increase in consolidation over the experiment time, which indicates that a significant molecular change occurred in the structure upon the alkali attack. Accordingly, the shift in the position of the main band over the designed reaction time revealed the presence of three stages of reaction.

Stage I; the band at 989 cm^{-1} for the calcined CRM shifted to low wavenumbers and reached the lowest value at 949 cm^{-1}, indicating the progressive depolymerization of silicate chains. As a result, the silicate (Si^{4+}) and aluminate (Al^{3+}) monomers released, and further developed into an Al-rich gel (i.e., less cementitious gel)**.**

Stage II; the main band started shifting toward high wavenumbers from 949 cm^{-1} to 952 cm^{-1}. This behaviour is assigned to the turning of Al-rich gel into a Si-rich gel where more Si^{4+} monomers are released into the system and subsequently more Si-O-Si bonds are formed. The formation of Si-O-Si bonds is responsible for the strength development in the geopolymer and for the gradual hardening of geopolymer paste over the setting time.[48]

Stage III; the main band shifted from 952 cm^{-1} to 957 cm^{-1}, reflecting the formation of a 3D aluminosilicate structure. Moreover, the reaction reached a maximum degree of polymerization with a band at 963 cm^{-1} under a hydrothermal curing condition (cementitious gel). The behaviour of the calcined CRM during alkali activation is consistent with the conceptual model of geopolymerization: (i) the calcined CRM dissolved in the alkali activator where the initial formed gel was rich in Al monomers, (ii) the system turned to be rich in Si where more Si released and the Si-O-Si bonds formed, and (iii) the geopolymer gel further condensed into a more cross-linked structure.[18] The main absorption band at 989 cm^{-1} shifted to 963 cm^{-1} after 30 min of reaction, implying a high degree of geopolymerization.[49] In the early stages of

reaction, a less cementitious gel rich in Al was formed as an intermediate phase. The predominance of Al at this stage is due to the fact that Al-O bonds are weaker than Si-O bonds and easily broken. Moreover, during the initial stages of geopolymerization, the dissolution of Si-O bonds is thermodynamically less favourable than the Al-O bonds, indicating a higher initial reactivity of the raw material.[50, 51] The shift in position of the main band after geopolymerization is due to the reduction in the T-O-T angel due to the substitution of Al^{3+} with Si^{4+}. Moreover, the Al-O bond is longer than the Si-O bond which means a smaller bonding force.[52]

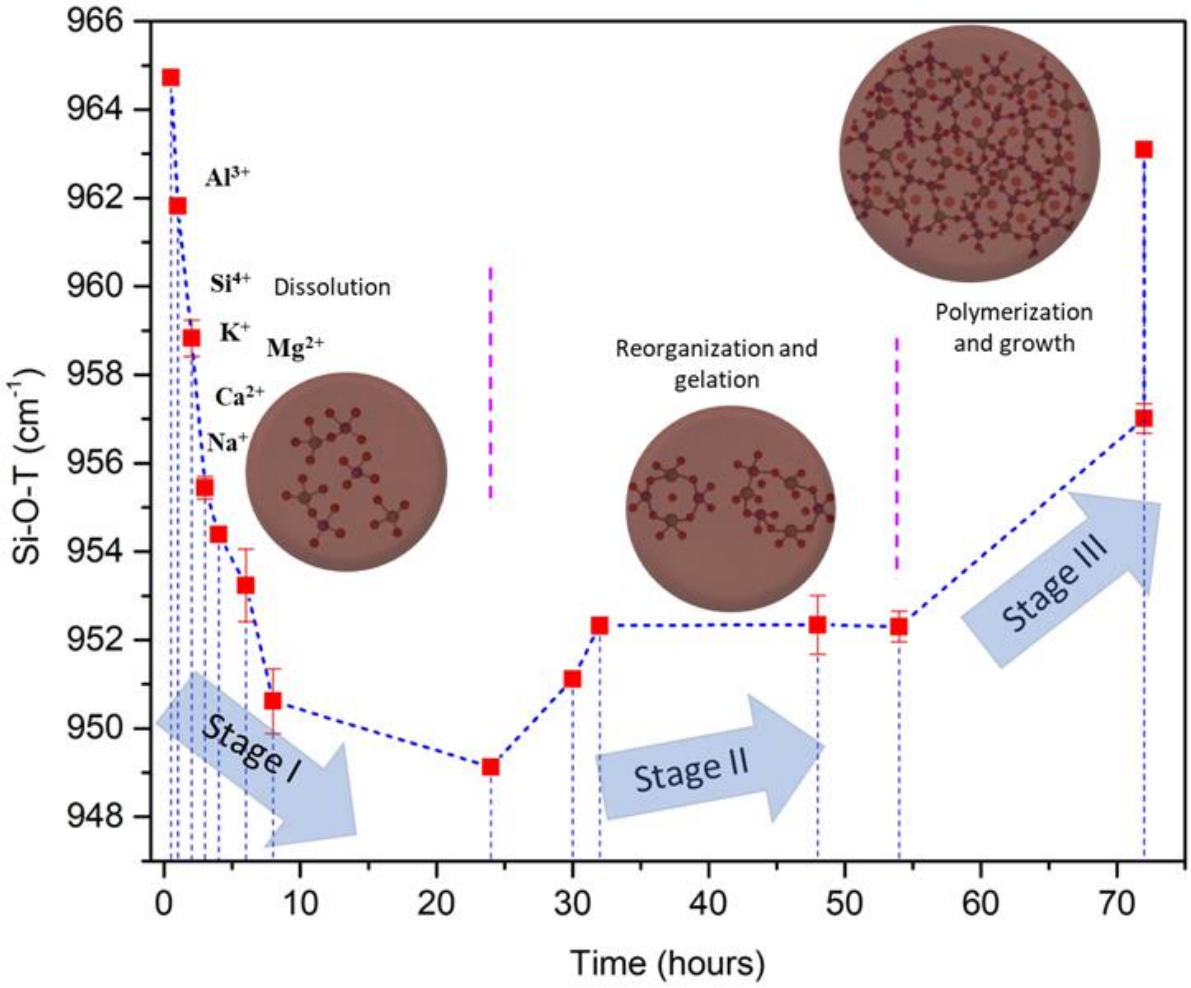


Figure 4-18: Time dependent shift of the Si-O-T bond asymetric streching band in NASH gel of the caclined CRM geopolymer. The geopolymeric behavior of the calcined CRM geopolymer is consistent with the conceptual model of geopolymerization, showing the three stages of reaction. The shift in the Si-O-T band after 30 min of reaction was high, confirming a high dissolution rate and hence a high reactivity which is consitient with other results mentioned above.

4.3.3.2 Alkali activation of calcined marlstone (Low and high silicate systems, 100 ^{o}C)

4.3.3.2.1 Chemical composition

Chemical composition based on the XRF analysis is shown in Table (4-1). Generally, there is a decrease in the concentration of Al, K, Ca, Fe, Na and Mg in MR-2 compared to the MR-1, while Si is higher in the MR-2 geopolymer. The decrease in these elements may be attributed to their incorporation in the geopolymer structure, reflecting different degrees of substitutions within the geopolymer matrix composition.[53] While the increase in SiO_2 is attributed to the high silicate amount introduced into the system from the alkaline solution.

4.3.3.2.2 Mineralogy (PXRD)

The XRD patterns of the geopolymer are depicted in Figure (4-19). An amorphous hump appeared between 22 and 39^{0} (2θ), which is a characteristic feature of the geopolymer structure.[54, 55] In both samples, a new hydration products formed including calcium silicate hydrate (C-S-H), gismondine [$CaAl_2Si_2O_8.4(H_2O)$] and chantalite [$CaAl_2SiO_4$ $(OH)_4$]. The coexistence of C-S-H gel and the geopolymeric gel is common in case of the Ca–bearing systems.[56] Quartz and feldspar are inactive, while the dehydroxylated illite and mica partly reacted. The hematite peaks diminished for the relatively higher silica system (MR-2), confirming the partial dissolution of hematite and the incorporation of Fe during the alkali activation. In contrast, the hematite pattern at the lower silica content showed an inactive aspect. It is evident that the periclase peaks disappeared in both systems while lime reacted partly in the low silica system and completely in the higher silica system. The appearance of calcite at lower silica content indicated the occurrence of a carbonation process, which was reduced in the case of a higher silica content. The shift in the position of the main quartz peak is due to the change in the amorphous hump position, which subsequently reflected the variation in the composition of the formed geopolymer gel [N-A (F)-S-H]. Moreover, the remarkable increase in the intensity of quartz peak and the decrease in C-S-H and calcite peaks in MR-2 compared to the MR-1 suggests that the geopolymer gel is the dominant product and C-S-H is a secondary hydration phase. This behaviour has previously been observed in the presence of a high concentration of NaOH (10 M).[56] Preferentially, the dissolved silicate species will react with the dissolved reactive Ca^{2+} rather than undergoing a polymerization reaction with the dissolved aluminate species. Formation of calcite was favoured due to the high dissolution rate of Ca^{2+} compared to Al^{3+} or Si^{4+}.[57] This fact indicated a reduction in the extent of the geopolymerization reaction.

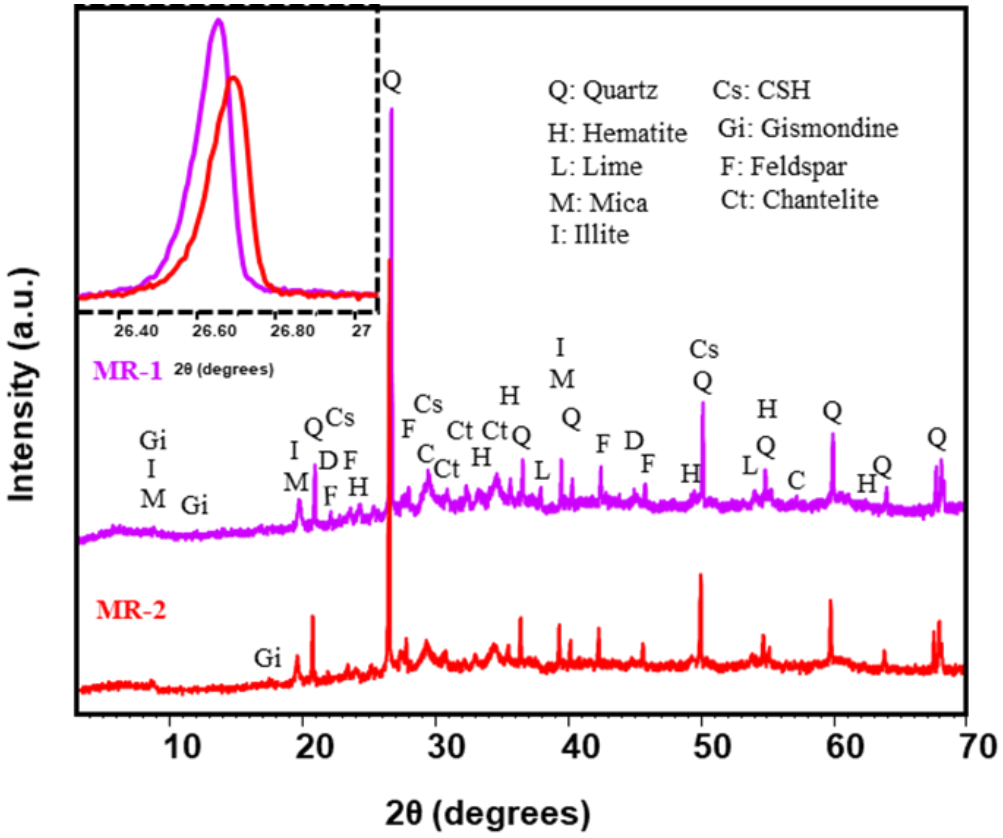


Figure 4-19: XRD analysis for the produced geopolymers, MR-1 and MR-2. Notice the development of the amorphous hump in the range between 20 and 40 (°2θ), confirming the formation of amorphous geopolymer gel. The difference in the silicate content of both samples resulted in a change in the position of the amorphous hump and the quartz peak, indicating a change in the molecular chemical environment. There is a reduction in the hematite and calcite peaks of sample MR-2, reflecting an increase in the incorporation of Fe in the formation of amorphous geopolymer gel in addition to a lower degree of carbonation in comparison with the MR-1 sample.

4.3.3.2.3 FT-IR

The FTIR spectra of the geopolymer samples are depicted in Figure (4-20). The main Si-O-T (T = Al, Fe or Si) band shifted to 960 cm^{-1} and 964 cm^{-1} for MR-1 and MR-2, respectively. Generally, this shift from a high wavenumber in the calcined CRM (988 cm^{-1}) to a low wavenumber in geopolymer elucidated the incorporation of Al, which substitutes for Si in the aluminosilicate framework. The formation of a successful geopolymerization occurs in the shift range of the Si-O-T band between 950-995 cm^{-1}.[58] However, the high value of this band at the MR-2 indicated a well–developed structure where more Si-O-Si bonds formed in the

geopolymer skeleton due to the high silicate content, reflecting an increase in the network connectivity of the formed geopolymer gel.[59] Therefore, the shift in MR-2 indicated a high degree of geopolymerization compared to the MR-1 geopolymer.[60]

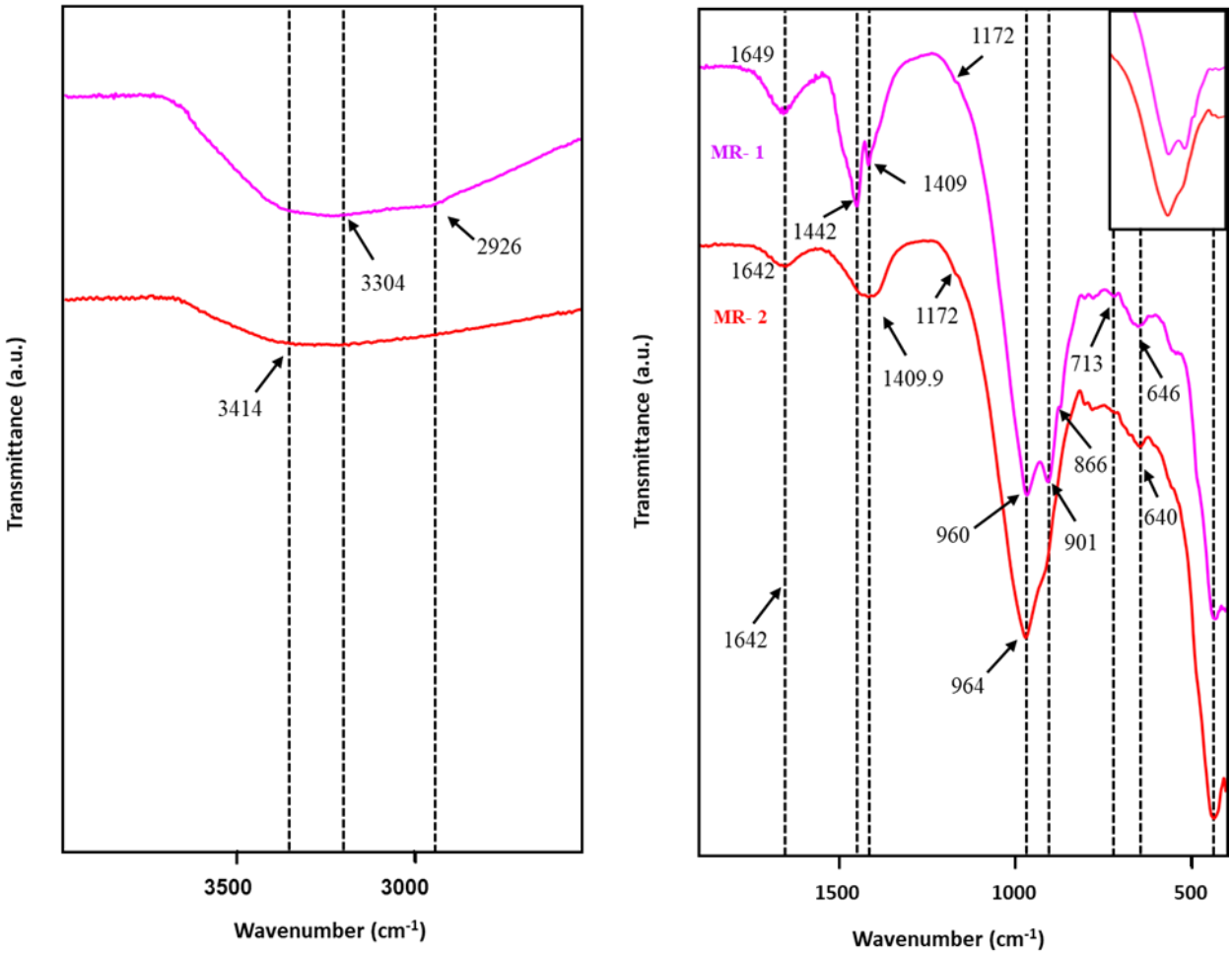


Figure 4-20: FTIR spectra of the formulated geopolymers, MR-1 and MR-2. As indicated, there is an increase in carbonation degree in MR-1 compared to MR-2 where calcite bands appeared at 866 and 1442 cm^{-1}. The increase in the intensity of H-O-H band of MR-1 indicated the increase of hygroscopicity level. The MR-2 geopolymer is well-developed compared to the MR-1 geopolymer where the main Si-O-T bands reached 964 and 960 cm^{-1} for the MR-2 and MR-1, respectively.

The appearance of the band at 901 cm^{-1} is attributed to silicate vibration in the alkali activator, indicating an incomplete reaction. The position of the Si-O-T band in MR-1 (960 cm^{-1}) and in MR-2 (964 cm^{-1}) is more typical for the C-A-S-H and N-A-S-H gels, respectively.[61-64] The appearance of absorption bands at 713 cm^{-1}, 866 cm^{-1}, 1409 cm^{-1} and 1442 cm^{-1} is attributed to the carbonate vibrations, indexing a high degree of carbonation, where the absorption band at

713 cm^{-1} is ascribed to calcite. The absorption bands at 1409 cm^{-1} and 1442 cm^{-1} are associated with calcite and thernadite (Na_2CO_3).[65] A distinctive doublet in the carbonate group (1409-1442 cm^{-1}) appeared in the MR-1 geopolymer. The appearance of such a doublet is due to the distortion in the carbonate group which is mainly controlled by the nature of metal ion (Ca^{2+}, Mg^{2+} and Na^{+}) linked to the CO_3^{2-}.[66] The high degree of distortion in the carbonate group of MR-1 indicted that the local environment of CO_3^{2-} is attributed to the Ca-carbonate ion complex.[66] In contrast, the degree of distortion is low in the MR-2 geopolymer, confirming that the local environment of CO_3^{2-} is only attributed to Na^{+} ion (Na_2CO_3). The absorption bands at 1649, 1642 and at 3304, 2926 and 3414 cm^{-1} are assigned to the stretching vibration of OH and H-O-H bending modes of the water molecules.[67] The appearance of bending and stretching vibrations of the OH group indicated that the water molecules reorganized and incorporated into the geopolymer network.[60] Usually, the amount of water trapped in the well-developed geopolymer is small.[67] The presence of silicate, calcite, and the high intensity (hygroscopicity) of water band in the MR-1 indicated a lower degree of reaction compared to the MR-2 geopolymer, and the formation of a geopolymer gel during the alkali activation was limited. The absorption area between 600 and 800 cm^{-1} differentiated into small vibrational bands as a response to the new formed alumino-silicate bonds (Al-O-Si and Si-O-Si vibrations). This differentiation is clearer for the MR-2 geopolymer.

4.3.3.2.4 SEM - EDX

The SEM images showing the morphological features of geopolymers are given in Figure (4-21&22). The low silica system showed various morphological features. The appearance of stretched and aligned pores, which were formed due to the air bubbles escaping, reflected the incomplete immiscibility between the alkali activator and calcined CRM particles during mixing. The presence of fibrous morphologies may be attributed to the presence of unreacted dehydroxylated illite. Some cracks clearly appeared in the MR-1geopolymer; usually the presence of cracking in the geopolymer matrix is attributed to the abrupt loss of water during the curing process.[60] However, the appearance of a triple junction cracking is probably due to the crystal growth of the new components such as, but not limited to, calcite and zeolites. Other studies have revealed that the appearance of cracking in the geopolymer matrix can be attributed to the volume changes due to the formation of a C-S-H gel of amorphous to semi-crystalline nature.[56] The formation of calcite is a defect point in addition to acting as a barrier between the precursor particles and the alkaline activator. The growth of calcite crystals was

extensive for the low silica system, which is consistent with the XRD, and FTIR data. This is attributed to the presence of a high proportion of a reactive Ca ions and insufficient silicates.

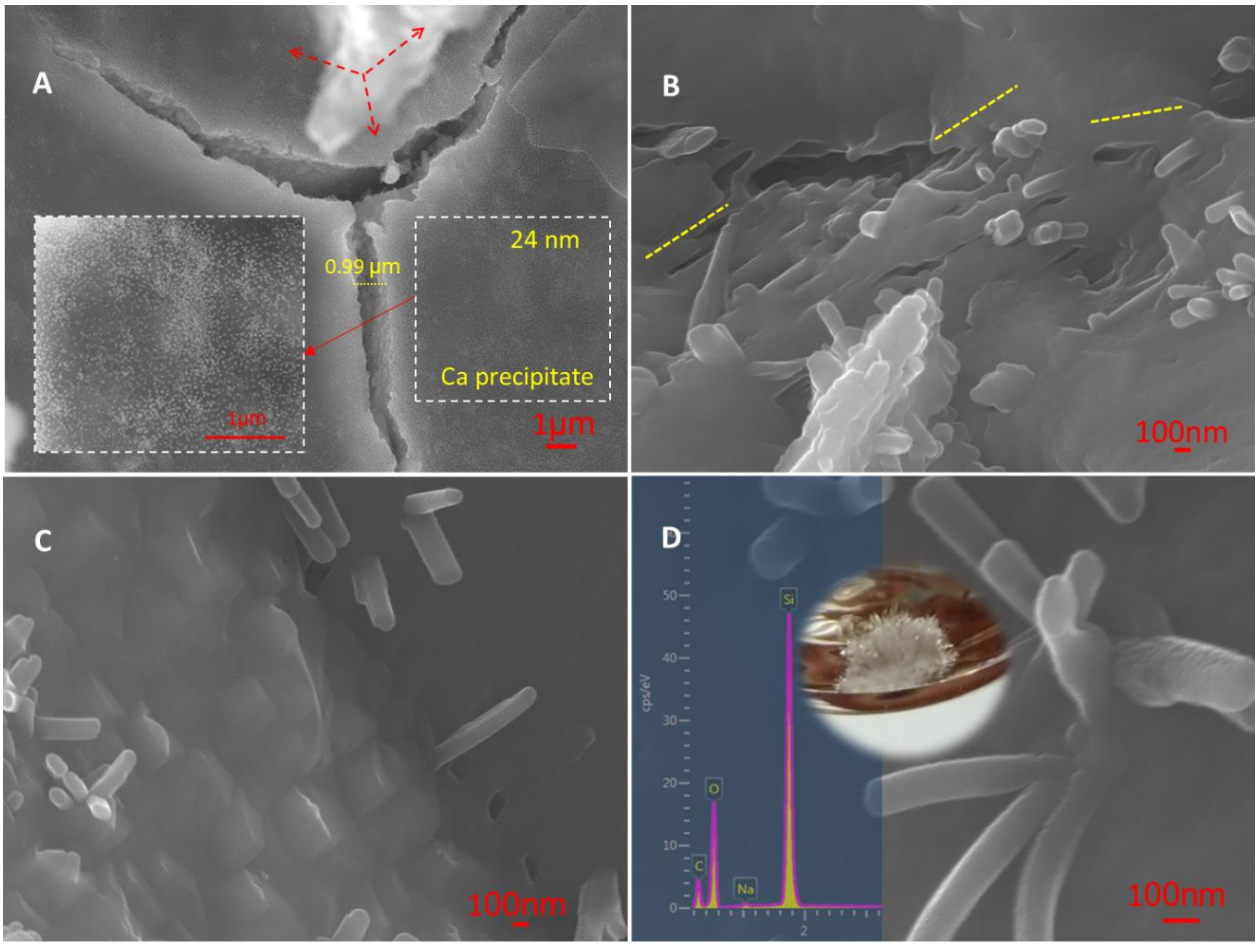


Figure 4-21: SEM micrographs of the MR-1 geopolymer. A) shows the presence of a triple junction microcrack and precipitated nanosized Ca due to the presence of insufficient silicate; B) Stretched pores and partially reacted phase, mostly dehydroxylated illite, appeared withing the geopolymer matrix ; C) Calcite crystals grown within the matrix, confirming a high degree of carbonation; and D) Unreacted crystalized finger-like silicate phases appeared within the geopolymer matrix, the purity of the corresponding EDX spectrum confirmed that the silicate phase originated from the alkali activation not from the used precursor. The crystallization of silicates was remarkable in the alkaline activator (a mixture of sodium silicates and sodium hydroxide) after 48 hours of preparation, notice the corresponding image.

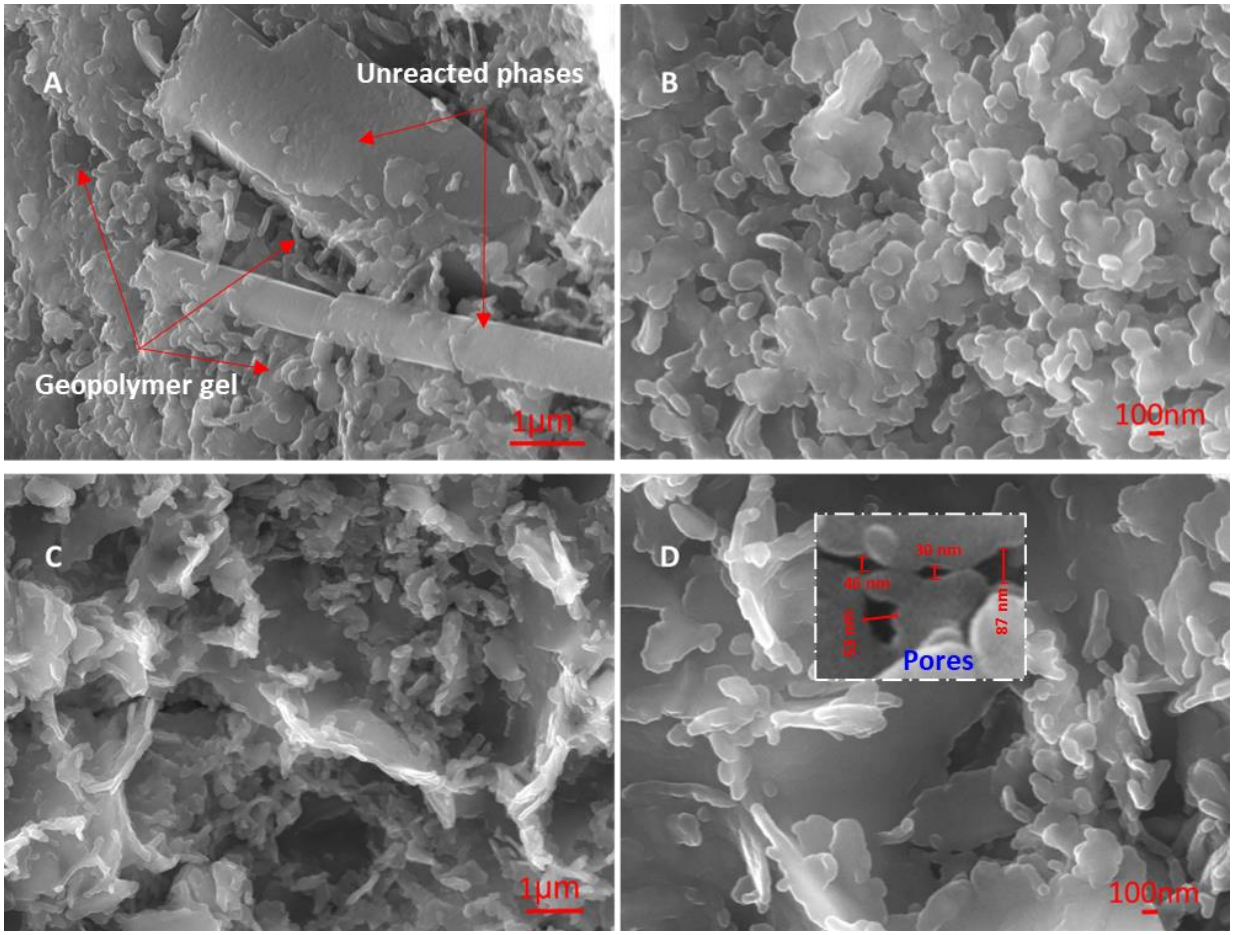


Figure 4-22: SEM micrographs of the MR-2 geopolymer. A) Unreacted phases bridged by the grown geopolymer gel, improving the mechanical strength of geopolymer; B) Homogeneous geopolymer gel matrix; C) and D) Inhomogeneous matrix showing two phases of geopolymer gels, reflecting the change in their chemistry. The MR-2 geopolymer did not show any crystalized carbonate-bearing phase (e.g., calcite).

The absence of calcite in MR-2 is consistent with the XRD patterns, and the appearance of the carbonate band in the FTIR of the MR-2 geopolymer is mostly attributed to the carbonation effect during the FTIR analysis. In addition, a small nano-sized calcium precipitates are disseminated throughout the geopolymeric matrix. The presence of the unreacted particles is prevalent, especially the unreacted silicates. The purity of silicate composition (according to EDS) indicated that they are probably inherited from the alkali activator rather than the precursor. However, it is interesting that to note the crystallization of silicate into a finger-like particle morphology. The formation of crystalized silicate phase in the alkaline solution after 48 hours of preparation is consistent with the precipitation of silicate due to the increase in carbonation and the decrease in the degree of geopolymerization. Growth in the geopolymer gel bridges the gaps between the unreacted phases meaning that the geopolymer gel is extended

thus giving a more homogenous matrix with nanosized pores. It is worth noting that geopolymerization is a surface process that occurs on the surface of the aluminosilicate grains.[68] With increase in the silicate content, a more geopolymer gel was formed interlocking the spaces between the CRM particles; this not only improves the mechanical properties but also increases the area occupied by the newly formed geopolymer gels. In contrast, for the high silicate system, the presence of unreacted phases is limited and a porous geopolymer gel is formed linking the unreacted phases. The elemental composition of the MR-1 and MR-2 is given in Table (4-2) and Figure (4-23&24). The reaction products in MR-1 had an elemental ratio of Si/Al = 2-2.7, Na/Al = 0.65-0.94, Ca/Si = 0.06-0.13, Na/Si = 0.24-0.49, Fe/Al = 0.7-1.3 and Fe/Si = 0.27-0.47. This variation in composition indicated the possibility of an intermixed microstructure of N-A-S-H, (Ca, Na, Mg)-A-S-H and C-S-H phases.

Table 4-2: Elemental composition for selected points in the MR-1 and MR-2 geopolymers.

Geop	Na	Mg	Al	Si	K	Ca	Ti	Fe
MR-1	7.8	6.4	8.3	22.7	4.7	3.1	0.54	6.2
	5.8	5.9	8.9	23.6	6.0	2.4	0.32	11.2
	9.0	5.2	9.1	18.2	3.1	1.2	0.33	8.2
MR-2	4.7	5.4	6.5	21.3	3.8	6.4	0.35	9.5
	3.4	3.2	7.0	19.6	6.9	3.3	0.0	16.7
	3.6	2.8	5.9	15	5.2	2.7	0.56	27.9
Calculated ratios based on the EDX analysis								
Geop/Ratio	**Fe/Al**	**Si/Al**	**Na/Al**	**Na/Si**	**Ca/Si**	**Fe/Si**	**K/Al**	**Ca/Al**
MR-1	0.7	2.7	0.94	0.34	0.13	0.27	0.56	0.37
	1.3	2.6	0.65	0.24	0.10	0.47	0.67	0.26
	0.9	2.0	0.99	0.49	0.06	0.45	0.34	0.13
MR-2	1.5	3.2	0.72	0.22	0.3	0.44	0.58	0.98
	2.4	2.8	0.49	0.17	0.16	0.85	0.98	0.47
	4.7	2.5	0.61	0.24	0.18	1.86	0.88	0.45

The reaction products also included potassium (3.1-6.0), titanium (0.32-0.54), iron (6.2-11.2) and magnesium (5.2-6.4), which were derived from the CRM particles. This sample has a suitable Na/Al ratio (0.94-0.99) which is close to the reported ratio of 1.0 for the aluminosilicate gel; this means that sodium ions were sufficient in balancing the negative charge in the geopolymer framework. However, some reaction products have a Na/Al ratio <1.0. The low calcium content in the reaction products reflected the consumption of reactive Ca ions in the formation of calcite. The Na/Si in some locations equal to 0.49 (average 0.35), which is near to the optimum ratio (0.5) reported for the NASH gel formation.[69] The Si/Al ratio in MR-1 (average 2.43) is slightly lower than the MR-2 (average 2.83), which corroborates the shift in

the FTIR bands to a slightly higher values and the change in the position of amorphous hump in the XRD patterns. The low Ca/Si ratios (<0.8) in both samples suggest the low likelihood of CSH gel formation gel; usually the Ca/Si ratio in C-S-H gel is (0.8-1.1).[70-74] The reaction products include the formation of C-S-H in the case of the initially Ca-rich system. As a result, the possibility of finding C-S-H in the formed geopolymer is low, which is not consistent with the XRD patterns that suggested the presence of a C-S-H gel. It is therefore clear that a full understanding of the mechanism and processes controlling the geopolymer formation remain an elusive challenge.[75]

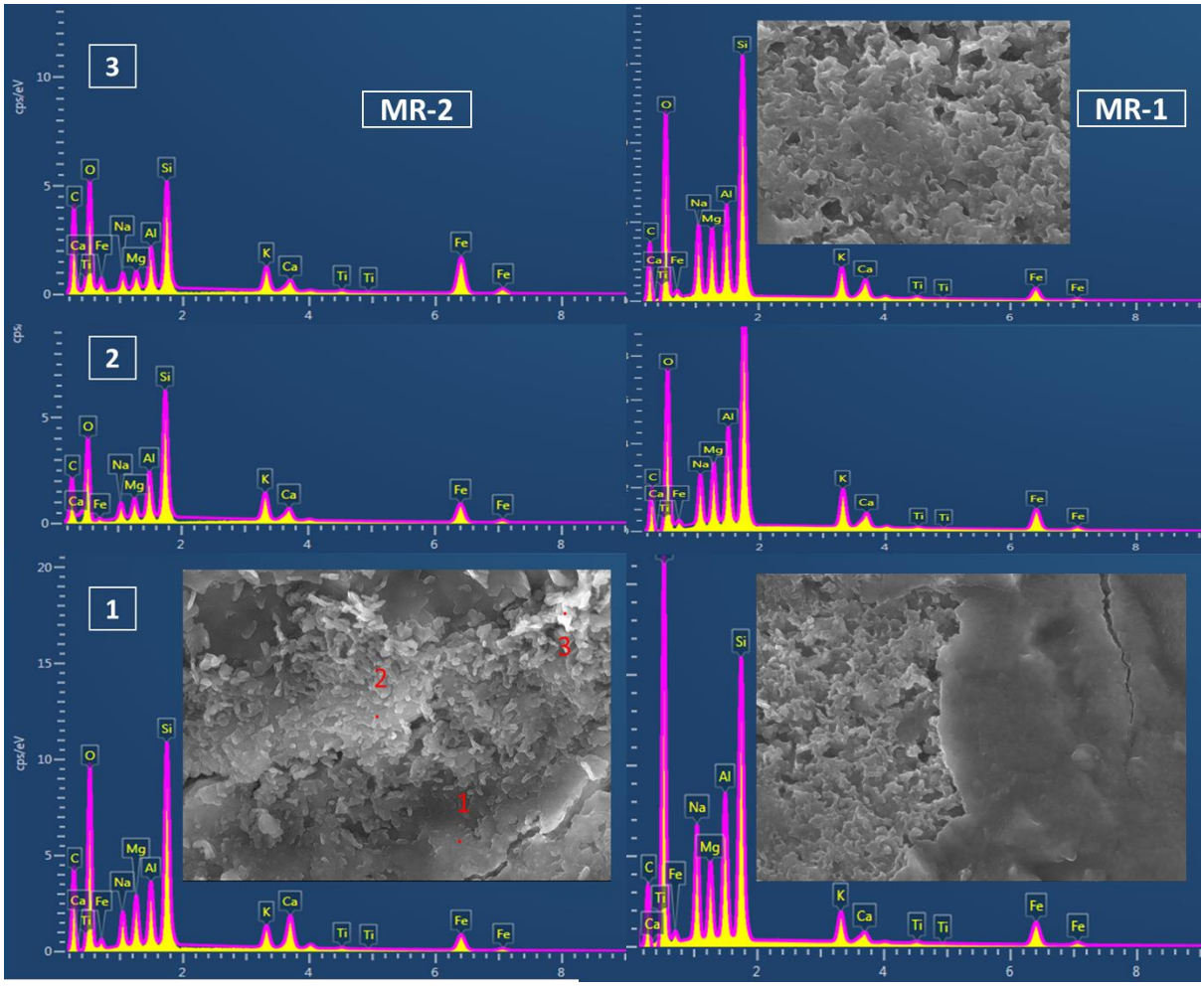


Figure 4-23: The EDX spectrum and associated SEM images for the MR-1 and MR-2 geopolymers. The analysis revealed the incorporation of Na in the structure of the MR-1 and MR-2 geopolymers; there is a variation in the chemical composition indicated various degrees of substitution between the reactive components. The change in the Fe signature is clearer in the case of the MR-2 geopolymers compared to the MR-1.

The reaction products in the MR-2 had an elemental ratio of Si/Al= 2.5–3.2, Na/Al= 0.49–0.72, Ca/Si= 0.16–0.3, Na/Si = 0.17–0.24, Fe/Al = 1.5–4.7 and Fe/Si = 0.44–1.86. The elemental analysis indicated a variation in the chemical composition of the formed reaction products with an intermixed microstructure similar to the MR-1 geopolymer. However, the Na/Al ratio (0.49-0.72), which is <1 indicated that the sodium ions are not sufficient for balancing the negative charge in the geopolymer framework. The reaction products had a high Fe/Al ratio of 1.5–4.7, and Fe/Si = 0.44–1.86, indicating the incorporation of Fe in the geopolymer framework substituting Al to varying extents. The Al/Ca ratio in the MR-1 was between 0.13-0.37, indicating the formation of a gel (N-A-S-H) of a low Ca and high Al. This is consistent with the FTIR, XRD and SEM analyses regarding the consumption of the reactive Ca in the formation of calcite. Conversely, the MR-2 had a higher Al/Ca ratio (0.45-0.98), indicating the presence of a suitable amount of Ca and Al forming the C-A-S-H gel. Figure (4-23) shows the ternary diagram of Al_2O_3, CaO and SiO_2. As shown, the MR-1 and MR-2 have a C-(N)-A-S-H gel with a high contribution from the Na ions in balancing the negative charge. However, for the MR-2, a more contribution from the Ca ions was obvious in some instances, confirming the heterogeneity of the formed geopolymer gel. It is known that the Ca and Na can be ionically exchanged in the geopolymer system forming a (C, N)-A-S-H gel.[76]

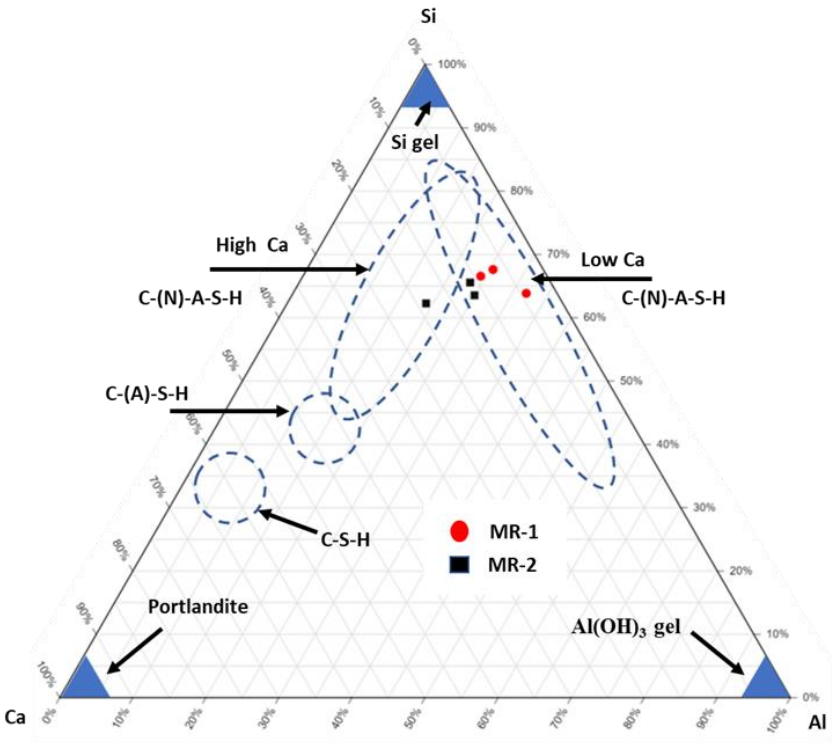


Figure 4-24: Ternary diagram of Si, Ca and Al showing the possible chemical composition of geopolymer gel of MR-1 and MR-2.

4.3.3.2.5 Mössbauer spectroscopy (Transformation of Fe species)

The Mössbauer hyperfine parameters of the three samples are presented in Table (4-3). The Mössbauer spectra of the raw CRM, calcined CRM, and the MR-2 geopolymer are depicted in Figure (4-25). The Mössbauer spectrum of the raw CRM showed the presence of two distinctive doublets containing an inconsistent isomer shifts and a quadrupole splitting. One of these doublets corresponds to Fe^{3+} (Qs = 0.57 mm/s and IS = 0.36 mm/s). The low value of isomer shift is a feature of the octahedral Fe in clay minerals and/or muscovite, but a contribution from the tetrahedral iron cannot be ruled out.[77] The other doublet (Qs = 2.58 mm/s and IS = 1.16 mm/s) is attributed to the Fe that is mostly associated with the octahedral Fe^{2+} on the surface of mica (muscovite). Correlating the hyperfine parameters of this doublet with the Mössbauer parameters for the structural Fe in mica (muscovite) mineral, confirms that the Fe^{2+} populations are accommodated in *cis* octahedral sites.[77-79] In addition, the Mössbauer spectra were well-fitted with a sextet having an isomer shift of 0.38 mm/s and a quadrupole splitting of -0.110 mm/s, which is mostly associated with hematite.[77, 80] The presence of hematite was confirmed on the XRD, mineral chemistry analysis and the FTIR, confirming that it is the only crystalized iron-bearing phase.

Table 4-3: Hyperfine parameters obtained from fitting of Mössbauer spectra.

Parameters	**Sextet1**				**Doublet1 Fe (III)**				**Doublet2 Fe (II)**			
Material	**IS** (mm/s)	**QS** (mm/s)	**BHT** (T)	**RA** (%)	**IS** (mm/s)	**QS** (mm/s)	**LW** (mm/s)	**RA** (%)	**IS** (mm/s)	**QS** (mm/s)	**LW** (mm/s)	**RA** (%)
Raw CRM	0.383	-0.110	50.60	37.7	0.369	0.574	0.360	39.5	1.165	2.585	0.239	22.8
CRM-800	0.361	-0.105	50.68	38.6	0.377	1.197	0.461	61.4	-	-	-	-
MR-2	0.368	-0.112	50.79	36.8	0.370	1.294	0.405	63.2	-	-	-	-
IS = Isomer shift, QS = quadrupole splitting, BHT = magnetic field, LW= line width, RA= relative spectral area												

After thermal activation the central doublet (IS = 0.37 mm/s and QS = 1.197 mm/s) and the sextet (IS = 0.36 mm/s and Qs = -0.105 mm/s) remain. The absence of doublet 2 revealed the transformation of the octahedral Fe^{2+} into the octahedral Fe^{3+} species. This transformation was concurrent with a modification in the magnetically split sextet of hematite, where the quantity of hematite increased. The relative area of the coordinated Fe^{3+} in the raw CRM increased after thermal activation at 800 ^{0}C and was accompanied by an increase in the relative area of the sextet (hematite). This behaviour is consistent with the XRD patterns, which indicated that hematite is the only Fe-bearing phase and its peak intensity increased at 800 ^{0}C. After geopolymerization of the calcined CRM, a decrease in the hematite quantity confirmed the transformation of Fe in Fe_2O_3 to the structural Fe^{3+}. Moreover, the decrease in the relative area

of sextet from 38.6 to 36.8 was accompanied by an increase in the doublet's spectral area from 61.4 to 63.2 due to the alkali activation of the calcined CRM. This reflected the increase of Fe^{3+} in the octahedral sites substituting Al^{3+} in the geopolymer framework. The change in the ratio R proved the transformation of Fe species. The ratio R for the CRM, calcined CRM, and the MR-2 geopolymer was estimated to identify the relative amount of iron-bearing phases. The calculations showed that R = 1.04 for the raw CRM, R = 1.59 for calcined CRM and R = 1.71 for the MR-2 geopolymer. There is, therefore, an increase in the R values from the raw to calcined phase, and a further increase in the formed geopolymer. The wide linewidth of 0.40 mm/s in geopolymer suggest that the Fe^{3+} occurs in a heterogenous sites.[81] However, the contribution of iron during geopolymerization is controlled by its chemical and mineralogical state in the precursor.

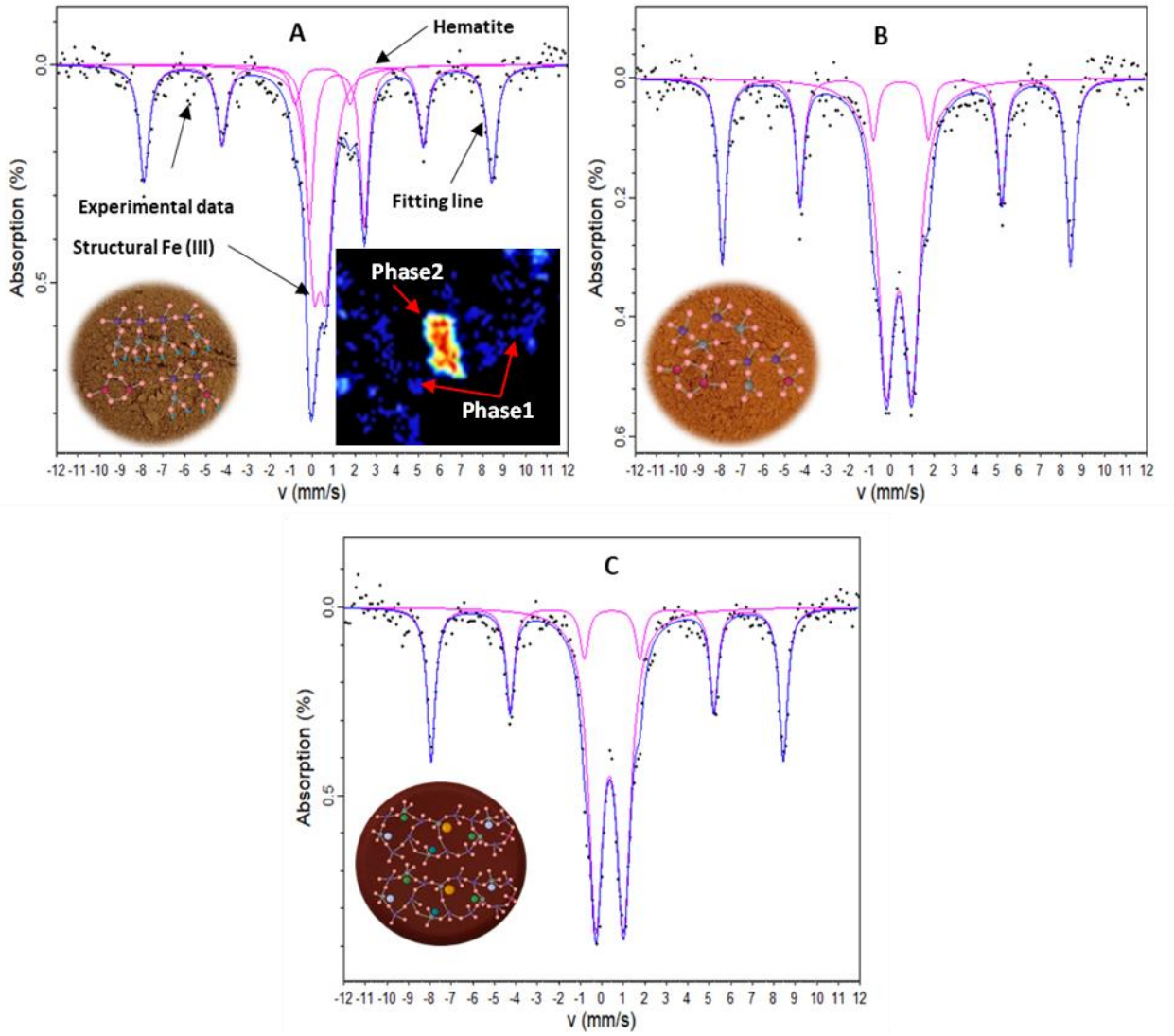


Figure 4-25: Mössbauer spectra: A) Raw CRM, B) Calcined CRM at 800 ºC, C) MR-2 geopolymer. EBSE image, Phase1) shows the structural Fe in clay and micaceous minerals,

Phase2) shows the crystalized Fe-bearing phase (hematite).Notice the change in the colour of samples at different conditions (raw material, thermally activated phase, and geopolymer).

4.4 Conclusion

The chemical composition of the raw CRM reflected its suitability to undergo an alkali activation reaction. The mineralogical composition indicated that the clay minerals were the dominant mineral phase in the rock, in addition to, the presence of other carbonate-bearing phases, including calcite and dolomite. Thermal activation behaviour of the CRM showed a modification in its forming minerals where the dehydroxylation and decarbonation was the predominant processes from 500 to 800 °C, while the recrystallization was the prevalent process between 800 and 900 °C. The leaching test revealed that the release of Si and Al species increased with increasing temperature from 500 to 800 °C then decreased at 900 °C, confirming the occurrence of the dehydroxylation, decarbonation and recrystallization processes. Moreover, the change in the physicochemical characteristics of the thermally activated phase at different temperature was remarkable. The alkali activation affinity of the calcined CRM was consistent with the conceptual model of geopolymerization where the presence of three stages of gel evolution were documented (dissolution, reorganization and gelation, and polymerization). The geopolymerization of the CRM in the presence of insufficient soluble silicate promoted the formation of calcite (mineralized carbonate). The degree of carbonation in the formed geopolymer was high, in addition to the predominance of unreacted phases and microcracks. On the contrary, the geopolymerization of the CRM in the presence of the sufficient soluble silicate improved the formation of a well-connected and extended geopolymer gels and reduced the formation of calcite. The formation of geopolymer gel was accompanied by the formation of CSH and other crystalized phases such as zeolites. The elemental analysis indicated the formation of a geopolymer gel with an intermixed composition, including (C, N)-A-S-H, and (C, N)-A(F)-S-H geopolymer gels. The contribution of Fe in the geopolymerization was evaluated through the change in the Mossbauer characteristics of the Fe environment. After thermal activation the structural Fe^{2+} transformed into Fe^{3+}, this transformation was accompanied by the increase in the area percentage of doublet and sextet and the disappearance of the characteristic doublet of Fe^{2+} phase. After geopolymerization, the change in the Fe environment was confirmed through the degrease in the area percentage of sextet and the increase in area percentage of doublet, indicating the formation of a ferro-aluminosilicate geopolymer.

Therefore, the alkali activation of the calcined CRM in the presence of a moderate amount of soluble silicate is necessary to prevent the occurrence of carbonation and to reduce the presence of unreacted phases.

4.5 References

1. M. Amran, S. Debbarma and T. Ozbakkaloglu, *Construction and Building Materials*, 2021, **270**, 121857.
2. P. Gupta, G. Nagpal and N. Gupta, *Beni-Suef University Journal of Basic and Applied Sciences*, 2021, **10**, 89.
3. M. Łach, K. Korniejenko and J. Mikuła, *Procedia Engineering*, 2016, **151**, 410-416.
4. K. M. Klima, K. Schollbach, H. J. H. Brouwers and Q. Yu, *Construction and Building Materials*, 2022, **323**, 126529.
5. X. Chen, Y. Guo, S. Ding, H. Zhang, F. Xia, J. Wang and M. Zhou, *Journal of Cleaner Production*, 2019, **207**, 789-800.
6. I. C. Ferreira, R. Galéry, A. B. Henriques, A. Paula de Carvalho Teixeira, C. D. Prates, A. S. Lima and I. R. Souza Filho, *Journal of Materials Research and Technology*, 2022, **18**, 4194-4200.
7. I. Kara, D. Tunc, F. Sayin and S. T. Akar, *Applied Clay Science*, 2018, **161**, 184-193.
8. P. Duan, L. Song, C. Yan, D. Ren and Z. Li, *Ceramics International*, 2017, **43**, 5115-5120.
9. X. Peng, H. Li, Q. Shuai and L. Wang, *Materials (Basel)*, 2020, **13**.
10. K. J. D. MacKenzie, S. Komphanchai and R. Vagana, *Journal of the European Ceramic Society*, 2008, **28**, 177-181.
11. P. Duxson, A. Fernández-Jiménez, J. L. Provis, G. C. Lukey, A. Palomo and J. S. J. van Deventer, *Journal of Materials Science*, 2007, **42**, 2917-2933.
12. G. El-Habaak, M. Askalany and M. Abdel-Hakeem, *Applied Clay Science*, 2018, **162**, 90-100.
13. N. R. Rakhimova, R. Z. Rakhimov, V. P. Morozov, A. R. Gaifullin, L. I. Potapova, A. M. Gubaidullina and Y. N. Osin, *Journal of Non-Crystalline Solids*, 2018, **492**, 1-10.
14. I. Tole, K. Habermehl-Cwirzen and A. Cwirzen, *Mineralogy and Petrology*, 2019, **113**, 449-462.

15. H. Wang, C. Li, Z. Peng and S. Zhang, *Journal of Thermal Analysis and Calorimetry*, 2011, **105**, 157-160.

16. B. R. Ilić, A. A. Mitrović and L. R. Miličić, *Hemijska industrija*, 2010, **64**, 351-356.

17. K. S. P. Karunadasa, C. H. Manoratne, H. M. T. G. A. Pitawala and R. M. G. Rajapakse, *Journal of Physics and Chemistry of Solids*, 2019, **134**, 21-28.

18. M. Olszak-Humienik and M. Jablonski, *Journal of Thermal Analysis and Calorimetry*, 2015, **119**, 2239-2248.

19. J. M. N. Robert W. Gerlach, *Guidance for Obtaining Representative Laboratory Analytical Subsamples from Particulate Laboratory Samples* Lockheed Martin Environmental Services and U.S. Environmental Protection Agency, 2003.

20. T. Luukkonen, H. Runtti, M. Niskanen, E.-T. Tolonen, M. Sarkkinen, K. Kemppainen, J. Rämö and U. Lassi, *Journal of Environmental Management*, 2016, **166**, 579-588.

21. T. d. S. Rocha, D. P. Dias, F. C. C. França, R. R. d. S. Guerra and L. R. d. C. d. O. Marques, *Construction and Building Materials*, 2018, **178**, 453-461.

22. M. Górski, N. Wielgus, K. Loska, M. Kozioł, M. Landrat, W. Ścierski and K. Pikoń, *Polymers (Basel)*, 2021, **13**.

23. W. I. Khalil, Q. J. Frayyeh and H. T. Abed, *IOP Conference Series: Materials Science and Engineering*, 2019, **518**, 022056.

24. T. J. Medina, S. P. Arredondo, R. Corral, A. Jacobo, R. A. Zárraga, C. A. Rosas, F. G. Cabrera and J. M. Bernal, *Minerals*, 2020, **10**.

25. E. Sundhararasu, S. Tuomikoski, H. Runtti, T. Hu, T. Varila, T. Kangas and U. Lassi, *ChemEngineering*, 2021, **5**.

26. R. M. Kalombe, V. T. Ojumu, C. P. Eze, S. M. Nyale, J. Kevern and L. F. Petrik, *Materials*, 2020, **13**.

27. H. Ö. Öz, N. Doğan-Sağlamtimur, A. Bilgil, A. Tamer and K. Günaydin, *Materials*, 2021, **14**.

28. R. Bajpai, A. Shrivastava and M. Singh, *SN Applied Sciences*, 2020, **2**, 1846.

29. V. Ramasamy, P. Rajkumar and V. Ponnusamy, *Indian Journal of Physics*, 2009, **83**, 1295-1308.

30. M. Ostrooumov, *Geoarchaeology*, 2009, **24**, 619-637.

31. S. Alehyen, M. EL Achouri and M. Taib, *Journal of Materials and Environmental Sciences*, 2017, **8**, 1783-1796

32. C. N. Bewa, H. K. Tchakouté, C. H. Rüscher, E. Kamseu and C. Leonelli, *SN Applied Sciences*, 2019, **1**, 916.

33. R. M.-d. Gutiérrez, M. Villaquirán-Caicedo, S. Ramírez-Benavides, M. Astudillo and D. Mejía, *Coatings*, 2020, **10**, 157.

34. J. Ji, Y. Ge, W. Balsam, J. E. Damuth and J. Chen, *Marine Geology*, 2009, **258**, 60-68.

35. G. Jozanikohan and M. N. Abarghooei, *Journal of Petroleum Exploration and Production Technology*, 2022, DOI: 10.1007/s13202-021-01449-y.

36. E. Escalera, M. L. Antti and M. Odén, *IOP Conference Series: Materials Science and Engineering*, 2012, **31**, 012017.

37. H. Peng, J. Vaughan and J. Vogrin, *Applied Clay Science*, 2018, **157**, 189-197.

38. E. Murad and U. Wagner, *Clay Minerals*, 1996, **31**, 45-52.

39. I. Ben Messaoud, N. Hamdi and E. Srasra, *Advances in Materials Science and Engineering*, 2018, **2018**, 9392743.

40. J. Madejová, *Vibrational Spectroscopy*, 2003, **31**, 1-10.

41. W. K. W. Lee and J. S. J. Van Deventer, *Langmuir*, 2003, **19**, 8726-8734.

42. J. L. Rendon and C. J. Serna, *Clay Minerals*, 1981, **16**, 375-382.

43. Y. Hu, S. Liang, J. Yang, Y. Chen, N. Ye, Y. Ke, S. Tao, K. Xiao, J. Hu, H. Hou, W. Fan, S. Zhu, Y. Zhang and B. Xiao, *Construction and Building Materials*, 2019, **200**, 398-407.

44. S. Gunasekaran and G. Anbalagan, *Bulletin of Materials Science*, 2007, **30**, 339-344.

45. T. Danner, G. Norden and H. Justnes, *Applied Clay Science*, 2018, **162**, 391-402.

46. P. Chindaprasirt, T. Phoo-ngernkham, S. Hanjitsuwan, S. Horpibulsuk, A. Poowancum and B. Injorhor, *Case Studies in Construction Materials*, 2018, **9**, e00198.

47. H. A. Abdel-Gawwad, *Journal of Materials in Civil Engineering*, 2015, **27**, 04014236.

48. X. Y. Zhuang, L. Chen, S. Komarneni, C. H. Zhou, D. S. Tong, H. M. Yang, W. H. Yu and H. Wang, *Journal of Cleaner Production*, 2016, **125**, 253-267.

49. P. He, M. Wang, S. Fu, D. Jia, S. Yan, J. Yuan, J. Xu, P. Wang and Y. Zhou, *Ceramics International*, 2016, **42**, 14416-14422.

50. A. Fernández-Jiménez, A. Palomo, I. Sobrados and J. Sanz, *Microporous and Mesoporous Materials*, 2006, **91**, 111-119.

51. E. H. Oelkers and S. R. Gislason, *Geochimica et Cosmochimica Acta*, 2001, **65**, 3671-3681.

52. G. Kovalchuk, A. Fernández-Jiménez and A. Palomo, *Fuel*, 2007, **86**, 315-322.

53. H. Runtti, T. Luukkonen, M. Niskanen, S. Tuomikoski, T. Kangas, P. Tynjälä, E.-T. Tolonen, M. Sarkkinen, K. Kemppainen, J. Rämö and U. Lassi, *Journal of Hazardous Materials*, 2016, **317**, 373-384.

54. R. P. Williams, R. D. Hart and A. van Riessen, *Journal of the American Ceramic Society*, 2011, **94**, 2663-2670.

55. M. A. Longhi, B. Walkley, E. D. Rodríguez, A. P. Kirchheim, Z. Zhang and H. Wang, *Composites Part B: Engineering*, 2019, **176**, 107172.

56. C. K. Yip, G. C. Lukey and J. S. J. van Deventer, *Cement and Concrete Research*, 2005, **35**, 1688-1697.

57. S. Kumar, J. N. Yankwa Djobo, A. Kumar and S. Kumar, *Journal of Building Engineering*, 2016, **8**, 172-178.

58. J. Liu, Y. Fang and O. Kayali, Shenzhen University, Shenzhen, Guangdong Province, P.R.China, 2016.

59. C. A. Rees, J. L. Provis, G. C. Lukey and J. S. J. van Deventer, *Langmuir*, 2007, **23**, 8170-8179.

60. L. N. Tchadjié, J. N. Y. Djobo, N. Ranjbar, H. K. Tchakouté, B. B. D. Kenne, A. Elimbi and D. Njopwouo, *Ceramics International*, 2016, **42**, 3046-3055.

61. I. García Lodeiro, A. Fernández-Jimenez, A. Palomo and D. E. Macphee, *Cement and Concrete Research*, 2010, **40**, 27-32.

62. P. Yu, R. J. Kirkpatrick, B. Poe, P. F. McMillan and X. Cong, *Journal of the American Ceramic Society*, 1999, **82**, 742-748.

63. I. García-Lodeiro, A. Fernández-Jiménez, M. T. Blanco and A. Palomo, *Journal of Sol-Gel Science and Technology*, 2008, **45**, 63-72.

64. A. Fernández-Jiménez and A. Palomo, *Microporous and Mesoporous Materials*, 2005, **86**, 207-214.

65. C. Bobirică, C. Orbeci, L. Bobirică, P. Palade, C. Deleanu, C. M. Pantilimon, C. Pîrvu and I. C. Radu, *Sci Rep*, 2020, **10**, 19827.

66. G. Fine and E. Stolper, *Earth and Planetary Science Letters*, 1986, **76**, 263-278.

67. J. Liu, Y. Fang and O. Kayali, 2016.

68. A. Favier, G. Habert, J. B. d'Espinose de Lacaillerie and N. Roussel, *Cement and Concrete Research*, 2013, **48**, 9-16.

69. C. B. Cheah, L. E. Tan and M. Ramli, *Composites Part B: Engineering*, 2019, **160**, 558-572.

70. T. Bakharev, J. G. Sanjayan and Y. B. Cheng, *Cement and concrete research*, 1999, **29**, 1619-1625.

71. F. Puertas, A. Fernández-Jiménez and M. T. Blanco-Varela, *Cement and Concrete Research*, 2004, **34**, 139-148.

72. M. Palacios and F. Puertas, *Journal of the American Ceramic Society*, 2006, **89**, 3211-3221.

73. S. Aydın and B. Baradan, *Materials & design*, 2012, **35**, 374-383.

74. M. Chi, *Construction and Building Materials*, 2012, **35**, 240-245.

75. C. E. White, J. L. Provis, T. Proffen and J. S. J. van Deventer, *AIChE Journal*, 2012, **58**, 2241-2253.

76. I. García-Lodeiro, A. Fernández-Jiménez, A. Palomo and D. E. Macphee, *Journal of the American Ceramic Society*, 2010, **93**, 1934-1940.

77. O. Castelein, L. Aldon, J. Olivier-Fourcade, J. C. Jumas, J. P. Bonnet and P. Blanchart, *Journal of the European Ceramic Society*, 2002, **22**, 1767-1773.

78. A. A. T. Shabani, D. G. Rancourt and A. E. Lalonde, *Hyperfine Interactions*, 1998, **117**, 117-129.

79. W. Schmidt and C. Pietzsch, *Chem. Erde*, 1990, **50**, 27-38.

80. E. Murad, *Minerals Engineering*, 2005, **18**, 984-986.

81. R. L. Fletcher-Wood, C. Gorin, S. D. Forder, P. A. Bingham and J. A. Hriljac, *Hyperfine Interactions*, 2014, **226**, 499-508.

CHAPTER 5: SIMULTANEOUS SEQUESTRATION OF Cd^{2+}, Co^{2+}, Mn^{2+} AND Ni^{2+} FROM AQUEOUS SOLUTION

Abstract

The feasibility of using the CRM geopolymer in the simultaneous sequestration of Cd^{2+}, Co^{2+}, Mn^{2+}, and Ni^{2+} from an aqueous solution is the focus of this Chapter. In order to formulate a more connective and expanded geopolymer gel, the findings from Chapter 4 were taken into consideration when synthesizing the geopolymer adsorbents. The impact of pH, adsorbent mass, initial concentration, temperature, and contact time, on the metal ions removal, was assessed in batch mode. The adsorption behavior of the CRM geopolymer improved when the pH of the solution increased from 4 to 8 where the removal efficiency changed from 7.14, 12.5, 10.14, 17.1 to 45.6, 64.6, 61.6, 78.3 % for Mn^{2+}, Co^{2+}, Ni^{2+}, and Cd^{2+}, respectively. Moreover, the CRM geopolymer adsorbent showed an improved adsorption capacity with the increase in the initial concentration of the metal ions solution from 5 to 100 mg/L and reached up to 7.5, 14.6, 15.5, and 20.3 mg/g for Mn^{2+}, Co^{2+}, Ni^{2+}, and Cd^{2+}, respectively. The increase in the solution temperature induced an effective removal of Mn^{2+}, Co^{2+}, Ni^{2+}, and Cd^{2+} metal ions, reaching the maximum removal at 55 °C. Furthermore, the adsorption of metal ions was operated in an up-flow dynamic mode, ensuring the applicability in an industrial scale basis. The increase in the bed height from 4 to 9 cm increased the adsorption removal of Mn^{2+}, Co^{2+}, $Ni^{2+,}$ and Cd^{2+} from 61.5%, 72.2%, 70.8%, and 66.9% to 97.1%, 96.5%, 96.8%, and 96.9%, respectively. The geopolymer adsorbents demonstrated an improved adsorption removal in comparison to the raw material. Metal ion sequestration on the geopolymer surfaces is hypothesized to occur by the ion exchange, surface complexation, and electrostatic interaction mechanisms. The effectiveness of removing metal ions from the groundwater, a highly competitive system, has been examined. The results indicated that the CRM geopolymer was effective in the removal of metal ions from the KH sample (crystalline rocks zone) compared to LQ1(Nile Valley zone) and QH2 samples (Coastal zone). The geopolymer adsorbent showed a good recyclability and can be used for more than 8 cycles. The removal efficiency reduced from 94.04, 94.43, 92.60, and 95.30 for Mn^{2+}, Co^{2+}, Ni^{2+}, and Cd^{2+}, respectively to 51.4, 54.4, 52.3, and 56.2 % after 8 cycles. The statistical regression analysis showed that the data best fit with the Langmuir rather than Freundlich isotherm. Additionally, the interaction between the geopolymer adsorbent and metal ions could be described by the pseudo-second-order kinetic

model. Thermodynamics suggested an endothermic, spontaneous, and chemical adsorption mechanism.

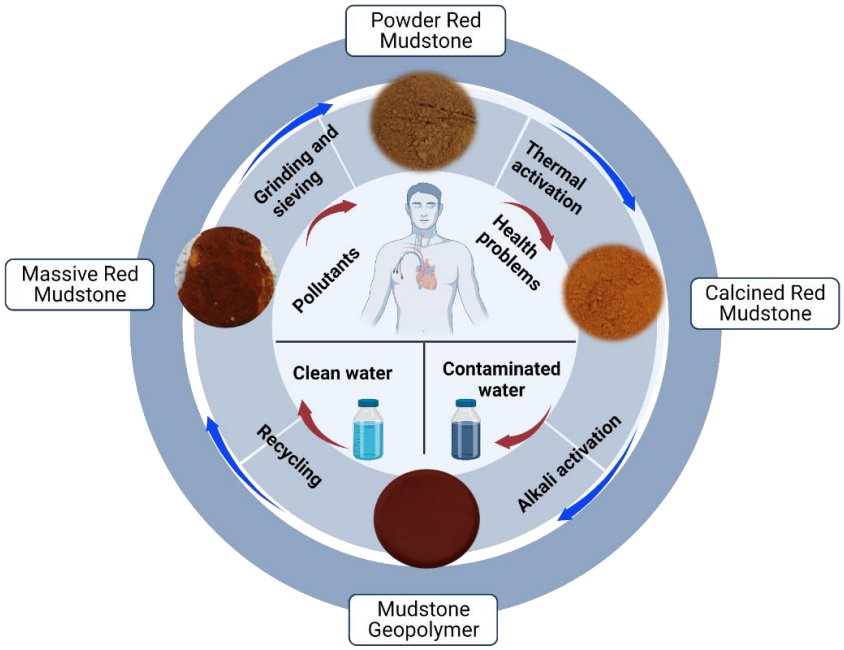


Figure 5-1: Geopolymerization of red mudstone for metal ions removal.

5.1 Introduction

In the past few years, the pace of economic growth around the world has increased; unfortunately, this is accompanied by a serious environmental degradation. Organic and inorganic contaminants in the water systems are mainly a consequence of industrial activities, which has led to a deteriorating water quality.[1] A significant proportion of the world's population has historically relied on the groundwater as a supply of water for their requirements, either for the agricultural, industrial, or human activities.[2] Groundwater quality is seriously threatened by the urbanization, agriculture, industry, and climate change; therefore, an immediate intervention is required. Heavy metals contamination is considered one of the most dangerous hazards to the environment system and living organisms.[3] Groundwater in arid regions is the main source of freshwater that can be used for the domestic, agricultural, and industrial purposes. Although the overuse of pesticides, fertilizers, and chemicals is one of the main causes of heavy metal contamination in groundwater, the heavy metals can also enter the groundwater naturally through the geogenic processes.[4] The co-existence of heavy metals contamination in the groundwater is prevalent, and its remediation is frequently challenging since the pollutant removal can be expensive and time-consuming.[5] Specific metals, such as

those found mostly in rock-forming minerals, Ni, Mn, Co, and Cd, may pollute the groundwater aquifers depending on the overall geology. Geopolymers, which are environmentally friendly materials, are hydrated aluminosilicates of the alkali metals (Ca, Mg, Na, K) having a porous amorphous to semi-crystalline structure and cavities.[6] The isomorphous substitution of Al^{3+} for Si^{4+} in geopolymer gives rise to a negative charge in their 3D framework. The negative charge is balanced by the exchangeable K^{+}, N^{+}, Ca^{2+} and Mg^{2+} cations that can be replaced by the metal ions (e.g., heavy metals) through an ion exchange process. Consequently, the geopolymers demonstrate a high level of efficiency in the removal of metal ions from wastewater.[7] However, the majority of investigations have so far covered their capacity to eliminate metal ions from a single system, and little is known about their efficiency in sequestrating metal ions from a multicomponent system. Moreover, the industrial by-products such as fly ash and blast furnace slag as well as the homogenous natural kaolinite were the most often employed precursors.[8-11] Little is known about the removal of metal ions, either from single or multi-component systems, using rock-based geopolymer adsorbents.

Here, a novel heterogeneous ferro-sialate geopolymer adsorbent was synthesized and evaluated for the simultaneous sequestration of Cd^{2+}, Mn^{2+}, Ni^{2+} and Mn^{2+} from an aqueous solution. Calcareous-red mudstone was chosen as a geopolymer precursor owing to its distinct mineral composition, chemical richness, and the widespread availability.

5.2 Materials and methods

5.2.1 Raw material preparation

The CRM, 10 kilograms of different sizes, was crushed to <5mm in size using Jaw Crusher, followed by a milling process for 5 minutes using Tema mill machine. The produced powder was further manually ground to get a more finer grain size. In order to get a representative and a homogeneous sample, the ground CRM was split manually using the quadrant method, followed by a sieving process to get a uniform grain size of 63 microns. The prepared powder was kept under vacuum and/or in an oven at 50 ºC until use.

5.2.2 Thermal activation

The raw CRM was thermally activated at 800 ºC with a heating rate of 5 ºC/min in a programmable box furnace (Carbolite) for 1 hour in static air. All the heated samples were kept in air-free and tightly closed desiccators and/or containers until use.

5.2.3 Geopolymer adsorbent synthesis

Three geopolymers of different compositions were synthesized by mixing the calcined CRM with the alkaline activator as indicated in Table (5-1). Based on the obtained results from Chapter 4, these mix designs were chosen to provide a well-developed structure and a low level of carbonation. The activation solution was prepared from a mixture of NaOH (Reagent grade, 98%) and extra pure Na_2SiO_3 solution (Na_2O = 7.5-8.5%, SiO_2 = 25.5 -28.5 %, Sigma Aldrich). The calcined CRM was mechanically mixed with the alkaline activator for 5 minutes to get a homogenous geopolymer slurry. Afterward, the slurry was shaken for 10 minutes using a vibrating table and then hydrothermally cured in an oven at 100 ºC for 24 hours. After curing, the formulated geopolymers were aged at room temperature for 7 days (Figure 5-2).

Table (5- 1): Geopolymer mix designs.

Geopolymer	S/L (g)	NaOH (g)	Na_2SiO_3 (g)	H_2O (g)
MR-3	5:3.5	8.08	18	18.5
MR-4	5:3.5	4.04	15	9.25
MR-5	5:3	8.08	18	18.5

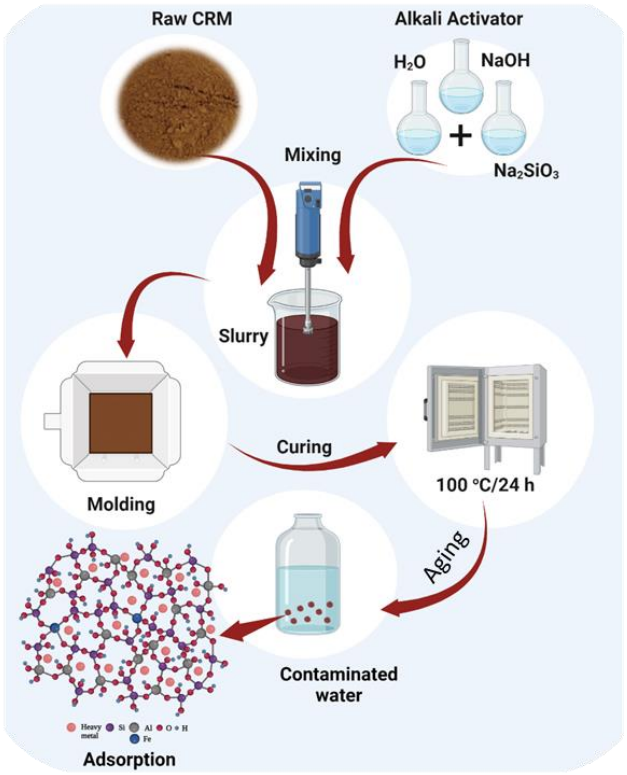


Figure 5-2: The synthesis procedure of the CRM geopolymer.

5.2.4 Adsorption experiments

The produced geopolymer adsorbents were crushed into fine powders. Before conducting the adsorption experiments all the geopolymers were rinsed several times with a deionized water to remove the unreacted alkali activator. A multicomponent solution of Cd^{2+}, Ni^{2+}, Mn^{2+}, and Co^{2+} was prepared by dissolving the appropriate amount of $Cd(NO_3)_2.4H_2O$ (Sigma Aldrich), $Ni(NO_3)_2.6H_2O$ (Sigma Aldrich), $Mn(NO_3)_2.4H_2O$ (Acros organics) and $Co(NO_3)_2.6H_2O$ (Sigma Aldrich) in the MilliQ water. The Na_2CO_3, NaCl and Na_2SO_4 salts were used as sources for the SO_4^{2-}, Cl^- and CO_3^{2-} anions. The adsorption experiments were conducted in the batch mode using Stuart ceramic hotplate stirrers. The reaction temperature was controlled by a Stuart temperature probe immersed in the experiment solution. All adsorption experiments were performed in 100 mL Erlenmeyer flasks under a variety of conditions (e.g., time interval, geopolymer mass, pH, and metal concentration). The pH of the solution was adjusted by adding 0.1 M HNO_3 and/or 0.1 M NaOH and monitored using the 8100 Plus pH meter. After each completed adsorption test, a suitable amount of the solution was taken using a syringe and filtered using a 0.22 μm PES filter. The adsorption capacity and % removal were calculated according to equations (5-1) and (5-2) respectively:

$$q_t = \frac{(Co - Ct)\mathrm{V}}{m} \qquad (5\text{-}1)$$

$$Removal\ efficiency\ (\%) = \frac{(Co - Ct)}{Co}\ X100 \qquad (5\text{-}2)$$

Where C_o is the initial concentration, C_t is the concentration at time (t), V is the volume of solution in litre, and m is the geopolymer mass in gram.

5.2.5 Analytical methods

Mineralogy was investigated using a powder X-ray diffraction (PXRD). The PXRD analysis was conducted on a PANalytical X'Pert Pro X-ray diffractometer, which uses CuKα radiation at a tube voltage of 40 kV and current of 40 mA. The raw material, thermally activated phase, and geopolymers were scanned over a sampling range of 3-70 º2θ, with a step size of 0.0066° and a scan speed of 0.023 °2θ per second. The obtained data were analysed using the X'Pert HighScore Plus software for phase identification. The CRM and/or geopolymers were also analysed using a Panalytical Epsilon 3XL energy dispersive X-ray spectrometer.

The Brunauer-Emmett-Teller (BET) surface area was determined using a Micromeritics Tristar instrument with nitrogen sorption at 77 K for all samples except the calcined CRM-800, which was measured using a Micromeritics 3Flex instrument. All samples were degassed before being

measured. The analysis of morphology was conducted using a JEOL7100F scanning electron microscope equipped with an EDX detector. The microstructure characteristics of the raw material, thermally activated phase, and geopolymer fragments and/or powders were coated with carbon to obtain the required conductivity. The vibrational functional groups were identified using an Attenuated Total Reflection Fourier Transform Infrared (ATR-FTIR) spectrometry using a Bruker Alpha FTIR spectrometer to record transmittance in the range of 400–4000 cm^{-1}, and the data were analysed using OPUS software. The metal ions concentration was analysed using the inductively coupled plasma-optical emission spectrometry (ICP-OES), Perkin Elmer spectrometer Optima 2000 DV. The standard calibrations were prepared using a standard solution (100 mg/L multi-element solution, Fisher Chemicals).

5.2.6 Quality control and precision

The reproducibility of the experimental data was demonstrated by repeating the experimental processes, and the results presented in this work are the mean values of these independent repeat experiments with the error bars representing the standard deviation (SD). The liquid blanks were measured before and after analysis. Additionally, the potential interference from the used syringe filters was evaluated. A total of six standard calibration solutions were prepared to establish the calibration curves. The correlation coefficient (R^2) of calibration curves for the measured metal ions were 0.99967, 0.99945, 0.99908, and 0.99999 for Mn, Co, Ni and Cd, respectively. The detection limit of the investigated metal ions was determined ensuring a high accuracy. All the fluid samples were measured in triplicates. All the used glassware and containers were prepared by soaking in HNO_3 (10%) for 24 hours before being rinsed with deionised and MilliQ water to exclude any external interferences, and subsequently oven dried at 100 ^oC. The statistical regression analysis (analysis of variance) was applied to determine the quality and goodness of isotherm and kinetic equations to the experimental data. The statistical parameters were calculated by using the following equations:

$$\text{Correlation coefficient } (R^2) = \frac{SS_{Regression}}{SS_{Total}} \qquad (5-3)$$

$$\text{Mean square error } (MSE) = \sqrt{\sum_{i=1}^{N}(p_i - o_i)^2/N} \qquad (5-4)$$

$$\text{Residual sum of squares } (RSS) = \sum_{i=1}^{N}(y_i - \tilde{y}_i)^2 \qquad (5-5)$$

$$\text{F-Value (F)} = \frac{(\mathrm{RSS}_1 - RSS_2)/(p_2 - p_1)}{RSS_2/(n - p_2 - 1)} \qquad (5-6)$$

5.3Results and discussion

5.3.1 Characterisation of geopolymer adsorbents

5.3.1.1 Chemical composition

The chemical composition of the raw material and geopolymers is given in Table (5-2). After geopolymerization, there is an increase in the Si and Na contents which are inherited from the alkali activator. A remarkable decrease in the concentration of Al, Fe, Mg, K and Ca is attributed to dissolution during the geopolymerization process.

Table (5-2): Chemical composition of raw CRM and geopolymer adsorbents.

Samples	SiO_2	Al_2O_3	Na_2O	K_2O	CaO	Fe_2O_3	MgO
Raw material	44.41	14.45	0.90	3.15	10.07	6.3	10.15
MR-3	45.57	9.25	18.48	2.31	6.88	4.06	7.74
MR-4	50.23	10.72	15.38	2.41	7.32	4.23	8.00
MR-5	45.29	9.57	16.26	2.35	7.10	4.16	7.85

5.3.1.2 Mineralogy

The XRD patterns of the geopolymers are depicted in Figure (5-3). An amorphous hump appeared between 22 and 39^{o} ($^{o}2\theta$), which is a characteristic feature of the geopolymer structure.[12, 13] After geopolymerization, various hydration products formed including; calcium silicate hydrate, gismondine [$CaAl_2Si_2O_8.4(H_2O)$], hisingerite [$Fe_2Si_2O_5(OH)_4.2H_2O$], chantalite [$CaAl_2SiO_4\ (OH)_4$], cowlesite [$CaAl_2Si_3O_{10}6H_2O$], clinozeosite [$Ca_2Al_3(SiO_4)(Si_2O_7)O(OH)$], and tobermorite [$Ca_5Si_6O_{16}(OH)_2$]. Quartz is inactive, while mica and dehydroxylated illite partly reacted, their dissolution was obvious in the case of the MR-3 geopolymer. The intensity of feldspar peak reduced in the MR-3 and MR-4 compared to MR-5 geopolymer, indicating a partial dissolution. The hematite peaks decreased in all geopolymers with a notable reduction for MR-3, indicating increased Fe dissolution and integration into the amorphous phase as well as the structure of the mineral hisingerite. The intensity of feldspar, calcite and CSH decreased for the MR-3 compared to MR-4 and MR-5. This reduction in the peak intensities confirmed the partial dissolution of feldspar, low carbonation effect, and a less developed CSH phase. Periclase and lime completely dissolved in all geopolymers. The change in the position and intensity of the quartz peak at 26.6^{o} (2θ) in the three samples indicated a different geopolymer composition and varying levels of dissolution. When compared to MR-4 and MR-5, the quartz peak for MR-3 showed less intensity, indicating a partial dissolution of quartz. Furthermore, compared to MR-4 and MR-5, calcite, CSH, and feldspar peak intensities were lower for MR-3, reflecting an increased reaction with more reactive phases involved.

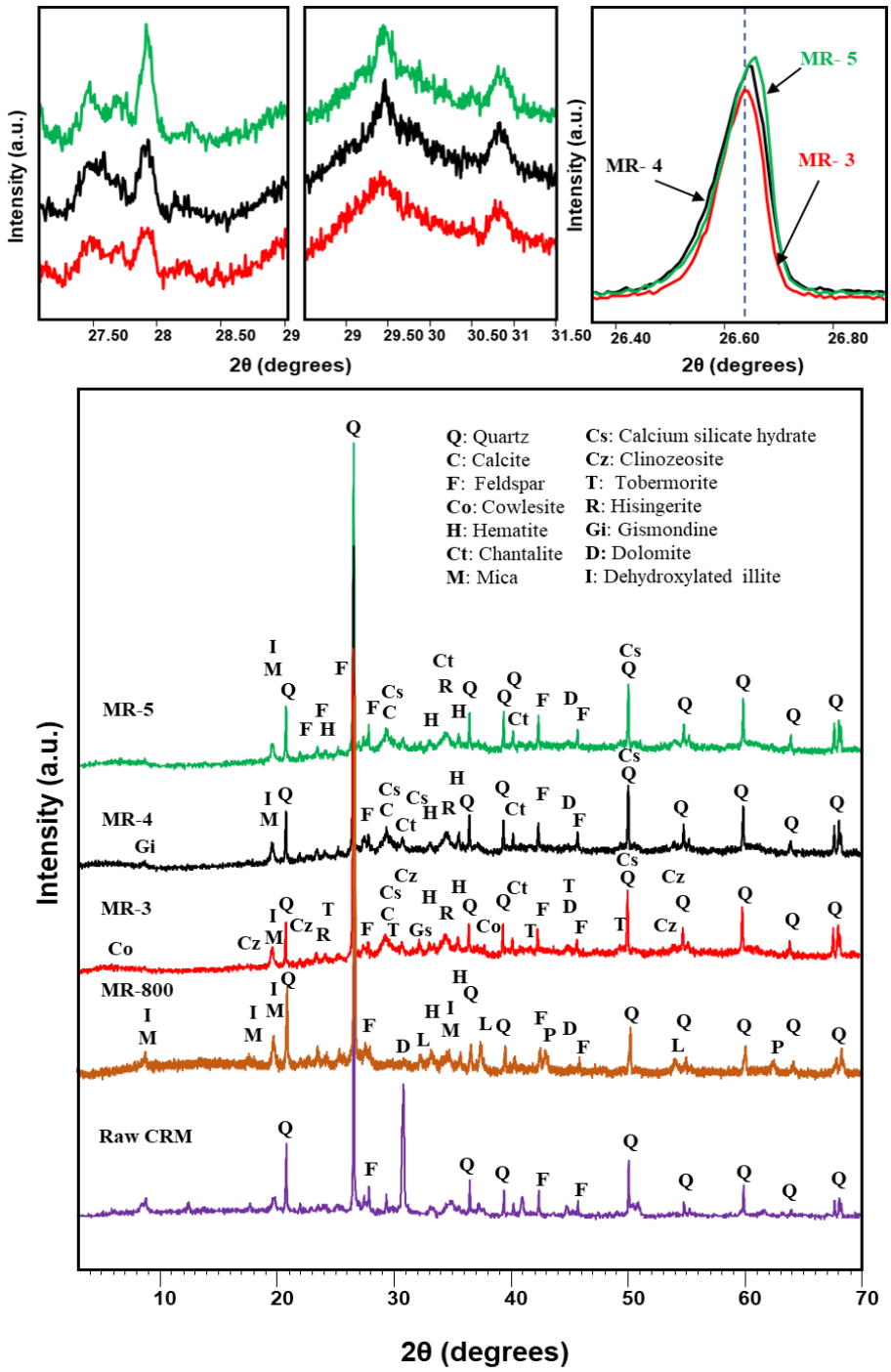


Figure 5-3: XRD analysis of geopolymer adsorbents, raw material and thermally activated phases.

5.3.1.3 FT-IR

Figure (5-4) shows the FTIR spectra of geopolymer samples. After geopolymerization, the main Si-O-T band shifted to 963.1, 963.9 and 959 cm^{-1} for MR-3, MR-4, and MR-5, respectively. The isomorphic replacement of Al^{3+} for Si^{4+} in the aluminosilicate framework was revealed by the shift from high wavenumber in the calcined CRM (988 cm^{-1}) to low

wavenumber in the geopolymers. In comparison to MR-4, the geopolymer gel of MR-3 and MR-5 appeared to have a greater network connectivity. While the absorption bands at 3300, 3365 and 3341 cm^{-1} are attributed to O-H stretching mode, the absorption bands at 1657, 1647 and 1642 cm^{-1} are ascribed to H-O-H bending modes.[14] The absorption bands at 1442, 1410, 1440 and 1388 cm^{-1} are attributed to C-O stretching vibration mode of ν_3 (CO_3^{2-}). The decrease in the intensity and broadness of carbonate band in MR-3 and MR-5 compared to MR-4 indicated the presence of non-bonded free alkali ions. The absorption bands at 797, 793, 771, 762, 775 and 796 cm^{-1} are ascribed to Si-O-Si stretching vibrations.[15] The absorption bands at 713, 715 and 722 cm^{-1} are attributed to the vibrations bending modes of ν_4 (CO_3^{2-}).[16] The appearance of absorption bands at 738, 746 and 747 cm^{-1} are ascribed to Al-O-Si symmetric stretching vibrations.[17] While, the absorption bands at 759, 758 and 755 cm^{-1} are attributed to O-Si-O stretching, the absorption band at 590 cm^{-1} is assigned to Si-O-T (T=Si or Na).[18] Si-O-Al vibration is thought to be the cause of the absorption band at 539 cm^{-1}.[19]

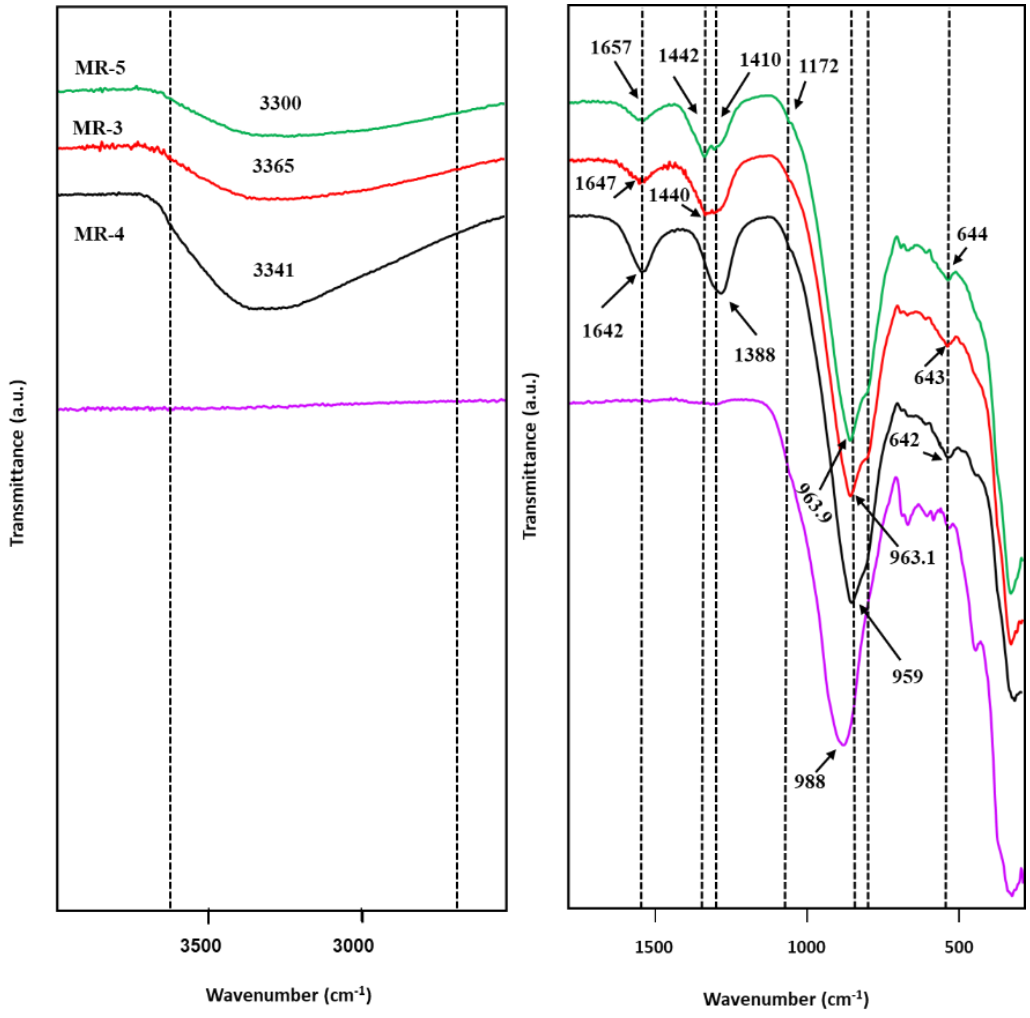


Figure 5-4: The FT-IR spectra of geopolymer adsorbents.

5.3.1.4 BET surface area

Figure (5-5) shows the nitrogen sorption isotherm (A) and corresponding PSD curves via the BJH method (B). The geopolymers exhibit type IV isotherms and hysteresis loops of type H3, reflecting a mesoporous nature which is a characteristic feature of the geopolymer structures.[20] The specific surface area, S_{BET}, and total pore volume, V_t, are given in Table (5-3). In comparison to the raw and calcined precursors, the surface area and pore volume increased after geopolymerization. A decrease in the surface area of the thermally activated CRM is due to the crystal deformation and channel plugging of clay minerals upon thermal activation.[3] The increase in the surface area of geopolymer is due to the formation of a 3D aluminosilicate framework, reflecting a significant structural modification upon alkali activation.

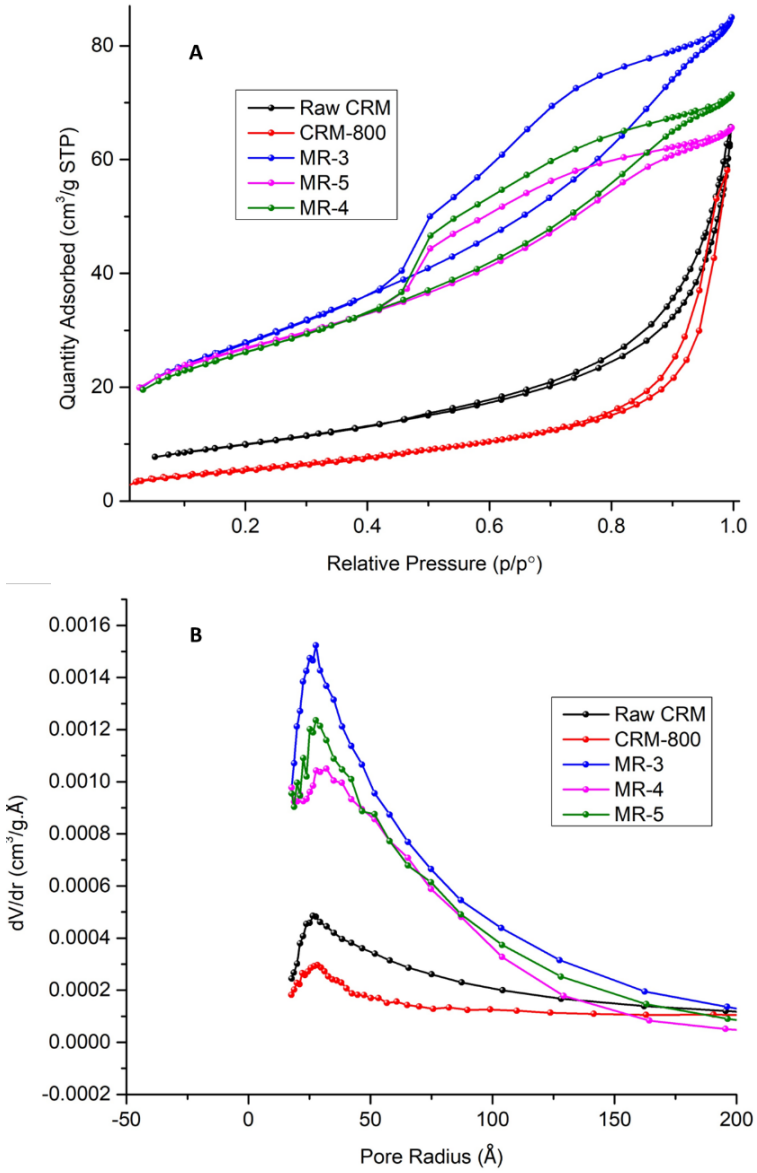


Figure 5-5: Nitrogen sorption isotherms (A) and corresponding pore size distribution curves (B) of geopolymer adsorbents and raw and thermally activated phases.

Table 5-3: Textural properties of geopolymer adsorbents, raw and thermally activated phases.

Sample	BET (m^2/g)	Average diameter (Å)	$S_{BET}/S_{BET\ (raw)}$	V_T (cm^3/g)	$V_T/V_{T(raw)}$
Raw CRM	35	90.3	1	0.0657	1
CRM-800	19	156.8	0.54	0.0619	0.94
MR-3	99	57.3	2.82	0.1257	1.91
MR-4	96	52.9	2.74	0.0852	1.29
MR-5	91	55.3	2.60	0.0974	1.48

5.3.1.5 SEM analysis

Figure (5-6) depicts the distinguishing morphological features of the geopolymer adsorbents. Compared to MR-4 and MR-5, the MR-3 geopolymer is more porous. Additionally, the appearance of crystalized phases, mostly zeolites, was prevalent which is in accordance with the XRD patterns. The appearance of surface carbonation on the MR-4 was dominant, which is consistent with the observations on the geopolymer sample prior to crashing. Surface carbonation, however, was absent or limited in the case of MR-3 and MR-5 geopolymers. The appearance of microcracks was dominant in the case of MR-4 geopolymer, this is in accordance with the presence of cleavage zones in the geopolymer sample which facilitated the splitting of MR-4 samples into small blocks and in specific directions. The elemental composition of the formed geopolymers is given in Table (5-4). The Si/Al ratio is ca. 2 for MR-3 and MR-5, indicating a desired formulation, while this ratio was above 2 for the MR-4 which is probably due to the presence of unreacted phases.[20] The reduction in the Fe content in geopolymer adsorbents, compared to its values in the calcined and raw CRM, showed a ferrosialate composition, where more Fe contributed to the geopolymer structure. The average concentrations of Fe in the MR-3, MR-4, and MR-5 were 3.8, 4.3, and 4, respectively. Although, the difference between the three geopolymer adsorbents, in terms of the Fe concentration, is not large, it can be deduced that the formation of ferro-aluminosilicate phase was higher in the MR-3 geopolymer compared to the MR-5 and MR-4. The difference in the Na/Al ratio suggested that various cations contributed to balancing the negative charge on the geopolymer surface.

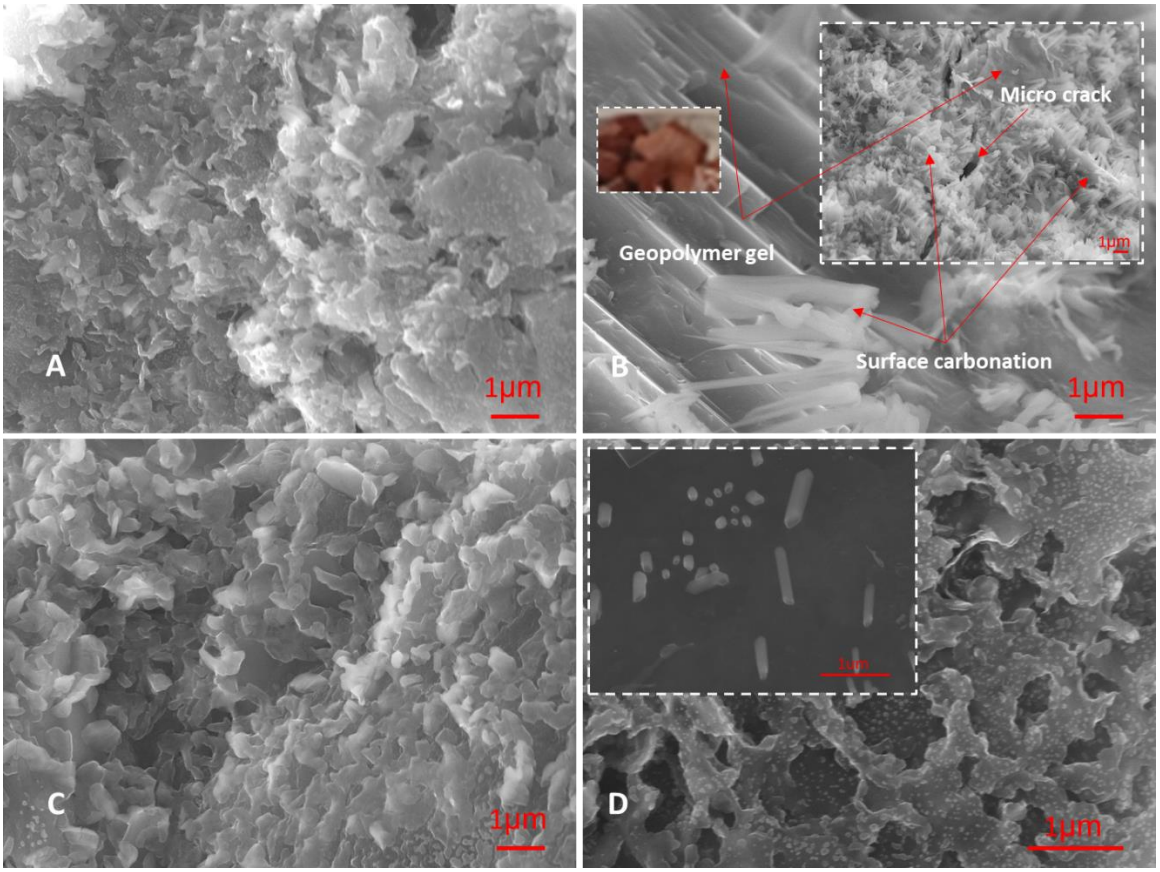


Figure 5-6: SEM micrographs of geopolymer adsorbents. A) MR-3 adsorbent, B) MR-4 adsorbent, C) MR-5 adsorbent, and D) shows porous structure and crystalline phases in MR-3 geopolymer adsorbent.

Table 5-4: Elemental composition for selected points in the MR-3, MR-4, and MR-5.

Sample	Na	Mg	Al	Si	K	Ca	Ti	Fe	Si/Al	Na/Al
MR-3	16.63±1.5	3.09±0.005	7.46±0.8	17.78±1.4	3.56±0.5	2.47±1.1	0.135±0.01	3.87±0.2	2.3	2.2
MR-4	8.78±1.4	4.33±0.9	5.48±0.2	24.3±0.7	2.8±0.5	7.2±2	0.4±0.19	4.35±0.9	4.4	0.79
MR-5	1.38±0.5	1.06±0.05	17.0±1	26.1±0.9	11.8±1.6	1.4±0.75	0.29±0.02	4.09±0.6	1.53	0.08

5.3.2 Adsorption experiments

5.3.2.1 Raw CRM evaluation in metal ion sequestration (preliminary study)

The efficiency of the raw CRM in sequestrating the co-existing metal ions was investigated. The outcomes of this experiment, which was carried out at various time intervals, are shown in Figure (5-7). The maximum removal of metal ions was 22.7, 22.0, 21.4 and 10 %, respectively, in the order of Ni^{2+}>Co^{2+}>Mn^{2+}>Cd^{2+}. These findings showed that the removal of metal ions

was rather limited, therefore the raw material will not be further considered in the trials that follow.

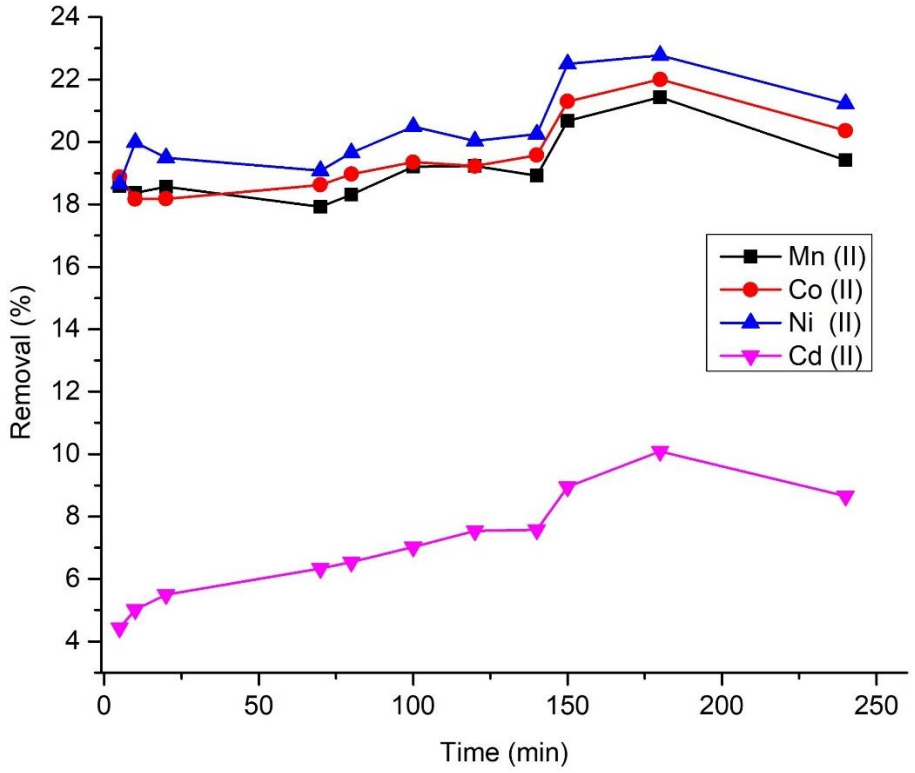


Figure 5-7: Adsorption removal efficiency of the raw CRM material at different time intervals. (Refer to Appendix C-1 for the applied experimental conditions).

5.3.2.2 Effect of operating parameters

5.3.2.2.1 Effect of contact time

As shown in Figure (5-8), the three adsorbents' reaction times were examined at various time intervals. Mn^{2+}, Cd^{2+}, Ni^{2+} and Co^{2+} clearance efficiencies in the three samples gradually rise with increasing reaction time. The adsorption rate was fast at the initial stages, but it slowed down over time until the equilibrium was reached. At the initial stages of reaction, a large number of empty binding sites were available, but when the equilibrium was reached the vacant binding sites became saturated with metal ions, in addition to the increase in the electrostatic repulsion between adsorbed metal ions and the incoming ones. The equilibrium contact time of such multicomponent systems is relatively short and anticipated to be even shorter in the event of sequestration from single component systems, which is advantageous from an economic perspective.[21] Even though the three adsorbents displayed the same behaviour, there was a striking variance in their removal efficiency. Compared to the MR-4 and MR-5, the MR-3 demonstrated a greater removal efficiency for all metal ions. Additionally, a selectivity order

for the removal of heavy metals was noticed for all adsorbents, with $Cd^{2+}>Co^{2+}>Ni^{2+}>Mn^{2+}$ having the highest removal efficiencies of MR-3 at 93.4, 88.3, 87.3 and 60.6 %, respectively. Surprisingly, compared to the raw material, the adsorption selectivity was completely different, indicating a significant structural modification after geopolymerization.

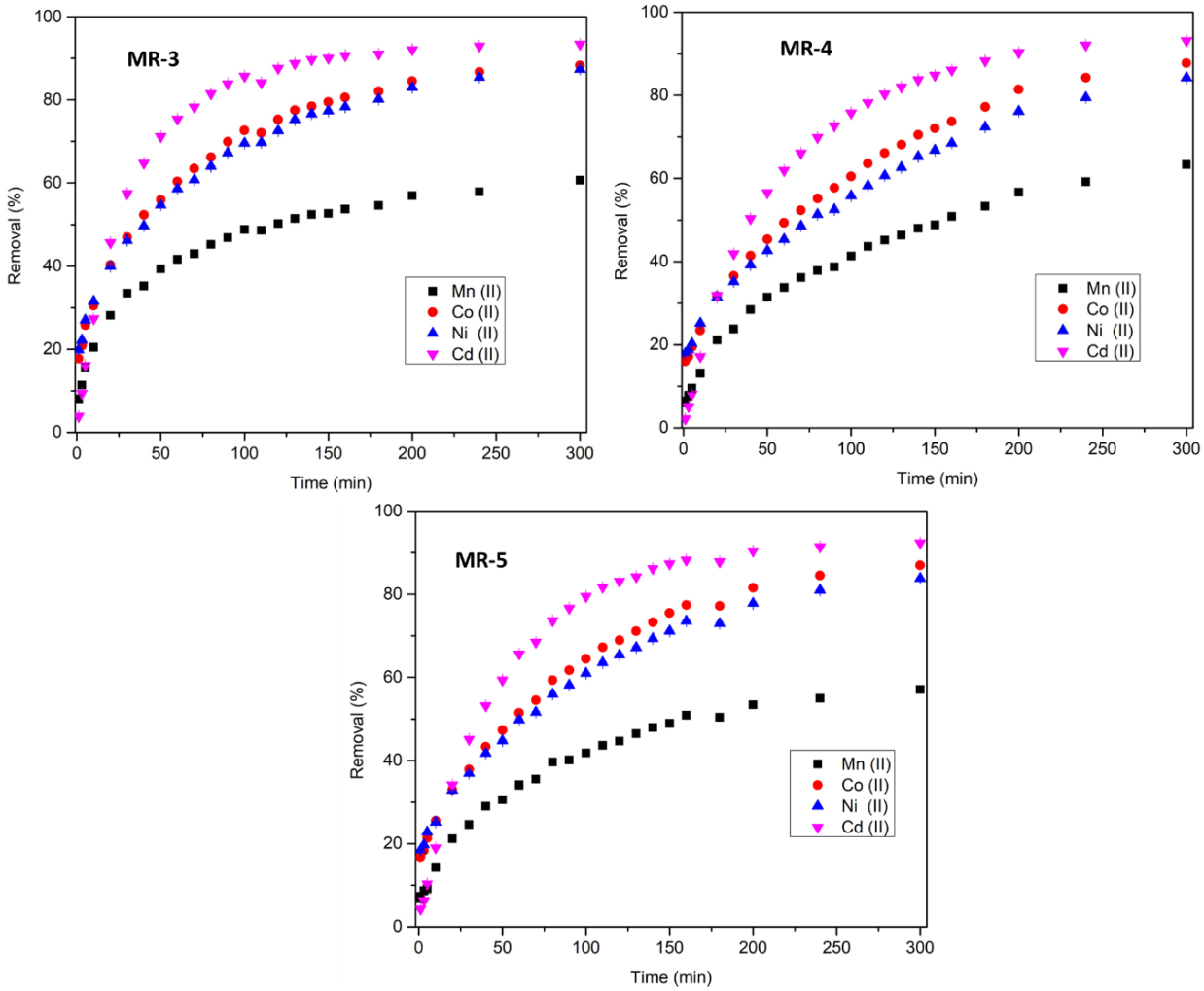


Figure 5-8: Effect of contact time on the removal of metal ions. (Refer to Appendix C-2, 3 and 4 for the applied experimental conditions).

5.3.2.2.2 Effect of pH

One of the crucial factors affecting the adsorption process, the nature of adsorbent and adsorbate, and the adsorption mechanism is the pH of the solution. A wide pH profile (3-4-5-6-7-8) was explored, despite the fact that the dominating pH in the study area was in the range of 6.8 to 8.5, as illustrated in Chapter 3. In order to guarantee the applicability of the formulated adsorbents under a variety of conditions while considering the chemical stability of the adsorbent, it was important to select such a pH profile. Investigating the influence of pH beyond

pH value 8 was not considered so as to prevent the metal ions precipitation (hydroxides) and to ensure that metal ions are maintained as cationic species throughout the experiments. Adsorption of the metal ions under a range of pH conditions is presented in Figure (5-9). Generally, there is an increase in the removal efficiency of all metal ions as pH increased from 4 to 8. At pH 3, however, a notable reduction in the removal adsorption was noticed (Figure 5-10). This reduction was accompanied by a rise in the concentration of the metal ions, suggesting the geopolymer structure disintegration through the Al-O bonds rupturing. At lower pH levels, the Mn^{2+}, Ni^{2+}, Co^{2+}, Cd^{2+}, and positive protons (H_3O^+) compete for binding to the active sorption sites. Due to the electrostatic repulsion, this rivalry makes it harder for the metal ions to access active sites. On the other hand, as the pH rose, the removal efficiency increased due to a decrease in the abundance of positive protons in the solution, which encouraged the adsorption of the dominating positive metal ions. The three adsorbents had similar trends of the metal ions selectivity, with MR-3 outperforming the MR-4 and MR-5 in terms of its ability to remove all metal ions.

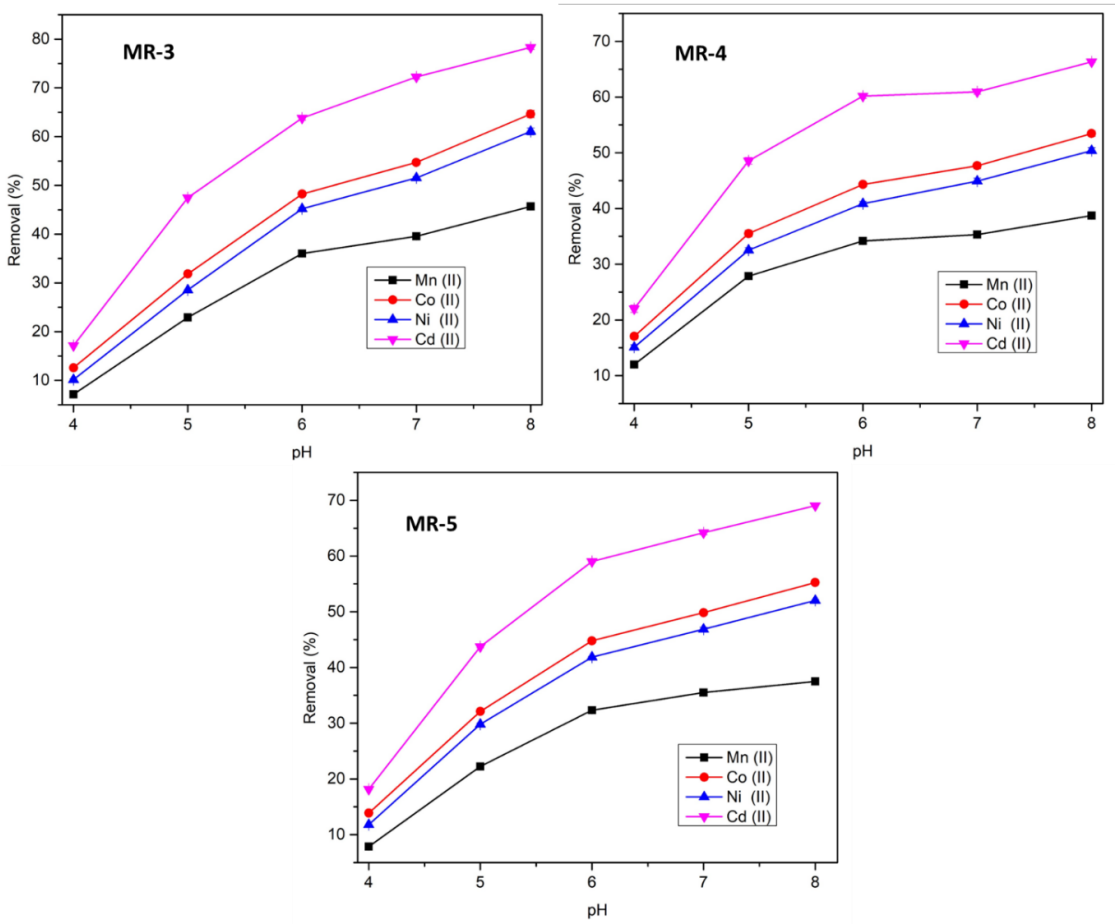


Figure 5-9: Effect of pH on the removal of metal ions. (Refer to Appendix C-5 for the applied experimental conditions).

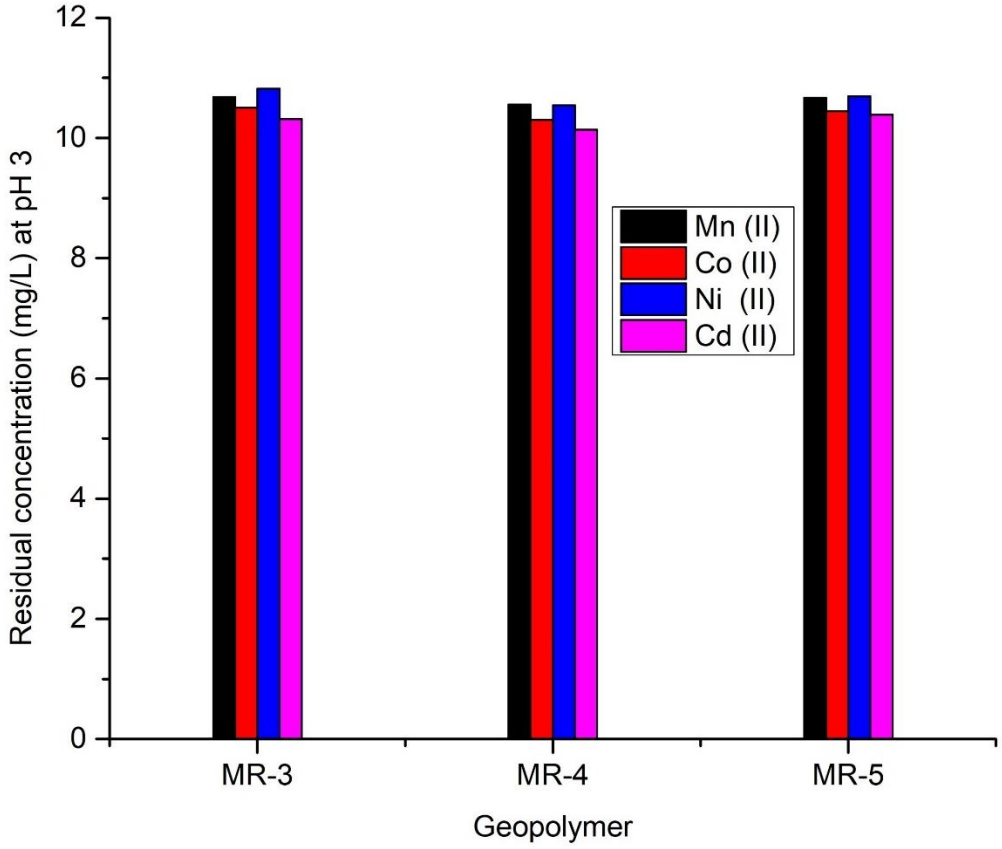


Figure 5-10: The residual concertation of metal ions at pH3. (Refer to Appendix C-5 for the applied experimental conditions).

5.3.2.2.3 Effect of geopolymer mass

The effect of geopolymer mass on the removal rate of metal ions was investigated and the results are shown in Figure (5-11). It is evident that the removal efficiency of the metal ions increased sharply with the geopolymer mass. The adsorption capacity, however, decreased as the geopolymer mass rose. This trend was ascribed to the increased surface area and number of binding sites, in addition to the enhanced distribution coefficient. On the other hand, the metal ion/active sites ratio drops in the presence of a constant metal ion concentration and increasing geopolymer adsorbent mass, showing a rise in the presence of unsaturated active sites and consequently reduced the adsorption ability. The highest adsorption efficiency was for the MR-3, with the adsorbents displaying a similar metal ion selectivity order. A distinctive behaviour in the removal of metal ions was noticed at MR-4 adsorbent, where the removal of metal ions increased with increasing the adsorbent dose up to 0.1 g then the removal rate plateaued for all metal ions except the Cd^{2+} which showed a striking decrease in the removal at

adsorbent mass of 0.14 g. This behaviour is probably attributed to the interactions between the sorption sites at a larger geopolymer amount.

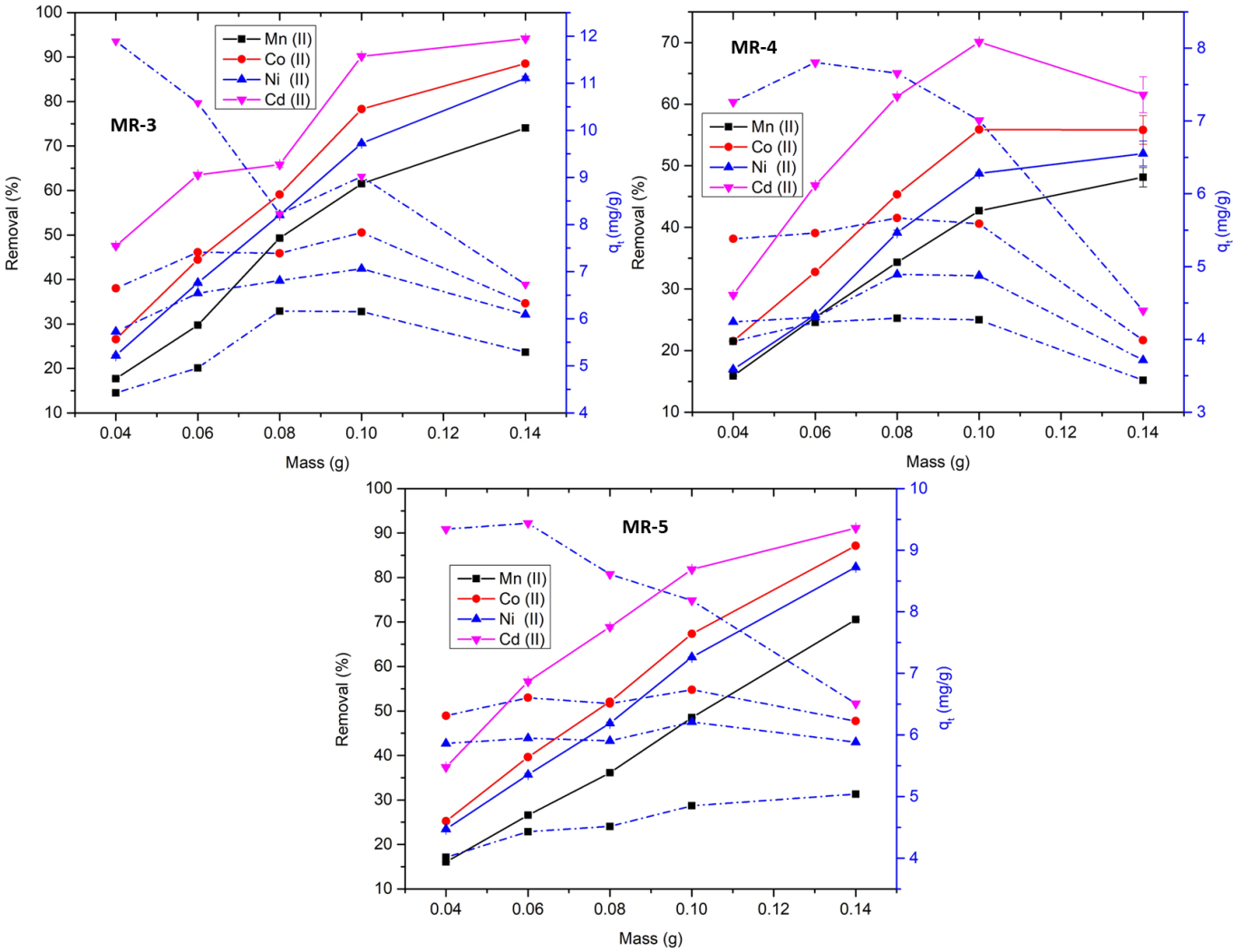


Figure 5-11: Effect of adsorbent mass on the removal of metal ions. (Refer to Appendix C-7 for the applied experimental conditions).

5.3.2.2.4 Effect of initial concentration

Although the metal ion concentrations in the study area were in ug/L, metal ion concentrations in mg/L were employed in the current experiments. These high concentrations were applied to mimic a high pollutant load to allow the effect of the CRM adsorbents to be evaluated. The effect of initial metal ion concentration on the metal ions sequestration was investigated and the results are depicted in Figure (5-12). As concentration increases, the removal efficiency decreases. The maximum adsorption capacity was achieved at an initial concentration of 100 mg/L, where the q_e values of MR-3 were 20.3, 15.5, 14.6, and 7.5 mg/g for Cd^{2+}, Ni^{2+}, Co^{2+}, and Mn^{2+}, respectively. For the Cd^{2+}, Ni^{2+}, Co^{2+}, and Mn^{2+}, the q_e values of MR-4 were 15.7,

14.6, 14.3, and 9.3 mg/g, respectively. For the Cd^{2+}, Ni^{2+}, Co^{2+}, and Mn^{2+}, the q_e values of MR-5 were 16.6, 16.14, and 9.4 mg/g, respectively. Regarding the heavy metals selectivity, all the geopolymer adsorbents exhibited the same behaviour. Although the MR-3 had the best metal ion adsorption capacity, its Mn^{2+} adsorption capacity decreased at initial concentration 100 mg/L, when compared to the MR-4 and MR-5. The removal effectiveness decreases when the metal ions compete for binding to the available active sorption sites at a greater metal ion concentration. On the other hand, a higher adsorption capacity can be linked to a rise in the driving force, which lowers the resistance to metal ion mass transfer between the solid and aqueous phase. This allows for the effective occupation of all active sites and internal pores.[22]

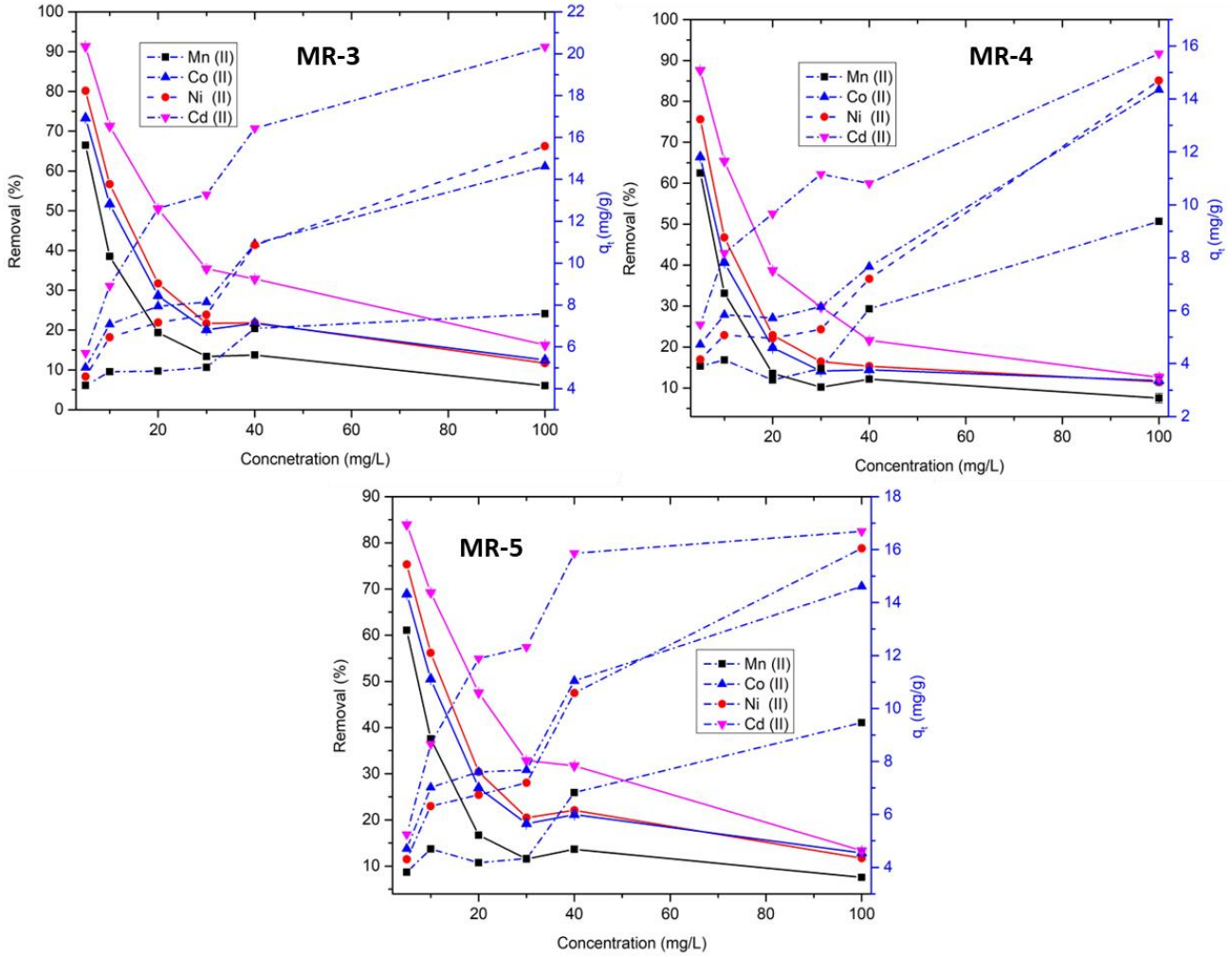


Figure 5-12: Effect of initial concertation on the removal of metal ions. (Refer to Appendix C-6 for the applied experimental conditions).

Figure (5-13) depicts the distribution factor (K_d) as a function of the concentration of heavy metals. As the concentration of the metal ions decreases, the K_d values rise. This behaviour

implied that the energetically unfavourable sorption sites are involved as the metal ion concertation in the solution increase.

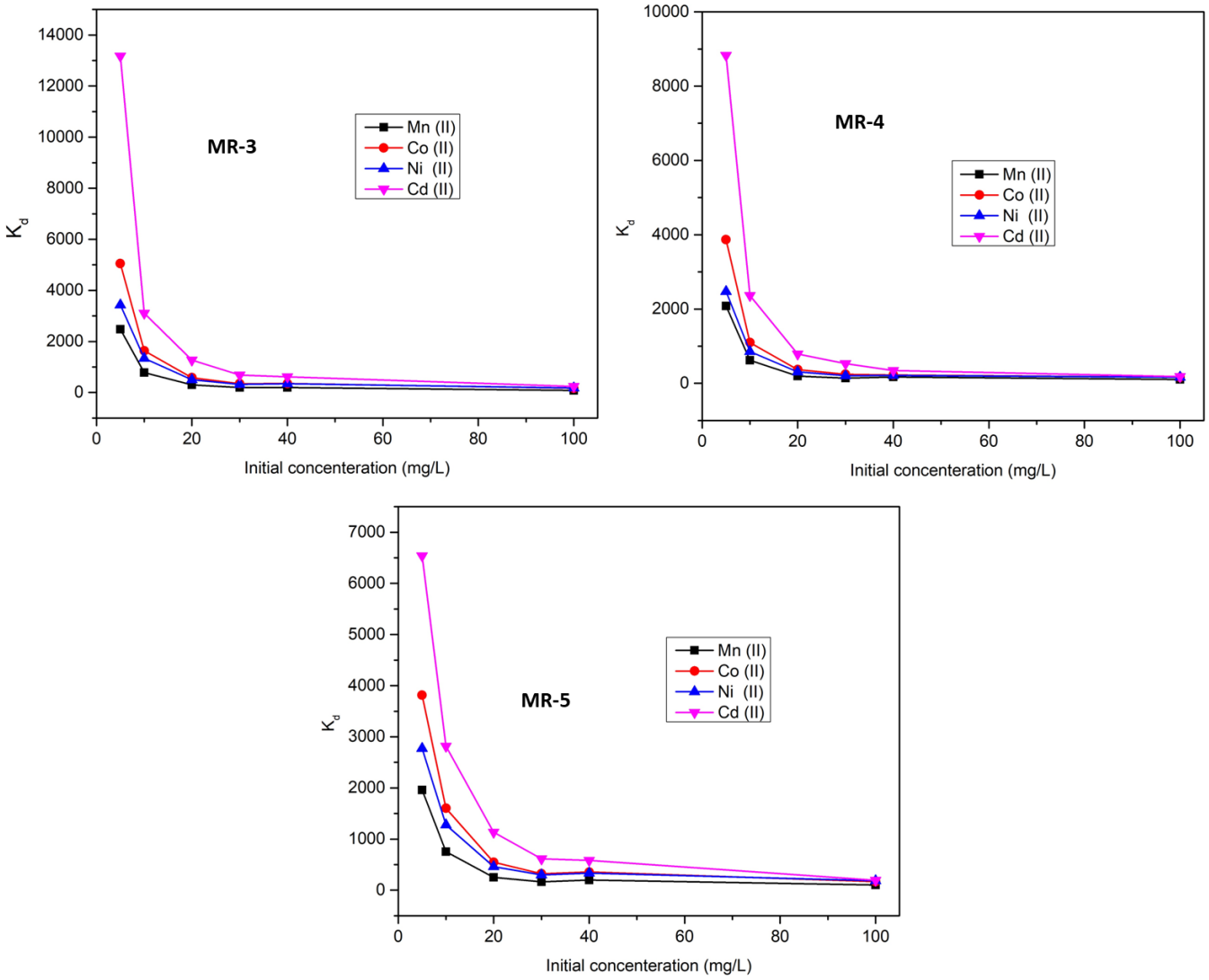


Figure 5-13: Distribution factor at different initial concentration of metal ions.

5.3.2.2.5 Effect of grain size

The effect of adsorbent grain size on the metal ions removal is depicted in Figure (5-14). The adsorption experiments were conducted at different grain sizes of 500-250, 250-125, and 125-63 microns. The decrease in the grain size of adsorbents was accompanied by an increase in the removal efficiency of metal ions. The increase in the removal is attributed to the increase in the corresponding surface area and hence more active sites are available for the metal ions binding. The MR-3 adsorbent showed a high removal efficiency at different sizes compared to the MR-4 and MR-5. The removal efficiency of MR-4 improved for the 125-63 micron size range compared to the MR-5 for all heavy metals, and to the MR-3 for Mn^{2+}. The increase in

the adsorption removal of MR-4 at 125-63 micron is probably attributed to the enhanced diffusion and accessibility as a consequence of the splitting of large particles, which creates channels and cracks. Splitting of the larger particles means that the encapsulated geopolymer particles are exposed for the interaction with metal ions.

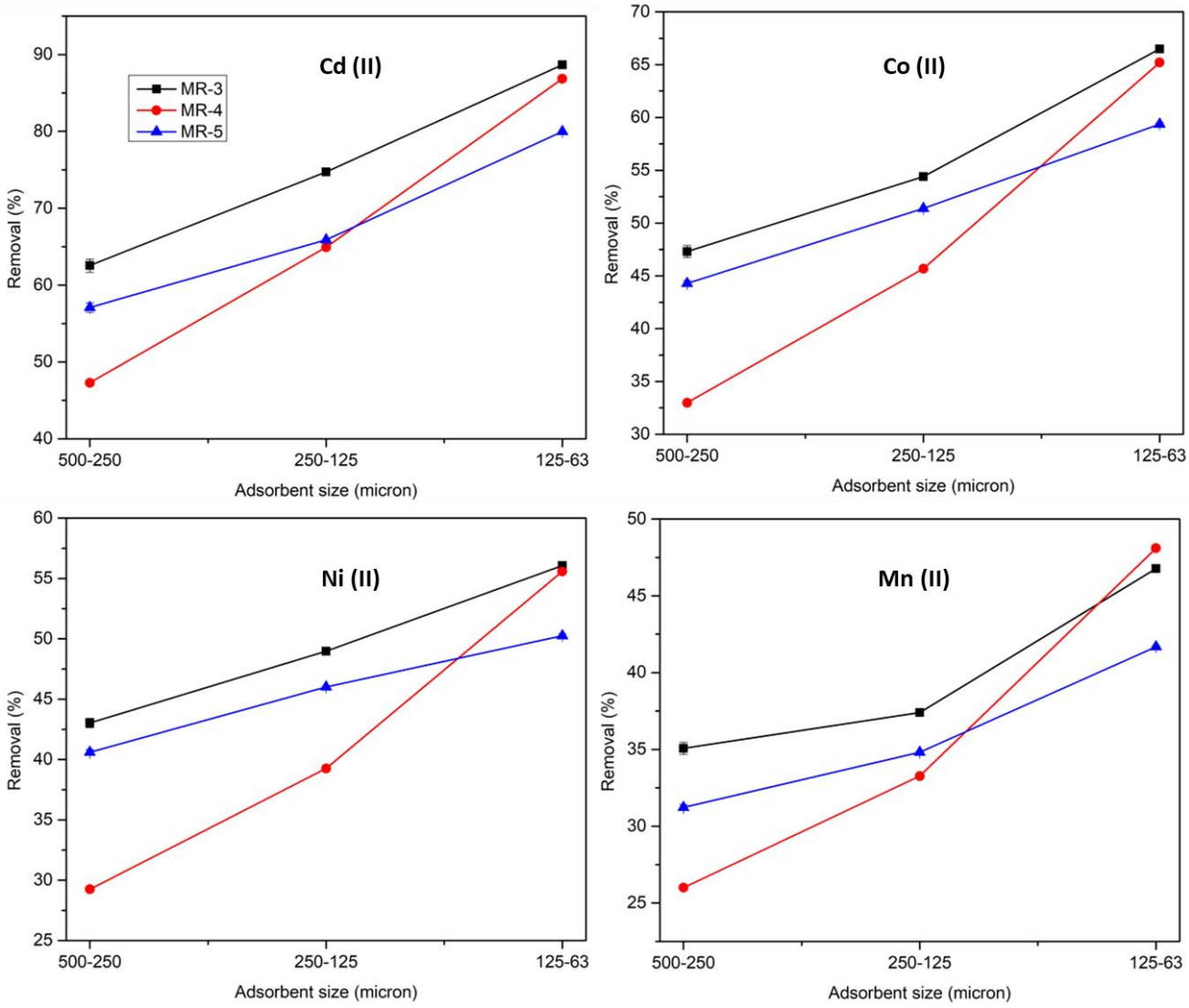


Figure 5-14: Effect of grain size of adsorbent on the removal of metal ions. (Refer to Appendix C-8 for the applied experimental conditions).

5.3.2.2.6 Effect of temperature

The effect of temperature on the elimination of metal ions was examined in the temperature range between 25 and 55 ^{0}C. As indicated in Figure (5-15), the removal efficiency improved with the increase in the solution temperature. This implies that the reaction is endothermic and therefore higher temperatures are advantageous. Additionally, the diffusion rate of the metal ions increases with rising the temperature crossing over the outer boundary layer and the

internal pores of adsorbent.[23] At 55 ^{0}C, the Cd^{2+} removal did, however, start to dimmish relative to Co^{2+} and Ni^{2+} removal. This can be explained by the fact that Cd^{2+} has a greater propensity to migrate into the solution phase due to the weakening of the attractive interactions between it and the surface of the geopolymer.[24, 25]

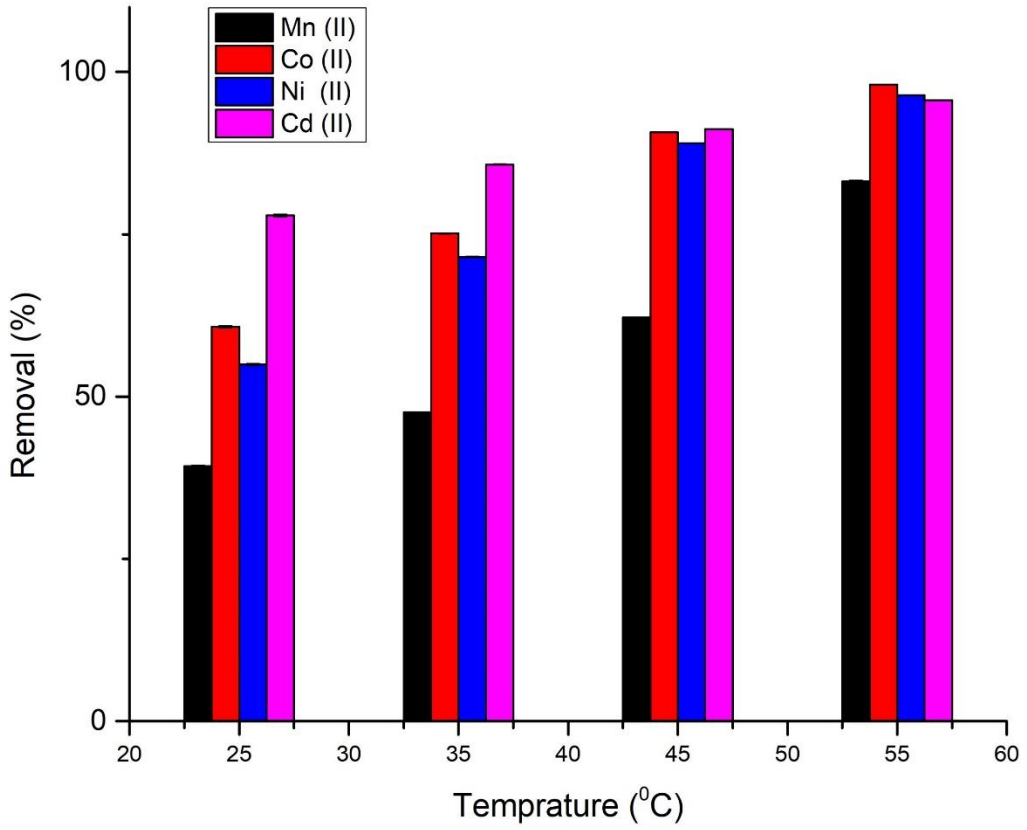


Figure 5-15: Effect of solution temperature on the removal of metal ions. (Refer to Appendix C-9 for the applied experimental conditions).

5.3.2.3 Cation exchange capacity (CEC)

Table (5-5) provides an illustration of the cation exchange capabilities of the raw material (CRM) and geopolymer adsorbents. The standard method of the ion exchange with NH_4Cl was used to determine the total cation exchange capacity.[26] It is important to note that the isomorphic replacement of Al^{3+} for Si^{4+}, which results in a negative net charge on the geopolymer surface, is primarily responsible for the origin of the cation exchange in geopolymers.[6] The released cations from the three geopolymers were in the following order: Ca^{2+}>Na^{+}>K^{+}>Mg^{2+}. This behaviour suggests that the Ca^{2+}, Na^{2+}, and K^{+}, with a minor contribution from the Mg^{2+}, essentially balanced the negative charge on the geopolymer

surface. The contributions of such exchangeable cations was further confirmed at different initial concentrations of the metal ions, as indicated in Figure (5-17).

In comparison to the cation exchange capacity of the raw material (26.1 cmol kg^{-1}), the cation exchange capacity increased after geopolymerization to 98.3, 111, and 66 cmol kg^{-1} for MR-3, MR-4, and MR-5, respectively. After geopolymerization, a negatively charged 3D aluminosilicate structure containing a more exchangeable sites was formed, which is responsible for the increase in cation exchange capacity. Compared to the MR-4, the MR-3 adsorbent had an excellent adsorption behaviour, although its cation exchange capacity was a little lower. The same behaviour was observed when the MR-4 and MR-5 were contrasted. This could be explained by the presence of unreacted phases in the MR-4, such as dehydroxylated illite and unreacted oxides whose contribution cannot be ruled out.

Table 5-5: Cation exchange capacity of geopolymer adsorbents.

Experimental data						Calculations				
Sample	Mass (g)	Ca (mg/L)	K (mg/L)	Mg (mg/L)	Na (mg/L)	Ca (cmol/kg)	K (cmol/kg)	Mg (cmol/kg)	Na (cmol/kg)	CEC (cmol/kg)
MR-3	1	149.6	14.56	0.87	44.32	74.67	3.72	0.71	19.2	98.3
MR-4	1	158.0	18.99	1.10	63.07	78.84	4.85	0.90	27.4	111
MR-5	1	97.19	12.01	0.53	32.29	48.49	3.07	0.44	14.0	66
CRM	1	30.41	2.02	8.08	8.80	15.17	0.51	6.64	3.82	26.1

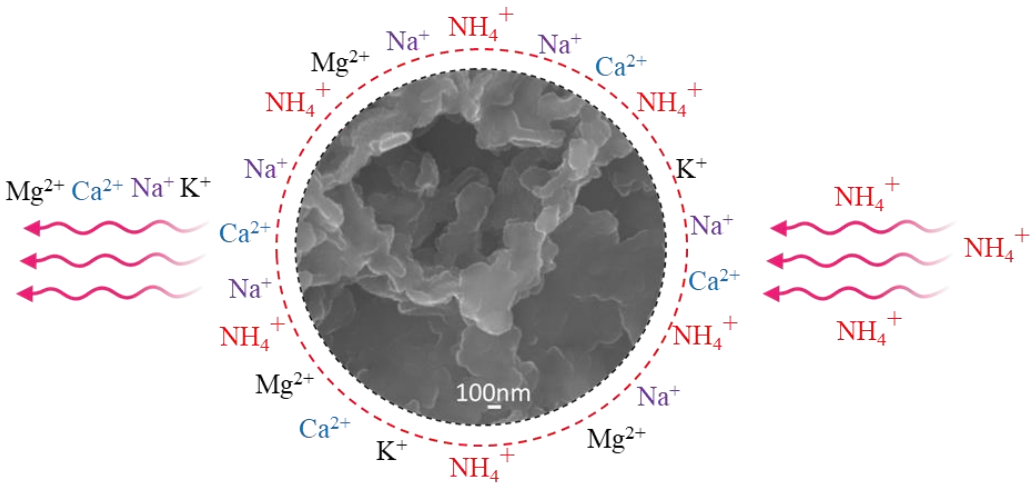


Figure 5-16: Saturation of the geopolymer surface with NH_4^+ after exchange with Ca^{2+}, Na^+, K^+, and Mg^{2+} cations.

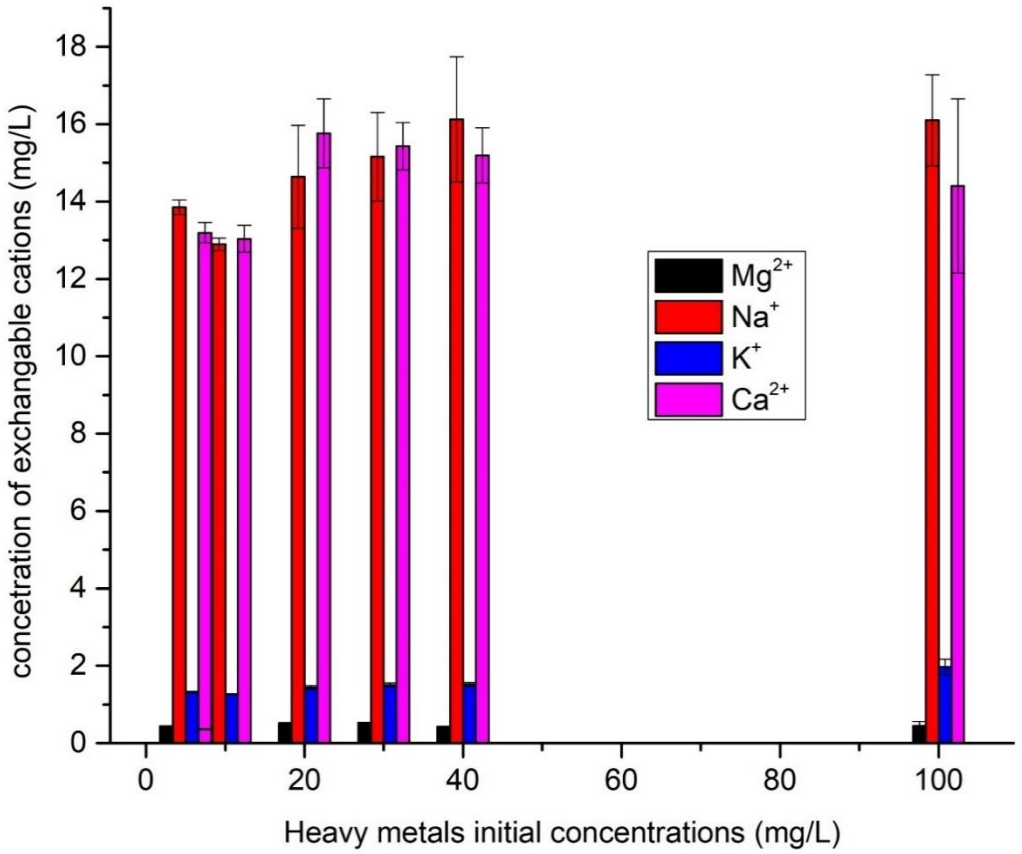


Figure 5-17: Exchanged cations at different metal ions initial concentration. The presented data is for the MR-3 geopolymer.

MR-4 demonstrated a substantial level of surface carbonation at both the macro-and microscales. High alkalinity geopolymer binder is often more susceptible to carbonation.[27] As a result, the presence of carbonation may cause the geopolymer structure to dissolve, releasing more cations into the solution. Additionally, the difference between the geopolymers structure resulted in organised porous networks with different permeabilities. Therefore, the cation exchange behaviour of the MR-4 can be influenced by carbonation and permeability evolution. In comparison to the MR-3 and MR-5, the MR-4 is more hygroscopic as indicated by the FTIR spectrum. The vast majority of unreacted and reactive free ions are entrapped in the pore solution of geopolymers. Different permeabilities make it easier for the free and non-bonded ions to be released into the solution, which raises the concentration of cations, especially Na^+ and Ca^{2+}.[28, 29] It should not be surprising that the degree of the alkali activation, the conditions of the synthesis, and the heterogeneity of the precursor all significantly affect the final chemical and physical properties of the generated geopolymers. Since the MR-4 is less reacted than MR-3 and MR-5, the pace of the creation of porous sorption sites, and associated permeabilities, is

anticipated to be much lower. Therefore, the role of surface carbonation in disrupting the CEC is more accepted than the permeability influence. The effect of microcracks formation, however, cannot be ruled out.

5.3.2.4 Adsorption kinetics

The adsorption kinetics were tested using the pseudo- first order (PFO) and pseudo-second order (PSO) kinetic models, which are represented by equations (5-7) and (5-8), respectively.[30]

$$\ln(q_e - q_t) = \ln q_e - k_1 t \qquad (5-7)$$

$$\frac{t}{q_t} = \frac{1}{k_2 q_e^2} + \frac{t}{q_e} \qquad (5-8)$$

Where q_e (mg/g) is the adsorption capacity at equilibrium, q_t (mg/g) is the adsorption capacity at time (t), k_1 (min^{-1}) and k_2 ($g.mg^{-1}.min^{-1}$) are the PFO and PSO rate constant, respectively. The kinetic plots In (q_e-q_t) and t/q_t against t for the PSO and PFO, respectively, are shown in Figure (5-18). The adsorption kinetics parameters are presented in Table (5-6). The PFO kinetic model (A) does not cover the whole range of contact time and is suitable only for the first 60 min of contact time for all metal ions. On the contrary, the PSO plot (B) displays an excellent linearity and cover the whole range of contact time and the calculated q_e is closer to the experimental q_e, the validity of the kinetic models is confirmed by comparing the calculated q_e with the experimentally identified q_e.[31, 32]

Table 5-6: PFO and PSO kinetic parameters for adsorption of Mn^{2+}, Ni^{2+}, Co^{2+} and Cd^{2+} on geopolymers.

Model	Metal	q_e exp(mg/g)	q_e clac. (mg/g)	K*	R^2	RSS	MSE	Persons'r	F value	Prob>F
PFO	Mn^{2+}	7.58	4.75	1.56	0.9624	0.314	0.044	-0.98344	206.126	6.30E-6
	Ni^{2+}	11	5.82	1.76	0.9471	0.353	0.050	-0.9766	144.33	1.29 E-7
	Co^{2+}	10.92	6.28	1.83	0.9706	0.170	0.024	-0.98708	265.612	7.97 E-7
	Cd^{2+}	11.06	10.65	2.36	0.9807	0.172	0.024	-0.99152	407.548	1.83 E-7
PSO	Mn^{2+}	7.58	7.86	0.005	0.9913	19.18	0.913	0.99584	2511.062	0
	Ni^{2+}	11.0	11.42	0.00345	0.9869	13.71	0.653	0.99374	1662.424	0
	Co^{2+}	10.92	11.63	0.00349	0.9901	9.97	0.475	0.99527	2204.708	0
	Cd^{2+}	11.06	12.88	0.00326	0.9985	1.18	0.056	0.99931	15143.47	0
K* is k_1 for PFO and k_2 for PSO model. q_e was calculated at C_i=10 ppm										

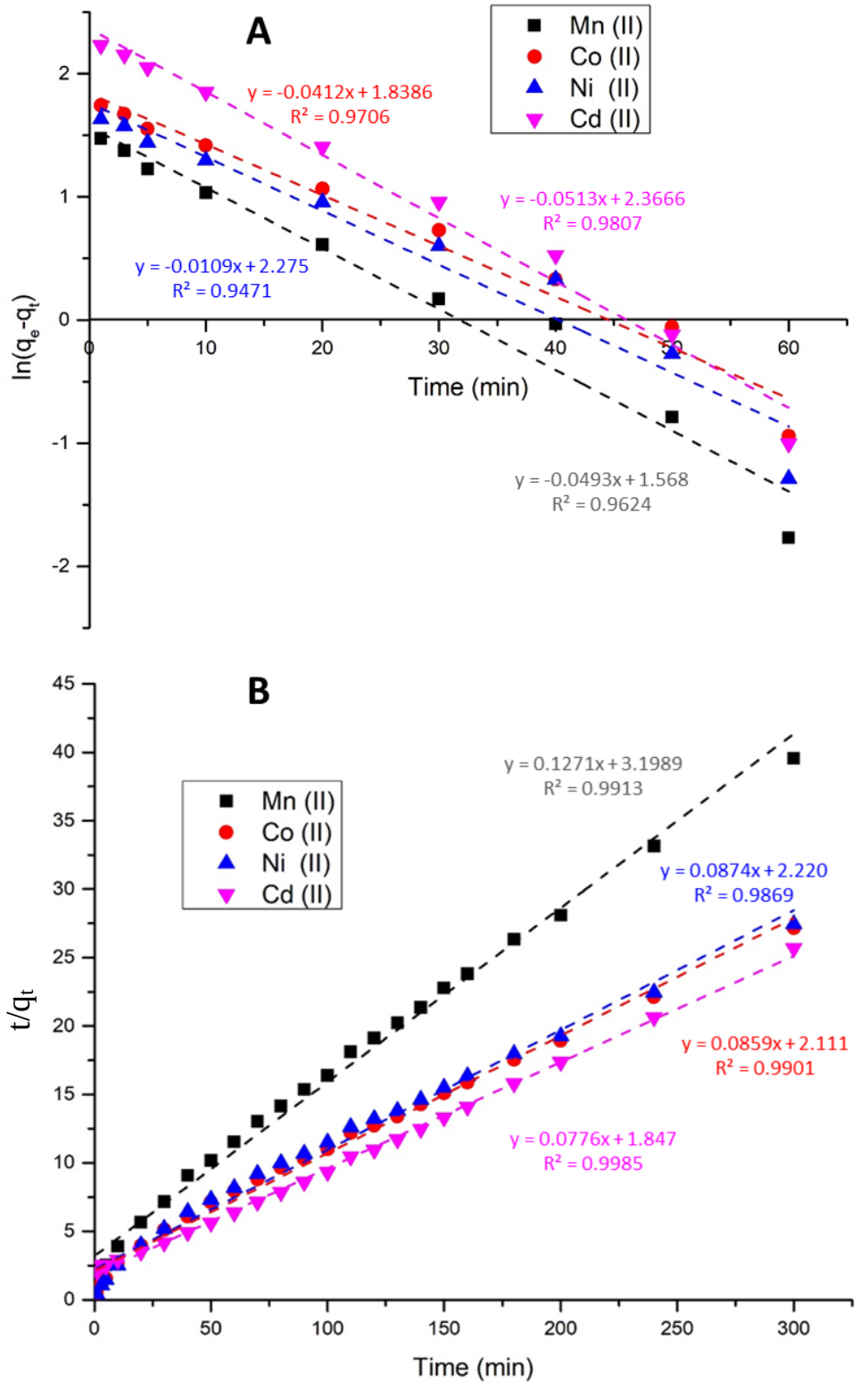


Figure 5-18: Kinetics plots for metal ion adsorption on geopolymer adsorbent (A-PFO; B-PSO plot). The presented data is for the MR-3 geopolymer.

Moreover, the statistical coefficients confirmed that the data better fits the PSO model. This model is more applicable to describe the sequestration of the metal ions on the geopolymer surface, indicating that the adsorption process was essentially chemisorption.

Nevertheless, although the PSO model explained the overall adsorption kinetics, information about the rate-limiting steps could not be highlighted. Therefore, the intraparticle diffusion models can be used to explain the likelihood of the intraparticle diffusion. The intra-particle diffusion model was used to evaluate the rate-limiting steps and diffusion processes in the metal ions adsorption on the mudstone geopolymer.

Generally, three diffusion adsorption stages are proposed: film diffusion, intra-particle diffusion and equilibrium adsorption. The intra-particle diffusion model is represented by the Weber-Morris equation (5-9).[33]

$$q_t = k_{id} t^{0.5} + C \qquad (5-9)$$

Where k_{id} is the IPD rate constant (mg g^{-1} $min^{-0.5}$), C describes the boundary layer thickness. The plot of q_t versus $t^{0.5}$ in Figure (5-19) shows multilinear sections on the surface of geopolymer and deviate from origin. The deviation from the origin reflects the differences in the mass transfer rate during the adsorption stages (initial and final). Moreover, this reflects the presence of some degree of a boundary layer control.[34] The first linear segment reflects the mass transfer prevalence where the Cd^{2+}, Co^{2+}, Ni^{2+} and Mn^{2+} transferred from the bulk solution to the geopolymer surface. This stage is relatively rapid with a higher k_{id} (0.73, 0.71, 0.78 and 1.57 mg g^{-1} $min^{-0.5}$ for Mn^{2+}, Ni^{2+}, Co^{2+} and Cd^{2+}, respectively) and a smaller boundary layer thickness.

As indicated in Table (5-7), the IPD rate constant decreases ($k_{id1}>k_{id2}>k_{id3}$) as time increases, which can be attributed to the increase in the boundary layer thickness (C) with time ($C_1<C_2<C_3$). The higher the values of C, the higher the effect of the boundary layer on the adsorption of Cd^{2+}, Co^{2+}, Ni^{2+} and Mn^{2+}.

Table 5-7: Intraparticle diffusion parameters for sequestrating Mn^{2+}, Ni^{2+}, Co^{2+} and Cd^{2+} onto geopolymers

Metal	Intraparticle diffusion parameters								
	Segment	k_{id1} (mg g^{-1} $min^{-0.5}$)	C	R^2	RSS	MSE	Persons'r	F value	Prob>F
Mn^{2+}	1	0.7327	0.266	0.9969	0.018	0.004	0.9987	1638.73	2.2252 E-6
	2	0.4360	1.769	0.9830	0.028	0.005	0.9929	349.20	8.0790 E-6
	3	0.2127	3.985	0.9722	0.047	0.005	0.9876	316.55	1.0194 E-7
Ni^{2+}	1	0.7126	1.762	0.9974	0.114	0.011	0.9988	4221.98	1.809 E-14
	2	0.4986	3.645	0.9605	0.028	0.007	0.9841	122.821	3.7704 E-4
	3	0.2434	6.814	0.9196	0.051	0.017	0.9694	46.7835	0.0064
Co^{2+}	1	0.7843	1.459	0.9972	0.148	0.014	0.9987	3943.10	2.5535 E-14
	2	0.4459	4.532	0.9304	0.041	0.010	0.9717	67.8670	0.00118
	3	0.2091	7.511	0.9171	0.039	0.013	0.9684	45.2643	0.0067
Cd^{2+}	1	1.5753	-1.344	0.9954	0.128	0.032	0.9981	1086.51	5.05149 E-6
	2	0.6099	4.577	0.9239	0.379	0.063	0.9668	85.9793	8.8950 E-5
	3	0.10935	9.890	0.8854	0.045	0.006	0.9485	62.8331	9.6659 E-5

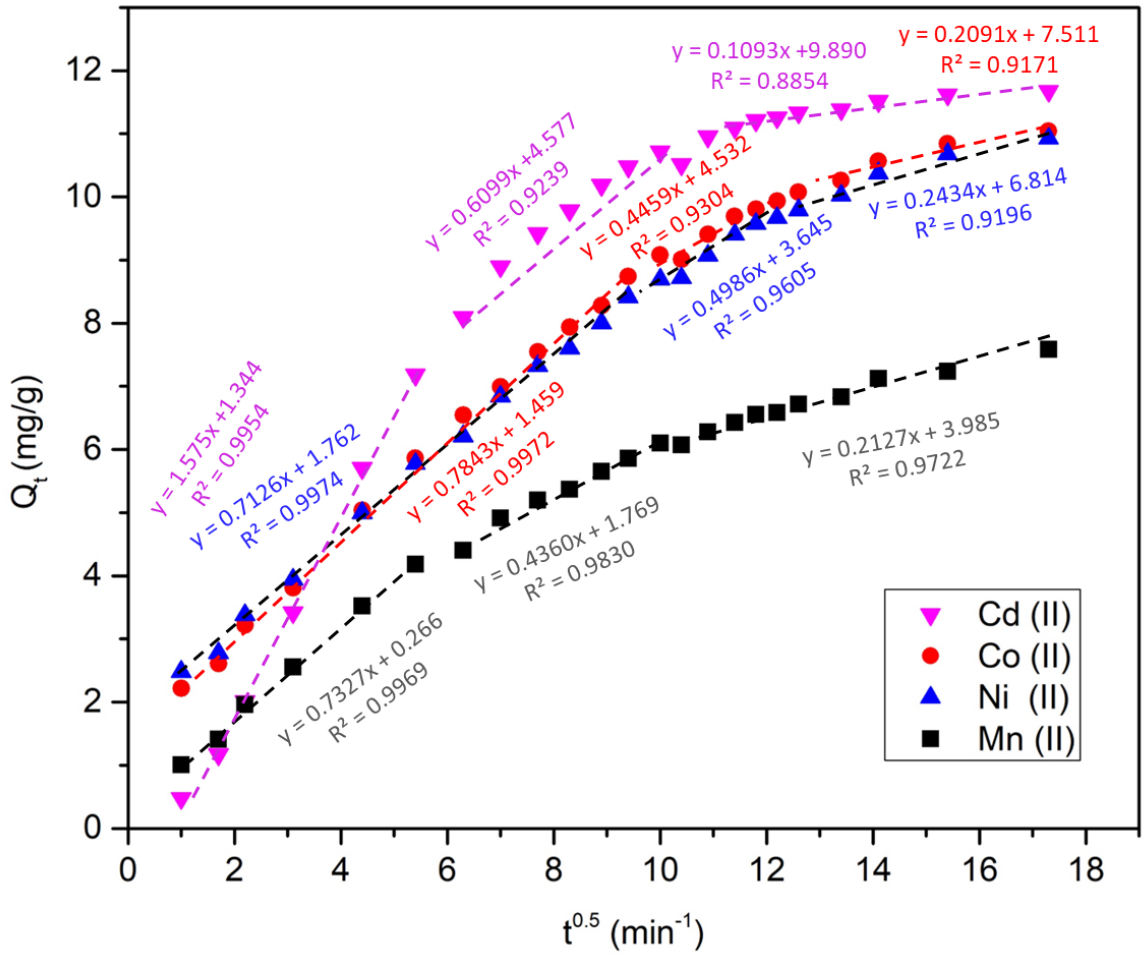


Figure 5-19: Intra particle diffusion plot for adsorption of metal ions on geopolymer adsorbent. The presented data is for the MR-3 geopolymer.

5.3.2.5 Adsorption isotherms

The interaction between Mn^{2+}, Ni^{2+}, Co^{2+} and Cd^{2+} and the surface of geopolymer adsorbent was examined using the Langmuir and Freundlich models which are represented by the empirical equations (5-10) and (5-11), respectively.[35-37] The Langmuir isotherm assumes monolayer adsorption where the adsorbate is chemically bound to the surface of the adsorbent with equal affinities of all sites for the metal ion.

$$\frac{C_e}{q_e} = \frac{1}{q_m b} + \frac{C_e}{q_m} \qquad (5\text{-}10)$$

q_e is the adsorption capacity (mg/g) at equilibrium, C_e represents the equilibrium concentration (mg/L), q_m is the Langmuir adsorption capacity, and b is the Langmuir constant (L/mg). Freundlich isotherm represents a heterogenous multilayer adsorption on the surface of the adsorbent and is represented by the following equation:

$$\log q_e = \log K_F + \frac{1}{n} \log C_e \qquad (5\text{-}11)$$

Where 1/n stands for the Freundlich heterogeneity factor, and K_F ((mg/g)/(mg/L)^n) stands for the Freundlich affinity constant. The calculated isotherm parameters are presented in Table (5-8). The plots of Freundlich isotherm (log q_e vs log C_e) and Langmuir isotherm (C_e/q_e vs C_e) are shown in Figure (5-20). According to the calculated statistical coefficients, the adsorption of all metal ions at the surface of geopolymer showed a better fit with the Langmuir isotherm. Accordingly, the adsorption process is monolayer and chemosorption in nature, which is consistent with the thermodynamics, shown below.

Table 5-8: Adsorption isotherm parameters for adsorption of metal ions on geopolymer adsorbents.

Langmuir isotherm parameters									
Metal	**q_e (Exp.)**	**q_m (mg g^{-1})**	**b (L mg^{-1})**	**R^2**	**RSS**	**MSE**	**Pearson's r**	**F Value**	**Probe>F**
Mn^{2+}	7.75	7.97	0.1443	0.9729	1.97	0.494	0.98913	181.03	1.76518 E-4
Ni^{2+}	15.58	17.23	0.0663	0.8868	1.67	0.419	0.95367	40.193	0.00317
Co^{2+}	14.62	15.62	0.097	0.9407	1.05	0.263	0.97601	80.36	8.56687 E-4
Cd^{2+}	20.32	21.28	0.1689	0.9824	0.15	0.037	0.99296	281.181	7.41227 E-5
Freundlich isotherm parameters									
Metal	**q_e (Exp.)**	**K_f ((mg/g)/(mg/L)^n)**	**1/n**	**R^2**	**RSS**	**MSE**	**Pearson's r**	**F Value**	**Probe>F**
Mn^{2+}	7.75	3.63	0.1458	0.7212	0.01	0.002	0.88149	13.9386	0.02024
Ni^{2+}	15.58	3.96	0.2716	0.8586	0.019	0.004	0.94176	31.373	0.00499
Co^{2+}	14.62	4.83	0.2212	0.8907	0.011	0.002	0.9553	41.763	0.00295
Cd^{2+}	20.32	6.97	0.2428	0.9870	0.002	5.018 E-4	0.99482	382.980	4.02047 E-5

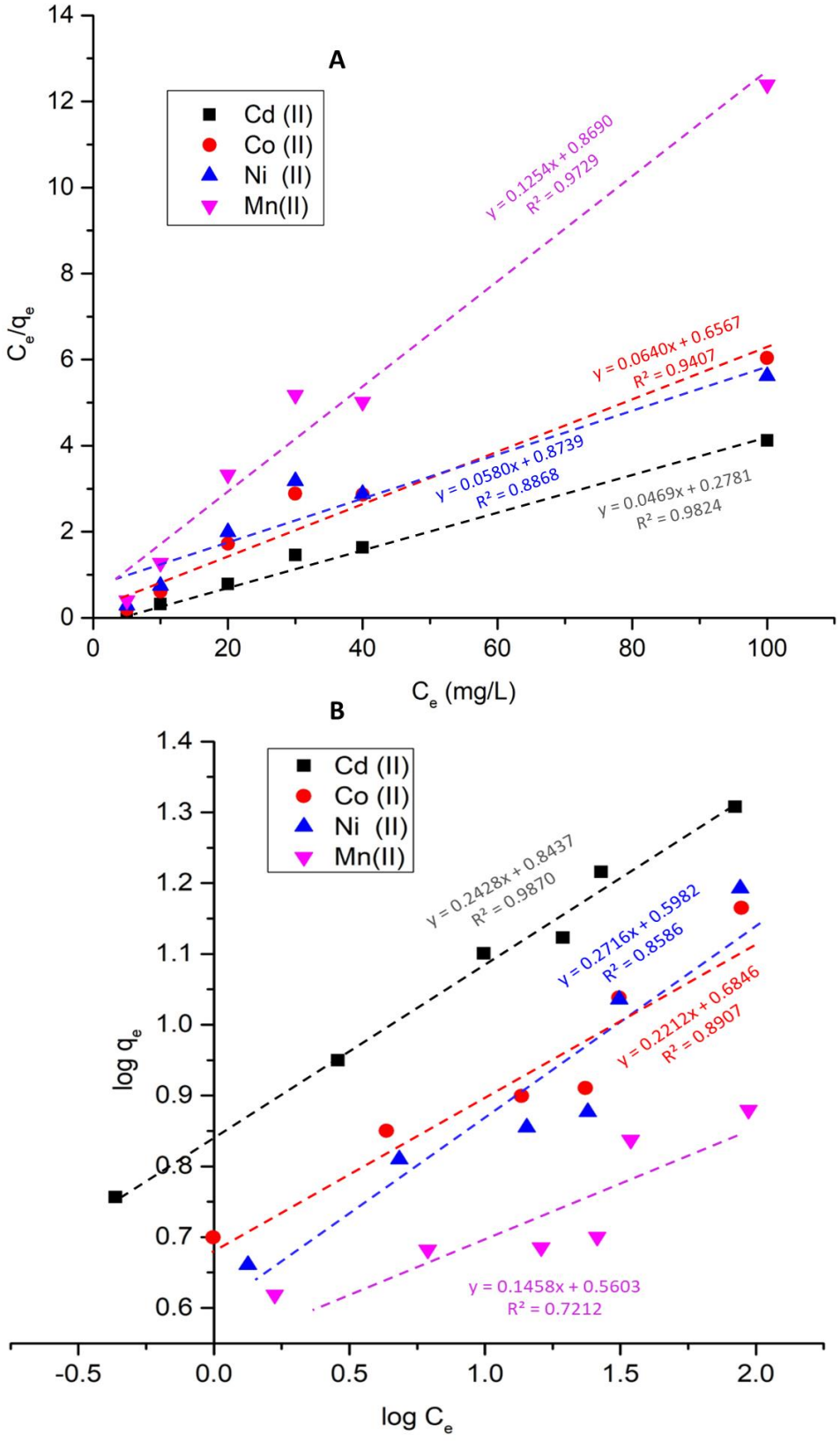


Figure 5-20: Adsorption isotherm for metal ions adsorption (A-Langmuir isotherm, B-Freundlich isotherm). The presented data is for the MR-3 geopolymer.

Moreover, the Langmuir maximum adsorption capacity indicated a selectivity adsorption affinity in the order 21.28, 15.63, 17.23 and 7.97 mg/g for the Cd, Co, Ni and Mn, respectively. The separation factor (R_L) is the distinguished index of the Langmuir model which defines the adsorption efficiency, and is expressed by the following equation:

$$R_L = \frac{1}{1+bC_o} \qquad (5\text{-}12)$$

Where b is Langmuir constant (L/mg), and C_o is the initial concentration (mg/L). The adsorption is unfavourable when $R_L>1$, favourable ($0 < R_L< 1$) and irreversible when ($R_L=0$). The obtained R_L values ranged from 0.05 to 0.54 for Cd^{2+}, 0.09 to 0.67 for Co^{2+}, 0.13 to 0.75 for Ni^{2+}, and from 0.06 to 0.58 for Mn^{2+}. As indicated in Figure (5-21) the calculated R_L for all metal ions were between 0 and 1 indicating a favourable adsorption processes.[38]

Table 5-9: Langmuir separation factor (R_L) calculations.

Metal	**C_i**	**b**	**R_L**	**Metal**	**b**	**R_L**	**Metal**	**b**	**R_L**	**Metal**	**b**	**R_L**
Mn^{2+}	5	0.1443	0.58	Ni^{2+}	0.0663	0.75	Co^{2+}	0.097	0.67	Cd^{2+}	0.1689	0.54
	10		0.40			0.60			0.50			0.37
	20		0.25			0.42			0.34			0.22
	30		0.18			0.33			0.25			0.16
	40		0.14			0.27			0.20			0.12
	100		0.06			0.13			0.09			0.05

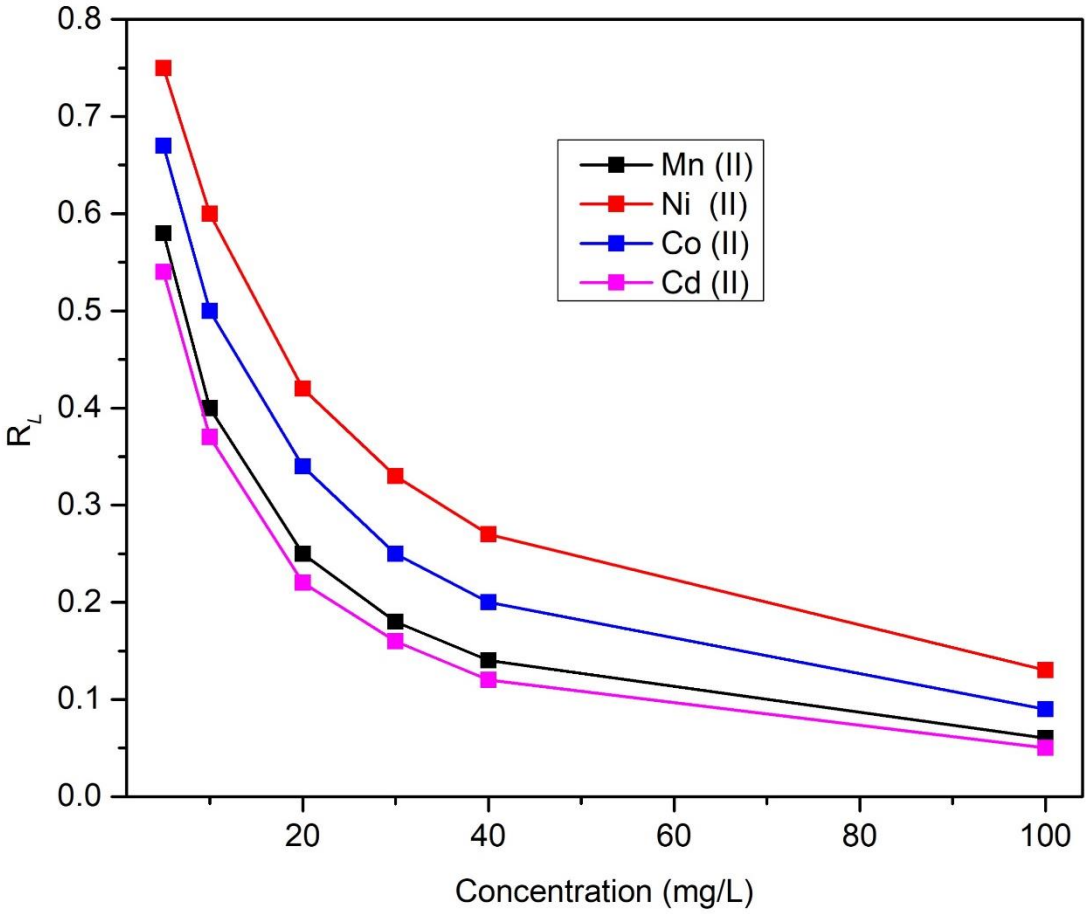


Figure 5-21: Langmuir separation factor as a function of metal initial concentration. The presented data is for the MR-3 geopolymer.

5.3.2.6 Thermodynamic study

The thermodynamic study was performed in the temperature range 298-328 K to determine the thermodynamic parameters. These parameters are important to evaluate the spontaneity degree and related energy requirements. The reaction thermodynamics were calculated using the Van't Hoff equations as per Figure (5-22) and equations (5 – 13), (5 – 14) and (5 – 15).[39]

$$\ln K_d = \frac{\Delta S^0}{R} - \frac{\Delta H^0}{RT} \qquad (5-13)$$

$$Kd = \frac{q_e}{C_e} \qquad (5-14)$$

$$\Delta G^0 = \Delta H^0 - T\Delta S^0 \qquad (5-15)$$

Where T is the absolute temperature (K), and R is the universal gas constant (8.314 J/mol K), K_d is the thermodynamic distribution factor. The ΔS^0(J mol^{-1} K^{-1}), ΔG^0 (kJ mol^{-1}) and ΔH^0 (kJ

mol^{-1}) are the change in entropy, free energy, and enthalpy, respectively. The calculated ΔH^0 and ΔS^0 values are presented in Table (5-10). As indicated, the calculated ΔG^0 values for all metal ions were negative except for the Mn^{2+} at 298 K. The reaction was spontaneous with increasing temperatures and was a non-spontaneous for the Mn^{2+} at 298 K (+ve ΔG^0 values). Th ΔH^0 values were positives indicating that the removal of metal ions was controlled by an endothermic adsorption process. In addition, the increase in the negativity of ΔG^0 rose at higher temperature, indicating that the sequestration of metal ions is favourable at the elevated temperatures.[40] The negative value of ΔS^0 for all metal ions reflected a low randomness (stable arrangement) of metal ions on the geopolymer surface during the adsorption process, confirming a chemical adsorption phenomenon, which occur through the ion exchange interactions.[34]

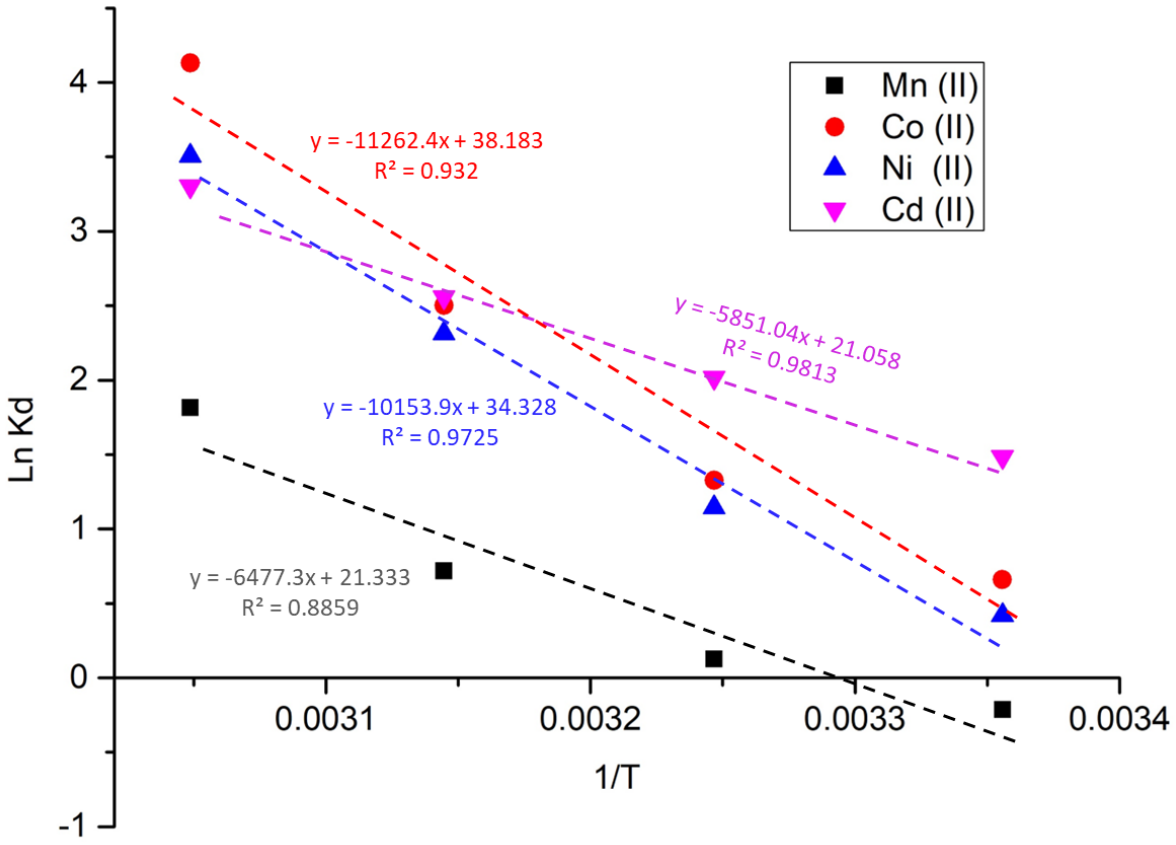


Figure 5-22: Van't Hoff plot of 1/T versus $\ln k_d$. The presented data is for the MR-3 geopolymer.

Table 5-10: Calculated thermodynamic parameters and related statistical analysis.

Metal	T (K)	$\triangle H^0$	$\triangle S^0$	$\triangle G^0$	R^2	RSS	MSE	Pearson's r	F value	Prob>F
Mn^{2+}	298	0.053	-0.175	0.526	0.885	0.18	0.090	-0.961	24.29	0.038
	308			-0.32						
	318			-1.90						
	328			-4.95						
Co^{2+}	298	0.093	-0.317	-1.63	0.932	0.30	0.154	-0.977	43.05	0.022
	308			-3.40						
	318			-6.61						
	328			-11.2						
Ni^{2+}	298	0.084	-0.285	-1.04	0.972	0.10	0.050	-0.990	107.22	0.009
	308			-2.92						
	318			-6.11						
	328			-9.56						
Cd^{2+}	298	0.048	-0.175	-3.67	0.981	0.02	0.011	-0.993	158.9	0.006
	308			-5.16						
	318			-6.76						
	328			-9.01						

5.3.2.7 Dynamic adsorption

The sorption capacity of geopolymer adsorbent was evaluated in a continuous dynamic mode. The effect of bed depth on the adsorption removal of metal ions at a constant flow rate (0.016 L/h) was investigated. The influent concentration was 10 mg/L for each metal ion and the initial solution pH was adjusted to 6.5 (lowest pH in the study area was 6.8). The breakthrough curves are shown in Figure (5-23). As shown, the increase in the bed height from 4 to 9 cm increases the adsorption removal of Mn^{2+}, Co^{2+}, Ni^{2+} and Cd^{2+} from 61.5%, 72.2%, 70.8% and 66.9% to 97.1%, 96.5%, 96.8% and 96.9%, respectively. The adsorption capacity at 50% breakthrough capacity increased from 800, 1333.33, 1333.33 and 1600 to 3200, 4800, 5200 and 6000 mg/g for Mn^{2+}, Co^{2+}, Ni^{2+} and Cd^{2+}, respectively. This indicated that the increase in the bed depth increase the adsorption capacity due to the increase in the total surface area, providing more sorption sites. Faster breakthrough curve was noticed for a bed depth of 4 cm, while it was slowest at bed depth of 9 cm. At higher bed depth the column is difficult to exhaust, and more time is needed due to the low influent concentration, while at bed depth 4 cm, the column is expected to exhaust after 500 min. Moreover, the empty bed contact time (EBCT) increased from 0.158 min at bed depth of 4 cm to 0.357 min at the bed depth of 9 cm, indicating a high diffusion.[41] The breakthrough curves of the four metal ions showed a gradual increase rather than a steep increase. The gradual increase assumed a high competition for sorption sites on the geopolymer surface. As indicated, the breakthrough order is Mn^{2+} first then Ni^{2+}, Co^{2+}, and

Cd^{2+}. Accordingly, the CRM geopolymer has a stronger metal uptake affinity for Cd^{2+} than the other three metal ions, which was confirmed in the batch adsorption mode.

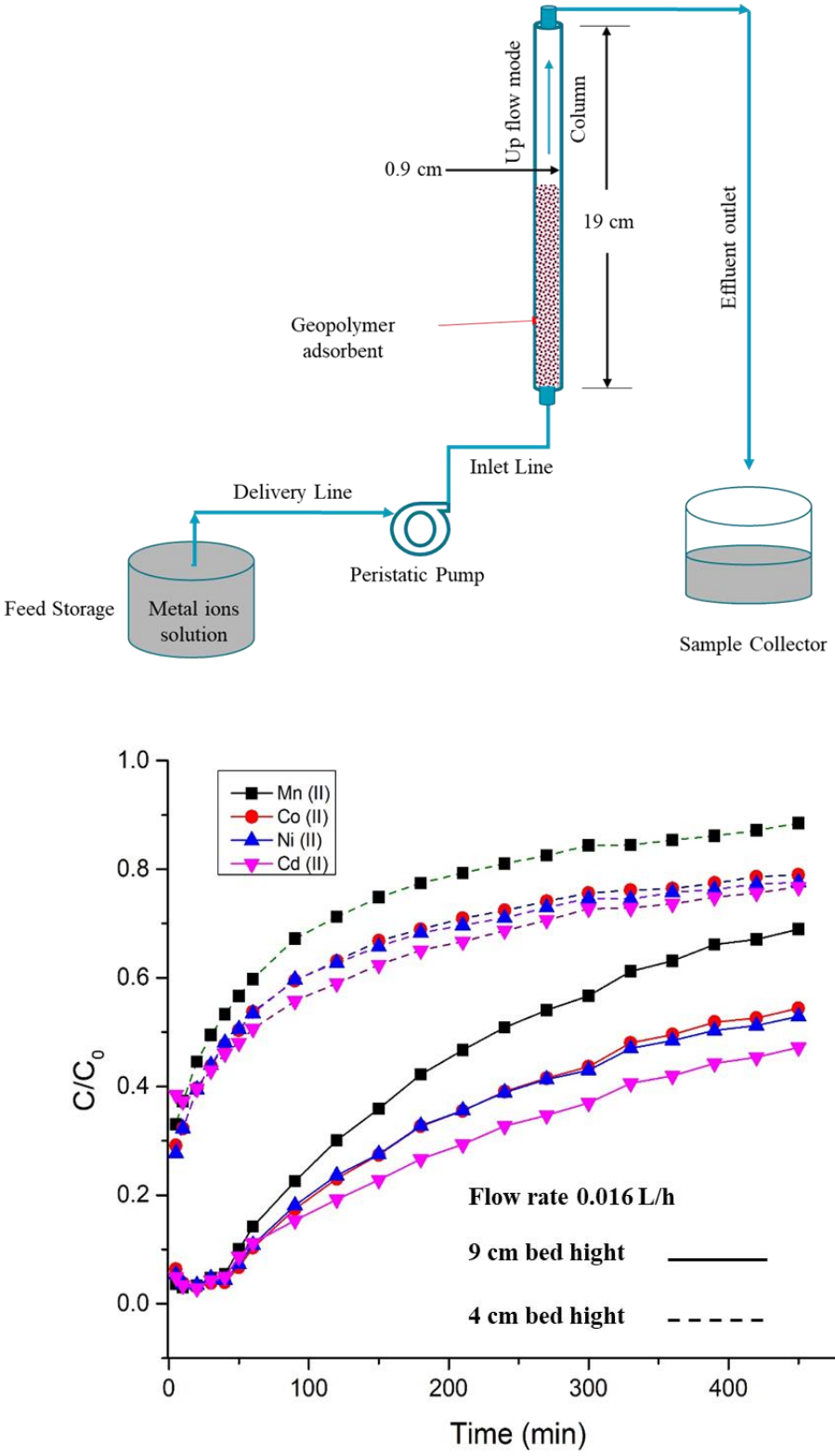


Figure 5-23: Column experiment design and breakthrough curves at different bed hight. The presented data is for the MR-3 geopolymer (Refer to Appendix C-10).

5.3.2.8 Reusable capacity of CRM geopolymer

The recyclability of the geopolymer adsorbent was evaluated and the obtained results are depicted in Figure (5-24). The experiment was conducted using a 10 mg/L initial concentration at 25 ^{0}C, where HNO_3 was used as an eluent. The geopolymer adsorbent showed a good recyclability and can be used for more than 8 cycles. The removal efficiency reduced from 94.04, 94.43, 92.60 and 95.30 for Mn^{2+}, Co^{2+}, Ni^{2+} and Cd^{2+}, respectively to 51.4, 54.4, 52.3 and 56.2 % after 8 cycles. The reduction in the removal capacity is attributed to the disintegration of the geopolymer structure impacted by hydrogen ions which cause rapturing of the Al-O bonds.[42] The CRM can be repeatedly used and can be considered as a potential candidate for the practical contaminant removal.

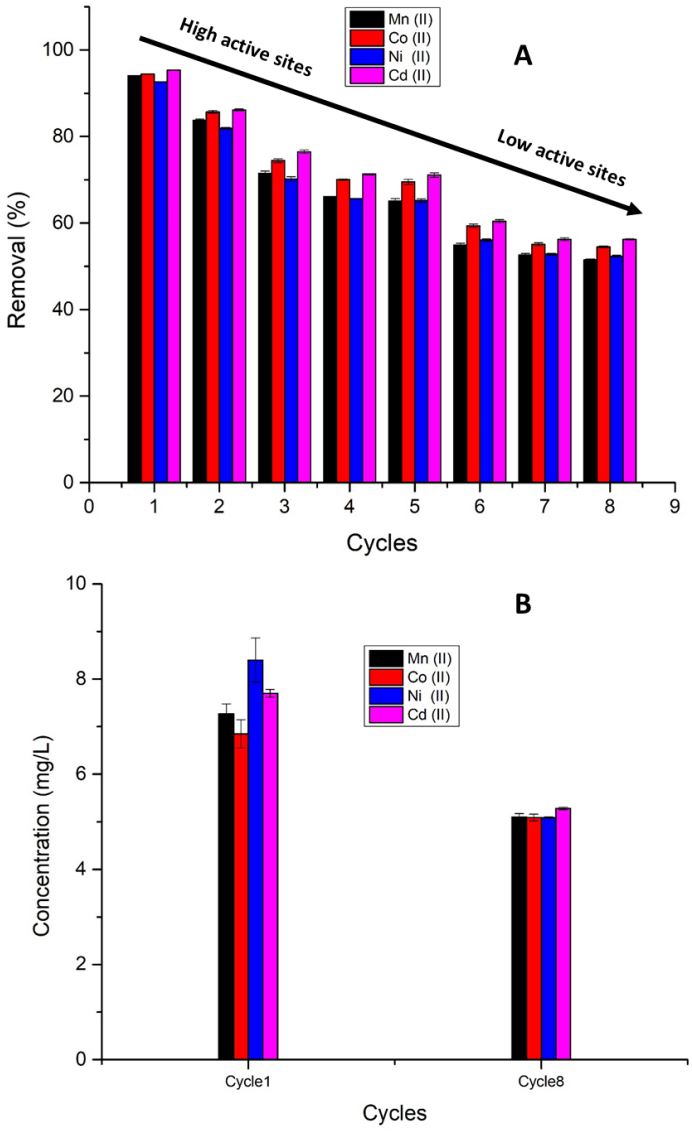


Figure 5-24: A) regeneration of the CRM geopolymer, and B) recovery of metal ions at first and last cycles. The presented data is for the MR-3 geopolymer (Refer to Appendix C-11).

5.3.2.9 A pilot study for groundwater decontamination

The applicability of the formulated geopolymer adsorbent in the real application was examined using natural groundwater samples from the Golden Triangle. The complex competitive effects of the different heavy metals in the real groundwater should be considered. Three samples, LQ1, KH and QH2 were collected from different locations (Nile Valley, Crystalline rocks zone, Coastal zone), reflecting various water chemistries, Figure (5-25). The groundwater in the study area has a complex chemistry where several factors and interferences control the metal ion sequestration. The groundwater samples were spiked with heavy metals solution (10 mg/L). Surprisingly, the sequestration of metal ions from the three samples exhibited the adsorption selectivity shown in the earlier batch and dynamic adsorption experiments. In addition, the removal efficiencies of the metal ions reached an acceptable level after 120 minutes of reaction as shown in Figure (5-26). It has been reported that the ionic strength of the aqueous solution can reduce the accessibility of surface active sites of the adsorbent.[43, 44] Moreover, the presence of other cationic species (Na^+, Ca^{2+}, Mg^{2+}, K^+…..etc) negatively impacted the concentration of the other electrostatically bound counterions that neutralize the negative charge on the adsorbent surface.[45] The high concentration of Cl^- ions favour the formation of metal chloride complexes (MCl_3^-, MCl_2, and MCl_4^{2-}) decreasing the population of free metal ions in the aqueous solution.[46, 47] Consequently, the magnitude of interactions between the metal ions and geopolymer active sites are reduced and hence decreased the metal adsorption capacity. As indicated in Chapter 3, the total dissolved solids for the QH2, LQ1 and KH are 572, 578 and 256 mg/L, respectively (Refer to Appendix A-1). Moreover, the concentration of Na^+, K^+, Ca^{2+} and Mg^{2+} ions were higher in the QH2 and LQ1 compared to the KH sample. This explains the efficiency of the adsorbent in removing metals ions of the KH compared to the QH2 and LQ2.

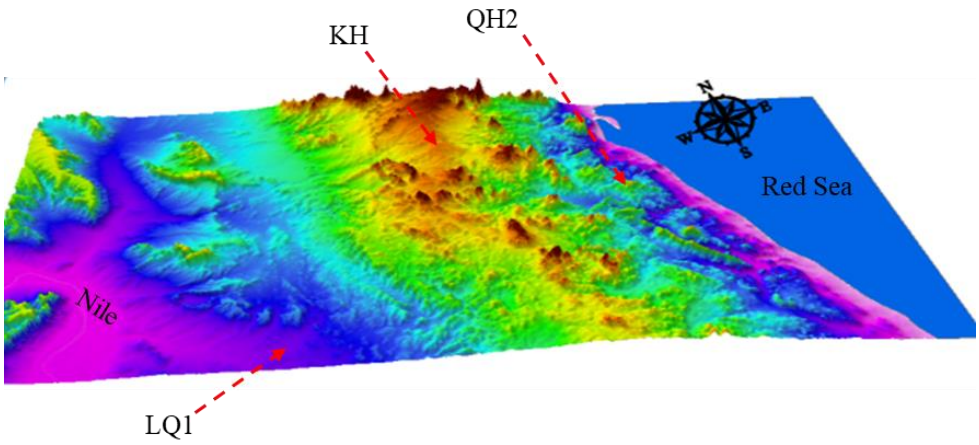


Figure 5-25: Groundwater samples location-Golden Triangle Economic Zone .

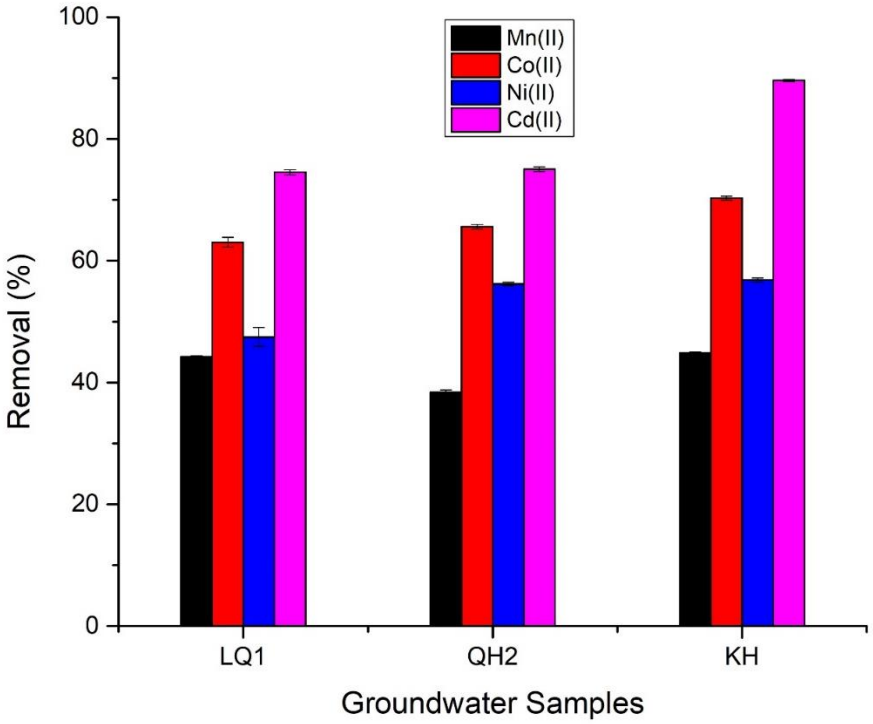


Figure 5-26: Metal ions removal from natural groundwater samples onto the CRM geopolymer. The presented data is for the MR-3 geopolymer (Refer to Appendix C-12).

5.3.2.10 Effect of co-existing anions

The presence of various anions in the natural water or wastewater effluents is expected. Therefore, the removal efficiency of the CRM geopolymer was evaluated in the presence of various anions to ensure the applicability under various scenarios. The experiments were conducted in the presence of 10 mg/L of metal ions (M^{2+}) and various concentrations of the co-existing anions (SO_4^{2-}, Cl^-, and CO_3^{2-}) in the range of 0.5 – 800 mg/L.

The dominant anions in groundwater of the Golden Triangle were SO_4^{2-}, Cl^-, and CO_3^{2-}.[48, 49] Figure (5-27) shows that the removal selectivity of all metal ions remained in the order $Cd^{2+}>Co^{2+}>Ni^{2+}>Mn^{2+}$. The removal of cadmium was influenced by the Cl^- concentration, where the removal percentage decreased from 76% to 58.7% when the Cl^- concentration increased from 0.5 to 800 mg/L, respectively. The removal of Mn^{2+}, Co^{2+} and Ni^{2+} experienced a similar decrease up to 400 mg/L and then increased at 800 mg/L. The presence of sulfate in the aqueous solution moderately interfered with the removal of cadmium; when the SO_4^{2-} concentration increased from 0.5 to 800 mg/L, the cadmium concentration decreased from 73.0 % to 65.8%. The same behaviour was noticed in the case of Mn^{2+}, Co^{2+}, and Ni^{2+}. Generally,

the CRM geopolymer is negatively charged and the sequestration of anions is not expected. However, the presence of such anions can supress the adsorption process by forming a metal-carbonate, sulfate and chloride complexes which hinder the removal of metal ions. As indicated, the significant impact on the removal of metal ions was noticeable in the presence of Cl^- compared to SO_4^{2-} and CO_3^{2-}.

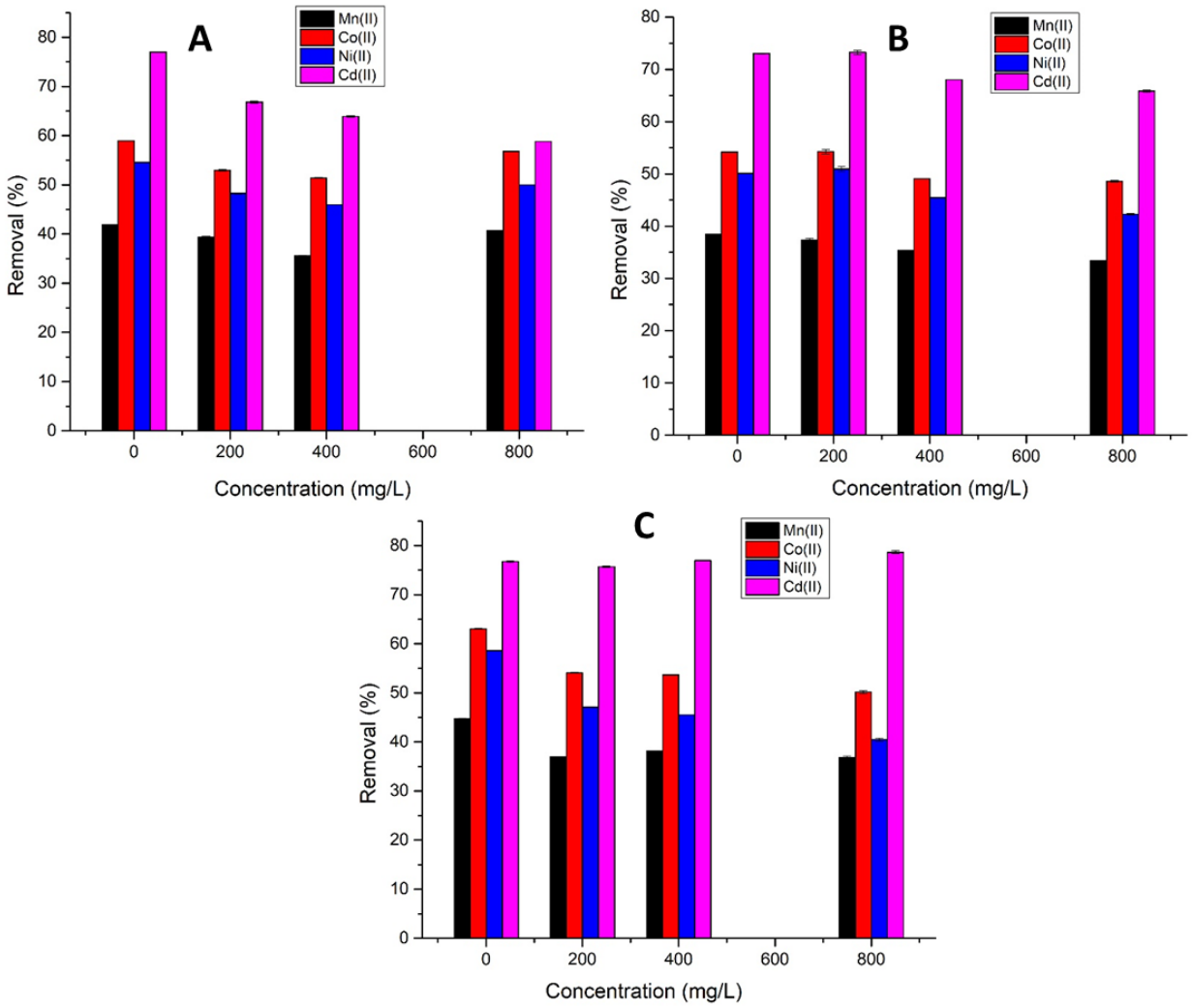


Figure 5-27: Effect of co-existence anions on metal ions removal. A) chlorides, B) sulphates, C) carbonates. The presented data is for the MR-3 geopolymer (Refer to Appendix C-13).

5.3.2.11 EDX analysis after adsorption

The adsorption of metal ions on the geopolymer adsorbent was evaluated by the energy dispersive x-ray analysis (EDX). Figure (5-28&29) show the EDX mapping and corresponding

spectrum before and after adsorption. The Cd^{2+}, Co^{2+}, Ni^{2+} and Mn^{2+} signals appeared after the adsorption process, confirming the sequestration in geopolymer cavities. The spatial distribution of Cd^{2+} is more extensive compared to other metal ions which is in accordance with other results, thus confirming a high selectivity for Cd^{2+}. Furthermore, there is a decrease in the Na, Ca, and K contents, suggesting that they were leached out from the geopolymer structure through an ion exchange reaction.

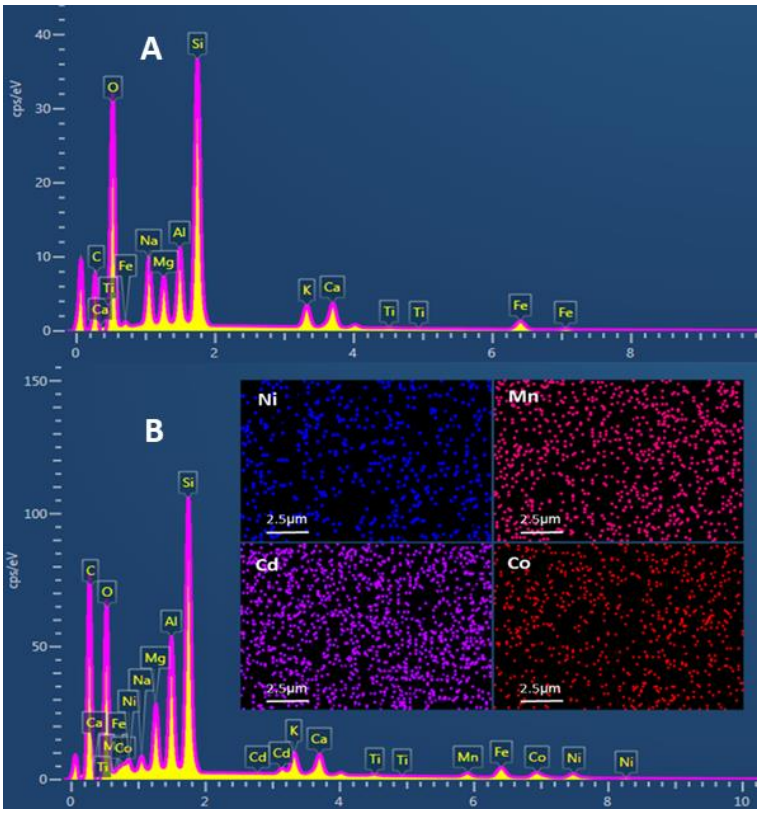


Figure 5-28: EDX spectrum of the CRM adsorbent. A-before adsorption, B- after adsorption. The presented data is for the MR-3 geopolymer.

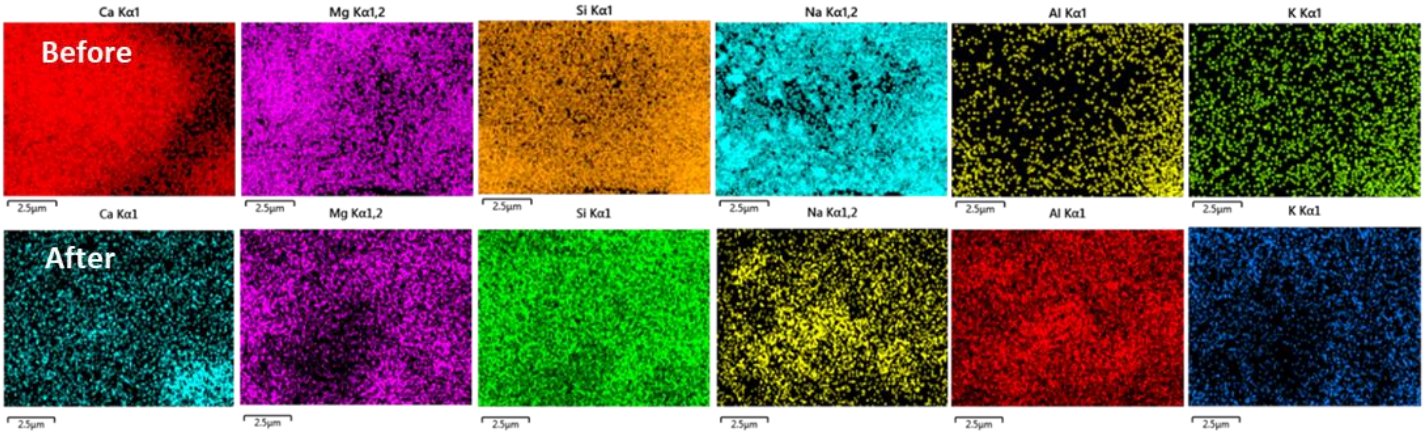


Figure 5-29: Elemental mapping for the CRM geopolymer before and after adsorption. The presented data is for the MR-3 geopolymer.

5.3.2.12 Mechanism of metal ions sequestration on CRM geopolymer

Figures (5-30) illustrates the mechanism of metal ions sequestration on the geopolymer adsorbent. The cation exchange of Na^{+}, Ca^{2+}, K^{+} and Mg^{2+} by Mn^{2+}, Co^{2+}, Ni^{2+} and Cd^{2+} can be considered as the primary mechanism of sequestration. This assumption was further supported by the adsorption kinetics and isotherms and the thermodynamic study, which confirmed that the interaction between the adsorbent and metal ions was a chemical process. Moreover, the EDX analysis and the CEC confirmed the prevalence of an ion exchange mechanism. Additionally, the mesoporous nature of the CRM geopolymer provides suitable transport channels for cation leaching and ion exchange interactions. However, complexation of the metal ions with the surface OH^{-} groups and electrostatic interaction processes also contributed to the metal ion sequestration.

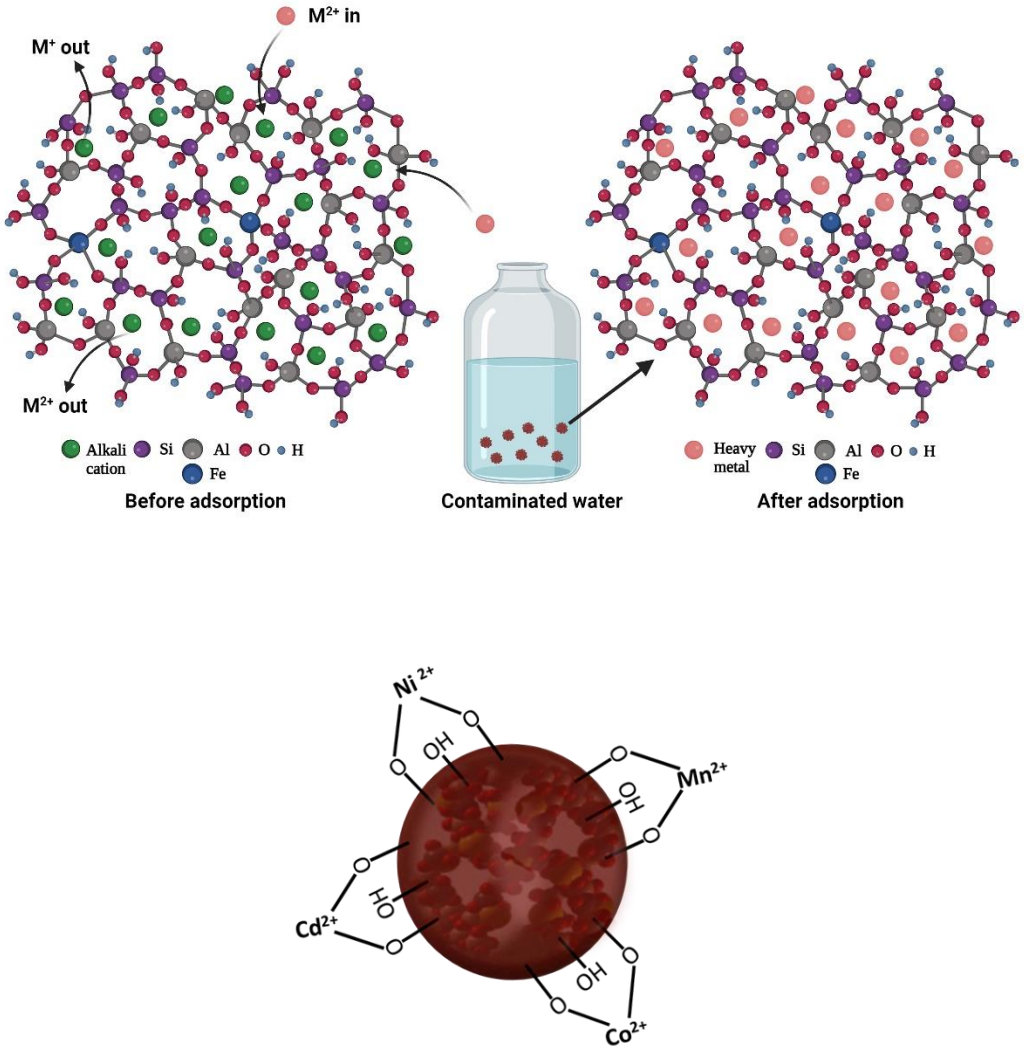


Figure 5-30: Mechanism of metal ions sequestration on the CRM geopolymer adsorbent.

5.3.2.13 Geopolymer active sites saturation

The surface adsorption saturation of the geopolymer adsorbent was determined, and the number of adsorbed atoms of Cd^{2+}, Co^{2+}, Ni^{2+} and Mn^{2+} was calculated, estimating both the occupied and/or unsaturated sorption sites, as shown in Figure (5-31). In the case of Cd^{2+}, the number of adsorbed atoms on the geopolymer surface reduced from 1.42×10^{25} to 7.19×10^{24} and decreased for Ni^{2+} from 1.54×10^{25} to 4.14×10^{24}, for Co^{2+} from 1.34×10^{25} to 4.01×10^{24}, and for Mn^{2+} from 1.87×10^{25} to 4.47×10^{24}. The decrease in the number of adsorbed atoms is attributed to the increase in the surface area, at constant metal ion concentration, which resulted in an increase in the proportion of the unsaturated active sites. In contrast, the geopolymer surface was saturated with the Cd^{2+}, Co^{2+}, Ni^{2+} and Mn^{2+} at low surface area, and active sites were extensively occupied.

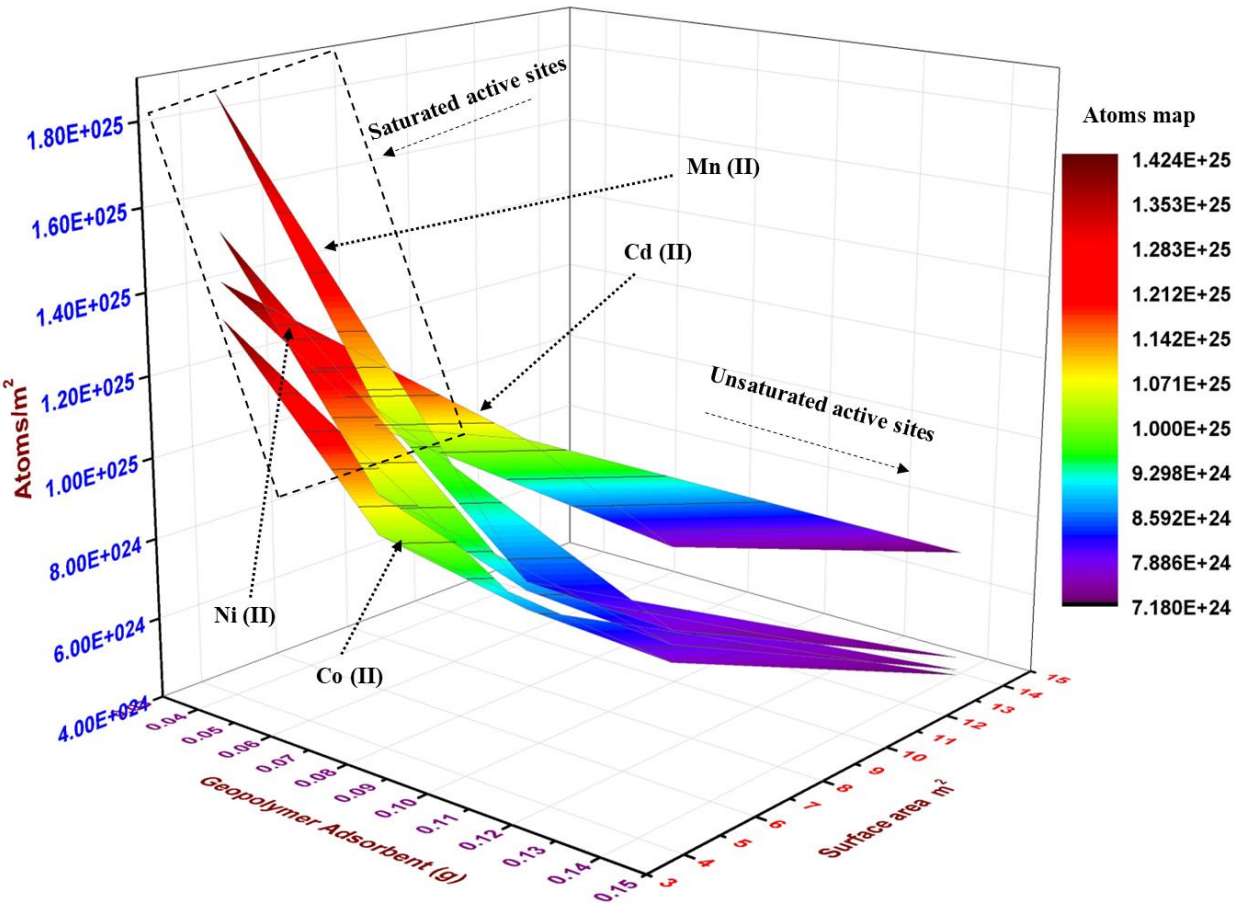


Figure 5-31: Surface saturation of the CRM geopolymer adsorbent. The presented data is for the MR-3 geopolymer.

5.3.2.14 Adsorption selectivity interpretation

The removal of the four metal ions, under similar experimental conditions, indicated that the adsorbent affinity followed the order $Cd^{2+}>Co^{2+}>Ni^{2+}>Mn^{2+}$, which was ascribed to the physicochemical characteristics of both the metal ions and geopolymer. The calculated adsorption selectivity ratio was 0.342, 0.251, 0.277 and 0.128 for the Cd^{2+}, Co^{2+}, Ni^{2+} and Mn^{2+}, respectively. Therefore, the removal selectivity of metal ions from a multicomponent system can be demonstrated in terms of the relative affinity of the solute towards the solid and liquid phases.[50] This behaviour is controlled by the difference in the ionic radius of the metal ions, distribution and nature of active groups on the geopolymer surface, and the nature of interaction between the metal ions and geopolymer, which can be further discusses as follow:

- The ionic radius of Cd^{2+}, Co^{2+}, Ni^{2+} and Mn^{2+} are 0.97, 0.72, 0.69 and 0.67 Å, respectively.[51-53] The Cd^{2+} showed the highest adsorption capacity and had the largest ionic radii. Therefore, the adsorption on the surface has a prevalent role and vital contribution to the adsorption capacity compared to the microporous adsorption which is less effective in the case of bigger ions.[54] This behaviour is clearer for the Cd^{2+} compared to the Co^{2+}, Ni^{2+} and Mn^{2+} ions.
- Metal ions with a smaller ionic radii has a larger hydration enthalpy, reducing their interaction with the adsorbent.[55]
- In case of the larger unhydrated ions, the charge density is low and more dispersed, therefore the hydration water is weakly held and hence a weaker binding of metal ions with the water molecules in the solution.[56] This explanation is acceptable for the studied metal ions. Since the ionic radii of the Cd^{2+} is bigger compared to the other metal ions, its affinity toward the geopolymer surface was high. Moreover, according to the thermodynamic study, the absolute values of ΔG^0 at 298 K for Cd^{2+}, Co^{2+}, Ni^{2+} and Mn^{2+} adsorption was in the order -3.67, -1.04, -1.63 and 0.526 kJ mol^{-1}, respectively. Therefore, the sorption of Cd^{2+} is more conducive compared to the co-existing metal ions.

5.4 Conclusion

The geopolymerization of calcined CRM resulted in the formation of a 3 D alumino-silicate framework. The cation exchange capacity increased from 26 cmol/kg in the raw material to 98 cmol/kg in the formed geopolymer. Moreover, the corresponding surface area reached up to 99 m^2/g with a mesoporous structure. The raw CRM showed a selective affinity for Cd^{2+}, Co^{2+}, Ni^{2+} and Mn^{2+} removal in the order of $Ni^{2+}>Co^{2+}>Mn^{2+}>Cd^{2+}$, while this order changed after geopolymerization to the order of $Cd^{2+}>Co^{2+}>Ni^{2+}>Mn^{2+}$, confirming a significant structural modification upon thermal activation. The adsorption selectivity ratios were 0.342, 0.251, 0.277 and 0.128 for Cd^{2+}, Co^{2+}, Ni^{2+}, and Mn^{2+}, respectively.

The adsorption behavior of the CRM geopolymer improved when the pH of the solution increased from 4 to 8 where the removal efficiency changed from 7.14, 12.5, 10.14, 17.1 to 45.6, 64.6, 61.6, 78.3 % for Mn^{2+}, Co^{2+}, Ni^{2+}, and Cd^{2+}, respectively. Additionally, its chemical stability decreased under highly acidic conditions, mostly below pH=4. Moreover, the CRM geopolymer adsorbent showed an improved adsorption capacity with the increase in the initial concentration of the metal ions solution from 5 to 100 mg/L, and reached up to 7.5, 14.6, 15.5, and 20.3 mg/g for Mn^{2+}, Co^{2+}, Ni^{2+}, and Cd^{2+}, respectively. The increase in the solution temperature from 25 °C to 55 °C induced the effective removal of Mn^{2+}, Co^{2+}, Ni^{2+}, and Cd^{2+} metal ions, reaching the maximum removal at 55 °C which confirmed an endothermic reaction.

Furthermore, the removal of the Cd^{2+}, Co^{2+}, Ni^{2+} and Mn^{2+} ions through dynamic mode showed that the formulated geopolymer can be used in an industrial scale basis. The increase in the column bed height from 4 to 9 cm increased the adsorption removal of Mn^{2+}, Co^{2+}, $Ni^{2+,}$ and Cd^{2+} from 61.5%, 72.2%, 70.8%, and 66.9% to 97.1%, 96.5%, 96.8%, and 96.9%, respectively. The increase in the bed depth was accompanied by an increase in the total surface area, providing more active sites to accommodate the co-existence heavy metals.

The interaction between the CRM geopolymer and Cd^{2+}, Co^{2+}, Ni^{2+} and Mn^{2+} ions was controlled by a chemical reaction and described by the pseudo-second-order model. Moreover, the adsorption isotherm could be explained by the Langmuir model, confirming a monolayer adsorption. The CRM geopolymer are recyclable and can be used at least 8 times. The ion exchange, surface complexation and electrostatic attraction are the main processes that controlled the mechanism of metal ions removal by the CRM geopolymer. The CRM geopolymer showed a high efficiency in treating a contaminated groundwater. The presence of

high TDS and Cl^- in groundwater supressed the removal of metal ions from the LQ1 and QH2 compared to the KH sample.

5.5 References

1. A. M. A. A. Tawfik, *Journal of Environmental Engineering and Landscape Management*, 2015, **23**, 288-294.
2. O. Al-Hashimi, K. Hashim, E. Loffill, T. Marolt Čebašek, I. Nakouti, A. A. H. Faisal and N. Al-Ansari, *Molecules*, 2021, **26**.
3. S. Balci, *Journal of Chemical Technology & Biotechnology*, 1996, **66**, 72-78.
4. A. Mora, J. Mahlknecht, L. Rosales-Lagarde and A. Hernández-Antonio, *Environmental Monitoring and Assessment*, 2017, **189**, 394.
5. M. K. Doula, *Water Research*, 2009, **43**, 3659-3672.
6. J. Davidovits, *Journal of thermal analysis*, 1989, **35**, 429-441.
7. G. Franchin, J. Pesonen, T. Luukkonen, C. Bai, P. Scanferla, R. Botti, S. Carturan, M. Innocentini and P. Colombo, *Materials & Design*, 2020, **195**, 109006.
8. I. Kara, D. Tunc, F. Sayin and S. T. Akar, *Applied Clay Science*, 2018, **161**, 184-193.
9. H. Javadian, F. Ghorbani, H.-a. Tayebi and S. H. Asl, *Arabian Journal of Chemistry*, 2015, **8**, 837-849.
10. T. Luukkonen, H. Runtti, M. Niskanen, E.-T. Tolonen, M. Sarkkinen, K. Kemppainen, J. Rämö and U. Lassi, *Journal of Environmental Management*, 2016, **166**, 579-588.
11. İ. Kara, D. Yilmazer and S. T. Akar, *Applied Clay Science*, 2017, **139**, 54-63.
12. R. P. Williams, R. D. Hart and A. van Riessen, *Journal of the American Ceramic Society*, 2011, **94**, 2663-2670.
13. M. A. Longhi, B. Walkley, E. D. Rodríguez, A. P. Kirchheim, Z. Zhang and H. Wang, *Composites Part B: Engineering*, 2019, **176**, 107172.
14. J. Liu, Y. Fang and O. Kayali, Shenzhen University, Shenzhen, Guangdong Province, P.R.China, 2016.
15. V. Ramasamy, P. Rajkumar and V. Ponnusamy, *Indian Journal of Physics*, 2009, **83**, 1295-1308.

16. J. Ji, Y. Ge, W. Balsam, J. E. Damuth and J. Chen, *Marine Geology*, 2009, **258**, 60-68.

17. P. Rożek, M. Król and W. Mozgawa, *Spectrochimica Acta Part A: Molecular and Biomolecular Spectroscopy*, 2018, **198**, 283-289.

18. O. A. Panitsa, D. Kioupis and G. Kakali, *Environ Sci Pollut Res Int*, 2022, DOI: 10.1007/s11356-022-20081-9.

19. H. Elsayed, F. Gobbin, M. Picicco, A. Italiano and P. Colombo, *Additive Manufacturing*, 2022, **56**, 102909.

20. L. Bouna, A. Ait El Fakir, A. Benlhachemi, K. Draoui, M. Ezahri, B. Bakiz, S. Villain, F. Guinneton and N. Elalem, *Applied Clay Science*, 2020, **196**, 105764.

21. M. Karatas, *Journal of Hazardous Materials*, 2012, **199-200**, 383-389.

22. S. Agarwal, I. Tyagi, V. K. Gupta, F. Golbaz, A. N. Golikand and O. Moradi, *Journal of Molecular Liquids*, 2016, **218**, 494-498.

23. W. Zhang, Y. An, S. Li, Z. Liu, Z. Chen, Y. Ren, S. Wang, X. Zhang and X. Wang, *Sci Rep*, 2020, **10**, 16453.

24. Z. Aksu and T. Kutsal, *Journal of Chemical Technology & Biotechnology*, 1991, **52**, 109-118.

25. A. I. S. Michael Horsfall Jnr, *Electronic Journal of Biotechnology* 2005, **8**.

26. M. E. Sumner and W. P. Miller, in *Methods of Soil Analysis*, 1996, DOI: https://doi.org/10.2136/sssabookser5.3.c40, pp. 1201-1229.

27. K. Pasupathy, J. Sanjayan and P. Rajeev, *Journal of Building Engineering*, 2021, **35**, 102029.

28. V. F. F. Barbosa, K. J. D. MacKenzie and C. Thaumaturgo, *International Journal of Inorganic Materials*, 2000, **2**, 309-317.

29. F. Škvára, L. Kopecký, V. Šmilauer and Z. Bittnar, *Journal of Hazardous Materials*, 2009, **168**, 711-720.

30. J.-P. Simonin, *Chemical Engineering Journal*, 2016, **300**, 254-263.

31. G. McKay, Y. S. Ho and J. C. Y. Ng, *Separation and Purification Methods*, 1999, **28**, 87-125.

32. S. J. Allen, Q. Gan, R. Matthews and P. A. Johnson, *Journal of Colloid and Interface Science*, 2005, **286**, 101-109.

33. W. J. Weber and J. C. Morris, *J. Sanitary Eng. Div ASCE 90*, 1964, **(SA3)**, 79-107.

34. T. Sheela, Y. A. Nayaka, R. Viswanatha, S. Basavanna and T. G. Venkatesha, *Powder Technology*, 2012, **217**, 163-170.

35. S. Mnasri-Ghnimi and N. Frini-Srasra, *Applied Clay Science*, 2019, **179**, 105151.

36. S. K. Lagergren, *Sven. Vetenskapsakad. Handingarl*, 1898, **24**, 1-39.

37. H. Freundlich, *Zeitschrift für physikalische Chemie*, 1907, **57**, 385-470.

38. R. Gupta, S. K. Gupta and D. D. Pathak, *Microporous and Mesoporous Materials*, 2019, **288**, 109577.

39. M. Xie, L. Zeng, Q. Zhang, Y. Kang, H. Xiao, Y. Peng, X. Chen and J. Luo, *Journal of Alloys and Compounds*, 2015, **647**, 892-905.

40. H. Faghihian, M. Moayed, A. Firooz and M. Iravani, *Comptes Rendus Chimie*, 2014, **17**, 108-117.

41. S. T. Ramesh, R. Gandhimathi, P. V. Nidheesh, N. Badabhagni and K. S. Bharathi, *Electronic journal of environmental, agricultural and food chemistry*, 2011, **10**, 2487-2505.

42. A. Filippidis, A. Godelitsas, D. Charistos, P. Misaelides and A. Kassoli-Fournaraki, *Applied Clay Science*, 1996, **11**, 199-209.

43. E. Aranda-García, L. Morales-Barrera, G. Pineda-Camacho and E. Cristiani-Urbina, *Environmental Monitoring and Assessment*, 2014, **186**, 6207-6221.

44. S. Barnie, J. Zhang, H. Wang, H. Yin and H. Chen, *Chemosphere*, 2018, **212**, 209-218.

45. S. Schiewer and B. Volesky, *Environmental Science & Technology*, 1997, **31**, 2478-2485.

46. I. Villaescusa, N. Fiol, M. a. Marťınez, N. Miralles, J. Poch and J. Serarols, *Water Research*, 2004, **38**, 992-1002.

47. K. E. ASS, *Global NEST Journal*, 2018, **20**, 198-207.

48. R. Amer, R. Ripperdan, T. Wang and J. Encarnación, *Journal of African Earth Sciences*, 2012, **69**, 13-25.

49. F. A. Abdalla and I. H. Khalifa, *Arabian Journal of Geosciences*, 2013, **6**, 1273-1282.

50. S. Sen Gupta and K. G. Bhattacharyya, *Advances in Colloid and Interface Science*, 2011, **162**, 39-58.

51. I. M. El-Naggar, K.A.Hebash, E. S. Sheneshen and E. A. Abdel-Galil, *Inorganic Chemistry: An Indian Journal*, 2014, **9**.

52. G. Renaudin, S. Gomes and J. M. Nedelec, *Materials (Basel)*, 2017, **10**.

53. D. D. Purkayastha, R. Brahma, M. G. Krishna and V. Madhurima, *Bulletin of Materials Science*, 2015, **38**, 203-208.

54. M. Chiban, A. Soudani, F. Sinan and M. Persin, *Colloids and Surfaces B: Biointerfaces*, 2011, **82**, 267-276.

55. S. Ricordel, S. Taha, I. Cisse and G. Dorange, *Separation and Purification Technology*, 2001, **24**, 389-401.

56. B. Tansel, J. Sager, T. Rector, J. Garland, R. F. Strayer, L. Levine, M. Roberts, M. Hummerick and J. Bauer, *Separation and Purification Technology*, 2006, **51**, 40-47.

CHAPTER 6: SUMMARY AND RECOMMENDATIONS

Heavy metals species and concentrations in the groundwater of the Golden Triangle area of Egypt have been assessed. In particular, the Thesis demonstrates the degree of groundwater contamination with heavy metals in the three zones of the study area taking into consideration the role of geogenic and anthropogenic activities. Moreover, a novel geopolymer adsorbent was successfully synthesized from a heterogeneous natural aluminosilicate precursor for the metal ions sequestration.

In chapter 3, heavy metals concentrations and species were determined based on the multielement chemical analysis of groundwater samples. Based on the obtained results the heavy metal pollution index (HPI) was calculated for the heavy metals of water points. The calculated HPI index revealed that the groundwater in the Golden Triangle area is contaminated with serious heavy metals. The contamination level is in the order of coastal zone > crystalline rocks zone > Nile valley zone. The groundwater samples HW, BH and FKH are not suitable for drinking purposes due to the presence of high levels of toxic metal ions such as As, Mn, Cd, Co, Ni, Se, V, and Tl. Water-rock interaction, mining, and agricultural activities along with the impacts of the El-Salhyia sewage plant controlled the enrichment of groundwater with heavy metals.

Chapter 4 discusses the geopolymerization of a heterogeneous geological precursor, calcareous red mudstone. The analyses confirmed the heterogeneity of the used precursor, where the carbonaceous and aluminosilicate components were made up the main composition of the rock. The thermal activation step was crucial to attain an acceptable level of reactivity. Experimental and analytical techniques confirmed an improved reactivity with increasing thermal activation up to 800 ºC. Feeding the geopolymer slurry with more silicate was necessary during the geopolymerization process to reduce the effect of carbonation and to ensure a well-developed structure. The alkali activation of the calcareous red mudstone resulted in the formation of various hydration products, including calcium aluminium silicate hydrate, sodium aluminium silicate hydrate and sodium ferrosialate hydrate phases. Various ions, in addition to Na^+ from alkali activator, which were inherited from the precursor, participated, to some extent, in balancing the negative charge in the geopolymer aluminosilicate framework.

Chapter 5 discusses the feasibility of using the calcareous red mudstone geopolymer in the simultaneous sequestration of Cd^{2+}, Co^{2+}, Mn^{2+}, and Ni^{2+} from an aqueous solution. The impact

of pH, adsorbent mass, initial concentration, temperature, and contact time, on metal ions removal was assessed in batch mode. Furthermore, the adsorption of metal ions was operated in the up flow dynamic mode, ensuring applicability on an industrial scale basis. The geopolymer adsorbents demonstrated an improved adsorption removal in comparison to the raw material. Metal ion sequestration on the geopolymer surfaces was hypothesised to occur by the ion exchange, surface complexation and electrostatic interaction mechanisms. The effectiveness of removing metal ions from groundwater, highly competitive system, has been examined. Statistical regression analysis showed that the data best fit with Langmuir rather than Freundlich isotherm. Additionally, the interaction between geopolymer adsorbent and metal ions could be described by a pseudo-second order kinetic model. Thermodynamics suggested an endothermic, spontaneous, and chemical adsorption mechanism.

Recommendations

Based on the obtained results the following is recommended:

- Experimental studies are needed to explore the role of water-rock/mineral interactions in the enrichment of groundwater with heavy metals. This will help in expecting the climate change impacts on the groundwater quality.
- Investigating the role of structure (e.g., faults and joints) in migrating the deep fluids that may play a role in groundwater contamination, is necessary.
- The proposed geopolymer adsorbent is suitable for treating the cationic species of heavy metals but not the anionic ones; therefore, a modification step is needed to be suitable for the oxyanions removal such as As, V, Se, and Mo.
- Sulfate and chlorides are high in the study area and a suitable remediation methods are needed, especially in the desert regions, while in the cultivated land the level of nitrate is high, and a suitable action is needed as well.
- Investigating the reactivity of other rocks such as igneous and metamorphic along with mining wastes in the geopolymerization are recommended to ensure zero-waste activities and sustainable precursors.

APPENDIX A: EXPERIMENTAL DATA OF CHAPTER 3

Table A- 1: Physicochemical characteristic of groundwater samples.

Well No.	Code	Zone	Longitude	Latitude	Depth (meter)	Elevation (meter)	pH	EC	TDS (mg/l)	Temp.	Well type	Lithology
1	HW	C	33°58'41.57"	26°32'39.29"	25	792	7.44	2.53	1510	25.2	Spring	Dawi limestone
2	NK1	C	34° 9'19.12"	26° 6'31.23"	4.25	128.3	8.58	1352	810	31.3	Borehole	Dawi limestone
3	NK2	C	34° 6'49.78"	26° 8'53.37"	17	91.8	7.85	1518	904	31.1	Borehole	Dawi limestone
4	QH1	C	34° 5'4.25"	26°19'54.09"	-	60	7.3	988	625	31.9	Borehole	Nubia Sandston
5	QH2	C	34° 5'40.12"	26°20'31.00"	-	83	7.7	-	572	30.6	Spring	Dawi limestone
6	QH3	C	34° 5'36.05"	26°20'40.08"	-	42.1	7.08	-	663	28.8	Borehole	Nubia Sandston
7	BH	B	33°36'13.50"	26° 0'41.32"	12	384.2	8.06	640	384	31.7	Hand Dug	Granite
8	FKH	B	33°36'7.91"	26° 0'45.04"	11.12	687	8.13	824	490	28.4	Hand Dug	Serpentinite
9	KH	B	33°27'33.33"	26°48'39.89"	21	682.1	8.23	434	256	27.1	Hand Dug	Granite
10	BSF1	B	33°22'14.63"	26°31'16.97"	17	505	8.07	219	134.5	29	Hand Dug	Granite
11	BSF2	B	33°21'57.93"	26°31'33.34"	19	501	8.2	-	220	28.6	Hand Dug	Granite
12	BSF3	B	33°22'1.83"	26°31'44.47"	20.32	504	8.15	317	190.4	29.2	Hand Dug	Granite
13	BSF4	B	33°21'46.83"	26°31'32.09"	19	501.1	8.22	960	583	28.26	Hand Dug	Granite
14	BSRK	B	33°26'56.79"	26°23'16.03"	20.37	608.3	7.23	-	245	28.1	Hand Dug	Granite
15	LQ1	NV	33° 0'57.21"	25°54'7.82"	>300	130.8	6.83	-	578	31.9	Borehole	Nubia Sandston
16	LQ2	NV	33° 7'20.20"	25°53'26.30"	>300	130.9	7.8	-	634	33.3	Borehole	Nubia Sandston
17	NQ1	NV	32°49'56.14"	26°43'0.88"	214	264	7.73	863	518	33.4	Spring	Nubia Sandston
18	NQ2	NV	32°47'4.96"	26°16'2.45"	>300	113.4	8.02	892	539	44.5	Borehole	Nubia Sandston
19	NQ3	NV	32°46'11.43"	26° 8'36.60"	2.72	79.3	8.13	663	410	28.7	Spring	Quaternary
20	NQ4	NV	32°46'30.57"	26° 8'31.36"	-	89.1	7.73	735	421	31	Borehole	Quaternary
21	NQ5	NV	32°47'10.54"	26° 8'25.95"	26	88.4	7.6	826	510	28.7	Borehole	Quaternary
22	NQ6	NV	32°46'28.07"	26° 8'54.68"	-	82.1	7.6	306	183.7	25.8	Borehole	Quaternary
23	NQ7	NV	32°58'39.13"	26°15'50.89"	-	289	7.56	1980	1122	26.3	Borehole	Nubia Sandston
EC= electrical conductivity, TDS= total dissolved solids, Temp. = temperature, C= coastal, B= Basement rock, NV= Nile Valley												

Table A-2: Groundwater chemistry data.

Well No.	Code	Co ug/L	Mn ug/L	Cd ug/L	As ug/L	Cu ug/L	Zn ug/L	V ug/L	Fe ug/L	U ug/L	Pb ug/L	Tl ug/L	Cs ug/L	Ba ug/L	Cr ug/L	Rb ug/L	Se ug/L	Ni ug/L
1	HW	0.116	12.76	11.30	0.477	8.845	1170	0.854	10.11	30.87	0.218	5.774	0.732	31.99	0.337	53.26	37.30	171.2
2	NK1	0.038	367.7	0.050	0.241	5.727	9.005	0.112	31.30	0.274	0.118	0.002	0.109	245.6	0.149	30.69	0.142	0.570
3	NK2	0.039	4.508	0.080	0.251	3.985	15.83	11.28	57.12	1.538	0.288	0.008	0.782	22.84	1.760	11.70	4.865	1.302
4	QH1	0.279	688.0	0.027	5.706	3.023	31.17	0.090	84.95	0.085	0.336	0.045	0.986	18.92	0.160	19.26	0.031	0.630
5	QH2	0.015	1.398	0.044	0.753	1.752	7.363	4.112	4.951	1.093	0.049	0.032	0.022	21.01	3.122	2.594	7.111	0.447
6	QH3	0.077	15.58	0.547	0.847	5.107	47.31	5.450	31.36	3.243	0.205	0.284	0.033	28.43	3.252	2.671	17.32	2.674
7	BH	5.022	7.389	0.050	7.836	18.63	26.43	14.58	25.01	2.810	0.454	0.004	0.010	41.97	17.85	2.816	24.84	0.803
8	FKH	3.221	1227	0.057	55.66	10.28	10.27	3.344	21.30	3.222	0.155	0.002	0.016	124.6	0.418	5.994	1.900	6.413
9	KH	0.404	360.9	0.047	2.063	7.370	16.82	4.103	156.5	1.135	0.228	0.002	0.004	54.28	0.466	0.863	1.462	1.502
10	BSF1	0.017	2.160	0.014	0.532	3.816	12.00	11.52	8.109	5.804	0.073	0.002	0.002	33.21	3.186	0.261	0.705	1.214
11	BSF2	0.118	4.900	0.076	0.792	12.13	19.39	19.56	32.80	4.037	0.200	0.007	0.014	43.71	1.463	1.634	5.430	0.771
12	BSF3	0.031	15.19	0.025	0.782	4.791	12.92	18.31	23.07	4.921	0.122	0.005	0.004	42.73	3.553	0.299	1.118	0.591
13	BSF4	0.116	6.497	0.083	0.845	9.720	25.78	22.07	50.67	4.401	0.280	0.018	0.013	51.18	1.654	1.469	5.884	1.069
14	BSRK	0.072	7.259	0.039	0.460	7.286	26.41	8.032	15.91	1.679	0.151	0.003	0.019	51.42	0.359	0.981	3.110	0.669
15	LQ1	0.019	110.4	0.027	0.050	4.324	19.47	0.126	201.9	0.077	0.231	0.001	0.486	37.67	0.133	18.90	0.040	0.466
16	LQ2	0.027	145.4	0.013	0.078	2.536	9.399	0.071	374.2	0.034	0.146	0.002	0.518	31.47	0.112	18.79	0.040	0.255
17	NQ1	0.040	143.5	0.018	0.117	4.020	4.326	0.607	30.09	1.023	0.058	0.008	0.079	41.90	0.150	4.052	1.366	0.311
18	NQ2	0.007	31.40	0.012	3.281	1.289	4.647	0.056	46.82	0.026	0.057	0.001	1.386	33.59	0.036	10.42	0.013	0.361
19	NQ3	0.553	211.0	0.022	2.065	14.00	10.00	23.68	13.69	0.00	0.133	0.003	0.015	111.0	1.238	6.573	2.281	4.887
20	NQ4	0.312	55.95	0.030	0.914	4.382	8.302	9.377	11.36	4.334	0.156	0.004	0.006	59.91	1.665	1.929	6.824	1.612
21	NQ5	0.878	23.89	0.021	0.381	5.012	30.61	10.07	2.304	6.467	0.027	0.005	0.007	71.33	6.389	2.227	39.30	2.500
22	NQ6	0.750	113.4	0.019	5.367	5.796	16.74	0.621	3.747	0.279	0.034	0.003	0.009	204.4	0.089	1.413	0.109	2.925
23	NQ7	0.035	245.4	0.012	0.045	1.693	37.14	0.124	81.55	0.600	0.055	0.000	0.042	18.94	0.083	3.881	0.182	0.329

Table A-3: Groundwater major cations chemistry and heavy metal pollution index calculations.

Well No.	Code	Na mg/L	Mg mg/L	Ca mg/L	Σ (Na+K) meq/L	Σ (Ca+Mg) meq/L	Total cations meq/L	Unit weightage (Wi)	Wi X Qi	HPI	Category
1	HW	4293	1047	864.1	189.4	129.4	318.88	3.663	2416	662.6	High
2	NK1	1049	51.26	139.5	46.59	11.19	57.79		40.2	11	Low
3	NK2	503.6	84.66	527.1	22.32	33.32	55.65		73.4	20.1	Medium
4	QH1	254.0	78.57	167.8	11.50	14.86	26.37		82	22.5	Medium
5	QH2	204.3	44.66	208.8	9.029	14.11	23.15		56.2	15.4	Low
6	QH3	302.3	67.04	303.1	13.34	20.67	34.02		162.9	44.6	High
7	BH	251.9	50.41	106.7	11.20	9.486	20.70		581	159.5	High
8	FKH	478.0	43.66	150.7	21.44	11.12	32.58		365	100.1	High
9	KH	199.4	6.547	47.62	8.766	2.920	11.69		83.2	22.8	Medium
10	BSF1	85.74	2.321	18.82	3.769	1.132	4.90		70.3	19.29	Medium
11	BSF2	735.8	24.00	128.6	32.23	8.407	40.64		108	29.6	Medium
12	BSF3	151.5	2.832	20.10	6.632	1.238	7.87		95.2	26.1	Medium
13	BSF4	837.0	27.97	132.4	36.65	8.924	45.58		120.7	33.1	Medium
14	BSRK	90.12	15.55	90.28	4.014	5.794	9.81		63.7	17.4	Low
15	LQ1	529.6	51.58	200.6	23.45	14.27	37.73		51.7	14.1	Low
16	LQ2	528.0	50.69	198.9	23.38	14.11	37.51		39.2	10.7	Low
17	NQ1	306.1	36.68	134.8	13.51	9.763	23.28		40.7	11.1	Low
18	NQ2	443.1	3.718	18.85	19.39	1.248	20.65		37.1	10.1	Low
19	NQ3	324.1	26.26	59.77	14.70	5.150	19.85		164.4	45	High
20	NQ4	277.6	59.16	163.9	12.43	13.06	25.50		92.6	25.4	Medium
21	NQ5	411.9	68.60	165.0	18.40	13.89	32.30		154.4	42.3	High
22	NQ6	78.93	26.56	54.81	3.639	4.927	8.57		109.4	29.9	Medium
23	NQ7	1468	193.6	644.4	64.21	48.16	112.38		38.9	10.6	Low

APPENDIX B: EXPERIMENTAL DATA OF CHAPTER 4

Table B-1: Leaching experiment data of Si and Al release from calcined mudstone at different temperature.

Element/Temperature	500 ^{o}C	600 ^{o}C	700 ^{o}C	800 ^{o}C	900 ^{o}C
Si (mg/L)	46.9	64.6	93.3	168.0	57.4
Al (mg/L)	16.3	20.7	40.7	96.5	53.8

APPENDIX C: EXPERIMENTAL DATA OF CHAPTER 5

Table C-1: Batch adsorption data of metal ions removal using raw material.

Time	Ct (Mn^{2+})	Ct (Co^{2+})	Ct (Ni^{2+})	Ct (Cd^{2+})	C_0 (mg/L)	Removal (%) Mn^{2+}	Removal (%) Co^{2+}	Removal(%) Ni^{2+}	Removal(%) Cd^{2+}	Temp. (^oC)	pH	Dose (g)
5	8.14	8.11	8.13	9.55	10	18.5	18.8	18.6	4.43	25	6.5	0.08
10	8.16	8.18	8.00	9.49		18.3	18.1	19.9	5.01			
20	8.14	8.18	8.05	9.45		18.5	18.1	19.4	5.49			
100	8.07	8.06	7.95	9.29		19.2	19.3	20.4	7.02			
120	8.07	8.07	7.99	9.24		19.2	19.2	20.0	7.54			
140	8.10	8.04	7.97	9.24		18.9	19.5	20.2	7.57			
150	7.93	7.86	7.74	9.10		20.6	21.3	22.5	8.95			
180	7.85	7.79	7.72	8.99		21.4	22.0	22.7	10.0			
240	8.05	7.96	7.87	9.13		19.4	20.3	21.2	8.64			

Table C-2: Batch adsorption data of metal ions removal at different time intervals for MR-3 geopolymer adsorbent.

Time	Ct (Mn^{2+})	Ct (Co^{2+})	Ct (Ni^{2+})	Ct (Cd^{2+})	Removal (%) Mn^{2+}	Removal (%) Co^{2+}	Removal(%) Ni^{2+}	Removal(%) Cd^{2+}	q_m (mg/g) Mn^{2+}	q_m (mg/g) Co^{2+}	q_m (mg/g) Ni^{2+}	q_m (mg/g) Cd^{2+}
1	9.19	8.22	8.01	9.61	8.06	17.7	19.8	3.83	1.00	2.22	2.48	0.47
3	8.86	7.91	7.77	9.06	11.3	20.8	22.2	9.38	1.415	2.61	2.77	1.17
5	8.43	7.42	7.29	8.39	15.6	25.7	27.0	16.0	1.95	3.22	3.38	2.00
10	7.95	6.95	6.84	7.26	20.4	30.4	31.5	27.3	2.55	3.80	3.94	3.42
20	7.18	5.97	6.00	5.43	28.1	40.2	39.9	45.6	3.52	5.03	4.99	5.70
30	6.65	5.30	5.37	4.25	33.4	46.9	46.2	57.4	4.18	5.86	5.77	7.18
40	6.47	4.76	5.03	3.52	35.2	52.3	49.6	64.7	4.40	6.54	6.21	8.09
50	6.06	4.40	4.52	2.88	39.3	55.9	54.7	71.1	4.91	6.99	6.84	8.89
60	5.83	3.96	4.13	2.46	41.6	60.3	58.6	75.3	5.20	7.54	7.32	9.42
70	5.70	3.64	3.91	2.17	42.9	63.5	60.8	78.2	5.37	7.93	7.60	9.78
80	5.47	3.37	3.59	1.85	45.2	66.2	64.0	81.4	5.65	8.27	8.00	10.18
90	5.31	3.00	3.26	1.61	46.8	69.9	67.3	83.8	5.85	8.74	8.41	10.47
100	5.11	2.73	3.04	1.42	48.8	72.6	69.5	85.7	6.10	9.08	8.69	10.71
110	5.14	2.79	3.02	1.58	48.5	72.0	69.7	84.1	6.07	9.00	8.71	10.51
120	4.97	2.47	2.74	1.23	50.2	75.2	72.5	87.6	6.27	9.41	9.07	10.95
130	4.85	2.24	2.47	1.12	51.4	77.5	75.2	88.7	6.42	9.69	9.40	11.09
140	4.75	2.15	2.33	1.03	52.4	78.4	76.6	89.6	6.55	9.80	9.57	11.21
150	4.73	2.05	2.26	0.99	52.6	79.4	77.3	90.0	6.58	9.93	9.66	11.25
160	4.62	1.93	2.16	0.93	53.7	80.6	78.3	90.6	6.71	10.07	9.79	11.33
180	4.53	1.79	1.98	0.89	54.6	82.0	80.1	91.0	6.82	10.25	10.02	11.38
200	4.30	1.54	1.69	0.78	56.9	84.5	83.0	92.1	7.12	10.56	10.37	11.51
240	4.20	1.32	1.45	0.70	57.9	86.7	85.4	92.9	7.23	10.84	10.68	11.61
300	3.93	1.16	1.26	0.65	60.6	88.3	87.3	93.4	7.58	11.03	10.92	11.67
Dose=0.08 g, Ci=10 mg/L, Temperature=25 ^{0}C, pH=6.5												

APPENDIXES

Table C-3: Batch adsorption data of metal ions removal at different time intervals for MR-5 geopolymer adsorbent.

Time	Ct (Mn^{2+})	Ct (Co^{2+})	Ct (Ni^{2+})	Ct (Cd^{2+})	Removal (%) Mn^{2+}	Removal (%) Co^{2+}	Removal(%) Ni^{2+}	Removal(%) Cd^{2+}	q_m (mg/g) Mn^{2+}	q_m (mg/g) Co^{2+}	q_m (mg/g) Ni^{2+}	q_m (mg/g) Cd^{2+}
1	9.28	8.32	8.15	9.57	7.13	16.7	18.4	4.23	0.89	2.09	2.31	0.52
3	9.13	8.16	8.02	9.36	8.64	18.3	19.7	6.33	1.08	2.28	2.46	0.79
5	9.07	7.86	7.71	8.97	9.21	21.3	22.8	10.2	1.15	2.67	2.85	1.28
10	8.56	7.44	7.47	8.10	14.3	25.5	25.2	18.9	1.79	3.18	3.15	2.37
20	7.88	6.70	6.71	6.58	21.1	32.9	32.8	34.1	2.64	4.11	4.11	4.26
30	7.53	6.21	6.30	5.48	24.6	37.8	36.9	45.1	3.07	4.73	4.62	5.63
40	7.10	5.66	5.81	4.68	28.9	43.3	41.8	53.1	3.62	5.41	5.22	6.64
50	6.94	5.26	5.52	4.06	30.5	47.3	44.7	59.3	3.82	5.91	5.59	7.42
60	6.58	4.85	5.01	3.43	34.1	51.4	49.8	65.6	4.26	6.43	6.22	8.20
70	6.44	4.54	4.83	3.15	35.5	54.5	51.6	68.4	4.44	6.81	6.45	8.56
80	6.03	4.06	4.40	2.63	39.6	59.3	55.9	73.6	4.95	7.41	6.99	9.20
90	5.98	3.82	4.18	2.33	40.1	61.7	58.1	76.6	5.01	7.71	7.27	9.58
100	5.81	3.55	3.89	2.05	41.8	64.4	61.0	79.4	5.23	8.06	7.62	9.93
110	5.63	3.27	3.64	1.83	43.6	67.2	63.5	81.6	5.45	8.40	7.94	10.21
120	5.52	3.10	3.45	1.68	44.7	68.9	65.4	83.1	5.58	8.61	8.17	10.39
130	5.35	2.88	3.27	1.57	46.4	71.1	67.2	84.2	5.80	8.89	8.40	10.52
140	5.20	2.67	3.06	1.37	47.9	73.2	69.3	86.2	5.99	9.15	8.67	10.77
150	5.10	2.44	2.88	1.26	48.9	75.5	71.16	87.3	6.11	9.44	8.89	10.91
160	4.91	2.25	2.64	1.17	50.8	77.4	73.5	88.2	6.36	9.67	9.19	11.02
180	4.96	2.27	2.70	1.21	50.3	77.2	72.9	87.8	6.29	9.65	9.12	10.97
200	4.65	1.84	2.21	0.95	53.4	81.5	77.8	90.4	6.67	10.1	9.72	11.30
240	4.50	1.54	1.90	0.85	54.9	84.5	80.9	91.4	6.87	10.5	10.1	11.43
300	4.28	1.30	1.61	0.76	57.1	86.9	83.8	92.3	7.14	10.86	10.48	11.54
Dose=0.08 g, Ci=10 mg/L, Temperature=25 ^{0}C, pH=6.5												

Table C-4: Batch adsorption data of metal ions removal at different time intervals for MR-4 geopolymer adsorbent.

Time	Ct (Mn^{2+})	Ct (Co^{2+})	Ct (Ni^{2+})	Ct (Cd^{2+})	Removal (%) Mn^{2+}	Removal (%) Co^{2+}	Removal(%) Ni^{2+}	Removal(%) Cd^{2+}	q_m (mg/g) Mn^{2+}	q_m (mg/g) Co^{2+}	q_m (mg/g) Ni^{2+}	q_m (mg/g) Cd^{2+}
1	8.26	8.29	8.15	9.63	17.3	17.0	18.4	3.63	2.16	2.12	2.30	0.45
3	8.16	8.18	8.08	9.43	18.3	18.1	19.1	5.60	2.28	2.27	2.39	0.70
5	8.09	8.06	8.02	9.20	19.0	19.3	19.7	7.94	2.38	2.42	2.47	0.99
10	7.69	7.63	7.57	8.40	23.0	23.6	24.2	15.9	2.87	2.95	3.03	1.99
20	7.01	6.85	6.91	6.90	29.8	31.4	30.8	30.9	3.72	3.92	3.85	3.86
30	6.77	6.35	6.55	5.92	32.2	36.4	34.4	40.7	4.02	4.55	4.30	5.09
40	6.39	5.79	6.12	5.01	36.0	42.0	38.7	49.8	4.50	5.25	4.84	6.23
50	6.08	5.43	5.82	4.33	39.1	45.6	41.7	56.6	4.89	5.70	5.21	7.07
60	5.82	5.01	5.42	3.74	41.7	49.8	45.7	62.5	5.21	6.23	5.72	7.81
70	5.64	4.75	5.12	3.36	43.5	52.4	48.7	66.3	5.44	6.56	6.09	8.29
80	5.46	4.40	4.91	2.97	45.3	55.9	50.8	70.2	5.66	6.99	6.35	8.78
90	5.36	4.14	4.71	2.67	46.3	58.5	52.8	73.2	5.79	7.31	6.60	9.16
100	5.10	3.83	4.44	2.35	48.9	61.6	55.5	76.4	6.12	7.70	6.94	9.55
110	4.92	3.58	4.19	2.13	50.7	64.1	58.0	78.6	6.33	8.01	7.25	9.82
120	4.78	3.28	3.94	1.90	52.1	67.1	60.5	80.9	6.52	8.38	7.57	10.11
130	4.61	3.03	3.67	1.71	53.8	69.6	63.2	82.8	6.72	8.70	7.90	10.35
140	4.43	2.80	3.43	1.53	55.6	71.9	65.6	84.6	6.95	8.99	8.20	10.58
150	4.35	2.66	3.25	1.40	56.4	73.3	67.4	85.9	7.05	9.17	8.42	10.73
160	4.25	2.48	3.10	1.30	57.4	75.1	68.9	86.9	7.17	9.39	8.62	10.87
180	3.91	2.13	2.66	1.06	60.8	78.6	73.3	89.3	7.60	9.83	9.16	11.16
200	3.64	1.69	2.31	0.87	63.5	83.0	76.8	91.2	7.94	10.38	9.61	11.41
240	3.38	1.40	1.96	0.71	66.1	85.9	80.3	92.8	8.26	10.74	10.04	11.60
300	3.08	1.06	1.52	0.58	69.1	89.3	84.7	94.1	8.64	11.1	10.59	11.76
Dose=0.08 g, Ci=10 mg/L, Temperature=25 ^{0}C, pH=6.5												

Table C-5: Batch adsorption data of metal ions removal at different pH.

pH	Ct (Mn^{2+})	Ct (Co^{2+})	Ct (Ni^{2+})	Ct (Cd^{2+})	Removal (%) Mn^{2+}	Removal (%) Co^{2+}	Removal(%) Ni^{2+}	Removal(%) Cd^{2+}	q_m (mg/g) Mn^{2+}	q_m (mg/g) Co^{2+}	q_m (mg/g) Ni^{2+}	q_m (mg/g) Cd^{2+}
MR-3 geopolymer adsorbent												
3	10.68	10.50	10.82	10.31	-	-	-	-	-	-	-	-
4	9.28	8.74	8.98	8.28	7.14	12.5	10.14	17.1	0.89	1.57	1.26	2.14
5	7.70	6.81	7.14	5.25	22.9	31.8	28.5	47.4	2.86	3.97	3.56	5.93
6	6.39	5.17	5.47	3.61	36.0	48.2	45.2	63.8	4.50	6.02	5.65	7.97
7	6.04	4.52	4.84	2.77	39.5	54.7	51.5	72.2	4.94	6.83	6.44	9.03
8	5.43	3.53	3.89	2.16	45.6	64.6	61.0	78.3	5.70	8.07	7.63	9.79
MR-4 geopolymer adsorbent												
3	10.55	10.30	10.54	10.13	-	-	-	-	-	-	-	-
4	8.80	8.29	8.49	7.79	11.9	17.0	15.0	22.0	1.49	2.13	1.88	2.75
5	7.21	6.45	6.74	5.14	27.8	35.4	32.5	48.5	3.48	4.43	4.06	6.06
6	6.58	5.56	5.91	3.98	34.1	44.3	40.8	60.1	4.27	5.54	5.10	7.52
7	6.46	5.23	5.50	3.90	35.3	47.6	44.9	60.9	4.41	5.95	5.61	7.61
8	6.12	4.65	4.96	3.36	38.7	53.4	50.3	66.3	4.84	6.68	6.29	8.29
MR-5 geopolymer adsorbent												
3	10.66	10.44	10.69	10.38	-	-	-	-	-	-	-	-
4	9.21	8.61	8.82	8.18	7.86	13.8	11.7	18.1	0.98	1.73	1.47	2.27
5	7.77	6.78	7.01	5.62	22.2	32.1	29.8	43.7	2.77	4.01	3.72	5.46
6	6.76	5.52	5.81	4.09	32.3	44.7	41.8	59.0	4.04	5.59	5.23	7.38
7	6.44	5.01	5.31	3.58	35.5	49.8	46.8	64.1	4.44	6.22	5.85	8.02
8	6.25	4.47	4.79	3.09	37.4	55.2	52.0	69.0	4.68	6.90	6.50	8.63
Dose=0.08 g, Ci=10 mg/L, Temperature=25 ^{0}C												

Table C-6: Batch adsorption data of metal ions removal at different initial concentration.

C_i mg/L	Ct (Mn^{2+})	Ct (Co^{2+})	Ct (Ni^{2+})	Ct (Cd^{2+})	Removal (%) Mn^{2+}	Removal (%) Co^{2+}	Removal(%) Ni^{2+}	Removal(%) Cd^{2+}	q_m (mg/g) Mn^{2+}	q_m (mg/g) Co^{2+}	q_m (mg/g) Ni^{2+}	q_m (mg/g) Cd^{2+}
MR-3 geopolymer adsorbent												
5	1.68	0.99	1.34	0.43	66.5	80.2	73.3	91.3	4.15	5.01	4.58	5.71
10	6.15	4.33	4.83	2.87	38.5	56.7	51.7	71.3	4.81	7.08	6.46	8.91
20	16.12	13.65	14.27	9.91	19.4	31.7	28.6	50.5	4.85	7.94	7.16	12.61
30	25.99	23.49	23.97	19.38	13.4	21.7	20.1	35.4	5.02	8.14	7.53	13.27
40	34.50	31.26	31.31	26.85	13.8	21.8	21.7	32.9	6.88	10.92	10.86	16.44
100	93.94	88.30	87.53	83.74	6.1	11.7	12.5	16.3	7.58	14.62	15.58	20.33
MR-4 geopolymer adsorbent												
5	1.88	1.22	1.68	0.62	62.5	75.6	66.4	87.6	3.91	4.72	4.15	5.47
10	6.69	5.32	5.94	3.46	33.1	46.8	40.6	65.4	4.14	5.85	5.08	8.18
20	17.29	15.42	16.03	12.27	13.5	22.9	19.8	38.7	3.38	5.72	4.96	9.67
30	26.95	25.08	25.77	21.07	10.2	16.4	14.1	29.8	3.82	6.15	5.29	11.16
40	35.15	33.87	34.24	31.35	12.1	15.3	14.4	21.6	6.07	7.66	7.20	10.81
100	92.50	88.52	88.25	87.43	7.5	11.5	11.8	12.6	9.38	14.35	14.69	15.72
MR-5 geopolymer adsorbent												
5	1.95	1.23	1.55	0.80	61.1	75.3	68.9	84.0	3.82	4.71	4.31	5.25
10	6.25	4.38	4.95	3.08	37.5	56.2	50.5	69.2	4.69	7.02	6.31	8.66
20	16.66	13.92	14.61	10.49	16.7	30.4	26.9	47.5	4.18	7.60	6.74	11.89
30	26.54	23.86	24.24	20.14	11.5	20.5	19.2	32.9	4.33	7.67	7.19	12.32
40	34.54	31.17	31.53	27.31	13.6	22.1	21.2	31.7	6.82	11.04	10.58	15.86
100	92.43	88.31	87.16	86.65	7.6	11.7	12.8	13.4	9.47	14.61	16.05	16.69
Dose=0.08 g, pH=6.5, Temperature=25 ^{0}C												

Table C-7: Batch adsorption data of metal ions removal at different geopolymer dose.

Dose (g)	Ct (Mn^{2+})	Ct (Co^{2+})	Ct (Ni^{2+})	Ct (Cd^{2+})	Removal (%) Mn^{2+}	Removal (%) Co^{2+}	Removal(%) Ni^{2+}	Removal(%) Cd^{2+}	q_m (mg/g) Mn^{2+}	q_m (mg/g) Co^{2+}	q_m (mg/g) Ni^{2+}	q_m (mg/g) Cd^{2+}
MR-3 geopolymer adsorbent												
0.04	8.23	7.34	7.71	5.24	17.7	26.6	22.9	47.6	4.43	6.65	5.73	11.89
0.06	7.03	5.55	6.07	3.65	29.7	44.5	39.3	63.5	4.95	7.41	6.54	10.58
0.08	5.07	4.09	4.55	3.42	49.3	59.1	54.5	65.8	6.16	7.39	6.81	8.23
0.1	3.85	2.17	2.94	0.98	61.5	78.3	70.6	90.2	6.15	7.83	7.06	9.02
0.14	2.60	1.15	1.47	0.59	74.0	88.5	85.3	94.1	5.29	6.32	6.09	6.72
MR-4 geopolymer adsorbent												
0.04	8.41	7.85	8.30	7.10	15.9	21.5	17.0	29.0	3.97	5.38	4.24	7.26
0.06	7.46	6.72	7.42	5.32	25.4	32.8	25.8	46.8	4.23	5.46	4.30	7.80
0.08	6.57	5.47	6.09	3.87	34.3	45.3	39.1	61.3	4.29	5.67	4.89	7.66
0.1	5.73	4.41	5.13	2.99	42.7	55.9	48.7	70.1	4.27	5.59	4.87	7.01
0.14	5.19	4.42	4.80	3.85	48.1	55.8	52.0	61.5	3.44	3.99	3.71	4.39
MR-5 geopolymer adsorbent												
0.04	8.39	7.48	7.66	6.26	16.1	25.2	23.4	37.4	4.01	6.31	5.86	9.34
0.06	7.34	6.04	6.43	4.34	26.6	39.6	35.7	56.6	4.43	6.60	5.95	9.44
0.08	6.39	4.79	5.28	3.11	36.1	52.1	47.2	68.9	4.51	6.51	5.90	8.61
0.1	5.15	3.27	3.79	1.82	48.5	67.3	62.1	81.8	4.85	6.73	6.21	8.18
0.14	2.94	1.29	1.77	0.89	70.6	87.1	82.3	91.1	5.04	6.22	5.88	6.51
pH=6.5, Ci=10 mg/L, Temperature=25 ^{0}C												

Table C-8: Batch adsorption data of metal ions removal at different grain size.

Size (um)	Ct (Mn^{2+})	Ct (Co^{2+})	Ct (Ni^{2+})	Ct (Cd^{2+})	Removal (%) Mn^{2+}	Removal (%) Co^{2+}	Removal(%) Ni^{2+}	Removal(%) Cd^{2+}	q_m (mg/g) Mn^{2+}	q_m (mg/g) Co^{2+}	q_m (mg/g) Ni^{2+}	q_m (mg/g) Cd^{2+}
MR-3 geopolymer adsorbent												
500-250	6.49	5.27	5.70	3.75	35.1	47.3	43.0	62.5	4.38	5.91	5.38	7.82
250-125	6.26	4.56	5.10	2.53	37.4	54.4	49.0	74.7	4.68	6.80	6.12	9.34
125-63	5.32	3.35	4.39	1.13	46.8	66.5	56.1	88.7	5.85	8.31	7.01	11.08
MR-4 geopolymer adsorbent												
500-250	7.40	6.70	7.08	5.27	26.0	33.0	29.2	47.3	3.25	4.12	3.66	5.91
250-125	6.67	5.43	6.07	3.51	33.3	45.7	39.3	64.9	4.16	5.71	4.91	8.12
125-63	5.19	3.48	4.44	1.31	48.1	65.2	55.6	86.9	6.01	8.15	6.95	10.86
MR-5 geopolymer adsorbent												
500-250	6.88	5.57	5.94	4.29	31.2	44.3	40.6	57.1	3.90	5.54	5.08	7.14
250-125	6.52	4.86	5.40	3.41	34.8	51.4	46.0	65.9	4.35	6.42	5.75	8.24
125-63	5.83	4.06	4.97	2.00	41.7	59.4	50.3	80.0	5.21	7.42	6.28	10.00
pH=6.5, Ci=10 mg/L, Temperature=25 ^{0}C, Time=60 min												

Table C-9: Batch adsorption experimental data for metal ions removal at different temperature, MR-3 geopolymer.

Temp ^{o}C	**Ct (Mn^{2+})**	**Ct (Co^{2+})**	**Ct (Ni^{2+})**	**Ct (Cd^{2+})**	**Removal (%) Mn^{2+}**	**Removal (%) Co^{2+}**	**Removal(%) Ni^{2+}**	**Removal(%) Cd^{2+}**	**q_m (mg/g) Mn^{2+}**	**q_m (mg/g) Co^{2+}**	**q_m (mg/g) Ni^{2+}**	**q_m (mg/g) Cd^{2+}**
25	6.07	3.93	4.50	2.21	39.3	60.7	55.0	77.9	4.91	7.59	6.87	9.74
35	5.24	2.49	2.85	1.43	47.6	75.1	71.5	85.7	5.95	9.39	8.94	10.72
45	3.78	0.93	1.10	0.88	62.2	90.7	89.0	91.2	7.77	11.34	11.12	11.40
55	1.69	0.20	0.36	0.44	83.1	98.0	96.4	95.6	10.39	12.25	12.05	11.95
pH=6.5, Ci=10 mg/L, Temperature=25 ^{0}C												

Table C-10: Dynamic adsorption experimental data.

Time	Ct (Mn^{2+})	Ct (Co^{2+})	Ct (Ni^{2+})	Ct (Cd^{2+})	C_t/C_0 Mn^{2+}	C_t/C_0 Co^{2+}	C_t/C_0 Ni^{2+}	C_t/C_0 Cd^{2+}	Ct (Mn^{2+})	Ct (Co^{2+})	Ct (Ni^{2+})	Ct (Cd^{2+})	C_t/C_0 Mn^{2+}	C_t/C_0 Co^{2+}	C_t/C_0 Ni^{2+}	C_t/C_0 Cd^{2+}
5	3.304	2.913	2.775	3.848	0.330	0.291	0.277	0.385	0.360	0.635	0.534	0.489	0.036	0.063	0.053	0.049
10	3.726	3.225	3.228	3.729	0.373	0.323	0.323	0.373	0.303	0.375	0.375	0.336	0.030	0.038	0.037	0.034
20	4.455	3.964	3.946	3.958	0.445	0.396	0.395	0.396	0.331	0.312	0.343	0.283	0.033	0.031	0.034	0.028
30	4.947	4.379	4.393	4.290	0.495	0.438	0.439	0.429	0.469	0.383	0.468	0.427	0.047	0.038	0.047	0.043
40	5.323	4.766	4.803	4.608	0.532	0.477	0.480	0.461	0.546	0.396	0.441	0.492	0.055	0.040	0.044	0.049
50	5.666	5.037	5.055	4.804	0.567	0.504	0.506	0.480	0.999	0.673	0.731	0.868	0.100	0.067	0.073	0.087
60	5.975	5.374	5.346	5.061	0.598	0.537	0.535	0.506	1.423	1.030	1.082	1.117	0.142	0.103	0.108	0.112
90	6.723	5.948	5.969	5.573	0.672	0.595	0.597	0.557	2.259	1.743	1.812	1.533	0.226	0.174	0.181	0.153
120	7.121	6.310	6.273	5.898	0.712	0.631	0.627	0.590	3.007	2.301	2.365	1.919	0.301	0.230	0.236	0.192
150	7.482	6.681	6.576	6.240	0.748	0.668	0.658	0.624	3.588	2.741	2.753	2.278	0.359	0.274	0.275	0.228
180	7.745	6.892	6.829	6.505	0.774	0.689	0.683	0.651	4.219	3.267	3.276	2.666	0.422	0.327	0.328	0.267
210	7.929	7.094	6.967	6.668	0.793	0.709	0.697	0.667	4.669	3.552	3.559	2.937	0.467	0.355	0.356	0.294
240	8.105	7.243	7.104	6.868	0.811	0.724	0.710	0.687	5.088	3.905	3.891	3.269	0.509	0.391	0.389	0.327
270	8.251	7.411	7.295	7.063	0.825	0.741	0.730	0.706	5.406	4.153	4.133	3.471	0.541	0.415	0.413	0.347
300	8.439	7.559	7.461	7.273	0.844	0.756	0.746	0.727	5.668	4.364	4.301	3.698	0.567	0.436	0.430	0.370
330	8.445	7.613	7.449	7.287	0.844	0.761	0.745	0.729	6.117	4.801	4.699	4.056	0.612	0.480	0.470	0.406
360	8.538	7.640	7.573	7.361	0.854	0.764	0.757	0.736	6.313	4.955	4.845	4.194	0.631	0.495	0.485	0.419
390	8.611	7.744	7.626	7.484	0.861	0.774	0.763	0.748	6.611	5.182	5.032	4.428	0.661	0.518	0.503	0.443
420	8.715	7.860	7.727	7.564	0.871	0.786	0.773	0.756	6.709	5.259	5.124	4.537	0.671	0.526	0.512	0.454
450	8.846	7.898	7.762	7.670	0.885	0.790	0.776	0.767	6.896	5.438	5.292	4.719	0.690	0.544	0.529	0.472
Bed depth=6 cm, Ci=10 mg/L, Temp=25 ^{0}C, Flow rate=0.016 L/h									Bed depth=12 cm, Ci=10 mg/L, Tempe=25 ^{o}C, Flow rate=0.016 L/h							

Table C-11: Regeneration experiments data using MR-3 geopolymer adsorbent.

Cycle	Ct (Mn^{2+})	Ct (Co^{2+})	Ct (Ni^{2+})	Ct (Cd^{2+})	Removal (%) Mn^{2+}	Removal (%) Co^{2+}	Removal(%) Ni^{2+}	Removal(%) Cd^{2+}	q_m (mg/g) Mn^{2+}	q_m (mg/g) Co^{2+}	q_m (mg/g) Ni^{2+}	q_m (mg/g) Cd^{2+}
Adsorption												
1	0.60	0.56	0.74	0.47	94.0	94.4	92.6	95.3	0.45	0.45	0.44	0.45
2	1.63	1.43	1.81	1.39	83.7	85.7	81.9	86.1	0.40	0.41	0.39	0.41
3	2.85	2.56	2.98	2.35	71.5	74.4	70.2	76.5	0.34	0.35	0.33	0.36
4	3.39	2.99	3.44	2.87	66.1	70.1	65.6	71.3	0.31	0.33	0.31	0.34
5	3.50	3.05	3.48	2.89	65.0	69.5	65.2	71.1	0.31	0.33	0.31	0.34
6	4.51	4.06	4.40	3.95	54.9	59.4	56.0	60.5	0.26	0.28	0.27	0.29
7	4.74	4.49	4.72	4.38	52.6	55.1	52.8	56.2	0.25	0.26	0.25	0.27
8	4.85	4.55	4.76	4.38	51.5	54.5	52.4	56.2	0.25	0.26	0.25	0.27
Desorption												
1	7.27	6.84	8.40	7.70								
8	5.10	5.09	5.09	5.28								
Dose=0.08 g, Ci=10 mg/L, Temperature=25 ^{0}C, Dose=2.1g, Time=60 min, pH=8												

Table C-12: Batch adsorption data for groundwater decontamination using MR-3 geopolymer adsorbent.

Sample	**Ct (Mn^{2+})**	**Ct (Co^{2+})**	**Ct (Ni^{2+})**	**Ct (Cd^{2+})**	**Removal (%) Mn^{2+}**	**Removal (%) Co^{2+}**	**Removal(%) Ni^{2+}**	**Removal(%) Cd^{2+}**	**q_m (mg/g) Mn^{2+}**	**q_m (mg/g) Co^{2+}**	**q_m (mg/g) Ni^{2+}**	**q_m (mg/g) Cd^{2+}**
LQ1	8.36	5.55	7.88	3.82	44.3	63.0	47.5	74.5	8.30	11.8	8.90	14.0
QH2	9.24	5.16	6.57	3.75	38.4	65.6	56.2	75.0	7.20	12.3	10.54	14.1
KH	8.27	4.46	6.48	1.56	44.9	70.3	56.8	89.6	8.42	13.2	10.66	16.8
Dose=0.1 g, Ci=10 mg/L, Temperature=25 ^{o}C, Time=120 min, pH=8												

Table C-13: Batch adsorption data of co-existing anions experiments.

	Ct (Mn^{2+})	Ct (Co^{2+})	Ct (Ni^{2+})	Ct (Cd^{2+})	Removal (%) Mn^{2+}	Removal (%) Co^{2+}	Removal(%) Ni^{2+}	Removal(%) Cd^{2+}	q_m (mg/g) Mn^{2+}	q_m (mg/g) Co^{2+}	q_m (mg/g) Ni^{2+}	q_m (mg/g) Cd^{2+}
Carbonate												
0.5	5.52	3.70	4.14	2.32	44.8	63.0	58.6	76.8	5.60	7.88	7.33	9.60
200	6.30	4.59	5.29	2.43	37.0	54.1	47.1	75.7	4.62	6.76	5.89	9.46
400	6.18	4.64	5.45	2.30	38.2	53.6	45.5	77.0	4.78	6.71	5.69	9.62
800	6.31	4.98	5.95	2.14	36.9	50.2	40.5	78.6	4.61	6.27	5.06	9.83
Sulphate												
0.5	6.15	4.58	4.99	2.70	38.5	54.2	50.1	73.0	4.81	6.77	6.27	9.13
200	6.27	4.57	4.90	2.68	37.3	54.3	51.0	73.2	4.67	6.78	6.37	9.16
400	6.47	5.09	5.46	3.20	35.3	49.1	45.4	68.0	4.41	6.14	5.68	8.51
800	6.66	5.14	5.77	3.42	33.4	48.6	42.3	65.8	4.18	6.07	5.29	8.23
Chloride												
0.5	5.81	4.10	4.54	2.30	41.9	59.0	54.6	77.0	5.23	7.37	6.82	9.62
200	6.06	4.70	5.17	3.31	39.4	53.0	48.3	66.9	4.93	6.62	6.03	8.36
400	6.44	4.86	5.40	3.61	35.6	51.4	46.0	63.9	4.45	6.43	5.74	7.99
800	5.93	4.32	5.00	4.12	40.7	56.8	50.0	58.8	5.08	7.11	6.25	7.35
Dose=0.08 g, Ci=10 mg/L, Temperature=25 ^{0}C, Time=60 min												